Double-Sided 3D Silicon Detectors for the High-Luminosity LHC

Dissertation
zur Erlangung des Doktorgrades
der Fakultät für Mathematik und Physik
der Albert–Ludwigs–Universität Freiburg im Breisgau

vorgelegt von
Michael Köhler

Juli 2011

Dekan:	Prof. Dr. K. Königsmann
1. Gutachter:	Prof. Dr. K. Jakobs
2. Gutachter:	Prof. Dr. G. Herten

Datum der Prüfung: 12. September 2011

Contents

1 Introduction **6**

2 Luminosity Upgrades of the LHC **9**
2.1 Large Hadron Collider 9
2.1.1 ATLAS Experiment 10
2.1.2 Physics at the LHC 13
2.2 High-Luminosity LHC 14
2.2.1 Physics Motivation for the HL-LHC 15
2.2.2 ATLAS Upgrade 16

3 Silicon and Silicon Detectors **20**
3.1 Production of Detector Grade Silicon 20
3.2 Properties of Silicon 21
3.2.1 Energy Band Structure of Silicon 21
3.2.2 Extrinsic Silicon 23
3.2.3 p-n Junction 24
3.3 Silicon Detectors 25
3.3.1 Diode with Application of External Voltage 25
3.3.2 Leakage Current 28
3.3.3 Principle Design of Planar Silicon Strip Detectors 28
3.3.4 Energy Loss of Particles in Silicon 31
3.3.5 Drift and Diffusion 35
3.3.6 Signal Generation in Silicon Detectors 35
3.3.7 Impact Ionisation 37
3.3.8 Noise Contributions 38

4 Radiation Damage of Silicon Detectors **41**
4.1 Radiation Damage Mechanisms 41
4.1.1 Surface Damage 41
4.1.2 Bulk Damage 42
4.2 The NIEL Scaling Hypothesis 44
4.3 Effects of Radiation Damage on Detector Properties 46
4.3.1 Effective Doping Concentration and Depletion Voltage 46
4.3.2 Leakage Current 50
4.3.3 Trapping 51
4.3.4 Double Junction 54

4.3.5 Charge Collection . . . 55
4.4 Approaches for Radiation Hard Silicon Detectors . . . 57
4.4.1 Material Engineering . . . 57
4.4.2 Planar Detectors with n-Side Readout . . . 58
4.4.3 Thin Detectors . . . 60
4.4.4 Operation with Forward Bias . . . 60
4.4.5 3D Detectors . . . 60

5 Devices Under Test and Experimental Methods 64
5.1 Devices Under Test . . . 64
5.1.1 Double-Sided 3D Detectors . . . 64
5.1.2 Planar Detectors . . . 70
5.1.3 Proton Irradiations . . . 71
5.2 Alibava Readout System . . . 72
5.3 Beta Source Measurements . . . 74
5.3.1 Measurements and Analysis Procedure . . . 76
5.3.2 Calibration . . . 78
5.4 Laser Measurements . . . 79
5.4.1 Measurements and Analysis Procedure . . . 81
5.5 Beam Test Measurements . . . 84
5.5.1 Alignment . . . 85
5.5.2 Analysis Procedure . . . 89
5.5.3 Calibration . . . 91

6 Measurements of 3D Detectors 93
6.1 Measurements before Irradiation . . . 93
6.1.1 Beam Test Measurements . . . 93
6.1.2 Beta Source Measurements . . . 108
6.1.3 Noise . . . 111
6.1.4 Laser Measurements . . . 112
6.2 Measurements After Irradiation . . . 122
6.2.1 Punch-Through Biasing Problems in FBK Detectors . . . 122
6.2.2 Beam Test Measurements . . . 124
6.2.3 Beta Source Measurements . . . 132
6.2.4 Noise Studies . . . 141
6.2.5 Annealing Studies . . . 155
6.2.6 Laser Measurements . . . 163

7 Measurements of Planar Detectors 177
7.1 Beta Source Measurements . . . 177
7.2 Noise Measurements . . . 179
7.3 Annealing Studies . . . 180
7.4 Laser Measurements . . . 183

8 Summary and Conclusions 190

Acronyms and Abbreviations 195

Bibliography **197**

Acknowledgements **207**

Chapter 1

Introduction

Silicon detectors are employed in all modern high-energy physics experiments. Due to the high spatial resolution, short signal collection time and low mass, silicon detectors are excellently suited for precise track and vertex measurements in particle collider experiments. The advanced technology of microelectronics allows the reliable production of highly integrated silicon sensors at an affordable cost.

Silicon detectors have made important contributions to electroweak and heavy quark physics, such as the discovery of the top quark [Abe95, Aba95] with the CDF[1] and D0 experiments at the Tevatron at Fermilab. A crucial contribution to this discovery was the tagging of b-quark jets. A jet containing a b-quark can be identified due to the presence of a secondary vertex in addition to the primary interaction point. The identification of secondary vertices is possible with the excellent spatial resolution of silicon detectors, which can be of the order of micrometers.

In current LHC[2] experiments, a high track density due to multiple interactions per collision poses a challenge for the tracking detectors. Therefore, very fine detector segmentations are required in order to perform precise measurements of the tracks of charged particles. The identification of secondary decay vertices and the tagging of b-quarks is of particular importance, since the final states of many interesting physics processes contain b-quarks. b-tagging plays a key role in top quark physics and in the searches for the Higgs boson and for supersymmetric particles. In all four large experiments at the LHC (ATLAS[3], CMS[4], LHCb[5] and ALICE[6]), silicon detectors are employed in the central tracking systems. Most experiments use both silicon pixel and strip detectors.

To extend the physics potential of the LHC, a luminosity upgrade is planned. The HL-LHC (High-Luminosity LHC) is foreseen to start operation approximately in the year 2024. The peak instantaneous luminosity will be increased by a factor of five compared to the design specification of the LHC. The increased track density requires a finer de-

[1] Collider Detector at Fermilab
[2] Large Hadron Collider
[3] A Toroidal LHC ApparatuS
[4] Compact Muon Solenoid
[5] Large Hadron Collider beauty
[6] A Large Ion Collider Experiment

tector segmentation. Over the projected lifetime of the HL-LHC, the tracking detectors will have to withstand a five to ten times higher radiation dose than that at the LHC. In silicon detectors, radiation damage increases the leakage current, the effective doping concentration and the charge carrier trapping probability. These effects lead to a decrease of the signal-to-noise ratio after high radiation fluences.

As the silicon detectors currently installed are not expected to be sufficiently radiation tolerant, novel detector technologies are under study. In the current ATLAS detector, planar n-in-n silicon pixel detectors and planar p-in-n silicon strip detectors are used. For the ATLAS upgrade, planar silicon n-in-p detectors are foreseen for the region to be equipped with strip detectors. In the inner pixel layer, which is closest to the interaction point, the detectors will have to withstand an unprecedentedly high radiation fluence of $2 \times 10^{16}\,\mathrm{n_{eq}/cm^2}$ (1 MeV neutron equivalent particles per square centimetre). An option for extremely radiation hard detectors are 3D detectors with columnar electrodes etched into the substrate perpendicular to the surface. In contrast to traditional planar detectors, where the electrodes are limited to the detector surface, the electrodes of 3D detectors extend into the third dimension, i.e. into the detector depth.

In 3D detectors, the distance for drift of generated charge carriers and for depletion is given by the spacing between columnar electrodes of opposite doping types rather than by the detector thickness as in planar detectors. Therefore, enhanced radiation hardness is expected due to reduced trapping and a reduced depletion voltage, while the total ionised charge is determined by the substrate thickness. As a simplification of the original 3D detector design, double-sided 3D detectors have been developed. The electrodes pass through the substrate only partially, which increases the mechanical stability and simplifies the fabrication technology.

In this thesis, the performance of double-sided 3D detectors is investigated in detail for the first time. The measurements were performed with strip detectors: on one side of the sensors, the columnar electrodes are connected to $4 - 8$ mm long strips. The response of the detectors to high-energy pions, electrons emitted by a beta source and an infrared laser is studied. Special emphasis is put on signal measurements as a function of the particle's point of incidence. Also, detailed noise measurements were conducted. In order to investigate the radiation hardness of the detectors, they were irradiated with protons up to fluences that are expected for the HL-LHC inner pixel layers. The measurements were performed before any radiation-induced modification of the detector properties and after irradiation to different fluences. The dependence of the detector performance on the radiation fluence was measured separately with 3D detectors in n-in-p and in p-in-n layout. A comparison of the radiation hardness of the two designs is presented. Furthermore, the radiation hardness of planar n-in-p detectors is studied and compared to double-sided 3D detectors.

A focus of this thesis is the investigation of charge multiplication effects, which can occur in the presence of high electric fields. While multiplication of the liberated charge carriers does not occur in conventional silicon tracking detectors before any radiation-induced modification of the detectors, it was recently observed in highly irradiated detectors. The high electric fields present in 3D detectors lead to an enhanced charge multiplication prob-

ability. Implications of charge multiplication on the detectors' signal and noise are studied.

This thesis is organised as follows: Chapter 2 gives an overview over the LHC and introduces the plans for the HL-LHC upgrade. In Chapter 3, the basics of silicon detectors are described and in Chapter 4, the mechanisms and the effects of radiation damage of silicon detectors are summarised. After a description of the devices under tests and the measurement procedures in Chapter 5, measurements of 3D detectors are presented in Chapter 6. Chapter 7 presents the results of measurements of planar n-in-p detectors. Finally, Chapter 8 provides conclusions and a summary of the results.

Chapter 2

Luminosity Upgrades of the LHC

2.1 Large Hadron Collider

The Large Hadron Collider (LHC) [Bru04] is a proton-proton and heavy ion collider at CERN, the European Organization for Nuclear Research. As the LHC will mostly be operating with protons and the LHC upgrade is focused on proton collisions, this thesis will not go into further details of ion collisions. The first proton-proton collisions took place in autumn 2009. The LHC is housed in the circular tunnel of the former Large Electron-Positron Collider (LEP), which has a circumference of 26.7 km. The tunnel is located between 50 and 175 m underground. A sketch of the CERN accelerator complex, including the LHC and its injector chain, is shown in Fig. 2.1.

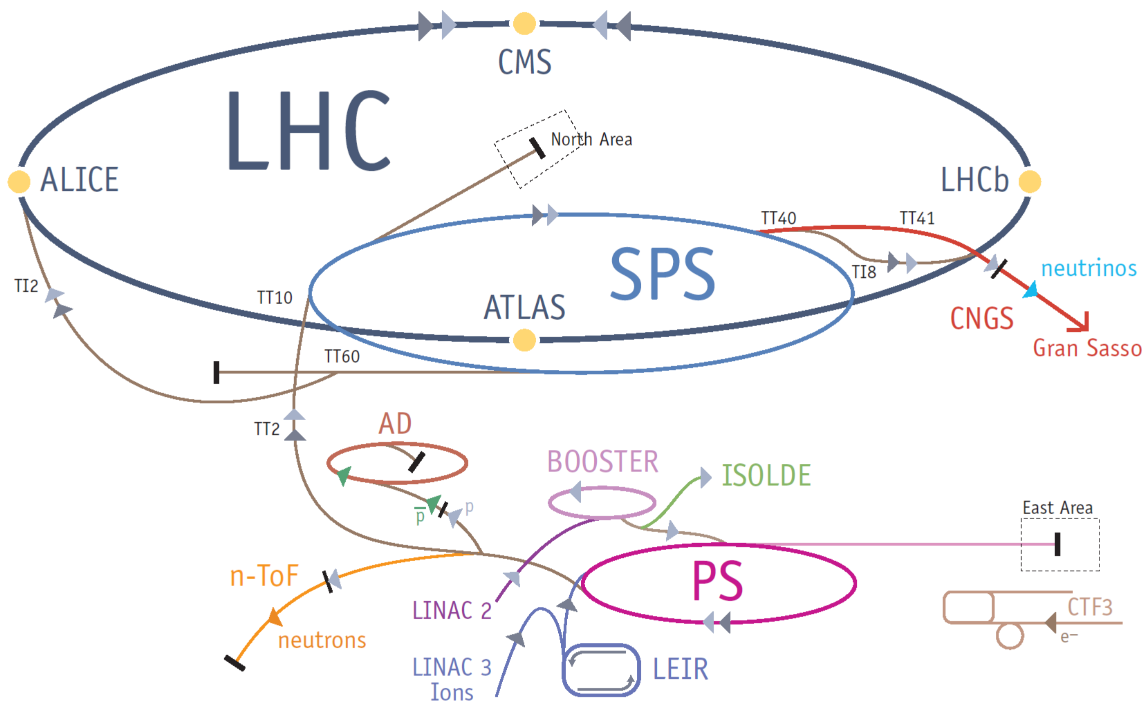

Figure 2.1: The CERN accelerator complex [Lef09].

The protons are pre-accelerated by an injector chain [Ben04], which begins with the linear accelerator LINAC2. Then, they are injected through the Proton Synchrotron Booster and the Proton Synchrotron (PS) into the Super Proton Synchrotron (SPS). In each step, the energy of the protons is increased by means of radiofrequency cavities. Finally, two counter-circulating beams are injected into the LHC. At this point, the protons have an energy of 450 GeV. In the LHC, the protons are further accelerated until they reach their final energy. The LHC is designed to accelerate protons up to an energy of 7 TeV, which leads to a centre-of-mass energy of $\sqrt{s} = 14\,\mathrm{TeV}$ in proton-proton collisions. However, the design energy should only be reached in 2014 after a further shutdown, which is required for installation of additional safety measures. Until the end of 2012, proton-proton collisions with an energy of 3.5 TeV per beam are foreseen [pr11].

The protons are bent on counter-circulating tracks by means of twin-bore superconducting dipole magnets. A maximum magnetic field of 8.3 T is required to keep protons at the design energy of 7 TeV on their orbit. The protons are arranged in bunches which are brought to collision at four interaction points. Around each interaction point a particle detector is constructed: ATLAS (A Toroidal LHC ApparatuS), CMS (Compact Muon Solenoid), LHCb (Large Hadron Collider beauty) and ALICE (A Large Ion Collider Experiment). Additionally, two smaller detectors, LHCf (Large Hadron Collider forward) and TOTEM (Total Cross Section, Elastic Scattering and Diffraction Dissociation at the LHC), are installed in the forward region of ATLAS and CMS, respectively. Two of the detectors, ATLAS and CMS, are general purpose detectors to study a wide range of potential new physics signatures. The remaining detectors are specialised for b-physics signatures (LHCb), heavy ion physics (ALICE) and forward physics (LHCf, TOTEM).

For ATLAS and CMS, the design luminosity is $10^{34}\,\mathrm{m}^{-2}\mathrm{s}^{-1}$. For this luminosity, which is foreseen to be reached approximately in 2014, bunches of approximately 10^{11} protons will collide every 25 ns. Currently, the luminosity is about an order of magnitude less and collisions take place every 50 ns. It is planned to record an integrated luminosity of approximately $300\,\mathrm{fb}^{-1}$ within the projected lifetime of the LHC.

2.1.1 ATLAS Experiment

The ATLAS detector [Aad08c], see Fig. 2.2, is one of the two general purpose detectors at the LHC. With its overall length of 44 m and its height of 25 m it is the largest LHC detector, however, its weight of 7000 t is less than that of CMS. The widely hermetic design and the large geometric acceptance assure a high particle detection efficiency. The sub-detectors of ATLAS in the barrel region are cylindrically arranged around the beam axis. In the forward region, the geometric acceptance is further enhanced by disc-shaped detector elements.

The inner detector, see Fig. 2.3, provides track and vertex measurements. Besides the required radiation hardness, a fine granularity is crucial, since approximately 1000 charged particles are expected for each bunch crossing at design luminosity. The inner detector is housed in a solenoid which provides a magnetic field of 2 T in the axial direction. Measurements of the bendings of the tracks of charged particles allow reconstructions of the particle momenta and the sign of the charge. The central part consists of a silicon pixel

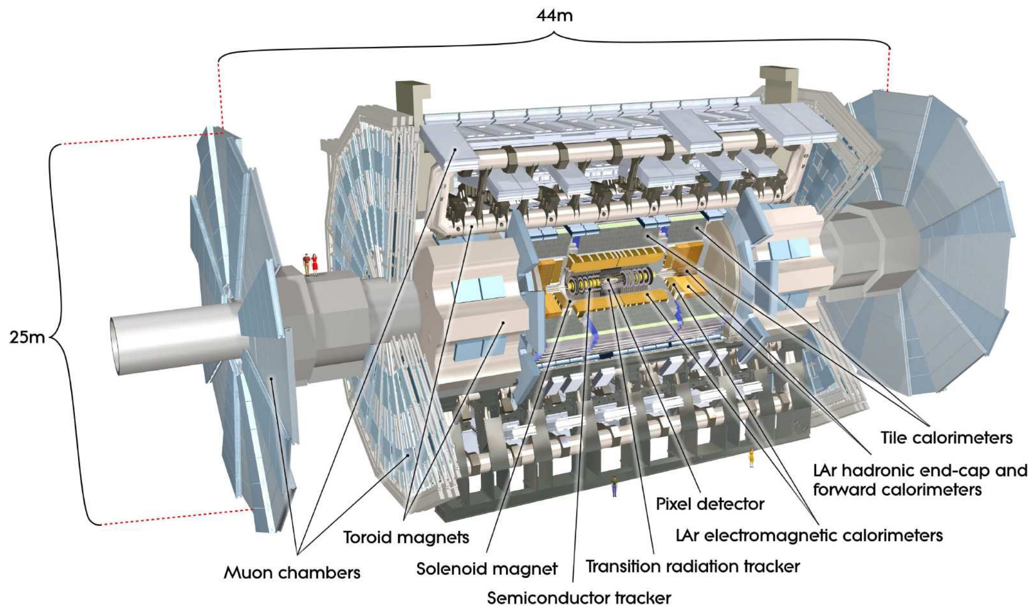

Figure 2.2: Cut-away view of the ATLAS detector [Aad08c].

detector [ATL98, Aad08c]. The layout of a pixel detector module is illustrated in Fig. 2.4. Most of the pixels have a size of 50 µm × 400 µm, while 10% of the pixels are somewhat larger with 50 µm × 600 µm. The sensors are made of n-in-n diffusion oxygenated float-zone (DOFZ) silicon to provide the required radiation hardness (see Chapter 4). The pixel detector has three cylindrical layers in the barrel region and three discs on either side in the end-cap region. The innermost layer, which is also referred to as B-Layer due to its great importance for b-tagging, has a radial distance of only 5 cm to the beam axis. The pixel detector plays a key role in pattern recognition, vertexing and b-tagging.

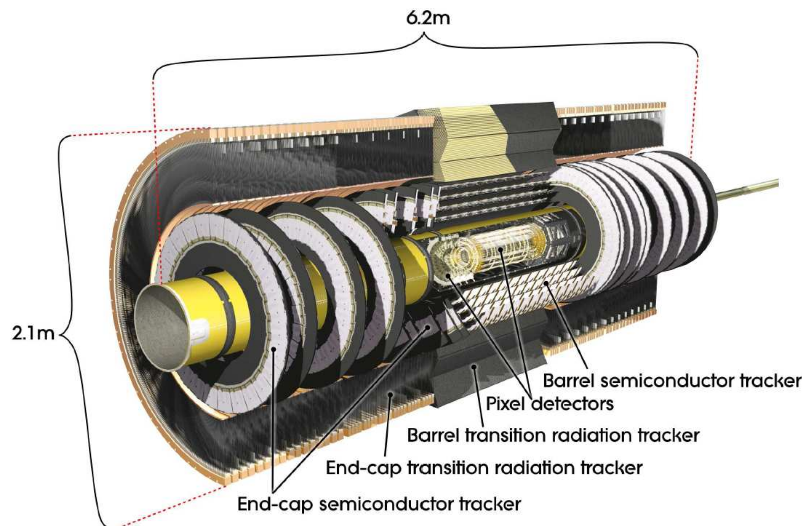

Figure 2.3: Layout of the ATLAS inner detector [Aad08c].

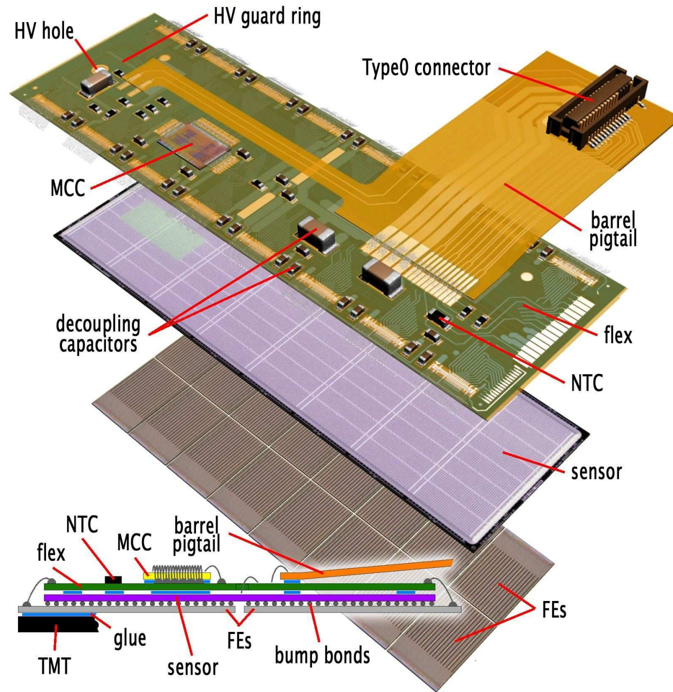

Figure 2.4: Schematic view of the different layers of an ATLAS pixel detector module [Aad08c]. The part of the module covered by the sensor has an area of approximately 6 cm × 2 cm.

The Semiconductor Tracker (SCT) [Ahm07, Aad08c] provides track measurements in the intermediate radial region. It consists of silicon strip detectors arranged on four barrel layers and nine discs on either side of the barrel region. Single-sided strip sensors are glued back-to-back with a stereo angle of 40 mrad to obtain two-dimensional tracking information. A drawing of an SCT barrel module is shown in Fig. 2.5. The sensors are made of p-in-n float-zone silicon with 6.4 cm long strips. In all barrel modules and in most of the end-cap modules, two sensors are daisy-chained on either side. The sensors installed in the barrel region have a constant strip pitch of 80 µm, whereas the end-cap sensors have radial strips with pitches between 60 µm and 90 µm.

The Transition Radiation Tracker (TRT) [Aba08, Aad08c] is the outermost part of the inner detector and provides track measurements at large radii. For charged particles with a transverse momentum of $p_T > 0.5$ GeV, on average 36 hits will be measured in $R - \phi$, where R is the radial distance to the interaction point and ϕ is the angle around the beam axis. The TRT is made of gas-filled drift tubes. These are interleaved with polypropylene in order to generate transition radiation. In addition to the tracking information, measurements of the transition radiation facilitate the identification of electrons. Electrons produce the highest amount of transition radiation, since these are the lightest charged particles and hence have the highest Lorentz factor for a given energy. The amount of transition radiation produced increases with the Lorentz factor.

The inner detector is surrounded by a calorimeter system [Aad08c], which is designed to

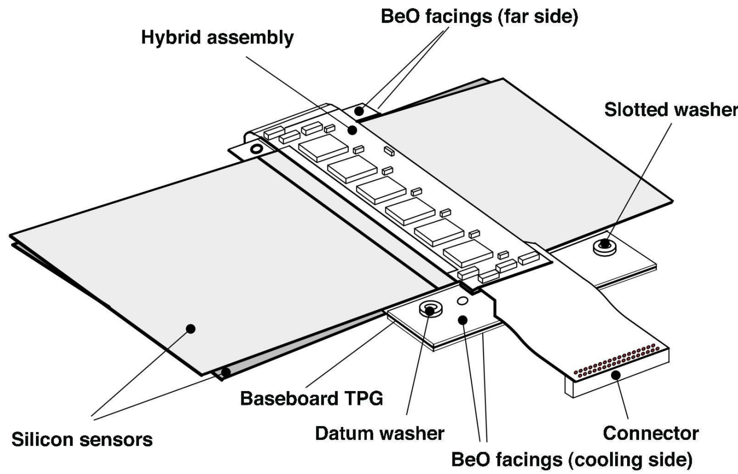

Figure 2.5: Drawing of an SCT barrel module [Aad08c]. The part of the module covered by the sensor has an area of approximately 13 cm × 6 cm.

absorb particles and to measure their energies. The electromagnetic calorimeter consists of accordion-shaped elements with lead as the passive material and liquid argon as the active sampling material. The hadronic calorimeter is placed outside the electromagnetic calorimeter. It is designed to absorb hadrons, as these are likely to penetrate the electromagnetic calorimeter. The hadronic calorimeter consists of different parts, which utilise different techniques: in the barrel part, steel, as the absorber material, and scintillating tiles, as the active material, are used. In the end-cap region, copper and tungsten constitute the absorber material and liquid argon is the active material.

Outside of the calorimeter system, a muon spectrometer [Aad08c] measures the tracks of charged particles which are not absorbed in the calorimeter. These are mostly muons, since other charged particles are likely to be absorbed in the calorimeters. In addition to track measurements, the muon system serves as an important trigger source, as muons are expected in many final states of interesting physics signatures. The muon spectrometer uses different gas detector technologies. A toroid magnet system provides a magnetic field to bend the tracks of muons in order to obtain a second independent muon-momentum measurement, in addition to the one obtained in the inner detector.

2.1.2 Physics at the LHC

The LHC is mainly designed for discoveries of new physics. With the unprecedented centre-of-mass energy of currently 7 TeV and 14 TeV from 2014 onwards, it is possible to study elementary particle physics interactions up to the TeV-scale. In the coming years, the investigation of the electroweak symmetry breaking and the search for physics beyond the Standard Model will be pursued. However, also precise measurements of established Standard Model parameters are foreseen. The general purpose detectors ATLAS and CMS cover a wide physics programme [Jak11, Aad08b, Bay06], examples will be mentioned below.

The high event rate at the LHC will facilitate to greatly improve current measurements of Standard Model parameters, like the masses of the W boson and the top quark. The acquisition of high statistic samples will facilitate a considerable reduction of the statistical uncertainties of these mass values.

A focus of the physics programme at the LHC is the investigation of electroweak symmetry breaking, which gives masses to the W and Z bosons. Within the Standard Model, electroweak symmetry breaking is achieved via the Higgs mechanism [Eng64, Hig64a, Hig64b, Gur64, Hig66, Kib67], formulated by Peter Higgs and others. The masses of the elementary fermions would be generated by interactions with the scalar Higgs field, which permeates the vacuum. The discovery of the Higgs boson as well as measurements of its mass and branching ratios are an important aim of the LHC. The Higgs boson is the only particle that is predicted by the Standard Model but which has not yet been discovered.

An essential part of the physics programme beyond the Standard Model is the search for supersymmetry (SUSY) [Mar08]. In SUSY theories, each elementary particle is assigned a superpartner, which has a spin that differs by one half from that of its partner. SUSY models provide a solution for the hierarchy problem. The lightest SUSY particle is a candidate to explain the dark matter in the universe. It is expected that the LHC will be able to detect squarks and gluinos, which are the superpartners of quarks and gluons, up to a mass of approximately $2.5\,\mathrm{TeV/c^2}$ [Jak11]. Furthermore, the physics programme beyond the Standard Model includes searches for extra dimensions, technicolor resonances, first generation leptoquarks and new vector bosons.

2.2 High-Luminosity LHC

To extend the physics potential and to facilitate precision measurements of discoveries made at the LHC, plans for luminosity upgrades exist [Gia05]. After the nominal LHC design luminosity of $\mathscr{L} = 10^{34}\,\mathrm{cm^{-2}s^{-1}}$ is reached, two upgrade stages, known as Phase-1 and Phase-2, are planned. Around 2018 the Phase-1 upgrade is planned to increase the instantaneous luminosity to approximately $\mathscr{L} = 2 \times 10^{34}\,\mathrm{cm^{-2}s^{-1}}$ [All11a]. It will mainly be accomplished by upgrades of the LHC injector chain in order to increase the quality of the beam injected into the LHC [Gar11].

During the Phase-2 upgrade, the peak luminosity will be increased up to $\mathscr{L} = 5 \times 10^{34}\,\mathrm{cm^{-2}s^{-1}}$. The phase-2 upgrade will lead to the High-Luminosity LHC (HL-LHC), formerly known as Super-LHC (sLHC). According to recent estimations, the HL-LHC will start operation about 2024 [All11a]. Together with the aim to collect an integrated luminosity of $3000\,\mathrm{fb^{-1}}$, the upgrade will lead to a highly increased track rate and higher radiation damage in the tracking detectors compared to the conditions at the LHC. The number of pile-up events per bunch crossing will increase from ~ 23 at the LHC (for $\mathscr{L} = 10^{34}\,\mathrm{cm^{-2}s^{-1}}$) to 100-200 at the HL-LHC (for $\mathscr{L} = 5 \times 10^{34}\,\mathrm{cm^{-2}s^{-1}}$). It is planned to leave the energy of the colliding particles (7 TeV per beam) unchanged. To maintain the physics capabilities, upgrades of the detectors are necessary, especially in the inner detector region (see Section 2.2.2).

For the Phase-2 upgrade, modifications of the collision schemes are foreseen [Zim11]. Among different options, a reduction of the bunch lengths and the usage of crab cavities are promising candidates to increase the luminosity. In ATLAS the proton beams collide under a crossing angle of 0.3 mrad. The luminosity decreases with increasing crossing angle. In order to reduce the effective crossing angle, crab cavities can be used, see Fig. 2.6. These would rotate the colliding bunches to achieve head-on collisions. Crab cavities can also be used to maintain a relatively constant luminosity over an extended period, which is known as luminosity levelling. Thus, a decrease of the luminosity with time after a beam filling period can be avoided and a constant pile-up rate can be obtained.

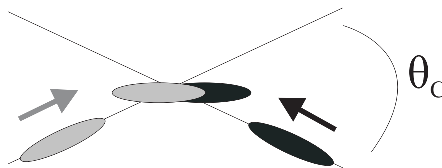

Figure 2.6: Bunch collisions with the usage of crab cavities. The crossing angle θ_C is shown larger than in reality at the LHC.

2.2.1 Physics Motivation for the HL-LHC

The tenfold increase of the integrated luminosity envisaged for the HL-LHC will enhance the physics potential of the LHC. It will extend the discovery reach and will facilitate the study of rare processes, which are out of reach at the LHC. Furthermore, improved measurements of Standard Model parameters and new physics parameters, which might be observed at the LHC, will be possible. Selected topics are presented below, based on discussions in Refs. [Gia05, Jak11].

While a discovery of the Standard Model Higgs boson over the entire allowed mass range is expected to be possible at the LHC, the HL-LHC will extend the discovery mass reach for SUSY particles. Discoveries of squarks and gluinos up to $3\,\mathrm{TeV/c^2}$ will be possible, in contrast to $2.5\,\mathrm{TeV/c^2}$ at the LHC. If SUSY exists, the reconstruction of supersymmetric decay chains, which are too rare to be investigated at the LHC, could be possible. Even if squarks and gluinos are found at the LHC, which indicates the existence of supersymmetric Higgs bosons, the discovery reach of heavy SUSY Higgs bosons is limited at the LHC. The HL-LHC would be able to extend the mass reach. Considering the discovery of other new physics beyond the Standard Model, as new vector bosons (Z', W'), excited quarks, first generation leptoquarks and technicolor resonances, the HL-LHC will probably increase the mass reach for new particle searches by approximately 30%.

The HL-LHC could facilitate measurements of rare decays of the top quark induced by flavour-changing neutral currents as described in theories beyond the Standard Model. At the LHC, the integrated luminosity will be not sufficient to study these processes. In particular, measurements of the decay $t \to qZ$, where q is either the up-quark or the down-quark, would greatly benefit from the increased luminosity at the HL-LHC. Also, it

will be possible to study rare decays of a Standard Model Higgs boson, as $H \to Z\gamma$ and $H \to \mu\mu$. At the LHC, the ability to investigate these channels is limited. Measurements of the Higgs boson self coupling may also be possible at the HL-LHC, however, detailed simulations are necessary to further investigate this option. At the LHC, studies of Higgs boson self coupling are not possible due to the rate limitation of Higgs pair production.

Studies of longitudinal gauge-boson scattering at high energies will be possible at the HL-LHC. These provide insight into the structure beyond that described by the Standard Model. If no light Higgs boson will be found at the LHC, investigations of these processes will be of particular importance. Simulations of a $W_L Z_L$ resonance at $1.5\,\mathrm{TeV/c^2}$ and a $Z_L Z_L$ resonance at $750\,\mathrm{GeV/c^2}$ show that a discovery at the LHC will probably not be possible, while the significance expected at the HL-LHC will be greatly increased.

Measurements of multiple gauge boson couplings could also be used to probe new physics beyond the Standard Model. As the couplings are uniquely defined by the Standard Model, deviations of these values would point to new physics. The HL-LHC will be able to improve significantly the measurements performed by the LHC and will facilitate to investigate further rare channels for which the luminosity of the LHC is too low.

2.2.2 ATLAS Upgrade

The increased track density and the increased radiation damage at the HL-LHC require extensive upgrades of the ATLAS detector, particular of the inner detector [Mue10]. However, minor detector upgrades are foreseen already before the HL-LHC upgrade. The timeline of the detector upgrades is to a large extent determined by shutdown periods of the LHC, which are necessary for maintenance and consolidation of the accelerator. These are very tentative, hence a defined schedule of the detector upgrades does not exist. The discussion in this section is based on a tentative schedule presented in Ref. [All11a] and is restricted to upgrade plans for the inner detector. Further upgrade plans exist also for other sub-detectors, including the trigger system [Mue10].

According to the current schedule, the first upgrade of the ATLAS detector is planned for the years 2013-2014. In this period, the LHC will be shut down in order to prepare for the design energy of 7 TeV per beam, commonly referred to as the Phase-0 upgrade. To improve the physics performance, it is planned to insert an additional pixel barrel layer at a radial distance of 3.2 cm with respect to the beam axis [Cap11]. This pixel detector layer is referred to as the Insertable B-Layer (IBL), motivated by its importance for b-tagging.

The Phase-1 shutdown of the LHC, in which the instantaneous luminosity should be increased to approximately $2 \times 10^{34}\,\mathrm{cm^{-2}s^{-1}}$, is planned for 2018. So far no major inner detector upgrades are foreseen during this shutdown period, however, the installation of a new pixel detector is currently being discussed.

The main upgrade of the inner detector is foreseen for the Phase-2 shutdown after approximately 2021, during which the LHC is upgraded to the HL-LHC. An installation of a completely new, all-silicon tracker is planned, as the TRT is not expected to function at

the high track rate expected at the HL-LHC. The proposed layout of the new inner detector is shown in Fig. 2.7. The innermost part will be covered by pixel detectors, followed by short strip detectors and then long strip detectors in the outermost region.

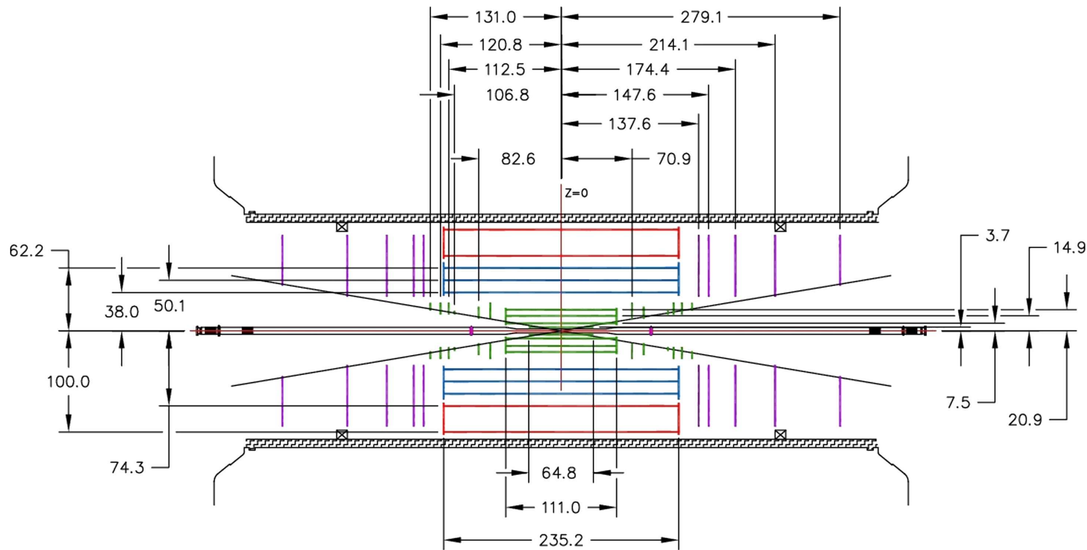

Figure 2.7: Projected layout of the inner detector of ATLAS at the HL-LHC: pixel detector (green), short strips (blue), long strips (red), end-cap discs (purple) [All11b].

In the barrel region, four pixel layers are planned, where the innermost one, the B-layer, will have a radial distance of 3.7 cm to the beam. In the end-cap region, six pixel discs will be located on either side. As the B-layer will have to withstand a radiation fluence of approximately $2 \times 10^{16}\ \mathrm{n_{eq}/cm^2}$ (see below), extremely radiation tolerant detector technologies are necessary. As a possible alternative to the planar silicon pixel detectors currently installed, several options are studied: 3D-detectors, diamond detectors, thin silicon detectors and, as a possible alternative to silicon, gaseous pixel detectors [Mue10].

Three barrel layers will be equipped with short strip detectors, which have a strip length of 2.4 cm. The innermost strip layer will be located at approximately 38 cm from the beam line. It is foreseen to use n-in-p silicon strip sensors. Further outwards, two barrel layers with long strip detectors with a strip length of 9.6 cm are planned. The end-cap region will be covered by 5 discs on either side of the interaction point. The discs will be equipped with sensors of different strip lengths. The outermost strip layer will be 1 m away from the beam line. In this way, the silicon strip detectors will cover the space where the TRT in the current inner detector of ATLAS is located.

Currently, extensive research programmes are conducted to investigate extremely radiation tolerant sensor technologies for the inner regions of the HL-LHC tracking detectors. In this thesis, the radiation hardness of double-sided 3D detectors is investigated. The work is performed in the framework of the CERN RD50 Collaboration “radiation hard semiconductor devices for very high luminosity colliders” [RD].

Expected Radiation Fluence for the ATLAS Tracker

The equivalent radiation fluence expected for the ATLAS HL-LHC tracking detector has been simulated [Daw11] using the Monte Carlo simulation package FLUKA [Bat07]. The projected tracker layout as described above and foreseen material distributions, including support and service structures, were considered for the simulation.

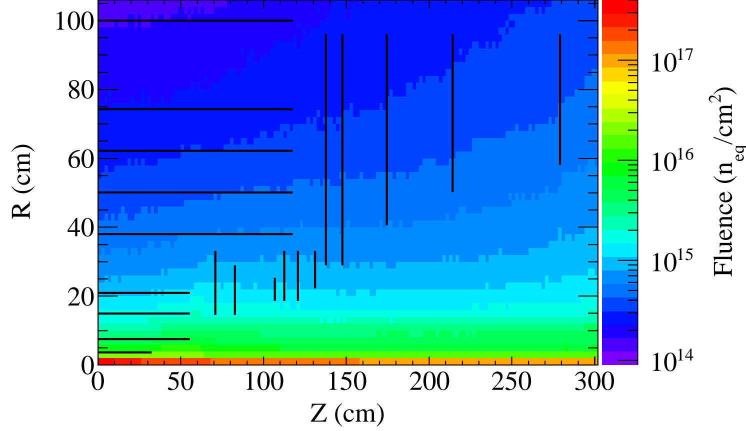

Figure 2.8: Equivalent fluence in the ATLAS HL-LHC tracker for an integrated luminosity of 3000 fb^{-1} (data from Ref. [Daw11]). R is the radial distance to the beam axis, Z is the longitudinal distance to the interaction point. The barrel layers and end-cap discs of the pixel and strip detector are indicated.

Figure 2.8 shows a map of the equivalent fluence expected for an integrated luminosity of 3000 fb^{-1}. The equivalent fluence is given in units of 1 MeV neutron equivalent particles per square centimetre (n_{eq}/cm^2, see Section 4.2) and contains contributions from all hadrons. Other components can be neglected when considering bulk radiation damage of silicon detectors. The locations of barrel layers and end-cap discs of the pixel and strip detector as foreseen for the tracker layout are indicated in the illustration. The expected radiation fluence decreases strongly with the radial distance to the beam axis, while the dependence on the longitudinal distance to the interaction point (Z) becomes important only for large Z and large R.

The equivalent fluence as a function of the radial distance to the beam axis is shown in Fig. 2.9 for a slice at $Z = 0$. The total fluence and the contributions of neutrons, pions and protons are shown. Most of the protons and pions originate from the primary proton collisions, whereas a large fraction of neutrons is emitted from the calorimeters. Moderators, which should lower the energy of back-scattered neutrons coming from the calorimeters, are already considered for the simulation of the fluences [Daw11]. A moderation of the neutrons minimises their damage to the silicon detectors.

The fluences of charged hadrons decrease more strongly as a function of the radial distance than the neutron fluence. Consequently, the radiation fluence in the pixel region is dominated by pions while that in the region to be equipped with strip detectors is dominated

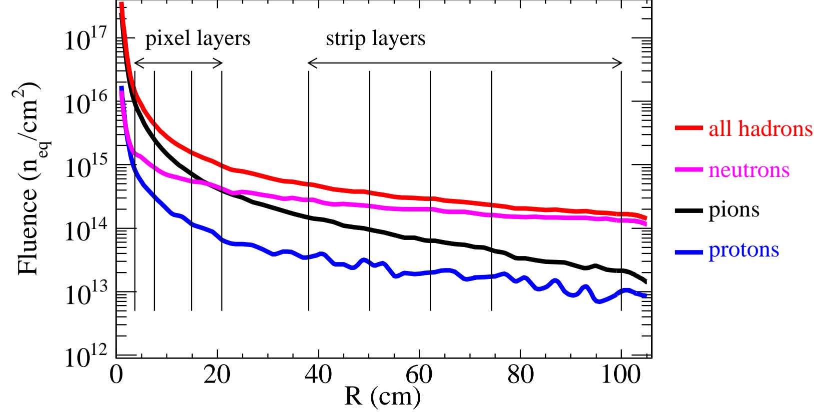

Figure 2.9: Equivalent fluence for different hadron types in the ATLAS HL-LHC tracker for an integrated luminosity of $3000\,\mathrm{fb}^{-1}$, data from [Daw11]. The data are shown for $Z = 0$. The positions of the pixel and strip layers are indicated.

by neutrons. Over the envisaged lifetime of the HL-LHC, the innermost pixel layer will receive an equivalent fluence of approximately $1.5 \times 10^{16}\,\mathrm{n_{eq}/cm^2}$ (see Fig. 2.9). Including a safety margin, it is typically specified that the detectors for the innermost pixel layer have to withstand a fluence of $2 \times 10^{16}\,\mathrm{n_{eq}/cm^2}$. In the region of the innermost strip detector layer, an equivalent fluence of $5 \times 10^{14}\,\mathrm{n_{eq}/cm^2}$ is expected for $Z = 0$. As can be seen in Fig. 2.8, the expected fluence increases with increasing Z and approaches almost $1 \times 10^{15}\,\mathrm{n_{eq}/cm^2}$ in the innermost part of the end-cap discs. Including a safety margin, a benchmark fluence of $1 \times 10^{15}\,\mathrm{n_{eq}/cm^2}$ is usually quoted for the strip detectors.

The fluences expected at the HL-LHC are considerable higher than that expected for the tracking detectors of the current ATLAS detector. The current ATLAS pixel sensors are specified to withstand a fluence of $8 \times 10^{14}\,\mathrm{n_{eq}/cm^2}$, the SCT sensors are designed for an expected fluence of $2 \times 10^{14}\,\mathrm{n_{eq}/cm^2}$ [Aad08c].

Chapter 3

Silicon and Silicon Detectors

3.1 Production of Detector Grade Silicon

For detector applications very pure monocrystalline silicon is required. High resistivity, which is needed to achieve full depletion of the detector volume at technically applicable voltages, and high minority carrier lifetimes are necessary. Therefore silicon with a high purity is required.

The production of monocrystalline silicon starts with the extraction of silicon from its bound state SiO_2, which is present in sand or quartz. First, polycrystalline silicon is produced and several steps of purification are applied [Sif04]. Then, ingots with monocrystalline silicon are grown, which are later cut into wafers. Silicon used for particle detectors is normally grown using the float-zone (FZ) method, see Fig. 3.1(a). Float-zone silicon exhibits a very high purity, however, it is more costly than silicon growth methods commonly applied for electronic grade silicon. In the float-zone process a rod of high-purity polysilicon is brought into contact with a monocrystalline seed crystal at the bottom. A surrounding coil supplies a high-frequency electric field and melts the silicon by means of induction. The silicon in contact with the seed crystal solidifies in a monocrystalline structure. By moving the molten zone upwards, the single crystal is expanded and impurities are pushed upwards, away from the single crystal. This process can be applied several times to further increase the purity.

The majority of monocrystalline silicon used for microelectronics applications is grown using the Czochralski (Cz) method, see Fig. 3.1(b). Polysilicon is melted in a rotating crucible made of SiO_2 and a seed crystal is placed on top of the melt. The seed crystal is slowly pulled upwards and large ingots of monocrystalline silicon can be produced. This method is cost-effective, however, it is not well suited for detector applications. The concentration of impurities, mainly originating from the crucible, is too high, resulting in low resistivity and low minority carrier lifetimes. Since Cz silicon has a relatively high oxygen concentration, which acts as a sink for radiation-induced defects (see Section 4.4.1), it has become interesting for the development of radiation hard detectors in recent years. A modified growth method, referred to as magnetic Czochralski (MCz), can produce silicon with a lower impurity concentration and higher homogeneity. The technology is the same as the standard Czochralski process, only the crucible is placed in a strong magnetic field.

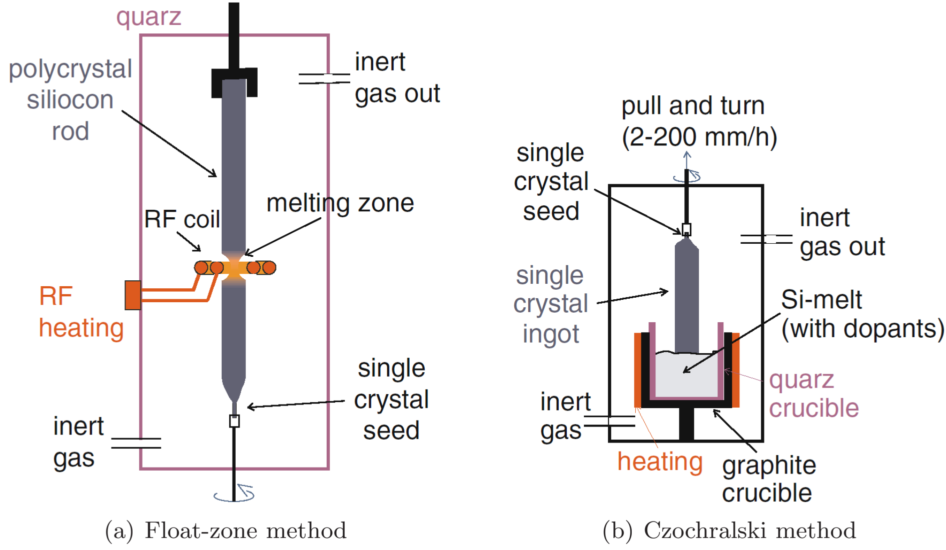

(a) Float-zone method (b) Czochralski method

Figure 3.1: Production technologies of monocrystalline silicon: (a) float-zone (FZ) method, (b) Czochralski (CZ) method [Har09]. See the text for explanations.

This reduces the mixing between the silicon melt and the crucible. Magnetic Czochralski silicon can be used for particle detectors, studies are being performed within the RD50 collaboration [RD] (see Section 4.4.1).

Another method of producing detector grade silicon is the epitaxial technology. A gaseous silicon compound is solidified on a seed crystal and grows following a monocrystalline structure. Thin epitaxially grown silicon sensors are also being investigated within the RD50 collaboration as a possible candidate for radiation tolerant detectors (see Section 4.4.1).

3.2 Properties of Silicon

3.2.1 Energy Band Structure of Silicon

Monocrystalline silicon has a diamond lattice structure. The diamond structure can be described as two interpenetrating fcc (face-centred cubic) lattices, which are displaced by one quarter of the body diagonal. Many of the electrical and physical properties of silicon result from the structure of the energy levels of the four valence electrons. Due to the periodic potential in the crystal lattice the solutions of the Schrödinger equation must be of the form

$$\psi_k(\vec{r}) = u_k(\vec{r}) \exp(i\vec{k} \cdot \vec{r}), \tag{3.1}$$

which is known as the Bloch theorem. $\psi_k(\vec{r})$ is the wave function, $\vec{r}$ describes the position and $\vec{k}$ is the wave vector, which can be limited to values within the first Brillouin zone. The function $u_k(\vec{r})$ has the periodicity of the crystal lattice. The energy levels of the valence electrons, which can be calculated using Eq. (3.1), take on quasi-continuous values within energy bands. The continuous distribution of energy states within these bands results from the superposition of the potentials of the large number of atoms in the crystal. In a periodic lattice the discrete energy levels of single atoms split up and

generate continuous bands. Some energy regions, for which no solutions of Eq. (3.1) exist, form forbidden regions, referred to as band gaps.

A theoretical calculation of the energy band structure of silicon is shown in Fig. 3.2. The upper band forms the conduction band, whereas the lower band forms the valence band. At a temperature of $T = 0\,\mathrm{K}$ all valence electrons occupy states in the valence band, whereby this band is completely filled and the conduction band is empty. Therefore, the total momentum of the electrons and the electrical conductivity are zero. At higher temperatures electrons can be transferred to the conduction band and silicon becomes conductive. The conductivity increases with increasing temperature, as a higher number of electrons is excited to the conduction band. When an electron is excited, an empty state, referred to as a hole, is generated in the valence band. Holes can be treated as physical objects carrying momentum, an effective mass and the opposite charge of an electron.

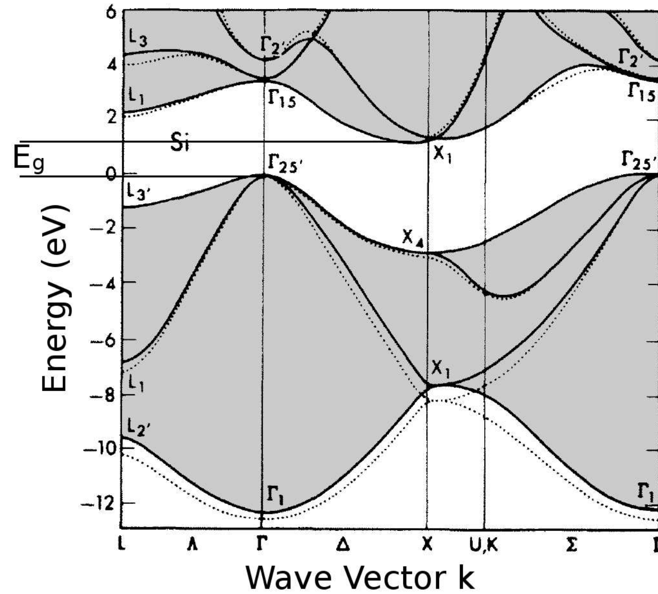

Figure 3.2: Energy band structure of silicon, after [Che76]. The solid lines show an energy-dependent nonlocal-pseudopotential calculation, the dotted lines show a local-pseudopotential calculation. Allowed energies in the conduction band and in the valence band are shown grey, forbidden regions are white. The width of the forbidden band gap between the conduction band and the valence band is labelled E_g. L, Γ, X, U and K are symmetry points in the first Brillouin zone. The symmetry lines Λ, Δ and Σ correspond to the axes $\langle 111 \rangle$, $\langle 100 \rangle$ and $\langle 110 \rangle$.

The band gap, corresponding to the difference between the maximum energy of the valence band and the minimum energy of the conduction band, is $1.12\,\mathrm{eV}$ for silicon at room temperature and under normal atmospheric pressure [Sze81]. The size of the band gap decreases with increasing temperature. As can be seen in Fig. 3.2, the minimum of the conduction band and the maximum of the valence band correspond to different wave vec-

tors. This is a property of indirect semiconductors (e.g. germanium, silicon), whereas in direct semiconductors (e.g. gallium arsenide), the maximum of the conduction band and the minimum of the valence band have the same wave vector. In indirect semiconductors additional momentum transfer is necessary to create an electron-hole pair by transferring energy corresponding to the band gap. The momentum transfer can originate from absorption or creation of a phonon. Without additional momentum transfer, an energy transfer higher than the size of the band gap is required for the creation of an electron-hole pair.

The size of the band gap determines the electrical conductivity of a material. Materials are usually classified as insulators if the band gap is several eV, leading to low conductivity. Materials having smaller band gaps are referred to as semiconductors. If the conduction band and the valence band overlap or if the conduction band is partially filled already at $T = 0\,\mathrm{K}$, the material can be regarded as a conductor or a metal.

3.2.2 Extrinsic Silicon

Important electrical properties of silicon can be modified by introducing impurity atoms, referred to as dopants, which have energy levels in the band gap (see Fig. 3.3). Doped silicon is called extrinsic silicon, to distinguish it from intrinsic silicon, which contains no significant amounts of impurities. The dopants have to replace silicon atoms on lattice sites in order to become electrically active. Elements with five valence electrons are applied as donors. As only four electrons are required to form the covalent bonds, the fifth electron can be easily excited to the conduction band. Therefore, the number of electrons in the conduction band is increased without increasing the number of holes in the valence band. Conversely, atoms of valence three can serve as acceptors. The fourth electron to form the covalent bond can be absorbed from the valence band, thus increasing the number of holes. Donors form positive ions, acceptors form negative ions, once an electron has been emitted to the conduction band or an electron has been absorbed from the valence band, respectively. Referring to the polarity of the majority charge carriers, doping with donors creates n-type silicon and doping with acceptors creates p-type silicon.

A simplified energy diagram of intrinsic, n-type and p-type silicon is shown in Fig. 3.3. In contrast to the band structure shown in Fig. 3.2 the dependence of the energy band edges on the wave vector is neglected. To be electrically active at room temperature, elements with energy levels slightly below the conduction band (as donors) or slightly above the valence band (as acceptors) have to be chosen. Elements commonly applied as donors are phosphorous and arsenic, which create energy levels of $0.045\,\mathrm{eV}$ respectively $0.054\,\mathrm{eV}$ below the bottom of the conduction band. Boron, creating energy levels of $0.045\,\mathrm{eV}$ above the top of the valence band, is often used as an acceptor [Lut99]. The presence of dopants, and hence the introduction of additional energy levels in the upper half or the lower half of the band gap, leads to a shift of the Fermi level. In n-type silicon the Fermi level moves towards the conduction band, whereas it is shifted towards the valence band in p-type silicon (see Fig. 3.3).

Doping of silicon is usually applied during the production of the monocrystalline material, to achieve low and uniform doping concentrations of the produced wafers. To achieve

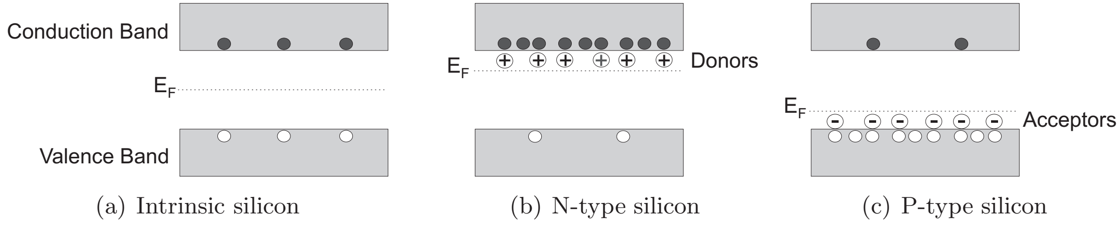

(a) Intrinsic silicon (b) N-type silicon (c) P-type silicon

Figure 3.3: Energy band structure of (a) intrinsic, (b) n-type and (c) p-type silicon. The Fermi level E_F and the energy levels introduced by donors and acceptors are shown. Electrons in the conduction band are represented as filled circles, holes in the valence band are illustrated as open circles.

higher doping levels and to restrict the doping to selected regions of the wafer, the doping atoms are introduced by means of ion implantation or diffusion into the silicon lattice. These techniques are applied to produce structures with p-n junctions, see the following section.

3.2.3 p-n Junction

Many technical applications of silicon are based on a p-n junction, which forms the basic structure of a diode and of silicon particle detectors. When regions with n-type and p-type silicon are in contact to each other, the majority carriers (electrons in n-type and holes in p-type silicon) diffuse into the other region. The effect on band edges, charge density and electric field in the region around an abrupt p-n junction is shown in Fig. 3.4.

The different concentrations of electrons and holes in the energy bands of isolated n-type and p-type silicon lead to unequal Fermi levels (Fig. 3.4(a)). When both regions are in contact, the majority charge carriers drift into the other region and partly recombine. The Fermi levels in both regions line up and the edges of the valence band and the conduction band are distorted (Fig. 3.4(b)). As no free charge carriers are left in a region around the p-n junction, the remaining ionised donors and acceptors create a space charge (Fig. 3.4(c)). In the illustration the doping concentration in the n-type region is assumed to be twice as high as in the p-type region, therefore leading to a higher charge density in the n-type region. The charge density in the space charge region, also referred to as depletion zone, creates an electric field (Fig. 3.4(d)). This electric field counteracts the diffusion of electrons from the n-type region into the p-type region and therefore limits the extension of the space charge region.

The electric potential ϕ and the electric field $\vec{E}$ in the space charge region are given by Poisson's equation

$$\Delta\phi = -\nabla \cdot \vec{E} = -\frac{\rho}{\varepsilon_0 \varepsilon_r}, \tag{3.2}$$

where ρ is the space charge density, ε_0 is the permittivity of vacuum and $\varepsilon_r = 11.9$ is the relative permittivity of silicon.

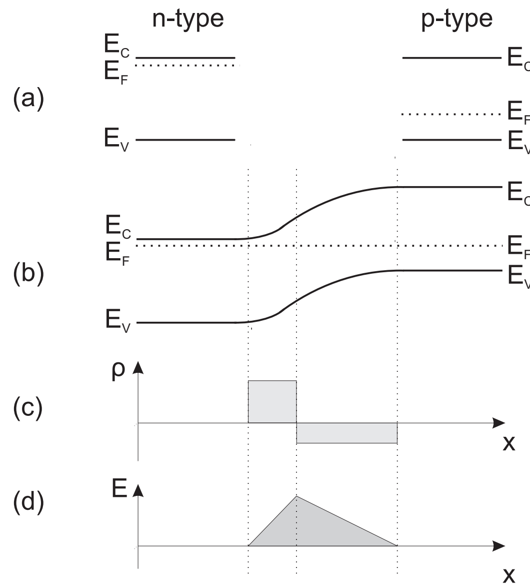

Figure 3.4: Abrupt p-n junction: (a) energies of conduction band edge (E_C), valence band edge (E_V) and Fermi level (E_F) of isolated n-type and p-type silicon. (b) Band edges and Fermi level when n-type and p-type silicon are in contact. (c) Charge density ρ and (d) electric field E around the p-n junction. The doping concentration in the n-type region is assumed to be twice as high as in the p-type region.

3.3 Silicon Detectors

3.3.1 Diode with Application of External Voltage

The electric field distribution and the width of the space charge region around a p-n junction can be adjusted by applying an external bias voltage. By applying a high potential to the n-side and a low potential to the p-side (reverse bias) free charge carriers are swept away from the junction. The width of the space charge region and the potential drop across the junction are increased. On the contrary, applying a so-called forward bias leads to a decreased space charge region and to a lower potential drop, therefore a higher current flow is possible.

The basic structure of a silicon detector is a diode, which consists of a p-n junction. It is usually made of a substrate with a low doping concentration and a small region having a high doping concentration. An n^+-p structure, where the "+" denotes a higher doping concentration, is shown in Fig. 3.5. An external voltage is applied to the diode in reverse bias mode. The n^+-side is grounded and a negative potential $-V$ is applied to the p-side. Silicon detectors are normally operated in reverse bias mode in order to increase the space charge region and therefore the sensitive detector volume. In the space charge region an electric field exists, which is necessary to separate free charge carriers created by penetrating particles. The space charge region and therefore the electric field should preferably extend throughout the entire detector volume.

As the doping concentration in the n^+-region is several orders of magnitude higher than

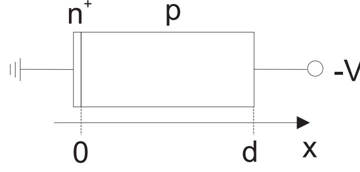

Figure 3.5: Sketch of an n^+-p structure. The n^+-side is grounded, while a negative potential $-V$ is applied to the p-side. The p-doped region extends from $x = 0$ to $x = d$.

the doping concentration in the p-region, the width of the depletion zone in the n-region can be neglected. In the following discussion the width of the space charge region and the electric field in the p-region are calculated as a function of the applied bias voltage. A constant space charge density in the depleted volume $\rho = -q_0 N_{\text{eff}}$ is assumed, where q_0 is the elementary charge and N_{eff} is the effective doping concentration. The effective doping concentration is the difference of the concentration of electrically active acceptors and donors in the p-doped region. Acceptors are electrically active if they have captured an electron from the valence band, donors are electrically active if they have emitted an electron to the conduction band. Free charge carriers in the depleted region are neglected and the space charge density is approximated by a step function. In a one-dimensional approach, Poisson's equation (Eq. (3.2)) becomes

$$\frac{\mathrm{d}^2\phi(x)}{\mathrm{d}x^2} = -\frac{\mathrm{d}E(x)}{\mathrm{d}x} = \frac{q_0 N_{\text{eff}}}{\varepsilon_0 \varepsilon_r}. \tag{3.3}$$

Integration leads to

$$E(x) = -\frac{q_0 N_{\text{eff}}}{\varepsilon_0 \varepsilon_r} x + E_0, \tag{3.4}$$

$$\phi(x) = \frac{q_0 N_{\text{eff}}}{2\varepsilon_0 \varepsilon_r} x^2 - E_0 x + \phi_0, \tag{3.5}$$

where E_0 and ϕ_0 are integration constants. As the n^+-side is grounded and the potential drop in the n^+-region is small due to the very shallow depletion zone, a potential of approximately zero can be assumed for the boundary between the n^+-region and the p-region. Exploiting the boundary condition $\phi(x = 0) = 0$ leads to $\phi_0 = 0$.

Under-Depletion

If the applied voltage V is below or equal the voltage V_{dep}, which is required to achieve full depletion in the p-region, the electric field is zero at the edge of the space charge region. With $E(x = w) = 0$, where w is the width of the depleted region, Eq (3.4) yields

$$E_0 = \frac{q_0 N_{\text{eff}}}{\varepsilon_0 \varepsilon_r} w. \tag{3.6}$$

The electric potential at the edge of the depletion zone is $\phi(x = w) = -V - V_{\text{bi}}$. The built-in voltage V_{bi} is caused by the presence of space charge without application of external voltage. It can be calculated that V_{bi} is small compared to external voltages V usually

applied to semiconductor detectors, hence $\phi(x = w) \approx -V$ can be assumed. Inserting this into Eq. (3.5) yields

$$V = -\frac{q_0 N_{\text{eff}}}{2\varepsilon_0\varepsilon_r} w^2 + E_0 w. \tag{3.7}$$

With Eq. (3.6) the width w of the depleted region becomes

$$w = \sqrt{\frac{2\varepsilon_0\varepsilon_r}{q_0 N_{\text{eff}}} V}. \tag{3.8}$$

For full depletion, $V = V_{\text{dep}}$, the depleted region extends through the entire thickness d of the p-region, thus $w = d$. Hence

$$V_{\text{dep}} = \frac{q_0 N_{\text{eff}}}{2\varepsilon_0\varepsilon_r} d^2. \tag{3.9}$$

From Eqs. (3.8) and (3.6) the maximum of the electric field E_{max}, which is present at the boarder between the n^+- and the p-region ($x = 0$), can be obtained:

$$E_{\text{max}} = E_0 = \sqrt{\frac{2q_0 N_{\text{eff}}}{\varepsilon_0\varepsilon_r} V} \tag{3.10}$$

In particle detectors with a typical thickness of 300 µm and a doping concentration of $N_{\text{eff}} = 10^{12}\,\text{cm}^{-3}$ the depletion voltage according to Eq. (3.9) is $V_{\text{dep}} \approx 70\,\text{V}$.

Over-Depletion

The electric field can be further increased by operating the diode over-depleted, that is increasing the bias voltage beyond the full depletion voltage. This increases the drift velocity of free charge carriers and decreases the charge collection time (see Section 3.3.6). With $\phi(x = 0) = 0$ and $\phi(x = d) = -V$ the maximum electric field according to Eq. (3.5) becomes

$$E_{\text{max}} = E_0 = \frac{q_0 N_{\text{eff}}}{2\varepsilon_0\varepsilon_r} d + \frac{V}{d}. \tag{3.11}$$

For voltages higher than the full depletion voltage, the maximum electric field therefore increases linearly with the external voltage. Below full depletion it increases proportionally to the square root of the external voltage (see Eq. 3.10).

Capacitance

The capacitance of a silicon detector is of particular importance, since it affects the noise (see Section 3.3.8) and measuring the capacitance provides an opportunity to determine the depletion voltage. In a diode the capacitance C is given by the area of the diode, A, and the width of the depleted region, w:

$$C = \frac{\varepsilon_0\varepsilon_r A}{w} \tag{3.12}$$

According to Eq. (3.8) the capacitance decreases with increasing bias voltage proportionally to $1/\sqrt{V}$. When full depletion is achieved, the capacitance reaches a constant value. By performing "$C - V$" measurements the depletion voltage can be determined as the voltage above which the capacitance is constant.

3.3.2 Leakage Current

The current of a reverse biased diode, the leakage current, is small compared to the current of a diode in forward bias. However, the leakage current is of importance in silicon detectors, especially due to its strong increase after irradiation (see Section 4.3.2). Several effects contribute to the leakage current, with the volume generation current in the depletion region dominating [Sze81]. Other effects, like surface generated current or current flowing through the cutting edges of the diode, are neglected here.

The volume generation current is dominated by charge carriers generated by emission through generation-recombination centres. These trapping centres are impurities or crystal defects presenting energy levels in the energy gap between the conduction band and the valence band. By capturing electrons from the valence band and emitting electrons to the conduction band, free charge carriers are generated. The generation rate is dominated by generation-recombination centres located close to the middle of the band gap [Sze81], therefore primarily these defects account for the leakage current. As the rate of generation and recombination cancels in undepleted silicon, only the generation in the space charge region is relevant. Therefore, the volume generation current is proportional to the depleted volume and to the width of the depletion zone. Hence the leakage current increases proportionally to the square root of the applied bias voltage (see Eq. (3.8)), as long as the diode is not fully depleted. When full depletion is reached, the current saturates. At very high bias voltages an electrical breakdown occurs and the leakage current increases strongly. Mechanisms leading to an electrical breakdown are the Zener breakdown, caused by tunneling of electrons from the valence band to the conduction band, and the avalanche breakdown due to impact ionisation (see Section 3.3.7).

The leakage current I_l depends strongly on the temperature T [Spi05],

$$I_l \propto T^2 e^{-E/2kT}, \tag{3.13}$$

and approximately doubles every 8 °C. The parameter E can be approximated by the band gap energy of silicon ($E_g = 1.12\,\text{eV}$) and k is the Boltzmann constant. The current measured at a temperature T_{meas} can be scaled to a reference temperature T_{ref} according to

$$I(T_{\text{ref}}) = I(T_{\text{meas}}) \left(\frac{T_{\text{ref}}}{T_{\text{meas}}}\right)^2 \exp\left[-\frac{E}{2k}\left(\frac{1}{T_{\text{ref}}} - \frac{1}{T_{\text{meas}}}\right)\right]. \tag{3.14}$$

To reduce shot noise (see Section 3.3.8) and to avoid thermal runaway, silicon detectors in particle physics experiments are usually operated at cold temperatures. For example, the ATLAS semiconductor tracker (SCT) is designed to operate at −7 °C [Aad08c]. An increase of the current increases the dissipated power, which increases the temperature and therefore in turn leads to a higher current. A critical and uncontrolled increase of the current is referred to as thermal runaway.

3.3.3 Principle Design of Planar Silicon Strip Detectors

By segmenting the readout electrode of silicon detectors into strips or pixels, the position of incident particles can be measured in one or two dimensions, respectively. The principle design of planar strip detectors as used in many particle physics experiments is

described below. Details on configuration and properties of pixel detectors can be found in Ref. [Ros06].

Silicon strip detectors currently employed in particle physics experiments are usually made by means of the planar process, introduced in 1979 [Kem80, Spi05]. A simplified sketch of a strip sensor in p^+-n-n^+ design, also termed p-in-n, is shown in Fig. 3.6. The sensor consists of a substrate made from a lightly n-doped wafer. Typical thicknesses are approximately 300 μm.

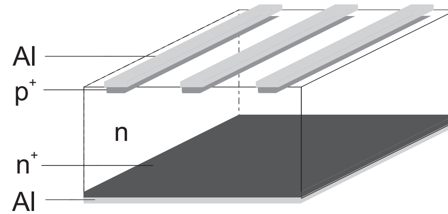

Figure 3.6: Simplified design of a p^+-n-n^+ silicon detector with aluminium (Al) metallisations.

On the front side, highly p-doped implantations form the strips of the sensor. The doping concentration is several orders of magnitude higher than the doping concentration of the substrate. Typical pitches between individual readout strips are in the range of 50-100 μm. Strip detectors often have metallisation strips above the implants, which are electrically insulated from the implants by an oxide layer. Thus, a capacitive coupling, also known as AC coupling, between the strip implantations and the metal strips is achieved. When the metal strips are connected to the readout electronics, the leakage current is prevented from flowing into the amplifier channels. In cases where the leakage current is low, the insulating layer between the implants and the metallisations can be left away. The implants are then directly connected to the readout electronics, which is referred to as DC coupling. This approach is usually realised in pixel detectors, where the leakage current is low due to the small pixel volume.

On the back of the sensor a layer with a high doping concentration, here n^+, is present. This layer is coated with a metal layer. While the p-n junction is formed close to the front surface, the n^+ layer at the back prevents the depletion zone from reaching the metal contact at the back, which could lead to an unequal potential distribution. Furthermore, it provides a good ohmic contact. The space charge region and the junction, which is created at the interface between the metal and the semiconductor, is kept very narrow by the high doping concentration of the n^+ layer. Therefore tunneling processes become important, which limits the contact resistance to values negligible compared to the resistance of the bulk [Lut99].

The pitch of the readout strips affects the spatial resolution of the detector. For the particle point of impact a uniform probability distribution over one strip pitch can be assumed. Provided that penetrating particles lead to signals on single strips only, the resolution, in this case called binary resolution, corresponds to the standard deviation of

the uniform probability density distribution

$$\sigma = \sqrt{\langle x^2 \rangle - \langle x \rangle^2} = \frac{p}{\sqrt{12}}. \tag{3.15}$$

Therein, x denotes the coordinate within one strip pitch and p is the pitch. For a typical pitch of 80 µm the binary resolution is $\sigma = 23.1\,\mu\text{m}$. Charge sharing (see Section 3.3.5) can lead to an improved resolution as the particle point of impact can be interpolated between different strips. However, charge sharing also leads to lower signals measured per readout strip and therefore might decrease the detection efficiency. As a smaller strip pitch increases the charge sharing probability, a compromise must be found between a good resolution (small pitch) and a high signal measured per strip (large pitch).

All strip detectors currently employed in the LHC experiments follow the p^+-n-n^+ layout. An alternative design, which is under discussion as a radiation-hard option for silicon strip detectors at the HL-LHC (see Section 4.4.2), is the n^+-p-p^+ design, also known as n-in-p. In this detector type, the strips, the substrate and the backplane layer have the opposite doping type as those in p^+-n-n^+ sensors. A further detector layout is the n^+-n-p^+ structure, which is for example realised in the current ATLAS pixel detector [Aad08c]. In those detectors n-doped pixels are implanted on n-type substrate and the p-n junction is created between the substrate and the backplane. In detectors with n-type strips or pixels, shorts between the readout segments can occur due to accumulation of negative charges resulting from radiation-induced damage of the oxide (see Section 4.1.1). Therefore, p-type implantations with moderate (p-spray) or high (p-stop) doping concentrations are added between the strips or pixels to maintain insulation.

AC-coupled detectors have a bias ring surrounding the strips, which is connected to the strip implants via bias resistors (see Fig. 3.7). This supplies the bias potential to the implants while the resistors maintain electrical isolation between the strips. The implants are usually kept on ground potential, while a negative or positive high potential (depending on the detector structure) is applied to the back contact. A further ring, the guard ring, limits the active volume and prevents the depletion region from reaching the highly conductive cutting edge of the sensor. Both guard ring and bias ring consist of implantations, of the same doping type as the strips, and a metallisation on top.

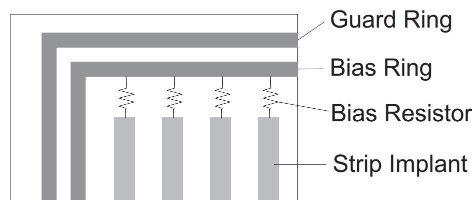

Figure 3.7: Top view of a strip detector illustrating guard ring and bias ring surrounding the readout strips. AC-coupling structures are not shown.

The strips of silicon detectors are usually connected to channels of readout chips, typically consisting of a charge sensitive preamplifier and a shaping amplifier. The shaping amplifier

integrates the input signal and provides output pulses with a semi-Gaussian shape. These pulses are then further processed by the subsequent readout electronics.

3.3.4 Energy Loss of Particles in Silicon

This section describes mechanisms and properties of energy loss of charged particles and photons in silicon. It concentrates on high-energy heavy charged particles, medium-energy electrons and low-energy photons. These particles were utilised for measurements described in this thesis.

Charged Particles

Charged particles traversing matter interact mainly with the electrons of the material atoms and lead to ionisation or excitation of the atoms. The traversing particles lose energy in discrete portions along the particle track and transfer it to the electrons of the material's atoms. For heavy charged particles, the mean energy loss per traversed material length $\langle -\mathrm{dE/dx} \rangle$ is given by the Bethe-Bloch equation (for a detailed discussion see e.g. Refs. [Nak10, Ler09]). The line labelled "Bethe" in Fig. 3.8 shows $\langle -\mathrm{dE/dx} \rangle$ for incident muons as a function of the muon kinetic energy (the other lines are explained further below). The mean energy loss reaches a minimum for muon kinetic energies around $0.2 - 0.3\,\mathrm{GeV}$ and increases for higher energies. A particle having the energy leading to the minimum in $\langle -\mathrm{dE/dx} \rangle$ is referred to as a minimum ionising particle (MIP). In general, the minimum of the energy loss is reached for particles wit $\beta\gamma \approx 3 - 4$, where β is the velocity of the particle in units of the speed of light and γ is the Lorentz factor.

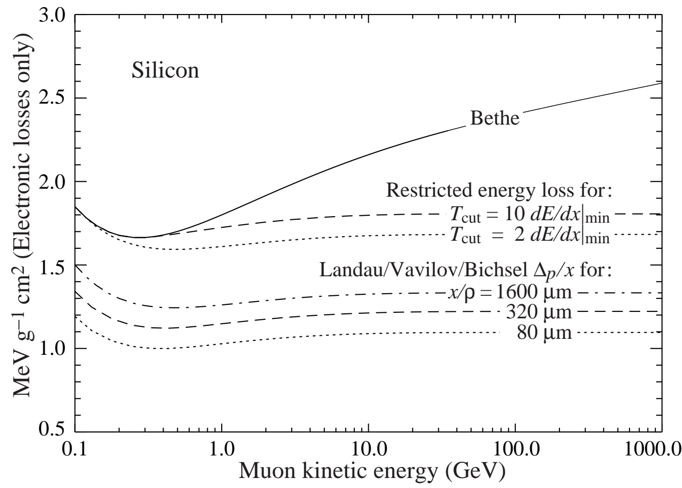

Figure 3.8: Energy loss of muons traversing silicon. Three different calculations are shown: $\langle -\mathrm{dE/dx} \rangle$ according to the Bethe-Bloch equation; $\langle -\mathrm{dE/dx} \rangle$ with restricting possible energy transfers to values smaller than T_{cut}; most probable energy loss per thickness according to the theory developed by Landau, Vavilov and Bichsel. The length of the traversed material is supposed to be in units of cm^2/g. Radiative losses are neglected [Nak10].

Due to the discrete nature of energy transfers to the material in single collisions, the total

energy loss of penetrating particles is subject to large fluctuations. High energy transfers creating energetic knock-on electrons (also referred to as δ-electrons) can occur. Although these events are relatively rare, they lead to an asymmetric shape and a tail to higher energies of the energy loss distribution. Especially in thin absorbers, as silicon detectors applied in particle physics, the energy loss distribution is highly skewed.

Calculated probability functions of energy losses of high-energy particles penetrating thin silicon detectors, known as straggling functions [Bic88], are shown in Fig. 3.9 for selected detector thicknesses. The mean value of the energy loss is considerably higher than the most probable value (MPV) and is largely affected by rare events exhibiting extraordinary high energy transfer. Therefore the MPV is often preferred when characterising the energy loss, respectively the measured signal, in silicon detectors. The straggling functions shown in Fig. 3.9 can be approximated by Landau distributions [Lan44], although the agreement is not perfect [Nak10]. For practical use a convolution of a Landau distribution and a Gaussian is often applied, which further takes into account the broadening of the spectrum due to noise. The MPV of a signal spectrum is often determined by fitting the convolution of a Landau function and a Gaussian to the signal distribution measured with a silicon detector.

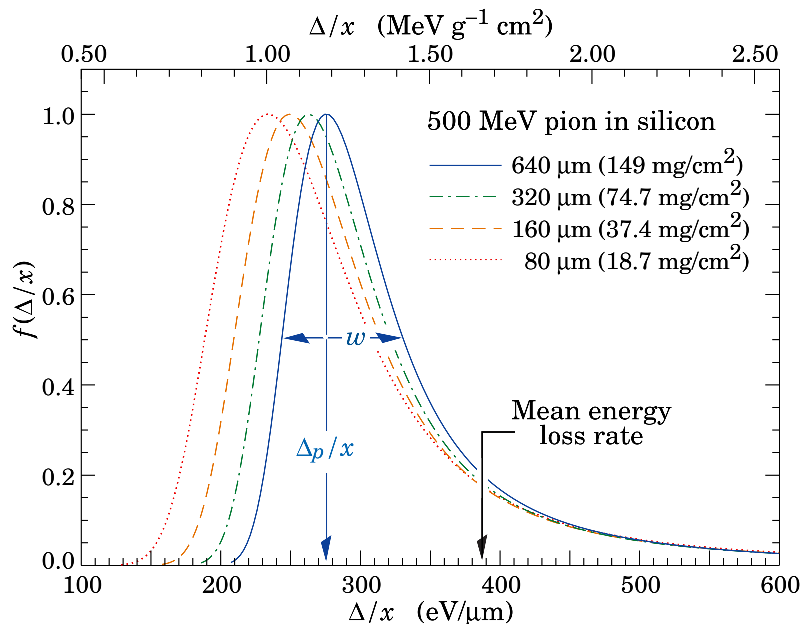

Figure 3.9: Straggling functions (=probability functions of the energy loss) for 500 MeV pions in silicon of four different thicknesses. Δ is the energy loss, Δ_p specifies the most probable value of the energy loss [Nak10].

Restricting the energy loss theory according to Bethe to individual energy transfers up to a value T_{cut} leads to a flatter curve of $\langle -\mathrm{dE/dx} \rangle$ as a function of the particle energy, see Fig. 3.8. The most probable energy loss in silicon detectors of different thicknesses is illustrated by the lines labelled "Landau/Vavilov/Bichsel Δ_p/x" in Fig. 3.8. It can be

seen that it is approximately constant for energies higher than 0.2 GeV. Therefore, the term "minimum ionising particle" can be extended to particles having energies equal or above the energy leading to the minimum of the Bethe equation. High-energy particles are often referred to as minimum ionising particles when the MPV of the energy distribution is relevant.

While the mean energy loss per path length calculated according to the Bethe-Bloch equation does not depend on the total thickness, the most probable value per path length shows a weak dependence on the thickness (as visible in Figs. 3.8 and 3.9). The most probable energy loss by minimum ionising particles, E_{MP}, in silicon detectors having a thickness t can be parameterised [Bic88]

$$E_{\mathrm{MP}}[\mathrm{eV}] = t(190 + 16.3 \cdot \ln t). \tag{3.16}$$

The thickness t is supposed to be given in µm and the equation is valid for $110\,\mu\mathrm{m} < t < 3000\,\mu\mathrm{m}$. On average, 3.68 eV is needed to create an electron hole pair in silicon [Bic88], which is more than three times the band gap energy in silicon ($E_g = 1.12\,\mathrm{eV}$). Therefore, a minimum ionising particle leads to a most probable signal of

$$Q[\mathrm{e}^-] = t(190 + 16.3 \cdot \ln t)/3.68, \tag{3.17}$$

where the signal is given in units of the elementary charge. In silicon detectors of the typical thickness $t = 300\,\mu\mathrm{m}$, a MIP deposits a most probable energy $E_{MP} = 85\,\mathrm{keV}$, leading to a signal of $23\,\mathrm{ke}^-$.

The energy loss of electrons is somewhat different from the energy loss of fast charged heavy particles, which is described above. Differences arise from the electrons' low mass and the indistinguishability of the incoming electrons and the electrons in the traversed material. While low-energy electrons primarily lose their energy by ionisation, at higher energies energy loss due to bremsstrahlung dominates. The critical energy, above which bremsstrahlung is the main mechanism of energy loss, is approximately 40 MeV in silicon [Nak10]. For the work described in this thesis, electrons originating from the β^- decay of ^{90}Y having an energy of approximately 2 MeV are relevant. In this case energy loss by ionisation largely dominates. The energy loss of electrons can be described by a formalism analogue to the Bethe theory with several additional terms [Ler09]. As a result, the mean energy loss and the most probable energy loss of electrons with an energy $E \approx 2\,\mathrm{MeV}$ are approximately equal to the energy loss discussed above for heavy particles. Electrons of this energy can be regarded as minimum ionising particles and therefore Eq. (3.17) is valid as well.

Photons

When traversing silicon, photons predominantly lose energy via the photoelectric effect, the Compton effect or by pair production. The total cross section for these interactions tends to decrease with the energy and approximately saturates at photon energies in the order of 10 MeV [Nak10]. The energy transferred by high-energy photons, which are for example generated in collisions at the LHC, to a silicon detector of typical thickness is very low. Therefore high-energy photons practically cannot be measured with silicon particle

detectors. However low-energy photons, as the ones created by an infrared laser used in the studies described here, can be measured. The laser creates photons of the wavelength $\lambda = 974\,\mathrm{nm}$, corresponding to an energy of $E = 1.27\,\mathrm{eV}$. In this energy region only the photoelectric effect is relevant. The low energy of the photons can only lead to indirect transitions of electrons from the valence band to the conduction band, which requires the creation or absorption of phonons to conserve the momentum of the electrons (see Section 3.2.1, Fig. 3.2). Direct transition from the top of the valence band to the bottom of the conduction band is not possible. When penetrating silicon, the intensity I of a photon beam exponentially decreases as a function of the traversed material depth x,

$$I(x) = I_0\, e^{-\alpha x}. \tag{3.18}$$

The initial intensity is I_0 and α denotes the absorption coefficient in silicon. The absorption coefficient α for temperatures $T = 20\,^\circ\mathrm{C}$ and $T = -30\,^\circ\mathrm{C}$ is shown in Fig. 3.10 as a function of the photon wavelength.

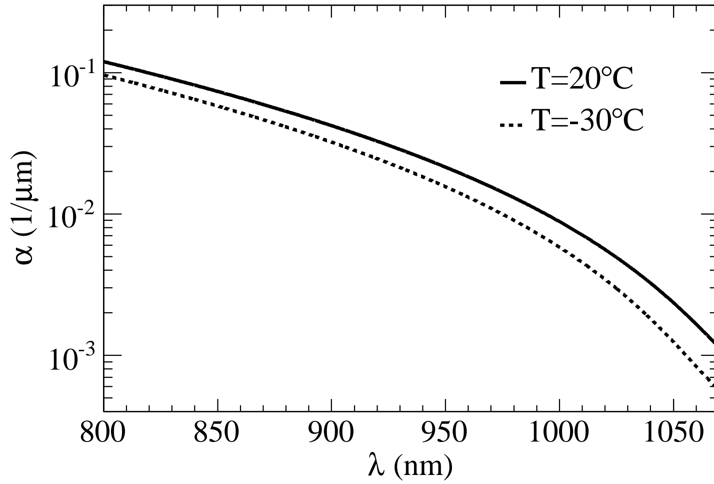

Figure 3.10: Absorption coefficient α of silicon as a function of the wavelength λ of the incoming photons, for temperatures of $+20\,^\circ\mathrm{C}$ and $-30\,^\circ\mathrm{C}$. The calculation is based on a parameterisation given in Ref. [Raj79].

It can be seen that the absorption coefficient and therefore the absorption length, defined as the depth where the intensity has decreased to $1/e$ ($\approx 37\%$), strongly depends on the temperature. The absorption length $1/\alpha$ for a wavelength $\lambda = 974\,\mathrm{nm}$ is $69\,\mu\mathrm{m}$ at room temperature ($T = 20\,^\circ\mathrm{C}$) and $98\,\mu\mathrm{m}$ at $T = -30\,^\circ\mathrm{C}$ [Raj79]. Therefore, the infrared laser used in these studies leads to signal generation primarily in the upper region of the silicon detector. The temperature dependence of the absorption coefficient arises from the temperature dependences of the band gap and the phonon distribution [Raj79]. The total energy measured can be adjusted by tuning the laser power and therefore adjusting the number of emitted photons.

3.3.5 Drift and Diffusion

Free charge carriers move randomly with the thermal energy $3/2\,kT$, where k is the Boltzmann constant and T is the temperature. During the movement the charge carriers are scattered at phonons or ionised impurity atoms. When an electric field is present, the charge carriers are accelerated between these collision. Therefore, a directed movement is superimposed on the thermal movement and a net drift with a constant average velocity results. At low electric fields, the drift velocity v is proportional to the electric field strength E,

$$v = \mu E. \tag{3.19}$$

The proportionality constant μ is the mobility, which is approximately $1500\,\mathrm{cm^2/Vs}$ for electrons and $500\,\mathrm{cm^2/Vs}$ for holes at room temperature [Sze81]. The mobility increases with decreasing temperature, as long as temperatures higher than about 50 K are considered. At electric fields higher than roughly $1\,\mathrm{V/\mu m}$ the mobility decreases and finally, at a field strength of approximately $10\,\mathrm{V/\mu m}$, the drift velocity is independent of the electric field. The saturation drift velocity of electrons and holes is similar and reaches 10^5 m/s at high electric fields.

In the presence of a concentration gradient, for example due to localised generation of free charge carriers by penetrating particles, the thermal movement leads to a broadening of the distribution of charge carriers. After a time t, the charge cloud has a Gaussian shape with the variance

$$\sigma = \sqrt{Dt}, \tag{3.20}$$

where D is the diffusion constant, which depends on the temperature. Due to the broadening of the charge cloud during the drift of the charge carriers towards the electrodes, the charge can be spread over several readout strips. For typical charge collection times, the broadening due to drift is in the order of micrometers for 300 µm thick planar silicon sensors.

3.3.6 Signal Generation in Silicon Detectors

After creation of electron-hole pairs the electron and the hole drift into opposite directions towards the electrodes along the electric field lines. The presence of charge carriers in the volume between the electrodes induces image charges on the electrodes. A drift of the charge carriers leads to a change of these images charges. Hence the drift induces a current on the electrodes, which creates the signal measured by the detector. Therefore, the signal starts already directly after the created charge carriers begin to drift and not only when these charge carriers reach the electrodes. The current $i(\vec{r})$ induced on an electrode by movement of a charge carrier with charge q, located at $\vec{r}$ and with the drift velocity $\vec{v}(\vec{r})$ can be expressed via Ramo's theorem [Ram39]

$$i(\vec{r}) = q\,\vec{v}(\vec{r}) \cdot \vec{E}_w(\vec{r}), \tag{3.21}$$

where $\vec{E}_w(\vec{r})$ is referred to as the weighting field. As Eq. (3.21) was independently derived by Shockley [Sho38], it is also known as the Shockley-Ramo theorem. The weighting field $\vec{E_w}$ for a selected electrode can be calculated as follows: the potential of the electrode under consideration is set to 1 while all other electrodes are grounded. Then, the

weighting potential ϕ_w and the weighting field $\vec{E}_w$ are given by the Laplace equation $\Delta\phi_w = -\nabla \cdot \vec{E}_w = 0$. The weighting potential is considered to be dimensionless, whereas the weighting field has the dimension 1/length. It should be noted that the weighting field is different from the electric field and only depends on the given geometry of the detector.

The total signal measured by the detector is the time integral of the induced current up to the maximum integration time of the amplifier. A ballistic deficit arises when the integration time is shorter than the charge collection time and the full signal cannot be measured. Charge collection times can be kept below 10 ns for electrons and holes in 300 µm thick planar silicon detectors if the bias voltages can be chosen sufficiently high and therefore over-depletion can be reached.

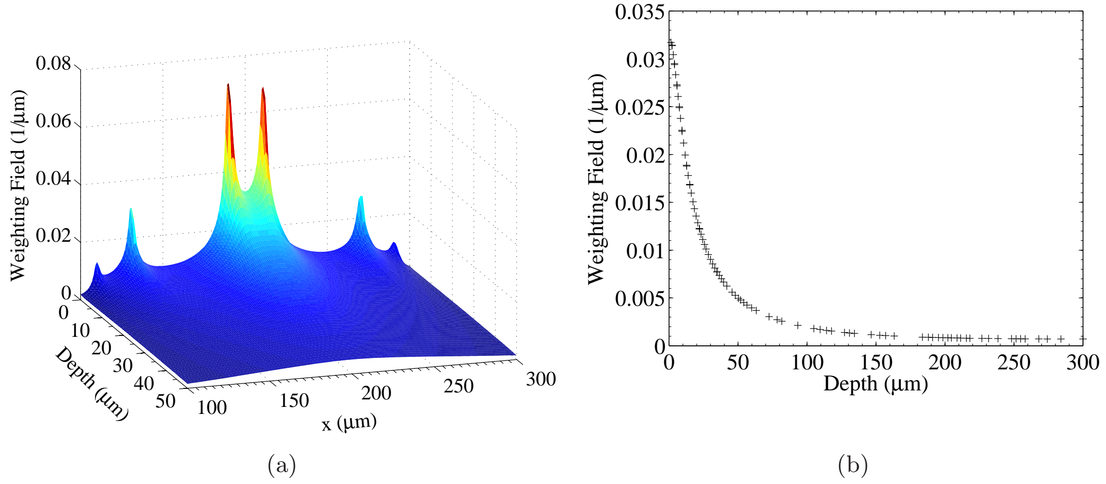

(a) (b)

Figure 3.11: Weighting Field of a 300 µm thick planar strip detector with 20 µm wide strip implants at a pitch of 80 µm. (a) Weighting field for the strip located around $x = 200$ µm in the first 50 µm of the depth. (b) Weighting field as a function of the depth at $x = 200$ µm.

The weighting field of a simple diode with one electrode at the front surface and one electrode at the back surface (cf. Fig. 3.5) is $E_w = 1/d$, where d is the thickness. This geometry, also known as a pad detector, therefore has a constant weighting field throughout the entire detector volume. Hence electrons and holes contribute to the total signal by an equal amount, considering a particle crossing the pad detector and depositing energy uniformly along the track. In a segmented detector the weighting field is considerably different and shows a strong dependence on the position in the detector volume. The weighting field in a strip detector with a thickness of 300 µm and a pitch of 80 µm is shown in Fig. 3.11. The strip implants have the shape of a circular segment and have a width of 20 µm at the detector surface. The calculation was performed using the software MATLAB [Mat10], which applies a finite element method for the solution of the equation $\nabla \cdot \vec{E}_w = 0$. It can be seen that the weighting field is high in the vicinity of the strip implant and decreases strongly towards the back electrode. Since the charge carriers drifting towards the strips experience on average a higher weighting field, their contribution to the total signal is larger than that of the charge carriers drifting away from the strips.

Therefore, the signal in segmented detectors with n-side readout is dominated by electrons and that in detectors with p-side readout is dominated by holes.

During the drift of charge carriers, the weighting field of a certain electrode might change the direction and hence the induced current according to Eq. (3.21) can change its sign. The current induced on an electrode where no charge carriers are collected has a bipolar shape and the integral of the induced current is zero. Therefore, neighbours of electrodes collecting the liberated charge carriers measure a vanishing signal if all charge carriers are collected within the integration time of the amplifier. However, there are also cases in which an electrode which does not collect any charge carriers can measure non-vanishing signals. These signals can be of opposite polarity compared to the usual polarity. An example is a ballistic deficit, where the integration time of the amplifier is not long enough to fully integrate the signal current of both polarities. Another reason can be incomplete drift, for example through trapping of charge carriers at crystal defects.

3.3.7 Impact Ionisation

In contrast to gas detectors, silicon particle detectors normally do not exhibit any internal amplification of the generated free charge carriers. Usually, the signal generated by penetrating particles is sufficiently high and amplification for subsequent data processing can be provided by the readout electronics. However, multiplication of charge carriers is possible in silicon when high electric fields are present [Gra73, Sze81, Mae90]. This effect, known as impact ionisation, is exploited in avalanche photodiodes (APD) and can for example occur in silicon particle detectors after strong irradiation (see Section 4.3.5, Chapter 6 and Chapter 7).

When a free charge carrier is accelerated by a sufficiently high electric field in between collisions, it can gain enough energy to create an additional electron-hole pair. The number of electron-hole pairs generated by a charge carrier per distance travelled is expressed as the ionisation rate α. The ionisation rate is strongly dependent on the electric field and is higher for electrons than for holes at a given electric field strength. Since the electric field depends on the position in the depleted volume, the ionisation rates and hence the probability for a charge carrier to cause multiplication strongly depend on the position. The ionisation rate α is often parameterised by the empirical expression $\alpha = A\exp(-B/E)$, where A and B are parameters and E is the electric field strength. Various measurements of the parameters A and B can be found in the literature. A parameterisation of α, which further takes into account the dependence on the temperature T (in °C), is [Gra73]

- for electrons:

$$\alpha_n = 6.2\times10^5 \exp\left(-\frac{1.40\times10^6 + 1.3\times10^3\,T}{E}\right) \quad (E < 24\,V/\mu\mathrm{m}) \quad (3.22)$$

$$\alpha_n = 6.2\times10^5 \exp\left(-\frac{1.05\times10^6 + 1.3\times10^3\,T}{E}\right) \quad (E > 24\,V/\mu\mathrm{m}) \quad (3.23)$$

- for holes:

$$\alpha_p \;=\; 2.0 \times 10^6 \exp\left(-\frac{1.95 \times 10^6 + 1.1 \times 10^3\, T}{E}\right). \tag{3.24}$$

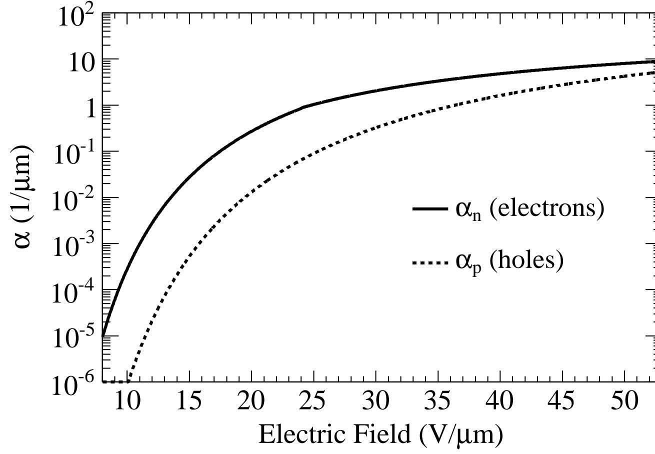

Figure 3.12: Ionisation rate α (at $T = -20\,°\mathrm{C}$) for electrons and holes as a function of the electric field according to Eqs. (3.22)-(3.24).

The ionisation rates for electrons and holes as a function of the electric field are shown in Fig. 3.12. Significant multiplication of electrons starts at an electric field strength between 10 and 15 $V/\mu\mathrm{m}$. The ratio of the number of charge carriers entering a multiplication region and the number of charge carriers leaving that region defines the multiplication factor M. If only electrons are entering the multiplication region, M becomes [Sze81]

$$M = \frac{1}{1 - \int_0^W \alpha_n \exp\left(-\int_0^x (\alpha_n - \alpha_p)\mathrm{d}x'\right)\mathrm{d}x}, \tag{3.25}$$

where W is the width of the multiplication region. At very high electric fields, the charge carriers generated by impact ionisation can in turn create further electron-hole pairs and possibly lead to an avalanche causing electrical breakdown of the device ($M \to \infty$). As the ionisation rates for electrons and holes increase with decreasing temperature (see Eqs. (3.22-3.24)), higher charge multiplication and a lower breakdown voltage are expected for lower temperatures.

Charge multiplication due to impact ionisation can be beneficial for the operation of silicon detectors as it leads to a higher signal. However, the multiplication of the leakage current and statistical fluctuations of charge multiplication might lead to higher noise of the detector (see Section 3.3.8).

3.3.8 Noise Contributions

Noise can originate from fluctuations of the number of free charge carriers (shot noise) and from fluctuations of the velocity of the charge carriers (thermal noise). Noise is a key

parameter of silicon detectors, since it affects the energy resolution of a detector and the ability to identify signal events. Therefore, the signal-to-noise ratio is frequently used as a figure of merit of detectors. Noise is often expressed as equivalent noise charge (ENC). Ideally, the broadening of the signal spectrum due to noise follows a Gaussian distribution with the variance given by the ENC. The following discussion treats noise originating in a silicon sensor and a shaping amplifier connected to it. External noise sources, like pickup of high-frequency electromagnetic radiation from the ambience, are neglected.

The most significant noise contribution in silicon strip detectors typically originates from the noise of the amplifier system due to the load capacitance. The load capacitance C_d is composed of the inter-strip capacitance and the strip-to-backplane capacitance of the detector. The corresponding ENC term is usually parameterised as

$$\mathrm{ENC_{load}} = a + b \cdot C_d, \tag{3.26}$$

where the parameters a and b are specific to the readout chip. The parameter b contains thermal noise contributions originating from conducting channels in the transistors of the amplifier system. For the Beetle ASIC [Lö06], which was used for various measurements presented in this thesis, $a = 465\,\mathrm{e}^-$ and $b = 45\,\mathrm{e}^-/\mathrm{pF}$ are specified if operated with a frontend shaper voltage $V_{fs} = 1\,\mathrm{V}$.

Thermal noise occurs in every resistor and is due to variations of the velocity of charge carriers. Further thermal noise contributions, parallel thermal noise originating from the bias resistors and serial thermal noise originating from the strip resistance [Har09], can be neglected here. The bias resistance is sufficiently high and the strip resistance of the short strip detectors investigated in this thesis are sufficiently low so that these components are small compared to the other contributions.

Charge carriers accounting for the leakage current are created by emission over a potential barrier. The number of charge carriers generated due to thermal excitation follows a Poisson distribution. The statistical fluctuation of the number of charge carriers leads to shot noise with a spectral density [Spi05]

$$\frac{di_n^2}{df} = 2eI_l, \tag{3.27}$$

where i_n^2 is the variance of the leakage current, f is the frequency, e is the elementary charge and I_l is the leakage current. It follows that the equivalent noise charge due to shot noise is proportional to the square root of the leakage current,

$$\mathrm{ENC_{shot}} = \sqrt{BI_l}\, e. \tag{3.28}$$

Assuming a first order CR-RC shaping system, the parameter B in Eq. (3.28) can be approximated by $B = 12\,\mathrm{nA}^{-1} \cdot \tau_p$, where τ_p is the peaking time of the output pulse in ns [Spi05]. In realistic amplifier systems, which do not correspond to ideal CR-RC shapers, the parameter B cannot directly be calculated using the peaking time. For the Beetle ASIC, $B = 210\,\mathrm{nA}^{-1}$ is valid for a frontend shaper voltage $V_{fs} = 1\,\mathrm{V}$ [Loi04]. The shot noise contribution in unirradiated detectors is often small compared to other noise

sources. However, it increases strongly after irradiation due to the radiation-induced increase of the leakage current. To reduce the leakage current and hence the shot noise, detectors in a harsh radiation environment are usually operated at cold temperatures.

Since the different noise contributions are uncorrelated, they can be added in quadrature and the total equivalent noise charge becomes

$$\mathrm{ENC} = \sqrt{\mathrm{ENC}_{\mathrm{shot}}^2 + \mathrm{ENC}_{\mathrm{load}}^2}. \tag{3.29}$$

Multiplication Noise

The presence of impact ionisation and charge multiplication (see Section 3.3.7) increases the shot noise. First, impact ionisation enhances the number of charge carriers contributing to the leakage current, therefore it leads to a higher I_l in Eqs. (3.27) and (3.28). Second, the multiplication processes are subject to fluctuations, which in turn increase the variance of the number of charge carriers present in the device. The multiplication factor M given in Eq. (3.25) specifies only the average multiplication. The spectral density of shot noise given in Eq. (3.27) becomes [McI66, Web74]

$$\frac{di_{n,\mathrm{mult}}^2}{df} = 2eI_l MF = 2eI_{l0}M^2F. \tag{3.30}$$

The multiplied leakage current is denoted as I_l, whereas I_{l0} is the primary, non multiplied leakage current and M is the average multiplication factor. The excess noise factor F arises due to fluctuations of the multiplication and would be equal to unity if all charge carriers would be multiplied by the same factor M. If only electrons are injected into the multiplication region [McI66], the excess noise factor becomes

$$F = kM + \left(2 - \frac{1}{M}\right)(1-k), \tag{3.31}$$

where $k = \alpha_p/\alpha_n$ is the ratio between the ionisation rates of holes and electrons. If there is no hole multiplication ($k = 0$), which leads to stable operation without avalanche breakdown, F increases monotonically between 1 and 2 as a function of M. If hole multiplication comes into effect, F increases strongly. Including excess noise, the ENC of shot noise is (cf. Eq. (3.28))

$$\mathrm{ENC}_{\mathrm{shot,\,mult}} = \sqrt{B\,I_l\,M\,F}\,e. \tag{3.32}$$

The parameter B is not affected by charge multiplication, as it is determined by the amplifier system. Further, charge multiplication does not affect thermal noise. Provided that the signal measured with a silicon detector is also multiplied by M, the signal-to-noise ratio can be increased by charge multiplication if F is not too large or if the shot noise contribution $\mathrm{ENC}_{\mathrm{shot,\,mult}}$ is small compared to the noise due to the load capacitance $\mathrm{ENC}_{\mathrm{load}}$.

Chapter 4

Radiation Damage of Silicon Detectors

4.1 Radiation Damage Mechanisms

As described in Section 3.3.4, particles penetrating a silicon detector can transfer energy to the silicon atoms by means of ionisation. The deposited energy then contributes to the signal measured by the detector. Ionisation in the silicon bulk is fully reversible and does not have detrimental effects. Ionisation in the silicon dioxide, which covers the silicon detector, can lead to irreversible effects, known as surface damage. In addition to the ionising energy loss, charged particles can interact with the atomic nuclei by means of the electromagnetic interaction. Hadrons can furthermore transfer energy to the nuclei by means of the strong interaction. Interactions with the nuclei can result in lattice defects, referred to as bulk damage. The discussion within this chapter focuses on bulk damage, as it has the most severe effects on silicon detectors and poses the main challenge in designing radiation-tolerant silicon detectors for hadron colliders. Effects of surface damage have not been studied in the scope of this thesis.

4.1.1 Surface Damage

Ionising energy loss in silicon dioxide (SiO_2) leads to the creation of electron-hole pairs as in the silicon bulk. Electrons are relatively mobile in the oxide and can leave the oxide layer quickly. In contrast to that, the mobility of holes is several orders of magnitude lower and they move only slowly through the oxide [Har09, Spi05]. This results in a large trapping probability, especially at the Si-SiO_2 interface at the top of the silicon detector. There, the density of hole traps is higher due to mismatch of the lattices and due to dangling bonds. Due to the large band gap of SiO_2 ($E_g = 8.8\,\mathrm{eV}$) detrapping of holes from traps having energy levels deep in the energy gap is practically impossible. Therefore, positive charges accumulate in the oxide, especially at the Si-SiO_2 interface. Predominantly, this has negative effects in electronic devices, but it affects also silicon sensors. These effects are of most importance for silicon detectors operating in environments with high X-ray doses.

In silicon sensors, the accumulation of positive charge in the oxide leads to attraction of

negative charge to the upper regions of the silicon bulk. This charge layer leads to a higher polarisability and therefore causes a higher capacitance between the readout strips, which in turn results in higher noise (see Section 3.3.8). Additionally, the presence of negative charge decreases the resistance between n-type readout electrodes.

The accumulation of positive oxide charge at the Si-SiO_2 interface can be mitigated by using silicon wafers with ⟨100⟩ orientation, which has fewer dangling bonds and therefore creates fewer hole traps near the surface than ⟨111⟩ or ⟨110⟩ silicon [Har09]. Electrical shorts between n-type readout strips or pixels caused by the attraction of negative charge can be avoided by applying p-spray or p-stop isolation schemes [Ric96, Pel07]. P-spray isolation consists of a relatively uniformly p-doped layer between the strips, which effectively neutralises the accumulation of negative charges. P-stops consist of narrow p-implants with higher doping concentrations compared to p-spray and disrupt the conducting channels between the n-implants.

4.1.2 Bulk Damage

Penetrating particles interacting with the nuclei directly can knock atoms out of the silicon lattice, which results in bulk damage. The mechanisms and the results of this non ionising energy loss (NIEL) are substantially different from energy loss due to ionisation. In contrast to ionisation of the atoms, displacement of atoms due to non ionising energy loss is not fully reversible. An atom knocked out from its lattice site forms an interstitial and leaves behind an empty lattice place, denoted as a vacancy. Interstitials and vacancies can migrate through the lattice and thereby create more complex defect structures, like di-vacancies or bindings with impurity atoms. If the energy transfer to a lattice atom is sufficiently high, this recoil atom can cause further lattice displacements and therefore cause further damage on its path. Additionally, it might lose part of its energy due to ionisation. At the end of the path, the decreased energy of the recoil atom has a higher cross section for elastic scattering. Therefore a region with a high concentration of defects, referred to as a cluster, is formed.

For the creation of point defects and cluster defects, energies larger than 25 eV and 5 keV, respectively, have to be transferred to a silicon atom [Lin80]. The energy is transferred by elastic scattering. The Coulomb force, which affects charged particles only, predominantly leads to small energy transfers, which mostly result in point defects. On the contrary, strong interactions mainly lead to collisions with large energy transfers, which mostly result in the creation of defect clusters. Therefore, charged hadrons (e.g. protons, pions) produce both clusters and point defects, whereas neutrons primarily produce clusters. As the energy which can be transferred to the recoil atom also depends on the energy of the penetrating particle, high-energy charged hadrons produce more clusters than charged hadrons of lower energy [Huh02]. This is illustrated in Fig. 4.1, which shows a simulation of the initial distribution of vacancies after irradiation with 10 MeV protons, 24 GeV protons and 1 MeV neutrons. Energetic electrons and photons, through the creation of free electrons via the Compton effect, can also lead to point defects. However, the bulk radiation damage in hadron colliders is dominated by hadrons.

Lattice defects can create energy levels in the band gap, which affect the properties of

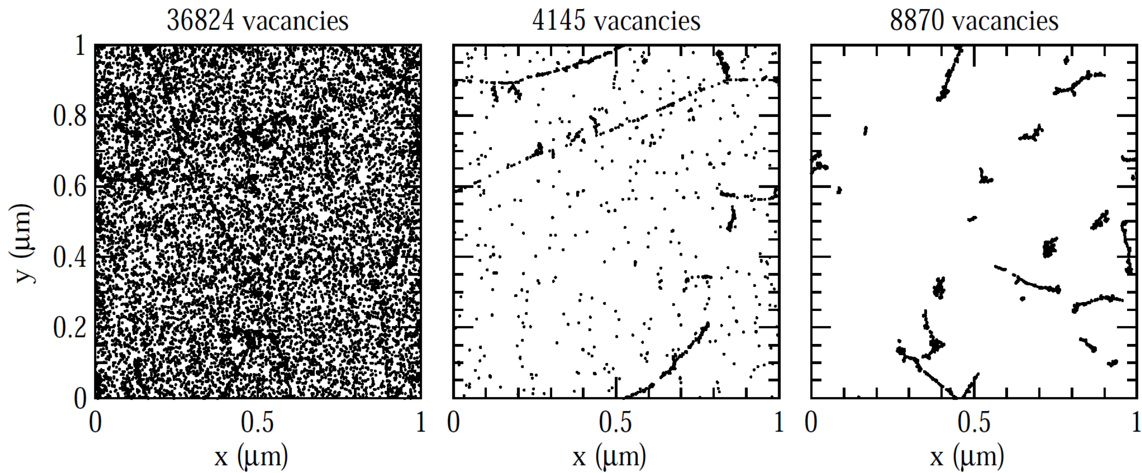

Figure 4.1: Initial distribution of vacancies after a hadron fluence of 10^{14} particles/cm^2 for 10 MeV protons (left), 24 GeV protons (middle) and 1 MeV neutrons (right). The plot shows a projection of 1 µm of depth [Huh02].

silicon detectors. Figure 4.2 illustrates different defect types which can be created by displacement damage and which affect different detector properties. The creation of donors and acceptors (see Fig. 4.2, left) leads to changes of the effective doping concentration and of the space charge density. Furthermore, doping atoms can form complexes with radiation-induced defects or can be knocked out of their lattice places. As a result, dopants can become electrically inactive.

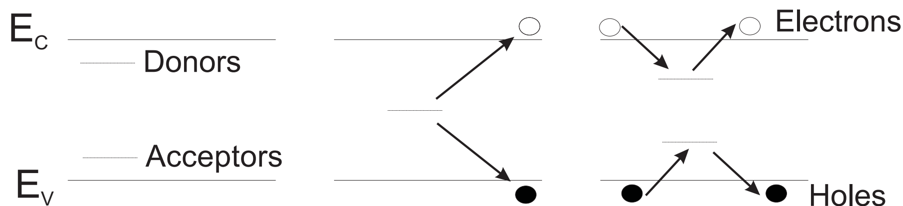

Figure 4.2: Defect levels located in the band gap can affect the properties of the silicon detector. Left: donor- and acceptor-like states can affect the effective doping concentration. Middle: generation-recombination centres in the middle of the band gap contribute to the leakage current. Right: deep defect levels can trap electrons and holes.

Defects having energy levels close to the middle of the band gap (see Fig. 4.2, middle) act as efficient generation centres and contribute to the leakage current (see also Section 3.3.2). Defects "deep" in the band gap can act as trapping centres for electrons and holes, see Fig. 4.2, right. Charge carriers can be trapped at these trapping centres during the drift towards the electrodes. If the detrapping times are longer than the integration time of the amplifier, trapping reduces the measured signal. The detrapping times increase with the energy difference between the defect level and the edge of the respective energy band. Defect levels which have an appreciable energy difference to the closest band edge are commonly referred to as deep defects.

Annealing

After irradiation, many defects remain mobile and can migrate through the crystal. Some defects are repaired, new defects are created and some defects change their configuration. For example, the formation of complex structures including several defects or impurities is possible. These processes are referred to as annealing. It is strongly temperature dependent: higher thermal energy increases the probability for a certain defect to migrate or to change its configuration. It can be assumed that the number of defects N changes with time proportionally to the number of defects present,

$$\frac{dN}{dt} = k\,N. \tag{4.1}$$

As the defects have to cross a potential barrier for the annealing processes, an Arrhenius relation can be assumed for the rate constant k [Mol99]:

$$k(T) = k_0 \exp\left(-\frac{E_a}{k_B T}\right), \tag{4.2}$$

where k_B is the Boltzmann constant, T is the absolute temperature and E_a is the activation energy for the annealing processes under consideration. Equation (4.2) allows to scale the effects of annealing performed at a certain temperature to the annealing effects expected at a reference temperature. Annealing at a temperature T_{ann} leads to the same effects as annealing at a temperature T_{ref}, if the annealing times t at the two temperatures correspond to

$$t(T_{\mathrm{ref}}) = t(T_{\mathrm{ann}}) \exp\left(\frac{E_a}{k_B}\left(\frac{1}{T_{\mathrm{ref}}} - \frac{1}{T_{\mathrm{ann}}}\right)\right). \tag{4.3}$$

The effects of annealing can be investigated by performing accelerated annealing measurements, that is studying the annealing effects at elevated temperatures. Within this thesis, annealing measurements were performed at $T = 60\,^{\circ}\mathrm{C}$. For the long term annealing of the effective doping concentration (see Section 4.3.1), an activation energy of $E_a = (1.33 \pm 0.03)\,\mathrm{eV}$ has been measured [Mol99]. Therefore, annealing at $T = 60\,^{\circ}\mathrm{C}$ leads to an acceleration of approximately 560 compared to room temperature ($T = 20\,^{\circ}\mathrm{C}$).

To reduce unwanted annealing effects, for example the increase of the effective doping concentration and hence the depletion voltage (see Section 4.3.1), irradiated silicon detectors are usually kept at cold temperatures even if they are not operated. Whereas the microscopic description of the annealing mechanisms is beyond the scope of this thesis, the effects of annealing on different detector properties will be discussed in Section 4.3.

4.2 The NIEL Scaling Hypothesis

The NIEL (non ionising energy loss) scaling hypothesis provides a method to scale the macroscopic radiation damage caused by particles of a given energy spectrum to the damage caused by reference particles. With this method, irradiation fluences Φ can be scaled to the equivalent fluence Φ_{eq}, denoting the fluence of $1\,\mathrm{MeV}$ neutrons leading to the same

macroscopic damage.

The effect of displacement damage for penetrating particles of the energy E is quantified by the damage function (see e.g. [Mol99, Ler09])

$$D(E) = \sum_i \sigma_i(E) \int f_i(E, E_R)\, P_i(E_R)\, dE_R, \tag{4.4}$$

where the sum extends over all relevant reactions leading to displacement damage with the cross section $\sigma_i(E)$. The integral extends over all energies E_R of the recoil atoms and $f_i(E, E_R)\, dE_R$ is the probability that an energy between E_R and $E_R + dE_R$ is transferred to a recoil atom by the i-th reaction. The Lindhard partition function $P_i(E_R)$ [Lin80] gives the fraction of the recoil energy used for displacement damage. Thus, the damage function $D(E)$ takes into account the cross section for scattering with atoms in the silicon lattice and the energy effectively going into displacement damage. Figure 4.3 shows calculations of the damage function for different particles as a function of the energy. For 1 MeV neutrons, which is used as a reference for the NIEL scaling of irradiation fluences, the calculations yield $D(E) = 95\,\mathrm{MeV\,mb}$, therefore $D(E)$ in Fig. 4.3 is normalised to this value.

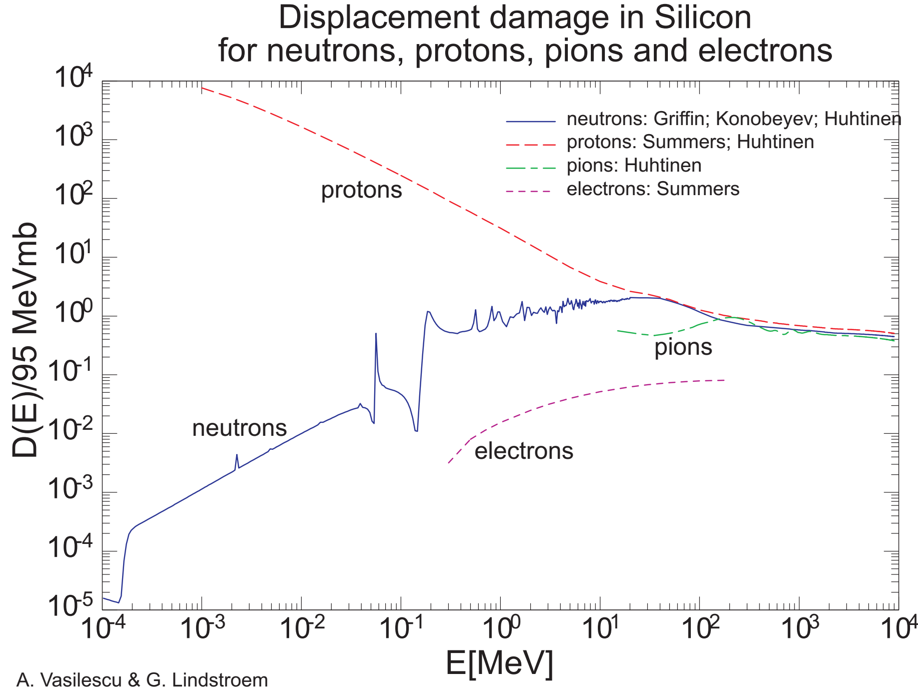

Figure 4.3: Calculated damage functions $D(E)$ for protons, pions, electrons and neutrons as a function of the particle energy. The values of $D(E)$ are scaled to 95 MeV mb, which is the value of $D(E)$ for 1 MeV neutrons [Vas11].

The displacement function can be used to define the hardness factor k, which relates the bulk damage of penetrating particles with energy spectrum $\phi(E)$ to the bulk damage of

1 MeV neutrons:

$$k = \frac{\int D(E)\phi(E)\mathrm{d}E}{D_n(1\,\mathrm{MeV})\int \phi(E)\mathrm{d}E} \tag{4.5}$$

with $D_n(1\,\mathrm{MeV}) = 95\,\mathrm{MeV\,mb}$. If the penetrating particles can be regarded as monoenergetic, the above equation reduces to $k = D(E)/95\,\mathrm{MeV\,mb}$. An irradiation fluence Φ can then be scaled to the equivalent fluence of 1 MeV neutrons :

$$\Phi_{\mathrm{eq}} = k\,\Phi. \tag{4.6}$$

The unit of Φ_{eq} is usually denoted as $\mathrm{n_{eq}/cm^2}$, standing for the number of 1 MeV neutrons per cm^2. In this thesis, silicon detectors are investigated which were irradiated with 25 MeV protons. All irradiation fluences given in this thesis are scaled to 1 MeV neutrons using Eq. (4.6), where a hardness factor $k = 1.85$ was used (see Section 5.1.3).

While the scaling of irradiation fluences using the NIEL scaling hypothesis works very well for various properties, as the radiation-induced leakage current after hadron irradiations, it is violated for other radiation effects. For example, it has been found that enrichment of silicon with oxygen reduces the radiation-induced change of the effective doping concentration when irradiated with protons, however, no beneficial effect of oxygen is seen in neutron irradiations [Lin01].

4.3 Effects of Radiation Damage on Detector Properties

In this section the main effects of radiation-induced bulk damage on measurable properties of silicon detectors are summarised. In general, the signal-to-noise ratio is considered as a figure of merit of a detector. Therefore, radiation effects are particularly detrimental if they lead to a decrease of the signal and to an increase of the noise.

4.3.1 Effective Doping Concentration and Depletion Voltage

In a silicon pad detector with a geometry of a simple diode (cf. Fig. 3.5, Section 3.3.1), the depletion voltage V_{dep} is proportional to the effective doping concentration N_{eff} and the square of the detector thickness (see Eq. (3.9)). In silicon strip detectors, the depletion voltage is actually higher than predicted by this simple equation due to the finite pitch and the width of the strip implants [Bar94]. However, the depletion voltage is still proportional to N_{eff} and Eq. (3.9) is often used as an estimation. In 3D detectors, see Section 4.4.5, the depletion voltage cannot be calculated according to Eq. (3.9), however, also in this case the effective doping concentration determines the depletion voltage.

In a simplified view, the signal measured with a pad detector is proportional to the width of the deletion zone. Therefore, it is desirable to keep the depletion voltage below the maximum operating voltage of the detector. This can be regarded as valid for unirradiated and lightly irradiated detectors, as long as charge carrier trapping (see Section 4.3.3), impact ionisation (see Section 3.3.7) and effects like non-negligible resistance of the undepleted bulk and a double junction (see Section 4.3.4) can be neglected. The effect of under-depletion can be different in segmented detectors due to the characteristic distribution of the weighting field. In strip detectors the weighting field is maximal close to the

strips (see Section 3.3.6) and therefore the signal will be formed predominantly by charge carriers drifting through this region.

In conventional float-zone (FZ) silicon, radiation-induced bulk damage leads to creation of acceptor-like states and to removal of existing donors, thus creating negative space charge. Therefore, after irradiation the silicon behaves more like a p-type material. However, it has to be noted that these acceptor-like states can behave differently than conventional shallow acceptors introduced by dopants. For example, deep electron traps can capture free electrons from the conduction band and therefore generate negative space charge without creating free holes.

An important contribution to acceptor creation is the generation of di-vacancy oxygen complexes [Lin01, Pin09]. Donor removal is caused by formation of complexes consisting of vacancies and phosphorus atoms. The energy level of phosphorus is changed and it does not act as a donor any more. It is worth mentioning that the modification of the doping concentration in the highly doped n^+ and p^+ implantations, which form the contacts at the front and back surface of the detector, can be neglected.

The effective doping concentration and the depletion voltage in p^+-n-n^+ pad detectors as a function of the equivalent fluence is shown in Fig. 4.4. Initially, the effective doping concentration decreases and finally the material becomes effectively p-type. The region with the maximum of the electric field moves to the back contact of the detector. This observation is often referred to as type inversion or space charge sign inversion (SCSI). P-doped FZ silicon does not undergo type inversion, the space charge remains negative. For high irradiation fluences, the effective doping concentration and the depletion voltage increase linearly with the fluence for both initially n-type and p-type materials. Ultimately, the depletion voltage might increase beyond the breakdown voltage or beyond the voltage which can be supplied to the silicon sensor.

A high concentration of oxygen and oxygen dimers in silicon can influence the modification of the effective doping concentration after irradiation. When irradiated with protons, the effective doping concentration in oxygen enriched FZ silicon increases less strongly as a function of irradiation fluence compared to standard FZ silicon [Lin01]. However, no beneficial effect of the oxygen concentration has been found if the detectors are irradiated with neutrons. Detectors with an n-type substrate made of oxygen enriched epitaxial silicon or magnetic Czochralski silicon (MCz) even show an increase of positive space charge when irradiated with charged hadrons [Pin09, Kra10a]. Therefore, these detectors do not exhibit space charge sign inversion and remain n-type like, while the effective doping concentration increases. Irradiation with neutrons, however, leads to the introduction of negative space charge and hence also to space charge sign inversion. MCz detectors with p-type substrate do not exhibit this extreme dependence on the type of irradiation, both charged and neutral hadrons lead to generation of negative space charge [Kra10a]. These observations show that the NIEL hypothesis is violated for the effective doping concentration. The different effects can be related to the different amount of point defects and defect clusters created by charged and neutral hadrons.

After irradiation, annealing effects lead to a further modification of the effective doping

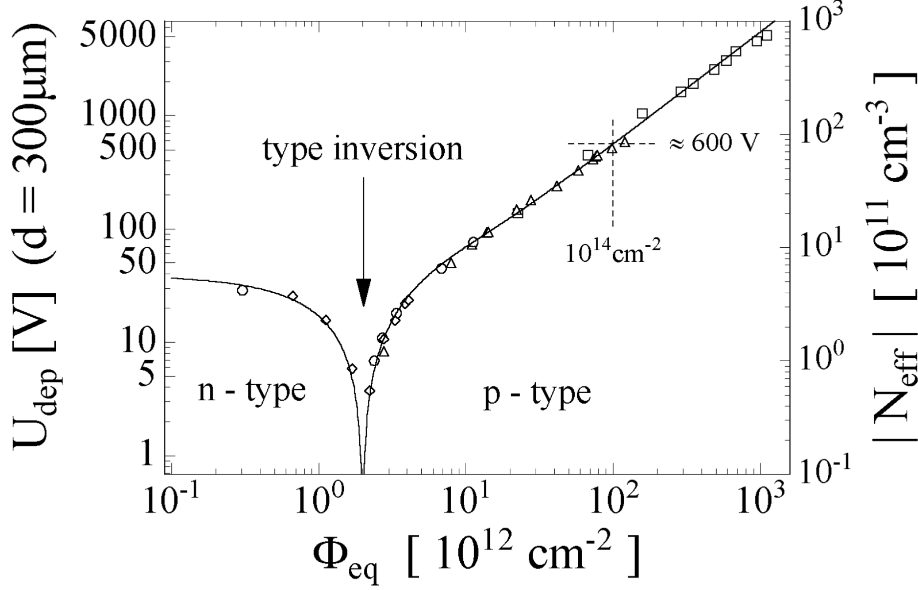

Figure 4.4: Depletion voltage U_{dep} and absolute value of the effective doping concentration $|N_{\text{eff}}|$ of 300 μm thick silicon pad detectors with n-type float-zone substrate as a function of irradiation fluence Φ_{eq}. The data were corrected for self-annealing during the irradiation, which explains why the values are considerably higher compared to results reported elsewhere and reflecting the measured values after irradiation. Plot taken from Ref. [Mol99], with data from Ref. [Wun92].

concentration [Mol99, Kra10a]. Results of annealing measurements for FZ and MCz silicon pad detectors, both with n-type and p-type substrate and irradiated with different fluences of pions, are shown in Fig. 4.5. The detectors have been stored at 60 °C for increasing periods of time and after each of these annealing steps the depletion voltage was measured with $C-V$ measurements. Initially, up to approximately 80 min at 60 °C, short term annealing leads to the creation of positive space charge. For p-type silicon and type inverted n-type silicon, this leads to a reduction of the depletion voltage, therefore this component is often called beneficial annealing. In n-type MCz silicon however, which does not type invert when irradiated with charged hadrons, the short term annealing can even lead to a slight increase of the depletion voltage.

Long term annealing, which is often referred to as reverse annealing, leads to the creation of negative space charge. As can be seen in Fig. 4.5, the depletion voltages increase strongly for FZ and p-MCz silicon. Therefore, irradiated silicon detectors are usually stored at cold temperatures, even when they are not operated. Investigations of the reverse annealing at different temperatures have revealed an activation energy (see Eq. (4.2)) of $E_a = (1.33 \pm 0.03)\,\text{eV}$ for n-type FZ silicon [Mol99], which can be used to scale annealing measurements performed at a certain temperature to a reference temperature (see Section 4.1.2).

After annealing of approximately 80 min at 60 °C, the effects of short term annealing are fading and the long term annealing starts. After beneficial annealing, the radiation-

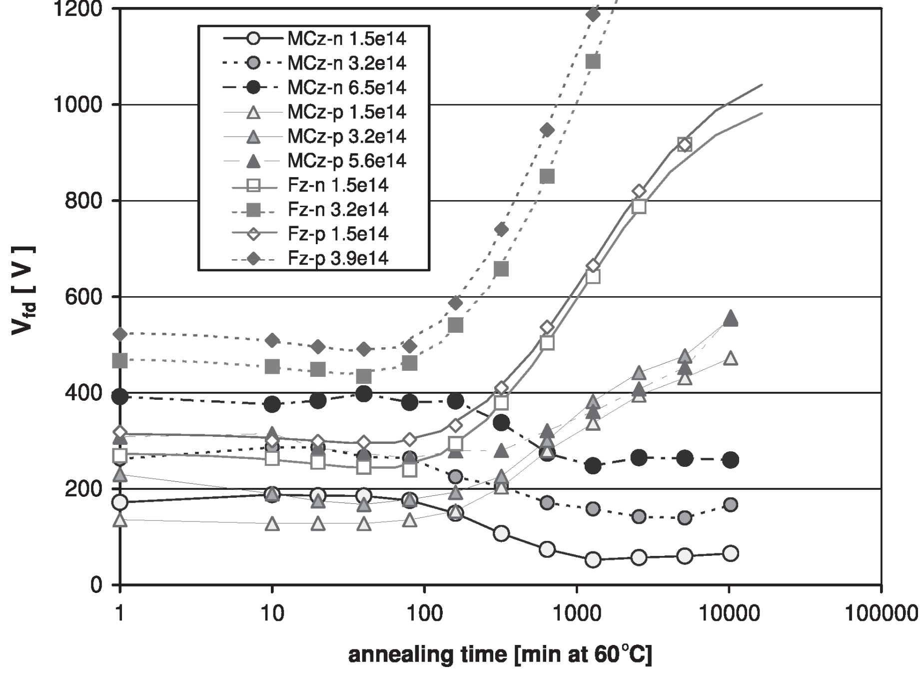

Figure 4.5: Depletion voltage V_{fd} of 300 µm thick silicon pad detectors irradiated with pions as a function of the annealing time at 60 °C [Kra10a]. The legend indicates the different substrate types and the equivalent fluences in $\text{n}_{\text{eq}}/\text{cm}^2$. The data of the FZ detectors are fitted with a model according to [Mol99], the MCz data are connected to guide the eye.

induced increase of the effective doping concentration ΔN_{eff} is approximately proportional to the equivalent fluence [Mol99]:

$$\Delta N_{\text{eff}} \approx g_c \, \Phi_{\text{eq}}, \tag{4.7}$$

with the so-called introduction rate of stable acceptors g_c. For proton irradiated FZ silicon, which is investigated within this thesis, an introduction rate of

$$g_c \quad = \quad (0.012 \pm 0.001)\,\text{cm}^{-1} \tag{4.8}$$

was measured [Cin09]. Typical values for N_{eff} are of the order of $10^{11} - 10^{13}\,\text{cm}^{-3}$ before irradiation. Therefore, the effective doping concentration is practically determined by radiation-induced defects after irradiation with fluences above approximately $10^{15}\,\text{n}_{\text{eq}}/\text{cm}^2$. The investigation of the effective doping concentration and the depletion voltage is in most publications limited to fluences below approximately $\Phi_{\text{eq}} = 10^{15}\,\text{n}_{\text{eq}}/\text{cm}^2$. At higher fluences, it is difficult to determine the depletion voltage since it exceeds values of about 1000 V for standard 300 µm thick detectors. Recent investigations indicate a deviation of Eq. (4.7) in highly irradiated detectors and point to a lower value of g_c above $\Phi_{\text{eq}} \approx 10^{15}\,\text{n}_{\text{eq}}/\text{cm}^2$ [Cas11b].

Due to the increase of the effective doping concentration after irradiation and during subsequent long term annealing, the maximum of the electric field in the sensor increases

as well. In highly irradiated sensors the electric field strengths can exceed values where charge multiplication due to impact ionisation (see Section 3.3.7) is possible. The investigation of charge multiplication in 3D and planar strip sensors is part of this thesis. Furthermore, even the undepleted silicon bulk becomes more resistive after irradiation and exhibits a non-negligible electric field (see Section 4.3.4). Hence charge carriers generated in this part may contribute to the signal as well and the concept of distinguishing between depleted and undepleted bulk becomes questionable when considering highly irradiated detectors. These reasons can lead to a much lower decrease of the measured signal after intense irradiation than expected from considerations based on the depletion voltage.

4.3.2 Leakage Current

The radiation-induced creation of generation centres close to the middle of the band gap leads to higher leakage current. The increase of the current ΔI is proportional to the irradiation fluence [Mol99]:

$$\Delta I = \alpha \, \Phi_{\mathrm{eq}} \, V, \tag{4.9}$$

with the current related damage rate α and the depleted volume V. Values for α are usually specified for the leakage current measured at 20 °C, which can be scaled to any reference temperature using Eq. (3.14). Annealing of irradiated detectors leads to a decrease of the leakage current. This can be expressed by considering the current related damage rate α to be dependent on the annealing state. Figure 4.6 illustrates α as a function of the annealing time at 60 °C.

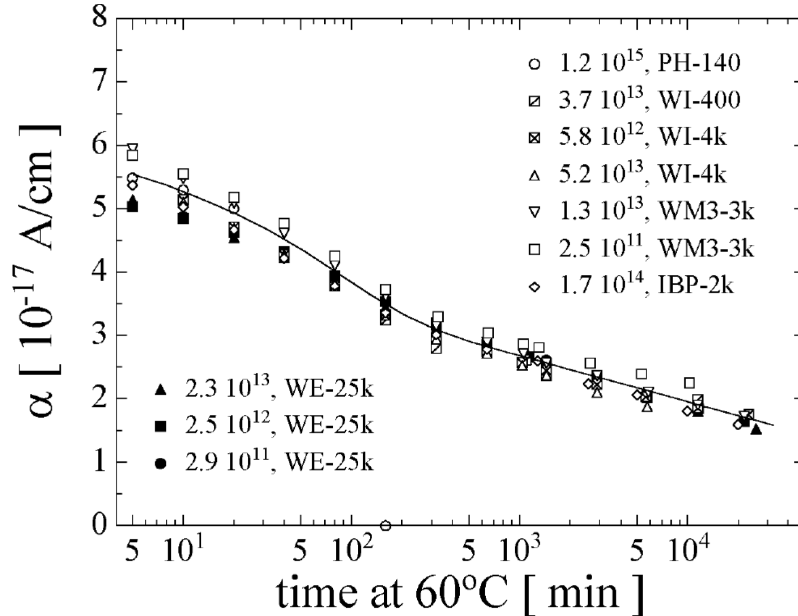

Figure 4.6: Current related damage rate α as a function of the annealing time at 60 °C. The legend indicates the serial numbers of different detector test structures and the equivalent fluence in $\mathrm{n_{eq}/cm^2}$. The line is a parameterisation according to Eq. (4.10) [Mol99].

The dependence of α on the annealing time t for an annealing temperature of 60 °C can be parameterised [Mol99]

$$\alpha(t)[10^{-17}\frac{\mathrm{A}}{\mathrm{cm}}] = 1.26 \cdot \exp\left(-\frac{t}{94\,\mathrm{min}}\right) + 4.87 - 0.316 \cdot \ln\left(\frac{t}{1\,\mathrm{min}}\right). \tag{4.10}$$

A dependence of α on the impurity concentration or the particles used for the irradiation has not been found, if the particles are hadrons. Therefore, the NIEL hypothesis holds extremely well for the radiation-induced leakage current. This allows to determine the hardness factor k (see Eq. (4.6)) experimentally for an irradiation facility [Mol99]. Since the leakage current of unirradiated detectors is usually very low, the total current is given by Eq. (4.9) already after a detector has received low irradiation fluences.

The increased leakage current of irradiated detectors leads to higher shot noise and to an increased danger of thermal runaway. These effects demand a strong cooling of irradiated detectors.

4.3.3 Trapping

Defects having energy levels in the band gap can capture electrons and holes and release them after some time. This process, called trapping, can decrease the measured signal if the detrapping times are larger than the integration time of the amplifier system. Since the detrapping time depends on the energy difference between the defect level and the respective edge of the energy band, only defects with energy levels deep enough in the band gap are relevant. After a time t, the number of initially created charge carriers N_0 decreases according to

$$N(t) = N_0\, e^{\frac{-t}{\tau_{e,h}}} \tag{4.11}$$

with the effective life time $\tau_{e,h}$ of electrons and holes, respectively. The radiation-induced increase of trapping centres leads to a higher trapping probability and therefore to shorter effective life times of free charge carriers. The inverse of the trapping time increases proportionally to the equivalent irradiation fluence [Kra02]:

$$\frac{1}{\tau_{e,h}} = \beta_{e,h}(t,T)\,\Phi_{\mathrm{eq}}. \tag{4.12}$$

The dependence of the trapping probability on the annealing time t after irradiation and on the temperature T is absorbed in the trapping constant $\beta_{e,h}(t,T)$. Measurements of the trapping constants for electrons and holes after irradiation with reactor neutrons and fast charged hadrons (protons and pions) are listed in Table 4.1. The values correspond to a state after completed beneficial annealing of the effective doping concentration and are scaled to a temperature of −10 °C [Kra07]. It appears that neutron irradiation leads to a higher trapping probability and the trapping constants are larger for holes than for electrons. However, the values given in Table 4.1 partly agree within the error margins, so these trends cannot be clearly proven.

Figure 4.7 shows the effective life times τ and drift lengths $l_{\mathrm{dr}} = v_{\mathrm{dr}}\,\tau$ as a function of the equivalent fluence after proton irradiation. The effective drift lengths are calculated in the limit of high electric fields, assuming a saturated drift velocity of $v_{\mathrm{dr}} = 10^5$ m/s.

Table 4.1: Trapping constants $\beta_{e,h}$ after completion of beneficial annealing of the effective doping concentration. The values are scaled to a temperature of $-10\,^{\circ}$C [Kra07].

	reactor neutrons		fast charged hadrons	
	electrons	holes	electrons	holes
$\beta_{e,h}[10^{-16}\,\frac{\mathrm{cm}^2}{\mathrm{ns}}]$	3.7 ± 0.6	5.7 ± 1.0	5.4 ± 0.4	6.6 ± 0.9

Therefore, the values of the effective drift length given in Fig. 4.7 have to be regarded as an upper limit. In reality, especially in a sensor which is not fully depleted, the drift velocity and hence the effective drift length can be significantly smaller. In the presence of low electric fields, the effective drift length of electrons is longer than for holes due to the three times higher mobility of electrons (see Section 3.3.5).

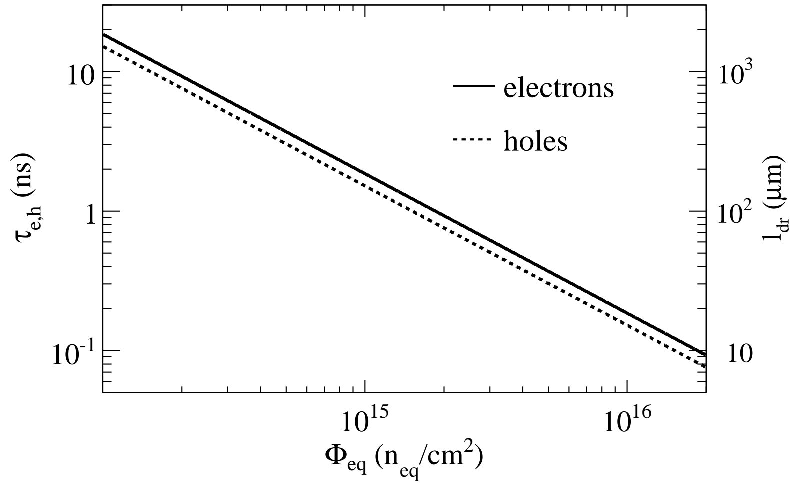

Figure 4.7: Effective life times τ according to Eq. (4.12) and drift lengths $l_{dr} = v_{dr}\,\tau$ for electrons and holes as a function of the equivalent fluence. The calculation was made using the trapping constants $\beta_{e,h}$ listed in Table 4.1 for charged hadrons and assumes a saturated drift velocity $v_{\mathrm{dr}} = 10^5\,\mathrm{m/s}$.

After irradiation fluences above $10^{15}\,\mathrm{n_{eq}/cm^2}$ the effective drift length decreases below $200\,\mu\mathrm{m}$ and is therefore shorter than the typical detector thickness of $300\,\mu\mathrm{m}$. At a fluence of $2 \times 10^{16}\,\mathrm{n_{eq}/cm^2}$, which is expected for the inner pixel detector layers at the HL-LHC, the drift length is even shorter than $10\,\mu\mathrm{m}$. Thus, trapping can be considered as the dominant effect leading to a decreased signal in highly irradiated silicon detectors. However, it has to be mentioned that the trapping constants summarised in Table 4.1 were measured at fluences below $10^{15}\,\mathrm{n_{eq}/cm^2}$. The calculation used for the effective life times and drift lengths shown in Fig. 4.7 assumes linearity of Eq. 4.12 up to the highest fluences, which is so far not verified experimentally.

Figure 4.8 shows the inverse of the effective trapping times of holes and electrons as a function of the annealing time at $60\,^{\circ}$C. After long annealing times, the trapping probability

of electrons decreases and the trapping probability of holes increases by approximately 30%. The dependence of the trapping constants on the temperature can be parameterised as [Kra02]

$$\beta_{e,h}(T) = \beta_{e,h}(T_0)\left(\frac{T}{T_0}\right)^{\kappa_{e,h}}, \tag{4.13}$$

where T_0 is a reference temperature given in Kelvin. For electrons, $\kappa_e = -0.86 \pm 0.06$ and for holes, $\kappa_h = -1.52 \pm 0.07$ has been measured [Kra02]. Therefore, the trapping probability increases with decreasing temperature. As an example, the trapping probability for electrons increases by 10% when lowering the temperature from $-20\,°\mathrm{C}$ to $-50\,°\mathrm{C}$. Given the large errors of the trapping constants, the temperature dependence is of minor relevance.

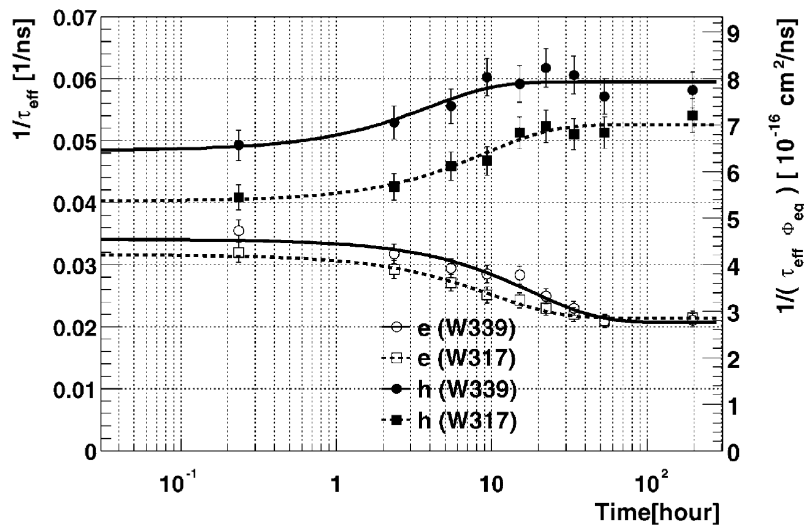

Figure 4.8: Trapping probability of electrons and holes as a function of the annealing time (at $60\,°\mathrm{C}$) for an irradiation fluence of $7.5 \times 10^{13}\,\mathrm{n_{eq}/cm^2}$. The different diodes indicated in the legend (W339 and W317) differ in the oxygen concentration. The lines are fits assuming a decay of the dominant trap into another stable one [Kra02].

The influence of trapping on the measured signal can be estimated by calculating the induced charge according to Ramo's theorem (see Section 3.3.6). In the following, the signal in a pad detector is calculated. In absence of trapping, the induced charge Q for one charge carrier moving in a sensor is

$$Q = \int q\,\vec{v} \cdot \vec{E}_w\,dt, \tag{4.14}$$

where q is the charge of the charge carrier, $\vec{v}$ is the drift velocity and $\vec{E}_w$ is the weighting field. In a pad detector, see Fig. 4.9, the drift velocity is always parallel to the weighting field and $E_w = 1/d$, where d is the thickness of the depleted layer. After high irradiation fluences, the weighting field also extends throughout the undepleted region of the detector due to the high resistivity even of the undepleted bulk [Kra10b].

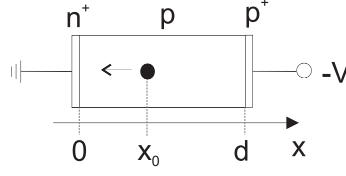

Figure 4.9: Layout of a pad detector. A free electron is created at $x = x_0$ and moves towards the electrode at $x = 0$.

The signal for one charge carrier moving from $x = x_0$ to $x = 0$ becomes

$$Q = q\,\frac{1}{d}\int_{t(x=x_0)}^{t(x=0)} \frac{dx}{dt}\,dt = q\,\frac{1}{d}\int_{x_0}^{0} dx. \tag{4.15}$$

A charged particle traversing a 300 µm thick silicon sensor creates (as the most probable value) approximately 77 electron-hole pairs per micrometer path length (see Eq. 3.17, Section 3.3.4). The electrons and holes drift into opposite directions. In the presence of trapping, this leads to a signal

$$Q = 77\,\frac{-e}{\text{µm}}\,\frac{1}{d}\int_0^d \left(\underbrace{\int_{x_0}^{0} e^{-\frac{x_0 - x}{l_{dr,e}}}\,dx}_{\text{electrons}} - \underbrace{\int_{x_0}^{d} e^{-\frac{x - x_0}{l_{dr,h}}}\,dx}_{\text{holes}} \right) dx_0. \tag{4.16}$$

The charge of one electron is $-e$, $l_{dr,e}$ and $l_{dr,h}$ specify the effective drift lengths of electrons and holes, respectively. Integration leads to

$$Q = 77\,\frac{-e}{\text{µm}}\,\frac{1}{d}\left[l_{dr,e}(d - l_{dr,e} + l_{dr,e}\,e^{-d/l_{dr,e}}) + l_{dr,h}(d - l_{dr,h} + l_{dr,h}\,e^{-d/l_{dr,h}})\right]. \tag{4.17}$$

For high irradiation fluences, if the effective drift length is small compared to the detector thickness d, Eq. 4.17 reduces to

$$Q \approx 77\,\frac{-e}{\text{µm}}\,(l_{dr,e} + l_{dr,h}). \tag{4.18}$$

For an equivalent fluence of $2 \times 10^{16}\,\text{n}_{\text{eq}}/\text{cm}^2$, this approximation leads to a signal of about 1500 electrons, which is less than 10% of the signal in an unirradiated detector of 300 µm thickness. However, the weighting field in segmented detectors, like strip or pixel detectors, is different from pad detectors and has a pronounced maximum close to the readout electrodes. Therefore, the signal is dominated by the charge carriers accelerated to the readout electrode and the above calculation can only serve as an estimation. As will be shown in Section 4.3.5, Chapter 6 and Chapter 7, the signals measured with highly irradiated detectors are substantially higher than expected from Eq. 4.18. Possible reasons are a non-linearity of Eq. 4.12, charge multiplication effects (see Section 3.3.7) and possibly trap-to-band tunnelling of trapped charge carriers [Ben10, Hur92] in regions with high electric fields.

4.3.4 Double Junction

The existence of peaks of the electric field at both contacts of a detector is called double junction effect. It is more pronounced in irradiated silicon detectors [Li92, Kra10b], but can also be observed in unirradiated detectors. Trapping of free charge carriers at deep defects created by radiation damage leads to an accumulation of space charge and hence generates an electric field. Large amounts of free charge carriers are always present in irradiated silicon due to the radiation-induced increase of the leakage current. Since the leakage current is generated uniformly in the silicon bulk, the concentration of holes is maximal at the p^+ contact, while the concentration of electrons reaches a maximum at the n^+ contact in a reverse biased detector. Therefore, regions with high electric field develop at both contacts of the detector [Ere02, Ver07]. The temperature dependence of the leakage current and of the occupation probability of the deep defects leads to a dependence of the electric field strength on the operating temperature.

The base region in between the regions with high electric field exhibits a significant resistivity and hence also an electric field in irradiated silicon detectors, even if the detector is only partially depleted [Li94]. Therefore, also charge carriers generated in these regions can drift towards the electrodes and contribute to the measured signal [Ver07, Kra10b].

In a partially depleted unirradiated detector, a double junction can be observed as well, however it has a different origin than in an irradiated detector. In a detector with p^+-n-n^+ layout, the region with the highest electric field and therefore the main junction is located at the front side, at the p^+-n contact. However, there is also a small space charge region at the n-n^+ contact at the back of the detector. As the effective doping concentration is much higher in the n^+-region, electrons diffuse into the n-region. This creates a space charge region and leads to an electric field analogue to a p-n junction, however to a much lesser extent due to the smaller difference of the Fermi levels in the n^+-region and the n-region. The existence of the two junctions can be observed experimentally [Kra10b].

4.3.5 Charge Collection

The measured signal, or the charge collection, is often investigated when evaluating a sensor technology in terms of radiation hardness. Although the signal-to-noise ratio is more meaningful as a figure of merit for silicon detectors, an investigation of the signal itself constitutes a more convenient comparison of measurements obtained under different conditions. The noise depends strongly on external parameters like the applied readout electronics, the operating temperature and the size of the detector segmentation (for example the strip length), see Section 3.3.8. Signal values commonly quoted are usually measured with minimum ionising particles and reflect the most probable values of Landau distributions. These are obtained by fitting a convolution of a Landau distribution and a Gaussian to the signal spectrum.

The signal measured with p-in-n and n-in-p detectors produced on float-zone substrate is shown as a function of the irradiation fluence in Fig. 4.10. The signal of p-in-n detectors operated at 500 V decreases rapidly with increasing irradiation fluence and is less than

5000 electrons at a fluence of $10^{15}\,n_{eq}/cm^2$. Detectors with p-in-n layout are frequently applied in current high-energy physics tracking detectors, as the ATLAS SCT. The SCT uses binary readout with a threshold of about 1 fC (corresponding to 6200 electrons) and bias voltages up to 500 V. Therefore, these detectors would not function at fluences above $10^{15}\,n_{eq}/cm^2$, which are expected for the inner detector layers of the HL-LHC experiments (see Section 2.2.2).

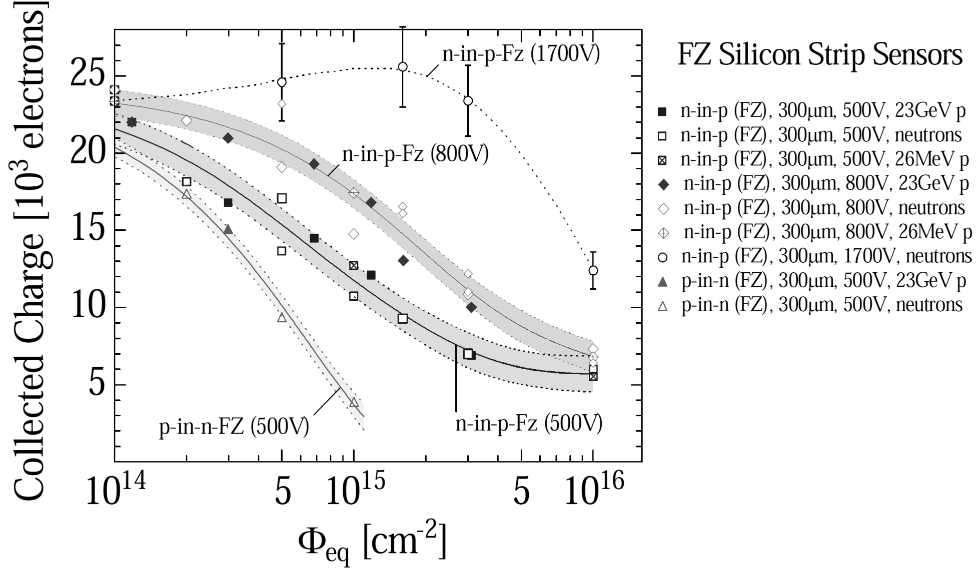

Figure 4.10: Signal in 300 µm thick p-in-n and n-in-p FZ silicon strip detectors operated at different bias voltages as a function of the irradiation fluence. The devices under test were irradiated with reactor neutrons and protons of different energies. Lines are shown to guide the eye and do not reflect any modelling [Mol10].

As can be seen in Fig. 4.10, higher signals can be measured with n-in-p detectors. This will be discussed in more detail in Section 4.4, which also summarises further approaches to increase the radiation hardness of silicon detectors. Higher bias voltages can be very advantageous for the measured signal in highly irradiated sensors. Thus, high voltage stability is essential for detectors designed for harsh radiation environments. At a bias voltage of 1700 V, the signal of irradiated n-in-p detectors can even exceed the signal of unirradiated detectors. Up to fluences of about $3 \times 10^{15}\,n_{eq}/cm^2$ the signal of unirradiated detectors can be reached with irradiated detectors. Higher bias voltages increase the electric field in the sensor and lead to higher drift velocities of the free charge carriers, therefore reducing the susceptibility to trapping. Furthermore, charge multiplication due to impact ionisation can be possible when the electric field is sufficiently high. It is assumed that trap-to-band tunnelling [Ben10, Hur92] of trapped charge carriers at high bias voltages can further enhance the signal, but this effect is less investigated.

Charge multiplication in highly irradiated silicon particle detectors was initially an unexpected effect. Recent measurements with silicon strip detectors [Man10, Cas11b, Cas10, Kra10b] and pad detectors [Lan10], however, established the effect. Within this thesis,

charge multiplication in 3D detectors and planar detectors is investigated (see Chapter 6 and Chapter 7). Impact ionisation in irradiated silicon detectors becomes possible due to the irradiation-induced increase of the effective doping concentration leading to higher electric field strengths. Furthermore, the space charge and hence the electric field can be increased by trapped charge carriers.

4.4 Approaches for Radiation Hard Silicon Detectors

In the framework of the CERN RD50 collaboration [RD], options for silicon detectors being able to operate in very intense radiation environments as expected at the inner radii of the HL-LHC experiments are investigated. Promising results are summarised in this section. Also, enhanced radiation hardness can be obtained by operating silicon detectors at cryogenic temperatures, which is studied by the RD39 collaboration [Tuo09]. In the framework of the RD42 collaboration diamond detectors are developed as a possible radiation tolerant alternative to silicon [Ada06].

4.4.1 Material Engineering

As described in Section 4.3.1, a high impurity concentration of oxygen and oxygen dimers leads to a reduced increase of the effective doping concentration in charged hadron irradiations. A possible explanation is that oxygen acts as a sink for vacancies and thus reduces the probability for the formation of di-vacancy oxygen complexes (V_2O). These defects are expected to be the dominant source of the buildup of negative space charge during irradiation [Lin01]. Oxygen dimers (O_2) can form shallow donors after irradiation, therefore creating positive space charge and counteracting the increase of negative space charge [Pin06].

The beneficial effects of oxygen are exploited for the pixel detectors of the ATLAS [Aad08c] and CMS [Cha08] experiments at the LHC. The oxygen concentration of the silicon substrate is increased by means of diffusion, the resulting material is called diffusion oxygenated float-zone (DOFZ) silicon. Beneficial effects are expected since the radiation fluence present in the pixel layers is dominated by charged hadrons. Measurements showed that the introduction rate of stable acceptors (see Eq. 4.7) in DOFZ silicon is approximately a factor of three lower than in standard silicon [Lin01]. However, neither the radiation-induced increase of the leakage current nor the increase of trapping is affected by the oxygen concentration. Since trapping can be regarded as the most severe problem at radiation fluences expected at the HL-LHC, oxygen enrichment alone will not be enough to achieve sufficient radiation hardness for the inner tracking layers at the HL-LHC.

In recent years, silicon produced by magnetic Czochralski (MCz) or epitaxial growth techniques (see Section 3.1) became interesting due to the intrinsically high concentration of oxygen and oxygen dimers. As in DOFZ silicon, the introduction rate of stable acceptors is lower than in standard silicon. Furthermore, irradiation with charged hadrons introduce positive space charge, whereas neutrons introduce negative space charge in n-type epitaxial and MCz silicon [Pin09]. Therefore, these materials do not exhibit space charge sign inversion. In standard silicon, only negative space charge is created by irradiation. The compensating effects of charged hadrons and neutrons in n-type MCz silicon could

be demonstrated by applying an irradiation with charged hadrons followed by a neutron irradiation [Kra09]. The depletion voltage after the second irradiation was lower than after the first irradiation. This reveals the superior radiation hardness of n-type epitaxial and MCz silicon in terms of the depletion voltage, since both charged hadrons and neutrons contribute to the radiation damage in hadron collider detectors. As a drawback, epitaxially grown silicon and high resistivity MCz silicon is more expensive than standard FZ silicon and only a limited number of suppliers are available.

4.4.2 Planar Detectors with n-Side Readout

An alternative approach to using different detector materials is the application of modified detector structures as n^+-p-p^+ (n-in-p) or n^+-n-p^+ (n-in-n) detectors. Planar detectors with segmented n-type readout electrodes yield a substantially higher signal after receiving high irradiation fluences compared to planar detectors with p-side readout [Aff10] (see also Section 4.3.5). In harsh radiation environments with fluences above $10^{15}\,n_{eq}/cm^2$, planar detectors with p-side readout practically do not come into consideration. The basic advantage of detectors with n-side readout is the fact that the maximum of the electric field is present at the structured side after irradiation and the collection of electrons at the readout segments.

Most conventional silicon detectors are made of p^+-n-n^+ structures, as only n-type substrate was available in detector grade quality for long times. Only the front surface, where the p-implantations are located, has to be patterned. After radiation-induced space charge sign inversion (or type inversion), the depletion zone starts to grow from the n^+ contact at the back. When operated partially depleted, the readout segments are connected via the undepleted bulk, but some degree of isolation is still maintained due to the resistivity of the radiation-damaged undepleted bulk [Li94]. Therefore, the signal is distributed over more channels below full depletion, however it is not spread over all channels [And98]. When charge carriers drift through the region with a low electric field close to the readout electrodes, their drift velocity decreases and hence the trapping probability increases. This becomes especially harmful in highly irradiated detectors, as most charge carriers get trapped before reaching the region with a high weighting field. Since the signal is predominantly formed in this region (see Section 3.3.6), a significant signal loss can be observed. However, it has to be noted that due to the double junction effect and the resistive bulk an electric field is also present in the region which is, in a simplified view, considered as undepleted.

The above mentioned drawbacks can be avoided by applying detectors with n-side readout. The depletion zone in n-in-p detectors grows from the structured side before and after irradiation. In n-in-n detectors this is the case after space charge sign inversion. As a result, the weighting field and the electric field have their maxima in the same region and a larger fraction of charge carriers can drift through the region where the main contribution to the signal is generated. Therefore, the effect of under-depletion is much less severe than in detectors with p-side readout. Operation is possible even after strong irradiation, when the depletion voltage has increased beyond the voltage which can be supplied to the sensor.

The signal in detectors with n-side readout is dominated by electrons, since electrons are drifting towards the readout electrodes. Since electrons have a three times higher mobility than holes, they are less prone to trapping when the drift velocity is below the saturation velocity. Furthermore, irradiation leads to a weaker increase of electron trapping than hole trapping. Another advantage is that annealing decreases the trapping of electrons, while it leads to an increase of the trapping of holes (see Section 4.3.3).

Charge multiplication has a higher influence on the signal in detectors with n-side readout. Since significant multiplication of holes requires much higher electric fields than multiplication of electrons (see Section 3.3.7), only electron multiplication is expected to be relevant. In detectors with n-side readout, electrons can create additional electron-hole pairs close to the front electrode. Both the created electron and the hole can give high contributions to the signal, as they are experiencing a large weighting field. Conversely, electrons can multiply close to the back electrode in p-in-n detectors. As the weighting field is low in that region, the created hole would have to drift until the vicinity of the readout electrodes to contribute to the signal significantly. In highly irradiated detectors, this is hardly possible due to the high trapping probability.

The pixel detectors of ATLAS [Aad08c] and CMS [Cha08] and the detectors of theLHCb vertex locator [Alv08], which are designed for radiation fluences up to approximately $10^{15}\,\mathrm{n_{eq}/cm^2}$, employ n-in-n sensors. Before irradiation, they have to be operated overdepleted, as the undepleted bulk of unirradiated silicon is highly conductive and would shorten the readout segments when operated partially depleted. To prevent the depletion zone from reaching the damaged and highly conductive cutting edge of the sensor, a guard ring structure is necessary on the back side of the sensor. This leads to higher costs, as double-sided processing has to be applied in contrast to single-sided processing as in p-in-n or n-in-p detectors.

Since detector grade p-type substrate became available in recent years, n-in-p detectors have been produced and were extensively studied [Cas00, Aff10]. After irradiation with an equivalent fluence of $2 \times 10^{16}\,\mathrm{n_{eq}/cm^2}$, which is the design fluence for the inner pixel layer of ATLAS at the HL-LHC, a signal of about 7000 electrons was measured with 300 µm thick n-in-p sensors at a bias voltage of 1400 V [Cas11b]. Measurements with planar n-in-p detectors are also discussed in Chapter 7, the specific design of the sensors is described in Section 5.1.2. It has been shown that the signal measured with highly irradiated n-in-p and n-in-n detectors is similar [Aff10]. The production of n-in-p detectors is cheaper than for n-in-n detectors, as the maximum of the electric field is located at the front side and hence no guard ring structure is required on the back of the sensor. However, the potential applied to the back contact is also present at the front side close to the detector edges due to the high conductivity of the cutting edge. This can be problematic for pixel detectors, where the readout chip is bump-bonded onto the sensor [Ros06], and requires additional isolation schemes [Mue10]. The potential difference between the chip, which is held on ground, and the high potential present at the sensor edges can lead to discharges. This problem does not occur for strip detectors. It is foreseen to employ n-in-p FZ strip detectors for the HL-LHC upgrade of ATLAS. At very high irradiation fluences, the application of p-type MCz substrate does not give any advantage compared to p-type FZ substrate [Aff10].

Detectors with n-type readout electrodes require additional isolation of the readout segments, which increases the production costs. Due to ionising radiation, the accumulation of positive charge in the oxide covering the sensor leads to accumulation of negative charge at the silicon surface (see Section 4.1.1). The isolation can be achieved by applying additional p-type doping, either as a uniform layer (p-spray) or as narrow lines (p-stop) or a combination of both [Ric96, Pel07].

4.4.3 Thin Detectors

Reducing the thickness of the detector leads to a lower depletion voltage and to higher electric fields in the sensor at a given voltage (see Section 3.3.1). According to the simplified trapping model presented in Section 4.3.3, the total signal measured after very high irradiation fluences does not depend on the sensor thickness, but only on the effective drift lengths of the charge carriers. An increased electric field can increase the drift velocity of the charge carriers and can enhance the charge multiplication probability in highly irradiated detectors. While the signal of thin detectors is lower than for standard detectors before irradiation, it can be higher after irradiation. After irradiation fluences above $10^{15}\,\mathrm{n_{eq}/cm^2}$, measurements of thin detectors with a thickness of $140\,\mu\mathrm{m}$ partly yield higher signals than standard $300\,\mu\mathrm{m}$ thick detectors [Cas11b]. Very encouraging results have also been obtained with detectors thinned down to $75\,\mu\mathrm{m}$ [Mac10].

A further advantage is the low mass of thin detectors compared to detectors of standard thickness. Thus, the probabilities of multiple scattering, photon conversion and bremsstrahlung emission of electrons are reduced. As thin detectors can be operated with lower voltages, less power is dissipated and hence less cooling is required. However, the reduced thickness increases the capacitance and therefore leads to higher noise.

4.4.4 Operation with Forward Bias

Heavily irradiated detectors exhibit a resistive bulk and application of forward bias is possible [Chi97, Ere07]. The resistivity of the bulk leads to an electric field, which facilitates a drift of charge carriers generated by traversing particles. The leakage current in forward bias mode is higher, which requires stronger cooling of the detector. On the other hand, traps can be filled by the high amount of charge carriers present in the detector due to the high leakage current. This can increase the trapping times of electrons and holes generated by traversing particles. Furthermore, the electric field distribution can be modified by the trapped charge. A model described in Ref. [Ere07] assumes that holes are injected into the detector via the n^+-contact, which can be captured by traps and therefore neutralise the radiation-induced negative space charge. At a certain current density, the trapped charge generates an electric field, which extends through the entire detector. Therefore, high electric fields can be obtained at any fluence.

At a given voltage, the signal measured under forward bias is considerably higher than in reverse bias mode [Chi97, Cas11b]. Despite a higher current, this can lead to lower power dissipation than operation in reverse bias with a higher operation voltage. However, due to the required temperatures of about $-50\,^{\circ}\mathrm{C}$ or lower it appears questionable whether

forward bias operation is of practical use in particle detectors at hadron collider experiments. Forward bias operation of heavily irradiated 3D detectors is investigated within in this thesis in Section 6.2.

4.4.5 3D Detectors

To increase the radiation hardness by a modified detector geometry, 3D detectors have been proposed [Par97]. Columnar electrodes are etched into the silicon substrate perpendicularly to the surface, see Fig. 4.11. The term "3D" indicates that the electrodes extend into the depth of the sensor and are not limited to the surface as in planar detectors. The columns typically have a diameter of approximately 10 µm and are doped to form junction electrodes and ohmic electrodes. In strip or pixel detectors, the readout electrodes are connected to larger segments. This can be achieved by joining sets of columns by means of a metallisation layer on the detector surface. These segments are then connected to amplifier channels as in planar pixel or strip detectors. All columns of the opposite doping type are connected together to form a common ohmic contact.

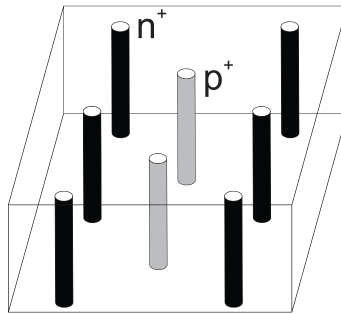

Figure 4.11: Schematic of a 3D detector with fully penetrating columnar electrodes. The columns are arranged periodically so that each p^+-doped column is in the middle between four n^+-doped columns and vice versa. The substrate can be either p-type or n-type, and sets of columns can be connected to strips or pixels. The bias voltage is applied between the n^+- and p^+- columns.

The distance for the drift of generated charge carriers and for the depletion is given by the spacing between columnar electrodes of opposite doping types rather than by the detector thickness as in planar detectors, see Fig. 4.12(a) and 4.12(b). In 3D strip detectors with a pitch of 80 µm and equal spacing between the columns, the distance between columns of opposite doping types is about 50 µm. This is considerably less than the thickness of common planar sensors. The specific geometry of 3D detectors can lead to higher electric field strengths compared to standard planar detectors, which is beneficial in irradiated detectors. Due to the high electric fields and the short charge collection distances, the signal pulses measured with 3D detectors can be much shorter than in planar detectors. Therefore, enhanced radiation hardness is expected due to reduced trapping and a reduced depletion voltage, while the total ionised charge is still determined by the substrate thickness. The thickness can be the same as in typical planar detectors. Furthermore, the higher electric field strengths can enhance the charge multiplication probability. 3D silicon detectors are candidates for the ATLAS insertable B-Layer (IBL) and the inner

pixel layers of ATLAS at the HL-LHC [Mue10].

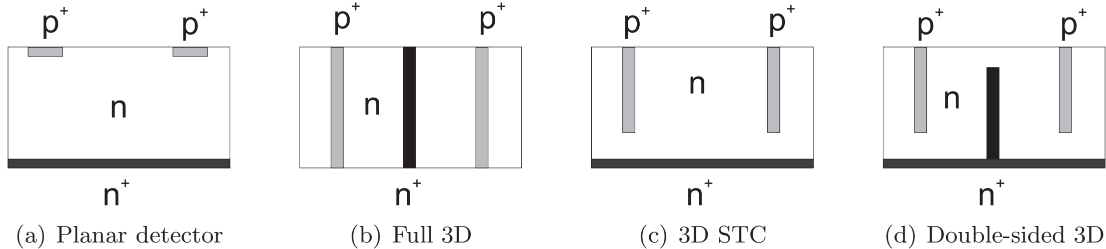

(a) Planar detector (b) Full 3D (c) 3D STC (d) Double-sided 3D

Figure 4.12: Simplified cross section of a planar sensor and different types of 3D sensors with p-in-n layout.

Strip or pixel sensors in 3D layout exhibit a lower charge sharing probability, as the main component of the electric field is directed parallel to the surface. Therefore, charge carriers are drawn away from the boundary between adjacent segments and have less chance for diffusion. The intrinsically reduced charge sharing has the potential to improve X-ray diffraction measurements at synchrotron experiments. The fast charge collection due to the short drift distance makes 3D detectors interesting for experiments where fast timing is required [Par11].

The original approach of 3D sensors [Par97] features columnar electrodes passing through the entire substrate, therefore these are often referred to as full 3D detectors. Alternative designs are mentioned further below. Full 3D sensors were so far produced by the Stanford Nanofabrication Facility [Sta] and by SINTEF [SIN]. As the production [Ken99, Kok10] is considerably more complex than for sensors produced in the planar technology, 3D sensors are more expensive and they were so far mainly produced on small production scales. The holes for the columnar electrodes are etched into the wafer by means of the deep reactive ion etching (DRIE) technique. After the etch process, the holes are filled with polycrystalline silicon to reduce the stress in the wafer. Then, gas phase doping is applied. The holes for the p^+-doped columns are made after the creation of the n^+-doped electrodes. To protect the sensor from damages, the sensor wafer is bonded to a support wafer. Therefore, all processing steps for production of the columns have to be performed from the front side, which requires a high number of steps. For example, the n^+-doped columns have to be protected during the production of the p^+-doped columns. Sets of columns can be connected to segments (strips or pixels) and all columns of the other doping type are connected together to form the bias contacts. The support wafer is removed from the sensor after the processing. Full 3D detectors were successfully tested with laboratory measurements and beam tests [Par01, Mat08, Gre11], measurements with highly irradiated pixel sensors are ongoing.

The production yield, which is reduced by the low stability of 3D sensors, and the complex processing technology of 3D sensors are critical aspects. To develop a simplified production technique, modified 3D designs were proposed. The research institute FBK [FBK] in collaboration with IMB-CNM [IC] has developed 3D single type column (STC) detectors, which consist of columns of one doping type only [Pie05, Pie07], see Fig. 4.12(c). The

columns, which are n^+-doped if the substrate is p-doped, extend into the wafer from one side only and do not penetrate the entire wafer. This limits the number of processing steps and leads to a higher stability of the sensors. The production does not require a support wafer and the columns are not filled with polycrystalline silicon. At the back of the sensor, a layer of uniform doping, which is covered by a metallisation layer, provides the ohmic contact. STC detectors were produced in strip configurations, where the columns are connected by a doping trace covered with a metallisation. Measurements of 3D STC detectors show reduced charge collection efficiencies, especially close to the middle between the columns [Ehr07, Kü08, Pah09]. As the columns are of the same doping type and are kept on the same potential, a low-field region develops in the middle between them. This leads to slow drift of the generated charge carriers and reduces the signal when fast shaping is applied. The work on 3D STC was meanwhile concluded.

As a next step, detectors with columns of both doping types, but not penetrating the wafer completely (see Fig. 4.12(d)), were developed by FBK [Zob08a] and IMB-CNM [Pel08]. The processing is still less complex than for full 3D sensors, no support wafer is required and the sensors are less fragile than 3D sensors with fully penetrating columns. The sensor layouts of the two manufacturers differ slightly, the IMB-CNM design is often referred to as double-sided 3D, the FBK layout is commonly called double-sided, double type column (DDTC) 3D sensors. Double-sided and 3D DDTC sensor are investigated within this thesis. The detailed design is described in Section 5.1.1, results of the performance before and after irradiation are described in Chapter 6.

The specific configuration of the electric field and the weighting field in 3D sensors leads to a different signal formation compared to planar sensors. Field simulations and consequences will be discussed in Section 5.1.1. A drawback of 3D detectors, besides the complex processing, is the enlarged capacitance due to the small spacing of the electrodes. This leads to higher noise, especially in detectors with large segments as strip detectors.

Chapter 5

Devices Under Test and Experimental Methods

5.1 Devices Under Test

Two different detector structures are investigated within this thesis: double-sided 3D strip detectors and planar strip detectors. The detectors were partly irradiated with fluences expected for the pixel detector layers at the HL-LHC upgrade of ATLAS. The 3D detectors can be regarded as an option for the inner pixel layers, where an extreme radiation hardness is required.

The measurements presented in this thesis were made with detectors in strip layout. Measurements with pixel detectors imply a significantly larger effort, since the sensors and the readout chips have to be connected by means of bump bonding techniques. Consequently, one readout chip has to be used for each sensor. Furthermore, commonly applied bump bonding procedures involve high-temperature steps, which would lead to extreme annealing and can destroy irradiated sensors. As a result, sensor and readout chip have to be bump bonded before irradiation, which in turn requires very radiation hard readout chips. Since pixel detector readout chips currently available suffer from ionising radiation, irradiations with high particle fluences are not easily possible. A further complication is the activation of the bump bond solder during the irradiation. Measurements with strip detectors require less effort, irradiated sensors can be connected to the electronics with wire bonds and the readout chips can be reused for various measurements.

5.1.1 Double-Sided 3D Detectors

The double-sided 3D detectors were fabricated by the research institutes IMB-CNM (Barcelona, Spain) [IC] and FBK-irst (Trento, Italy) [FBK]. This detector type is also referred to as double-sided, double type column (DDTC) 3D sensor. This term is mainly used for the detectors produced by FBK. The sensor designs of both manufacturers are similar, however, some differences exist.

Figure 5.1 illustrates the design principle of double-sided 3D detectors. Columns are etched into the substrate from the front and the back. However, the columns do not pass

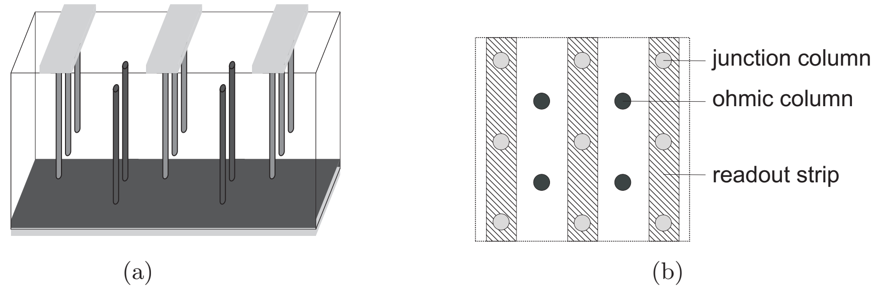

Figure 5.1: Principle of double-sided 3D strip detectors: (a) three-dimensional view, (b) horizontal projection (not to scale). The junction columns (light grey) extend into the substrate from the front side and are connected to readout strips. The ohmic columns (dark grey) extend into the substrate from the backplane and are all connected together.

through the entire sensor substrate. On the front surface of the sensor, the columns are connected to strips which serve as readout segments. These columns are doped with the opposite doping type than the substrate and are referred to as junction columns or readout columns. The other set of columns, which extend into the bulk from the sensor back, are all connected together on the sensor backplane. They are doped with the same doping type as the sensor substrate, therefore they provide the ohmic contact. Each column is centred between four columns of the opposite doping type. The doping concentration of both sets of columns is several orders of magnitude higher than the doping concentration of the substrate.

Detectors with both n-type and p-type substrate are investigated. High resistivity float-zone (FZ) silicon was used as detector material for all sensors. In the case of n-type substrate, the junction columns are p^+-doped and the ohmic columns are n^+-doped, hence the detectors have a p-in-n structure. It is the other way around in detectors with p-type substrate. Columns of the same doping type are arranged every 80 or 100 µm, with a column diameter of approximately 10 µm. Therefore, the distance between junction columns and ohmic columns is approximately 50 µm or 60 µm, respectively.

The performance of double-sided 3D detectors with only partially penetrating columns is expected to be similar to full 3D detectors, if the column depths approach the detector thickness. According to simulations [Zob08a, Pen07], the charge collection of double-sided 3D detectors is somewhat slower than for full 3D detectors. This deficit is reduced with increasing column depth. In the regions where the columns do not overlap, especially between the tips of the ohmic columns and the detector front surface, the electric field is lower. The mechanism of depletion can be divided in different stages: at low voltages, the depletion zone grows laterally in the region where the columns overlap. At higher voltages, once lateral depletion is reached, the volume above the column tips gets depleted.

CNM Design

Double-Sided 3D strip detectors produced by CNM are investigated before and after irradiation with 25 MeV protons (see Section 5.1.3). The maximum irradiation fluence is

$2 \times 10^{16}\,\mathrm{n_{eq}/cm^2}$, which is the expected fluence for the inner pixel layer of the ATLAS detector at the HL-LHC. The radiation hardness of detectors in p-in-n and n-in-p layout is compared directly. Measurements were conducted with beam tests, a radioactive source and an infrared laser.

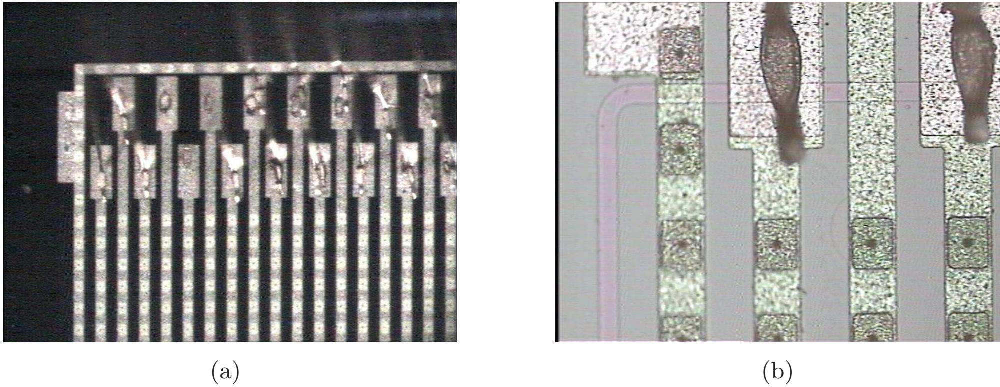

(a) (b)

Figure 5.2: Photograph of the surface of a CNM n-in-p detector. The picture in (b) is a magnification of the image shown in (a).

A photograph of a 3D detector fabricated by CNM is shown in Fig. 5.2. The details of the sensor design are described in Refs. [Pel08, Pen09]. The detectors have been produced on $(285 \pm 15)\,\mu\mathrm{m}$ thick float-zone silicon wafers with a resistivity of approximately $13\,\mathrm{k\Omega\,cm}$. The columns are designed to have a depth of $250\,\mu\mathrm{m}$, a diameter of $10\,\mu\mathrm{m}$ and a distance from centre to centre of $80\,\mu\mathrm{m}$ to each other. However, the columns are considerably shorter in the detectors produced in the very first production run. Implications on the detector performance will be further discussed in Chapter 6. Furthermore, some detectors produced in later production runs have column diameters of about $14\,\mu\mathrm{m}$. On the detector surface, 50 columns are connected to form readout strips, and 50 strips are present per sensor. The active sensor area is therefore $4\,\mathrm{mm} \times 4\,\mathrm{mm}$.

The columns are partially filled with doped polysilicon and passivated with a layer of silicon-dioxide. A rectangle with polysilicon is also present around the holes on the surface, as can be seen in Fig. 5.2(b). The junction columns in a row are tied together by means of a metallisation trace. The detectors do not have embedded structures providing AC coupling. Capacitive coupling between the detector readout strips and the front-end electronics was provided by fanins having integrated capacitors and bias resistors. The AC-coupled fanins were produced by HIP (Helsinki, Finland). These were employed for all measurements with CNM 3D detectors, except for the detector measured in the 2008 beam test. As this detector was measured unirradiated, the leakage current was low and it could be directly connected to the front-end chip.

The bottom of the detector substrate is coated with an oxide layer. The oxide is covered by doped polysilicon, which has the same doping type as the ohmic column extending into the substrate from the backplane. This polysilicon layer connects all ohmic columns through openings of the oxide layer at the column positions. The polysilicon is further

covered by a uniform metallisation layer. A guard ring, consisting of n^+- and p^+-doped columns, surrounds the sensor strips, see Fig. 5.2. In the n-in-p detectors, each junction column is surrounded by a p-stop implant to achieve electrical isolation of the readout strips after accumulation of radiation-induced oxide charge (see Section 4.1.1). These implantations are covered by polysilicon and the strip metallisation and hence are not visible in Fig. 5.2(b). Furthermore, a p-stop implantation surrounds the entire active area of the sensor. This structure can be seen in Fig. 5.2(b).

FBK Design

DDTC 3D strip detectors made by FBK were measured before and after irradiation. However, only the results of the unirradiated detectors could be analysed. The irradiated detectors could not be biased properly due to failures of the punch-through biasing structures. An investigation of this problem will be discussed in Section 6.2.1. Consequently, the performance of FBK detectors could only be studied in an unirradiated state. Detectors in n-in-p and p-in-n layout were measured in beam tests, an n-in-p detector was also measured with an infrared laser setup.

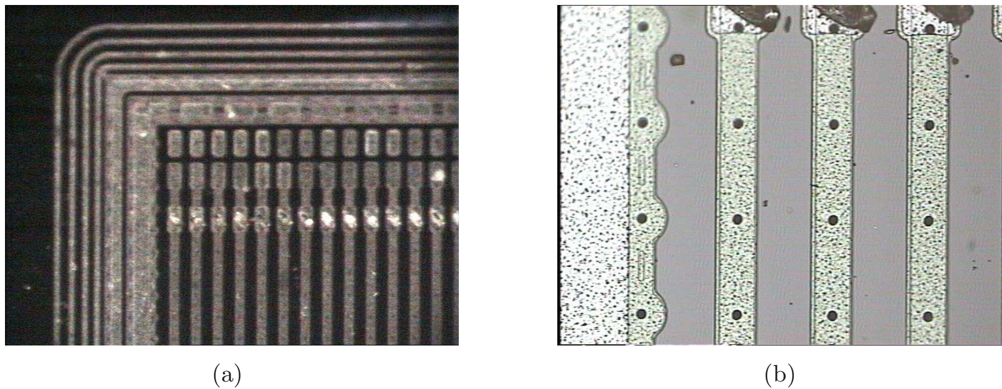

(a) (b)

Figure 5.3: Photograph of the surface of an FBK 3D n-in-p detector. The picture in (b) is a magnification of the image shown in (a).

Figure 5.3 shows a photograph of the front surface of a 3D DDTC strip detector made by FBK. A description of the sensor design can be found in Ref. [Zob08a]. The specific layout is slightly different from that of the CNM detectors described above. In the 2008 beam test, a p-in-n sensor produced on $(300 \pm 15)\,\mu$m thick float-zone silicon was measured. This sensor originates from the very first batch of DDTC detectors ever produced by FBK. The specified resistivity of the substrate is larger than $6\,\mathrm{k\Omega\,cm}$. The junction columns are $190\,\mu$m deep, while the ohmic columns have a depth of only $160\,\mu$m. The spacing between the columns of the same doping type is $100\,\mu$m. In the 2009 beam test, an n-in-p sensor with somewhat different characteristics was measured: the thickness is only $(200 \pm 10)\,\mu$m, the resistivity is approximately $18\,\mathrm{k\Omega\,cm}$. The junction columns are $160\,\mu$m deep, while the ohmic columns have a depth of $180\,\mu$m. Together with the reduced thickness, this results in a larger column overlap compared to the sensors produced in the first batch. The spacing of equally doped columns is $80\,\mu$m. The columns in all FBK detectors are $10\,\mu$m broad.

Contrary to the CNM detectors, the columns of the FBK sensors are unfilled. Polysilicon is not used in the entire production. On the surface, a highly doped implantation, of the same doping type as the junction columns, connects the columns in a readout strip. A metal trace, electrically isolated from the implantation by means of an oxide layer, provides capacitive coupling of the strips. Each strip has two AC-coupled pads and one DC-coupled pad, as can be seen in Fig. 5.3. On the sensor backplane, a uniform layer with a high doping concentration connects all ohmic columns. The doping type is the same as for the ohmic columns. Another important difference with respect to the CNM detectors concerns the biasing scheme of the readout strips. A bias ring surrounds the strips and provides the bias potential to the strips via punch-through structures. The bias ring is surrounded by a 3D guard ring, which consists of n^+- and p^+-doped columns. Further outwards, planar guard rings are located (see Fig. 5.3). In the n-in-p detector investigated, isolation of the readout strips is achieved by means of uniform p-spray.

Electric Field and Weighting Field Distributions

The electric field and the weighting field of 3D detectors were simulated using the software MATLAB [Mat10]. An adaptive mesh generation and a finite element method are performed to solve Poisson's equation $\nabla \cdot \vec{E} = -q_0 N_{\mathrm{eff}}/(\varepsilon_0 \varepsilon_r)$ for the electric field E and Laplace's equation $\nabla \cdot \vec{E}_w = 0$ for the weighting field E_w (see Section 3.3.1 and Section 3.3.6). The simulations are restricted on a two-dimensional approximation of the detector geometry and do not include any modelling of radiation damage. The devices were modelled in a plane parallel to the surface, where the ohmic columns and the junction columns overlap. Since the columns in double-sided 3D detectors penetrate the substrate only partially, this model can only serve as an estimation. It is assumed to approximate the real field distributions in the middle of the detector depth, however, the field will be considerably different close to the detector surfaces and around the column tips.

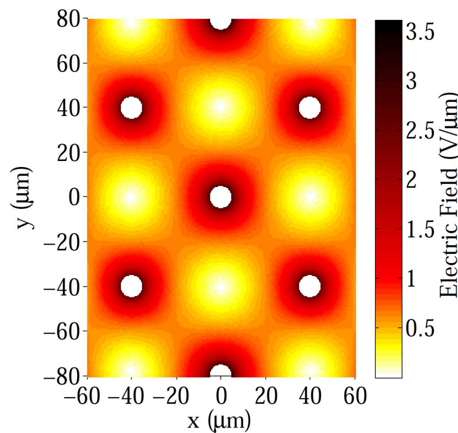

Figure 5.4: Simulation of the electric field for a bias voltage of 50 V and an effective doping concentration of $3 \times 10^{11}\mathrm{cm}^{-3}$. Junction columns are located at (0;-80), (0;0) and (0;80), ohmic columns are located at (-40;-40), (-40;40), (40;-40) and (40;40). The field inside the columns was not simulated.

A calculation of the electric field in a plane parallel to the detector surface is shown in Fig. 5.4. The calculation was made for a bias voltage of 50 V and an effective doping concentration of $3 \times 10^{11}\mathrm{cm}^{-3}$. The effective doping concentration corresponds to the one of the CNM p-in-n detectors before irradiation, which has a resistivity of 13 kΩ cm. The effective doping concentration N_{eff} and the resistivity ρ are related via the equation

$$\rho = \frac{1}{e\mu N_{\mathrm{eff}}}, \tag{5.1}$$

where e is the elementary charge and μ is the mobility of electrons (in n-type silicon) or holes (in p-type silicon). Regions with high electric field strengths are located around the columnar electrodes, while low-field regions are present in the middle between columns of the same doping type. An important aim of the analyses presented in Chapter 6 is to investigate whether lower signals are measured for tracks traversing these low-field regions. In the configuration illustrated in Fig. 5.4, the electric field around the junction columns and around the ohmic columns has approximately the same magnitude. This effect results from the low substrate resistivity. The electric field close to the ohmic columns decreases with the substrate resistivity, as the gradient of the electric field is proportional to the inverse of the resistivity.

In planar pixel or strip detectors, the signal is dominated by the type of charge carriers drifting towards the readout electrodes (see Section 3.3.6). At the back electrode of planar detectors, the weighting field approaches zero, hence charge carriers moving to this electrode contribute less to the signal. This is one reason why planar p-in-n detectors are less radiation hard than planar n-in-p detectors. In planar p-in-n detectors, the signal is dominated by holes, which have a lower mobility and are therefore more prone to trapping than electrons.

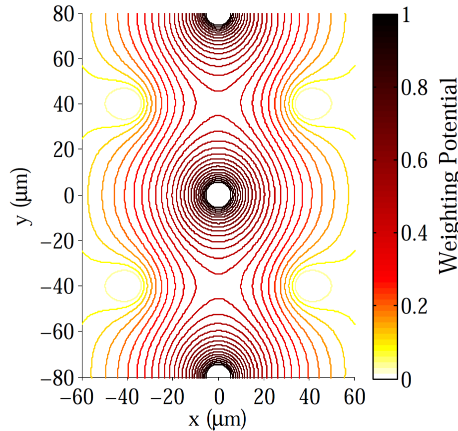

Figure 5.5: Equipotential lines of the weighting potential concerning the readout strip running vertically around $x = 0\,\mu\mathrm{m}$. Junction columns are positioned at (0;-80), (0;0) and (0;80), ohmic columns are located at (-40;-40), (-40;40), (40;-40) and (40;40).

The situation is fundamentally different for 3D detectors. Figure 5.5 shows the weighting potential in a 3D detector. The weighting potential of the electrodes forming the readout

strip, which runs vertically, is set to unity. The weighting potential of the ohmic electrodes is set to zero. Agglomerations of equipotential lines are visible close to the junction electrodes and close to the ohmic electrodes. The weighting field on the direct line between the central junction column of Fig. 5.5 and a neighbouring ohmic column is shown in Fig. 5.6. In contrast to planar detectors, the weighting field exhibits peaks close to both types of electrodes. Hence, both electrons and holes contribute to the signal significantly. This situation contributes to the expectation that 3D n-in-p and p-in-n detectors should exhibit a similar radiation hardness.

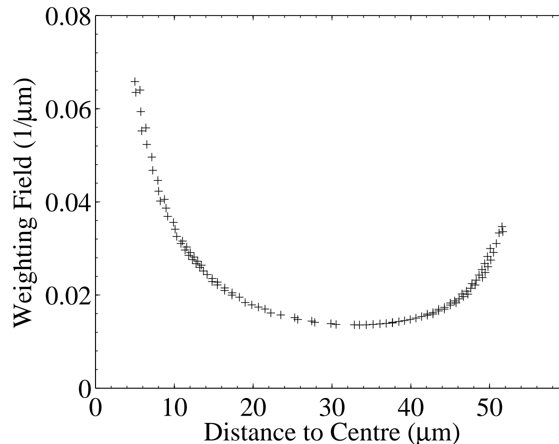

Figure 5.6: Weighting field on the line connecting a junction column and an ohmic column. The abscissa indicates the distance to the centre of the junction column.

5.1.2 Planar Detectors

Results of planar n-in-p strip detectors are presented in Chapter 7. Measurements were pereformed with a radioactive source and an infrared laser. The detectors were produced by Hamamatsu Photonics K.K. [Ham] (HPK). The development was performed in the framework of a prototyping project for the HL-LHC upgrade of the ATLAS strip tracker. The production series is referred to as ATLAS07. Within this thesis, measurements before irradiation and after irradiation with 25 MeV protons (see Section 5.1.3) are presented. The highest irradiation fluence is $5 \times 10^{15}\,\mathrm{n_{eq}/cm^2}$ and corresponds to the fluence expected for the outer pixel detector layers at the HL-LHC ATLAS upgrade. Measurements reported in Chapter 7 were performed with a radioactive source and an infrared laser setup.

A detailed description of the sensor design is provided in Ref. [Unn11]. The sensors consist of n^+-doped readout strips in (320 ± 15) μm thick p-type float-zone substrate. The resistivity of the substrate is approximately 6.7 kΩ cm. A photograph of the sensor surface is shown in Fig. 5.7. Each sensor has 104 strips with a length of 8 mm and a pitch of 74.5 μm, thus the active area is 8 mm × 8 mm. These miniature sensors were produced on wafers together with larger sensors (10 cm × 10 cm), which have the dimensions of the sensors foreseen to be installed in the barrel part of the ATLAS tracker upgrade. Isolation of the readout strips is provided by p-stop implantations between the strip metallisations,

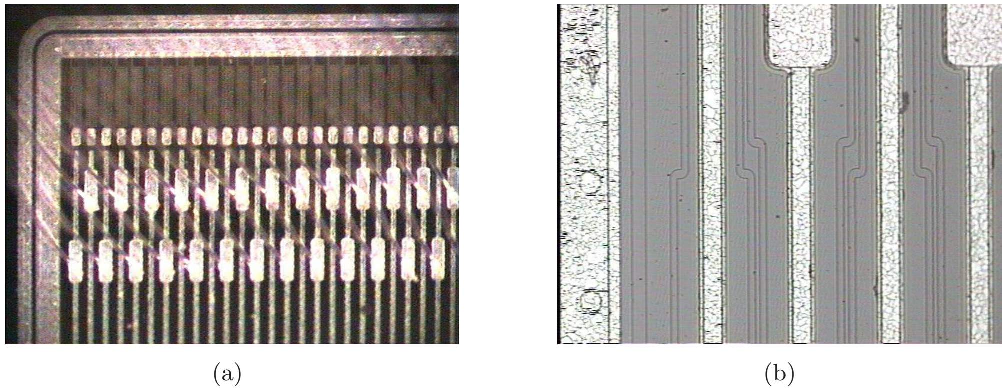

(a) (b)

Figure 5.7: Photograph of the surface of a planar n-in-p detector produced by Hamamatsu. The picture in (b) is a magnification of the image shown in (a). Two individual p-stop implantations are visible between the readout strips.

see Fig. 5.7(b). The displayed sensor has two p-stop traces between the strips. However, also sensors with only one p-stop implantation were used for the measurements.

On the strip ends, DC and AC coupled readout pads are present. Capacitive coupling is achieved by an insulating layer in between the strip metallisation and the strip implant. For the measurements, the AC pads were connected to the front-end electronics. The readout strips are biased by means of polysilicon bias resistors. A bias ring and a guard ring surround the active area.

5.1.3 Proton Irradiations

Irradiations of the devices under test were performed with 25 MeV protons at the Karlsruhe Compact Cyclotron [Die10]. The irradiation fluences are scaled to 1 MeV equivalent neutrons per square centimetre (n_{eq}/cm^2) using the NIEL hypothesis with a hardness factor of 1.85. For each fluence, a relative error of $\pm 20\%$ is assumed. During the irradiations the devices were kept unbiased. Annealing is suppressed by cooling the samples with cold gaseous nitrogen. Due to heating by the proton beam, the samples reach temperatures of approximately 10 °C during the irradiation. After the irradiation, the devices are stored in a freezer to prevent further annealing. However, the devices under test had to be stored at room temperature during some time for the preparation of the measurements. Typically, the sum of these periods was well below three days.

Usually, silicon sensors are kept unbiased when performing irradiation tests. Supplying a bias voltage to the devices under test requires a considerable effort and is not possible at all irradiation sources. However, silicon detectors in high-energy physics experiments are kept under bias during most of the time when radiation damage is accumulated. Recent studies [Vä11] indicate that the radiation-induced alteration of the effective doping concentration is somewhat reduced when a bias voltage is supplied to the detectors.

5.2 Alibava Readout System

The laboratory measurements described in this thesis were performed using a radioactive beta source (see Section 5.3) and an infrared laser (see Section 5.4). In both setups, the sensor is read out using the Alibava readout system. The Alibava system [MH09, MH08] was produced in the framework of the RD50 collaboration by institutes in Liverpool, Barcelona and Valencia. *Alibava* stands for *A*nalogue *Li*verpool *Ba*rcelona *Va*lencia readout system. It was designed to provide a system which utilises similar readout electronics as the LHC silicon tracking detectors. It is a compact and portable system and facilitates analogue readout of silicon microstrip sensors. The Alibava system is widely used within the RD50 collaboration and beyond to investigate silicon detectors before and after irradiation, mainly for possible HL-LHC applications.

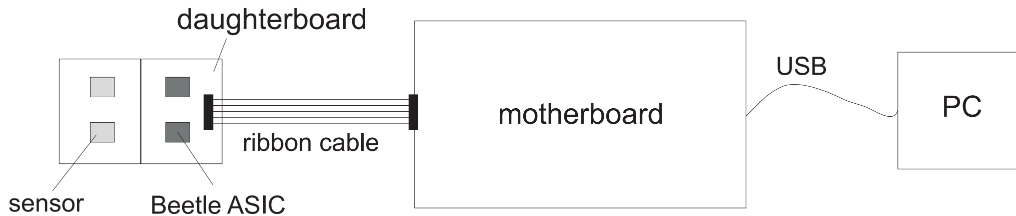

Figure 5.8: Schematic design of the Alibava system.

Figure 5.8 shows a sketch of the Alibava system. On the left hand side, the board carrying the silicon sensors (the devices under test) and the daughterboard are shown. The daughterboard is the first stage of the readout system and carries two analogue front-end chips, which perform amplification and shaping of the sensor signals. The analogue sensor signals are serialised and sent to the motherboard, which is the main control unit of the system, by means of a 1-2 m long ribbon cable. The sensor board and the daughterboard can be housed within a cooled environment for measurements, whereas the motherboard can be located outside and operated at room temperature. The motherboard communicates with a computer over a USB connection. The raw data are transferred to the computer and stored in binary format. The system can be operated and controlled by means of a graphical user interface. To analyse the data, custom software based on the ROOT framework [Bru97, ROO] was developed.

The silicon sensors are mounted on an aluminium nitride (AlN) board. Aluminium nitride was chosen for the base board due to its high thermal conductivity, which is necessary to remove the heat generated by the leakage current of the silicon sensor. The bias voltage for the silicon sensors is provided by an external power supply. A low pass filter circuit is interconnected to avoid voltage spikes and to reduce the pickup of external noise. The sensor base board is mounted on a support structure together with the Alibava daughterboard. The main units of the daughterboard are two Beetle ASICs (application specific integrated circuit) [Lö06], originally developed for the LHCb experiment [Alv08] at CERN. A Beetle chip consists of 128 channels, each channel performing amplification and shaping of the signals coming from the sensor. Each individual readout channel of the sensor is connected to an input channel of the Beetle chip via wire bonds and rebondable pitch

adapters.

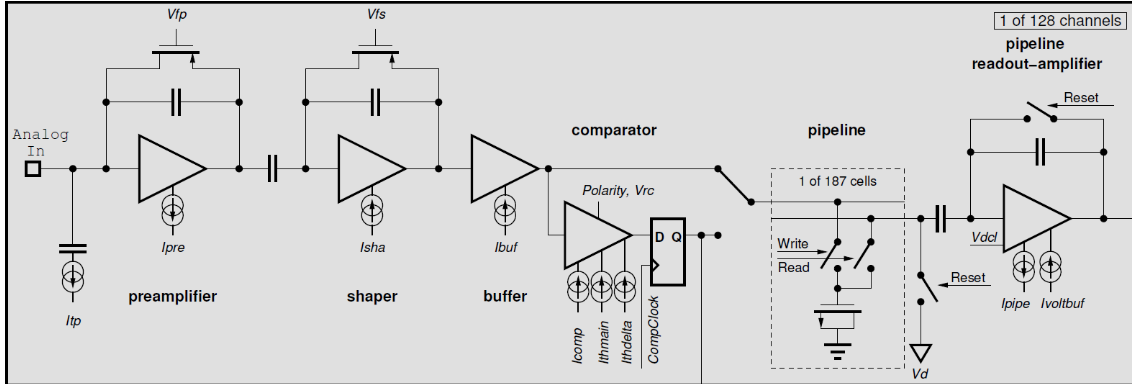

Figure 5.9: Schematic block diagram of one channel of the Beetle front-end chip [Lö06].

A schematic block diagram of a single channel of the Beetle chip is shown in Fig. 5.9 [Lö06]. The sensor signal is fed into a charge-sensitive preamplifier, followed by a CR-RC pulse shaper. Sensor pulses of both polarities can be handled, therefore detectors with p- and n-side readout can be used. A simulation of the semi-Gaussian output pulse of the shaper is shown in Fig. 5.10. The characteristics of the pulse shape, e.g. rise time t_r and peak voltage V_p, depend on the settings of configuration parameters and the detector load capacitance. A considerable influence is exercised by the front-end shaper voltage V_{fs} (see Fig. 5.9), which controls the feedback resistance of the shaper. For the laser measurements (see Section 5.4), $V_{\mathrm{fs}} = 0\,\mathrm{V}$ was chosen. For noise measurements and measurements with the beta source setup (see Section 5.3), a value of $V_{\mathrm{fs}} = 1\,\mathrm{V}$ was chosen. It is important to use the same configuration as in charge calibration measurements, in order to convert the measurements into charge properly. This was done for the beta source measurements and noise measurements, while only relative signals can be measured with the laser. A larger value of V_{fs} increases the rise time and reduces the noise. The rise time is below 30 ns if the detector capacitance is below 15 pF, which is the case for the detectors investigated in this thesis. The noise (see Section 3.3.8) of the Beetle front-end is $\mathrm{ENC}_{\mathrm{load}} = 465\,\mathrm{e}^- + 45\,\mathrm{e}^- \cdot C_d[\mathrm{pF}]$ for $V_{\mathrm{fs}} = 1\,\mathrm{V}$, where C_d is the detector capacitance [Lö06]. A comparator circuit (see Fig. 5.9) enables to operate the Beetle in binary mode, however, this is not applied in the Alibava system. The pulse of the shaper is sampled with a frequency of 40 MHz and the output is stored in an analogue pipeline. When a trigger signal is sent to the Beetle chip, the data are retrieved from the pipeline with a fixed latency, serialised and transferred to a buffer on the Alibava daughterboard. From there, the data are routed to the motherboard.

The motherboard is controlled by an FPGA (field programmable gate array). The analogue data, which are received from the daughterboard, are converted into digital counts using a 10-bit ADC (analogue to digital converter). A further important task of the motherboard is the handling and distribution of trigger signals. The system has inputs for external trigger signals, which can be used for example in conjunction with a beta source setup. After receiving a trigger signal, the readout of the Beetle chips is initiated. Consid-

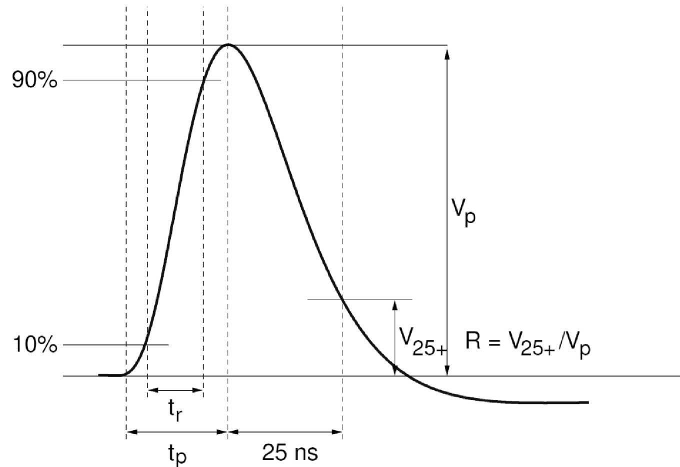

Figure 5.10: Output pulse of the shaper of the Beetle chip [Lö06].

ering the Beetle pulse is sampled every 25 ns, the value for the latency has to be adjusted in order to retrieve the data from the correct time bin. A TDC (time to digital converter) measures the phase of the trigger signals, which can occur randomly, with respect to a 10 MHz clock. The signal of the device under test can be investigated as a function of the time measured by the TDC. This facilitates a reconstruction of the shape of the analogue Beetle pulse in a 100 ns wide time window. For the subsequent data analysis, only events are used for which the Beetle pulse is sampled close to its maximum. An example will be discussed in Section 5.3.1.

For application in conjunction with a laser setup, the Alibava motherboard can generate a trigger to initiate the creation of a laser pulse. A fixed time interval after the trigger generation, the readout of the Beetle chips is initiated. The delay between the trigger for the laser and the Beetle readout can be adjusted in steps of 1 ns to ensure that the Beetle pulse is always sampled close to its maximum. By varying this delay, the Beetle pulse shape can be reconstructed and the optimum delay can be determined (see Section 5.4.1).

5.3 Beta Source Measurements

The beta setup allows to perform charge collection measurements with minimum ionising particles in a laboratory environment. The principle of the setup is shown in Fig. 5.11. Detailed descriptions of the design can be found in Refs. [Kü06, Pre10, Wal10]. Electrons are emitted by the beta decay of ^{90}Sr and its daughter nuclei. The radioactive source is housed in a plexiglas cylinder, which collimates the electrons towards the silicon sensor and provides shielding. Two plastic scintillator-photomultiplier combinations, located behind the silicon sensor, serve as a trigger for the readout of the sensor. The photomultiplier pulses are fed into the Alibava system, which initiates a readout of the sensor if two photomultiplier pulses are registered in coincidence. The scintillators have a thickness of 4 mm. The first one has an area of 4 mm $\times$ 4 mm, the second one has an area of 45 mm $\times$ 45 mm.

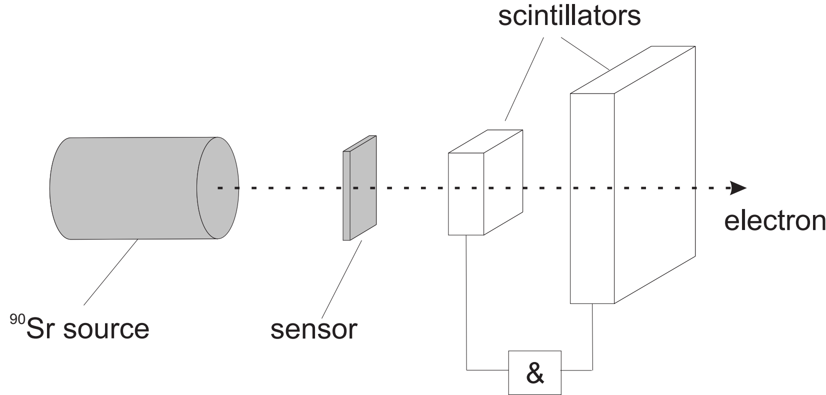

Figure 5.11: Schematic view of the beta source setup.

The radioactive isotope ^{90}Sr decays via the processes [B0́6]

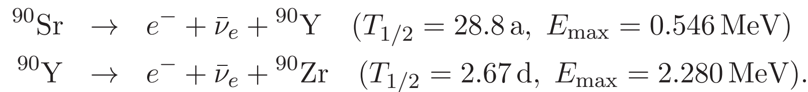

$$
\begin{aligned}
{}^{90}\mathrm{Sr} &\rightarrow e^- + \bar{\nu}_e + {}^{90}\mathrm{Y} \quad (T_{1/2} = 28.8\,\mathrm{a},\ E_{\mathrm{max}} = 0.546\,\mathrm{MeV}) \\
{}^{90}\mathrm{Y} &\rightarrow e^- + \bar{\nu}_e + {}^{90}\mathrm{Zr} \quad (T_{1/2} = 2.67\,\mathrm{d},\ E_{\mathrm{max}} = 2.280\,\mathrm{MeV}).
\end{aligned}
$$

$T_{1/2}$ is the half life time of the nuclei and E_{max} is the maximum kinetic energy of the emitted electron, if the neutrino mass is neglected. The end-product ^{90}Zr is stable. Only beta decays are relevant for the decay chain, generation of photons can be neglected. Electrons from the beta decay from ^{90}Sr to ^{90}Y are practically completely absorbed in the first scintillator. Considering the maximum kinetic energy of 0.546 MeV, the average range in a plastic scintillator with a density $\rho = 1.032\,\mathrm{g/cm^3}$ is approximately 2 mm [Ber10]. As the scintillators are 4 mm thick, most of these electrons do not reach the second scintillator. Since a coincidence of both scintillators is required for a trigger, only events induced by electrons originating from the decay of ^{90}Y to ^{90}Zr are selected. Electrons with a kinetic energy of 2 MeV have a range of 10 mm in the scintillator material [Ber10], therefore these can reach the second scintillator. As discussed in Section 3.3.4, electrons with a kinetic energy of 2 MeV can be regarded as minimum ionising particles (MIPs). Thus, the deposited energy is approximately equal to the energy deposited by high-energy particles usually considered for tracking and reconstruction in particle physics detectors.

The setup is housed in a commercial freezer, so that sensor temperatures between −16 °C and −19 °C can be achieved. The freezer is flushed with nitrogen to avoid condensation. Lower temperatures can be achieved by an additional cooling system based on liquid nitrogen. Nitrogen is evaporated and blown onto the backplane of the device under test. Sensor temperatures down to −60 °C can be achieved. Cooling of irradiated sensors is essential, since the leakage current increases strongly as a function of the irradiation fluence (see Section 4.3.2). A temperature sensor is glued on the aluminium nitride board next to the sensor and monitors the temperature with a precision of ±0.5 °C. The stability of the sensor temperature during a measurement is approximately ±1 °C.

5.3.1 Measurements and Analysis Procedure

Initially, the signal distribution in absence of traversing particles is measured. These measurements are referred to as pedestal runs and are performed using a random trigger. The pedestal for each readout channel is calculated as the mean signal of the spectrum. For the analysis of signal measurements, the pedestal is subtracted from the data. The noise is given by the width of the spectrum measured in a pedestal run. It is calculated either as the root mean squared (RMS) deviation or the width of a Gaussian which is fitted to the spectrum. Ideally, the noise follows a Gaussian distribution, therefore the RMS noise and the noise calculated by the Gaussian width should coincide. However, as will be discussed in Section 6.2.4, the noise distribution sometimes has non-Gaussian tails. In these cases, the RMS value of the noise distribution is larger than the Gaussian width. Channels exhibiting extraordinarily high noise are excluded from the analysis. Excessive noise can have its origin in the readout strip of the sensor, in a faulty wirebond or fanin connection or in the channel of the readout chip. Typically, of the order of 10% of all sensor channels were excluded.

Pickup of external noise can lead to a common shift of the signals of groups of channels or of all channels from event to event. These common mode fluctuations broaden the signal distributions and can be regarded as a contribution to the noise. Since these fluctuations are common to various channels, they can be reduced. A common mode correction is applied for the analysis of the pedestal measurements and the radioactive source measurements. After subtracting the pedestal values, the common mode for each event is calculated as the mean signal over a range of channels. If the sensor has fewer channels than the readout chip, the calculation of the common mode is done separately for the channels of the chip which are connected to the sensor and those which are not. Furthermore, the group of connected channels is sub-divided into two groups. Channels having extraordinary high signals are neglected for the calculation of the common mode. This assures that signals induced by traversing electrons do not influence the calculation of the common mode. For the subsequent data analysis, the common mode is subtracted from the data event by event.

Figure 5.12 shows a reconstruction of the pulse shape delivered by the Beetle chip. It was measured using particles emitted by the beta source. The time between a trigger signal and an edge of a 10 MHz clock is measured by the Alibava TDC. For each event, the channel having the highest signal-to-noise ratio is determined. Then, the mean of these signals is calculated for each 1 ns wide time bin. Only events within a 10 ns wide time window around the maximum of the pulse are accepted for the subsequent data analysis. The starting point of this interval is varied manually to maximise the most probable value of a Landau distribution, reconstructed from a fit to the resulting spectrum (see below).

A signal spectrum is shown in Fig. 5.13. It was generated using a clustering algorithm to account for charge sharing between neighbouring readout strips. First, the channel having the highest signal-to-noise ratio in each event is determined. This channel is accepted if the signal-to-noise ratio is higher than a seed cut, which is usually varied between three and four. The signals of neighbouring channels are added as long as the ratio between their signal and their noise exceeds a threshold. This threshold is typically varied between

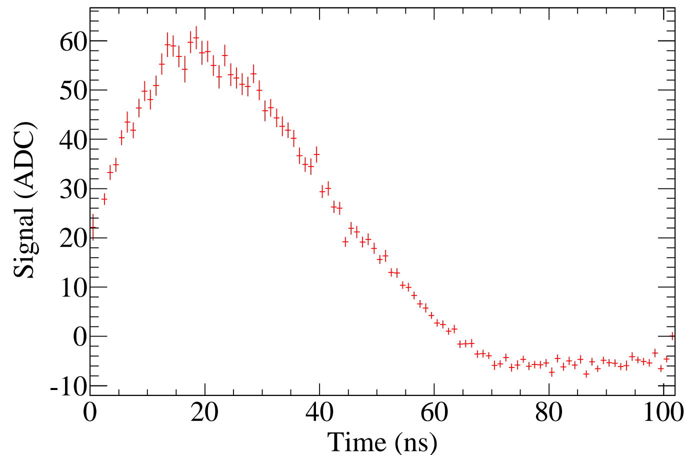

Figure 5.12: Signal as a function of the time measured by the TDC, which is the phase between a trigger signal and an edge of a 10 MHz clock. The measurement was made using an unirradiated n-in-p 3D detector with a bias voltage of 60 V.

two and three of the signal-to-noise ratio. The resulting spectrum is fitted by a convolution of a Landau function and a Gaussian. The Gaussian takes into account the noise. Signal values quoted as results from beta source measurements reflect the most probable value (MPV) of the Landau function which was extracted from the fit. The most probable value of the extracted Landau function does not necessarily coincide with the most probable value of the convoluted function. Especially if the spectrum is very broad, the most probable value of the Landau function can be considerably lower. Since the Landau function is asymmetric, a Gaussian broadening of the spectrum does shift the location of the most probable value.

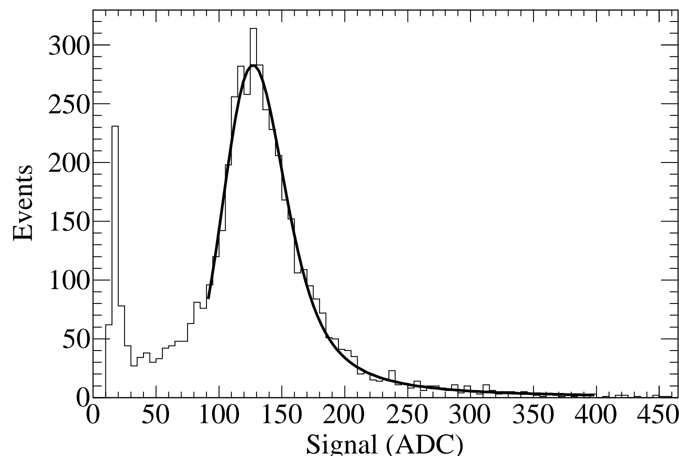

Figure 5.13: Signal spectrum of an unirradiated n-in-p 3D detector with a bias voltage of 60 V. A fit of a convolution of a Landau function and a Gaussian is superimposed. The remainder of the noise distribution can be seen at the left margin.

5.3.2 Calibration

The system was calibrated using a planar reference detector to obtain a conversion between ADC counts and charge. An unirradiated n-in-p strip detector as described in Section 5.1.2 was used. It is assumed that this sensor yields the full signal according to Eq. (3.17). The gain of the system, which relates the signal measured in ADC counts to the signal in units of charge, was calculated as a function of the operation temperature. Figure 5.14 shows the signal of the reference sensor, measured in ADC counts, as a function of the sensor temperature. The measurements were performed at bias voltages significantly higher than the full depletion voltage of the sensor, which is approximately 100 V.

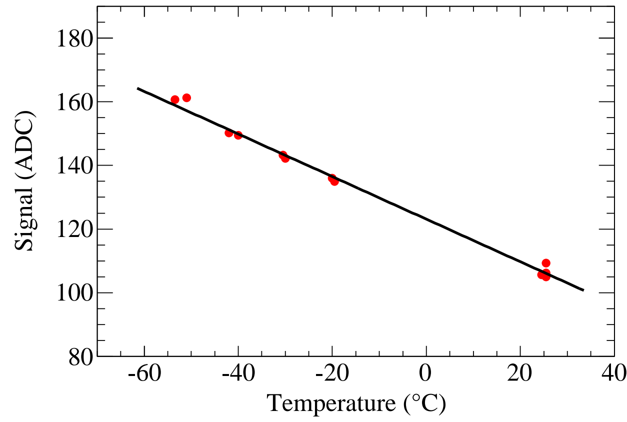

Figure 5.14: Signal, measured in ADC counts, of a planar reference detector as a function of the sensor temperature. Statistical errors are not visible as they are smaller than the markers. A fit of a straight line is superimposed.

A linear function $A + B \cdot T$ is fitted to the data shown in Fig. 5.14. The gain G as a function of the temperature T (measured in °C) is

$$G(T) = \frac{Q}{A + B \cdot T} \frac{f(C_{\text{load, dut}})}{f(C_{\text{load, cal}})} \tag{5.2}$$

with the error

$$\sigma_G = G \sqrt{\left(\frac{\sigma_Q}{Q}\right)^2 + \frac{\sigma_A^2 + (T \cdot \sigma_B)^2 + (B \cdot \sigma_T)^2}{(A + B \cdot T)^2} + \left(\frac{\sigma_{f(C_{\text{load, dut}})}}{f(C_{\text{load, dut}})}\right)^2 + \left(\frac{\sigma_{f(C_{\text{load, cal}})}}{f(C_{\text{load, cal}})}\right)^2}. \tag{5.3}$$

Therein,

$$\begin{aligned}
Q &= (24.7 \pm 1.2)\,\text{ke}^- \\
A &= (123.10 \pm 0.06)\,\text{ADC} \\
B &= (0.669 \pm 0.002)\,\text{ADC}/^\circ\text{C} \\
f(C_{\text{load}}) &= 0.999 + 0.018\,\text{pF}^{-1} \cdot C_{\text{load}} \\
\sigma_f &= \sqrt{0.006^2 + (0.001\,\text{pF}^{-1} \cdot C_{\text{load}})^2 + (0.018\,\text{pF}^{-1} \cdot \sigma_{C_{\text{load}}})^2}
\end{aligned} \tag{5.4}$$

Q is the signal expected for the $(320 \pm 15)\,\mu$m thick reference detector according to Eq. (3.17). The dependence of the Beetle chip amplification on the detector load capacitance C_{load} is corrected for by the function $f(C_{\text{load}})$. The derivation of this function is described in Ref. [Wal10]. In Eq. (5.2), $f(C_{\text{load, dut}})$ is the capacitance correction function for the device under test and $f(C_{\text{load, cal}})$ is the correction function for the sensor which is used for the calibration. For the measurement of the sensor temperature, an error of $\sigma_T = 1\,^{\circ}$C is estimated.

The detector load capacitance C_{load} is given by the sum of the body capacitance between a readout strip and the backplane (C_b) and the interstrip capacitance between the strip and its neighbours (C_{is}). In this thesis, three different sensor types were measured with the beta source setup: 3D strip detectors produced by CNM in n-in-p and in p-in-n layout (see Section 5.1.1) and planar n-in-p strip detectors produced by HPK (see Section 5.1.2). The body capacitance C_b, the interstrip capacitance C_{is}, the load capacitance C_{load} and the correction function $f(C_{\text{load}})$ for these detectors are summarised in Table 5.1.

Table 5.1: Capacitances and correction functions for the gain (see Eq. 5.4) for different detectors. As an estimate, a relative error of ±10% is assumed for C_b and C_{is}.

Sensor	C_b (pF)	C_{is} (pF)	C_{load} (pF)	$f(C_{\text{load}})$
Planar n-in-p (HPK) [Unn11]	0.22 ± 0.02	0.64 ± 0.06	0.86 ± 0.06	1.01 ± 0.01
3D n-in-p (CNM) [Fle10]	2.8 ± 0.3	1.2 ± 0.1	4.0 ± 0.3	1.07 ± 0.01
3D p-in-n (CNM) [Fle10]	3.8 ± 0.4	0.80 ± 0.08	4.6 ± 0.4	1.08 ± 0.01

The signal measured in ADC counts, $S(\text{ADC})$, is converted into units of ke$^-$ according to

$$S(\text{ke}^-) = S(\text{ADC}) \cdot G(T) \tag{5.5}$$

with the total error

$$\sigma_{S(\text{ke}^-)} = \sqrt{\left(G(T) \cdot \sigma_{S(\text{ADC})}\right)^2 + \left(S(\text{ADC}) \cdot \sigma_{G(T)}\right)^2 + (0.02 \cdot S(\text{ke}^-))^2}. \tag{5.6}$$

Usually, $S(\text{ADC})$ is given by the MPV of a Landau function and is calculated as described above. Then, $\sigma_{S(\text{ADC})}$ is the statistical error of the fit. The last term in Eq. 5.6 is a systematic uncertainty originating from the variation of the fit range and the variation of the neighbour cut. A relative error of ±2% was estimated. The uncertainty of the thickness of the detector used for the calibration dominates the error given by Eq. (5.6). The total relative error is approximately ±6%. Equation (5.5) is also used to convert noise into units of ke$^-$. In this case, $\sigma_{S(\text{ADC})}$ is replaced by the error of the noise and the last term in Eq. (5.6) is ignored.

5.4 Laser Measurements

The laser setup can be used for space-resolved signal measurements. The principle of the setup is sketched in Fig. 5.15, a detailed description can be found in Ref. [Bre10]. The infrared laser is fed through an optical microscope and illuminates the silicon sensor from

the front side. The sensor is mounted on a cooling structure and can be moved in two dimensions. Thus, the laser point of incidence on the sensor surface can be varied and the signal can be measured as a function of the position.

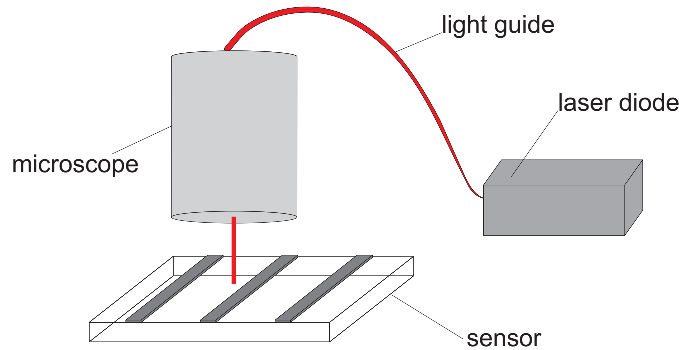

Figure 5.15: Schematic layout of the laser setup.

The laser pulses are generated by a laser diode[1], the power of which can be adjusted by an external controller[2]. The infrared laser has a peak wave length of 974 nm, the laser pulses are shorter than 1 ns. The trigger for generation of the laser pulses is provided by the Alibava system. An optical fibre connects the laser diode and the optical microscope[3], which provides focusing of the laser beam. The laser beam is focused on the sensor surface, where it has a Gaussian width of approximately 3 µm [Bre10].

The silicon sensor is mounted on the same carrier structure as used for the measurements with the beta source setup. The aluminium nitride board, which carries the sensor, is placed on a cooling block. Liquid nitrogen is evaporated and cold gaseous nitrogen flows through the cooling block. As for the beta setup, sensor temperatures down to $-60\,°C$ are possible and the temperature can be measured with a precision of $\pm 0.5\,°C$. Within a measurement, the temperature typically varies by $\pm 1\,°C$. The cooling block, the sensor board and the Alibava daughterboard are housed in an enclosure, which is flushed with nitrogen to avoid condensation.

The enclosure is mounted on motorised x-y stages[4]. These are operated by an external controller[5] that communicates with a computer. The control of the motion stages is embedded in the Alibava data acquisition software. The stages can be moved in steps of 0.5 µm. The measurements reported in Chapters 6 and 7 were performed by scanning the sensor surface with a step size of 2 µm.

The wavelength of 974 nm leads to an absorption length of approximately 100 µm in silicon at a temperature of $-30\,°C$ (see Section 3.3.4). Therefore, the creation of electron-hole

[1] PicoQuant GmbH, model LDH-P-C-980
[2] PicoQuant GmbH, model PDL 800
[3] Leica Microsystems GmbH, model Ployvar SC
[4] Newport Corporation, model M-UTM150CC.5HA
[5] Newport Corporation, model MM4005

pairs predominantly takes place close to the sensor surface. Surface effects can have a strong influence on the measured signal, whereas the collection of charge carriers created deep in the silicon bulk cannot be investigated. On the other hand, the relatively short absorption length prevents the laser from being reflected at the metallisation of the sensor backplane. Since the absorption length strongly depends on the sensor temperature, the relative contribution of the surface region to the total signal also depends on the temperature.

Different reflectivities of the sensor surface affect the measured signal. The region of the strip metallisations cannot be investigated by laser measurements, since the metal reflects the laser beam. The reflectivity of the sensor surface depends on the thickness of the oxide, which covers the silicon sensor [Ren09]. Hence, the oxide thickness affects the magnitude of the signal. As will be shown in Chapter 7, the signal is higher if the laser impinges on the region of the p-stop implants, where the reflectivity is lower. Furthermore, the measured signal depends on the adjustable laser power.

Due to these reasons, only relative measurements can be performed with the laser setup. It is hardly possible to compare the absolute signals measured with different detectors. A calibration, as it was done for the beta source setup, was not performed for the laser measurements. However, laser measurements can be used to investigate the relative variation of the signal as a function of the laser point of incidence.

5.4.1 Measurements and Analysis Procedure

As a preparation of the laser measurements, the sensor position and the laser focus have to be adjusted. An image of the sensor can be viewed via a camera. The camera uses the same microscope which is used for focusing the laser. The position of the sensor is levelled so that the optical focus coincides with the sensor surface across the entire sensor. The rotation of the sensor is adjusted in order to align the direction of the readout strips with the direction of one of the motion stages. Finally, the sensor is moved into the laser focus by lifting it by 10 μm [Bre10]. This offset is assumed to result from a dependence of the optical properties of the microscope on the photon wave length.

The calculation of pedestal and common mode is done in the same way as explained in Section 5.3.1 for the beta source measurements. In the final laser measurements, 500 laser pulses are generated for each laser point of incidence. The resulting signal spectrum of the channel that is illuminated by the laser approximately follows a Gaussian distribution, as shown in Fig. 5.16. The mean of this distribution is calculated and serves as the resulting signal for the respective laser position. Since the photons are completely absorbed in the silicon sensor, the distribution of the deposited energy does not follow a Landau distribution, as it is the case for traversing charged particles.

To sample the Beetle output pulse always at its maximum, the timing has to be adjusted. This is done in a different way than for the beta source measurements, since the triggers, which initiate the creation of laser pulses, are generated by the Alibava system. The delay between the generation of a laser pulse and the data acquisition can be varied in steps of 1 ns. As a preparation for the final laser measurements, a delay scan is executed. At a

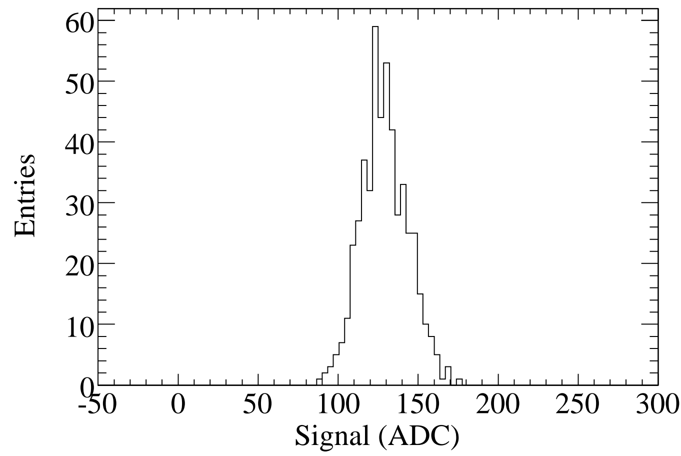

Figure 5.16: Signal spectrum of a laser measurement, measured with an unirradiated n-in-p 3D detector at a bias voltage of 50 V. The sensor temperature was −20 °C.

fixed laser position, measurements are performed for a range of delay settings. Figure 5.17 shows the mean signal of the illuminated channel as a function of the delay, in Fig. 5.17(a) with a step size of 5 ns and in Fig. 5.17(b) with 1 ns steps. A Gaussian is fitted to the results of the scan performed with 1 ns steps. The optimal delay is determined by the mean of the Gaussian.

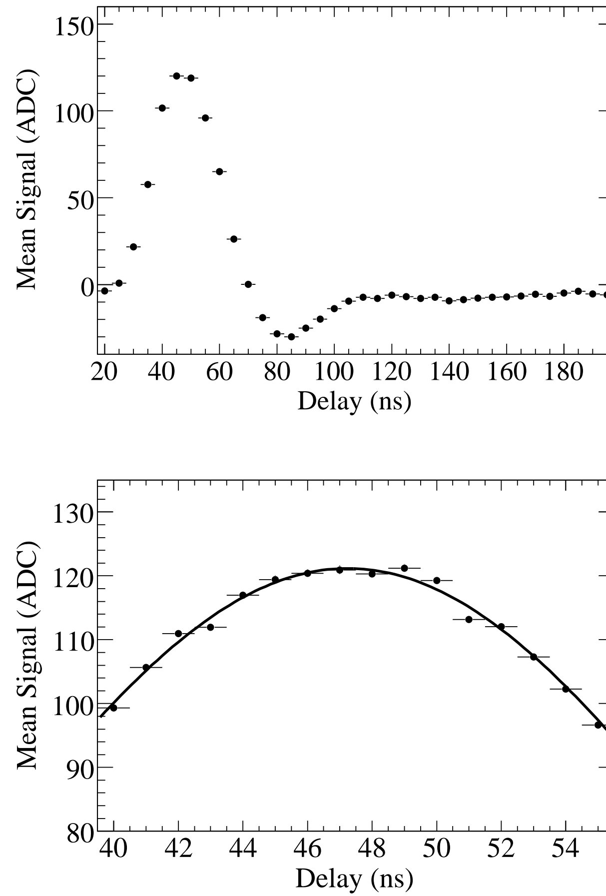

Figure 5.17: Results of a laser delay scan, measured with an unirradiated n-in-p 3D detector at a bias voltage of 50 V. The bias voltage is above the full depletion voltage. Displayed is the mean signal as a function of the delay. Top: delay scan with a step size of 5 ns, bottom: delay scan with 1 ns steps around the maximum. The optimal delay is determined by the mean of a Gaussian fitted to the data, as shown in the lower plot. In this case, the optimal delay is 47 ns.

5.5 Beam Test Measurements

The beam test measurements reported in this thesis were performed in the H2 beamline of the CERN SPS (Super Proton Synchrotron) in 2008 and 2009. The beam was composed of pions with a momentum of 225 GeV/c, which were created by sending protons that were extracted from the SPS on a beryllium target. Beam test measurements with high-energy particles are very well suited to study the performance of detectors in a realistic environment. The particles used for the measurements deposit the same amount of energy as particles usually considered for reconstruction in high-energy physics detectors. Furthermore, a beam telescope can be used to measure the tracks of traversing particles. Therefore, the signal can be studied as a function of the track point of impact. Thus, a beam test combines the advantages of a beta source setup and a laser setup. A telescope to measure the particle tracks could not be used together with a beta source. Electrons with a kinetic energy of approximately 2 MeV would not be able to traverse two sintillators and several telescope detector planes. Furthermore, electrons exhibit a high probability of multiple scattering, hence straight tracks would be unlikely.

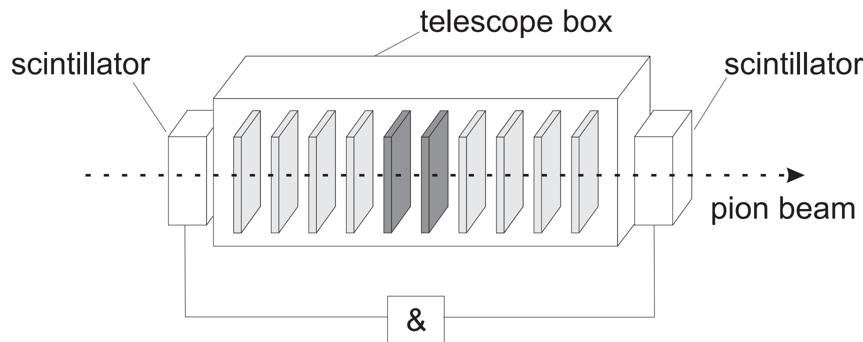

Figure 5.18: Sketch of the beam test setup. The telescope box houses eight reference detectors and two devices under test. The latter ones, shown in dark grey, are positioned in the centre of the reference detectors.

A simplified diagram of the beam test setup is shown in Fig. 5.18. The particle tracks were measured by the Silicon Beam Telescope (SiBT) [Mä08], which consists of eight planes equipped with silicon microstrip detectors. The devices under test and the reference detectors were positioned perpendicularly to the beam. The telescope sensors have a readout pitch of 60 µm and an electrically floating strip between two readout strips, resulting in an effective pitch of 30 µm. Pairs of two detectors are oriented with an angle of 90° to each other, thus the SiBT delivers four reference space points. The active area of the telescope is approximately 3.8 cm × 3.8 cm. In the middle of the telescope, two slots are available for modules with devices under test. The resolution of the reference tracks at the location of the devices under test in the beam tests was approximately 3 µm. The trigger is provided by the coincidence of two scintillators, which are placed in front and behind the telescope. The reference tracks were reconstructed according to the method described in Ref. [Kor09][6]. The box housing the telescope detectors and the devices under test can

[6]The reconstruction of the reference tracks was performed by the University of Helsinki.

be cooled using Peltier elements to achieve temperatures as low as $-25\,^{\circ}$C.

The readout and the data acquisition electronics of the SiBT are based on hardware used in the current CMS tracker [Cha08]. Some of the components are prototype versions. The reference detectors as well as the detectors under test are connected to CMS Tracker Outer Barrel hybrids. The CMS APV25 front-end chip [Jon99, Fre01] forms the first stage of the readout chain. The function of the APV25 can be compared to the Beetle ASIC as described in Section 5.2. A charge sensitive preamplifier and a CR-RC shaper transfer the detector signal pulse into a semi-Gaussian pulse. The APV25 has a shaping time of 50 ns, hence the pulses are broader than those of the Beetle, which applies a 25 ns shaping. The analogue pulses are sampled with a frequency of 40 MHz and stored in an analogue pipeline.

Upon registration of a trigger signal, the analogue value of the corresponding pipeline cells is retrieved. In peak mode, which is applied in the case of the SiBT, one pipeline cell is retrieved for each channel. The signals are further amplified and transmitted to Front-End Driver cards [Lea05], where the signals are digitised by means of ADCs. The ADC counts are stored for the subsequent data analysis. All data acquisition components are synchronised to the 40 MHz system clock. The equivalent noise charge due to the load capacitance is $\mathrm{ENC}_{\mathrm{load}} = 246\,\mathrm{e}^{-} + 36\,\mathrm{e}^{-} \cdot C_d[\mathrm{pF}]$, where C_d is the detector capacitance [Fre01].

An alternative mode of operation of the APV25, which is advantageous in presence of high track rates, is the deconvolution mode [Bin93, Jon99]. In this mode, three subsequent pipeline cells are read out and the final pulse height is reconstructed from these samples. The peaking time of the reconstructed pulse is reduced to about 25 ns and pile-up can be suppressed. This mode was not applied in the beam tests reported in this thesis. The deconvolution mode leads to higher noise than the peak mode.

The particle beam and the 40 MHz system clock were not synchronised, thus the analogue pulse of the APV25 was not always sampled at its maximum. In principle, it would be possible to measure the phase between the trigger signal and the edge of the system clock. Then, it would be possible to accept only events for which the trigger falls into a certain time window and the analogue pulse is sampled close to the maximum. This approach is realised for the beta source measurements, see Section 5.3.1. However, the trigger phase was not measured during the beam tests and therefore, the sampling point was randomly distributed within a 25 ns long time window. Prior to data taking, timing scans were conducted to find the correct trigger delay for which the resulting signal is maximised. This assures that the peak of the analogue pulse occurs in the middle of the 25 ns long time window. According to estimations based on the APV25 pulse shape [Mä08], the average signal is approximately 10% lower than it would have been if the pulse had been sampled at its maximum. Since the APV25 has a relatively long shaping time of approximately 50 ns, the signal loss is limited.

5.5.1 Alignment

The track parameters of the reconstructed tracks are provided in a global reference frame. To make use of the tracking information, the impact points of the reference tracks on the

surfaces of the devices under test have to be calculated. Therefore, the alignments of the sensors within the global reference frame must be determined. The alignment procedure is explained in detail in Ref. [Pah08]. A local coordinate system S' is defined for each sensor and the transformation of this reference frame with respect to the global coordinate system S is computed (see Fig. 5.19). In the local system S', the sensor is positioned in the x'-z' plane and the readout strips are running parallel to the z' axis.

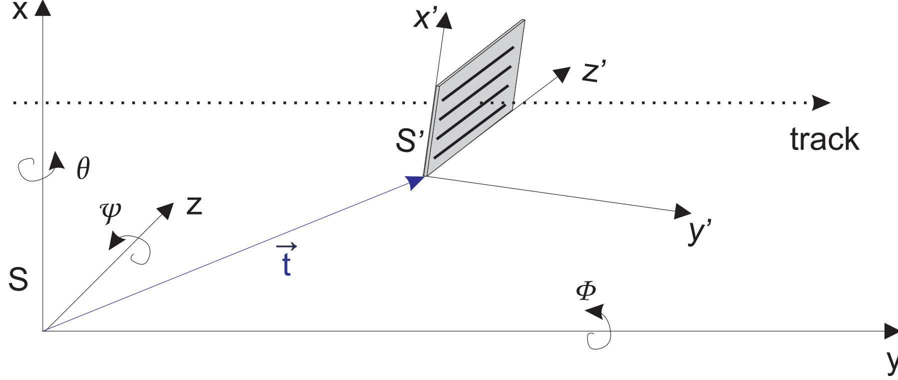

Figure 5.19: Global coordinate system S and local coordinate system S'. The system S' is fixed to the sensor, the readout strips are parallel to the z' axis. The translation $\vec{t}$ connects the origins of the two reference frames.

The position vector $\vec{r}$ and the direction vector $\vec{dr}$ of a reference track are given for a fixed y in the reference frame S. This y-value corresponds to the approximate position of the devices under test and is known from the construction of the telescope box. The aim of the alignment procedure is to find the track point of impact $\vec{p}$ (as defined below) on the sensor surface, given in the local frame S'. The translation from the origin of S to S' is given by $\vec{t}$. The rotation R between the two coordinate systems is composed of the three rotations around the axes of S,

$$R = R_z(\psi)\ R_y(\phi)\ R_x(\theta). \tag{5.7}$$

$R_x(\theta)$ etc. are rotation matrices. Then, the vectors $\vec{r}$ and $\vec{dr}$ given in S are transformed into S' according to

$$\vec{r'} = R^{-1}\,(\vec{r} - \vec{t}) \tag{5.8}$$
$$\vec{dr'} = R^{-1}\,\vec{dr}. \tag{5.9}$$

For the transformation of $\vec{dr}$, only the rotation is relevant. The vectors $\vec{r'}$ and $\vec{dr'}$ give the position vector and the direction vector of the reference track in the local coordinate system S', which is fixed to the sensor under test. The position vectors of all tracks are given in an x-z plane of the global coordinate system S. This plane is chosen to approximately coincide with the sensor plane, however, the sensor can be somewhat tilted or shifted from this plane. The point $\vec{p}$, where the track intersects the sensor (see Fig. 5.20), is given by

$$\vec{p} = \vec{r'} - \frac{r'_y}{dr'_y}\vec{dr'}. \tag{5.10}$$

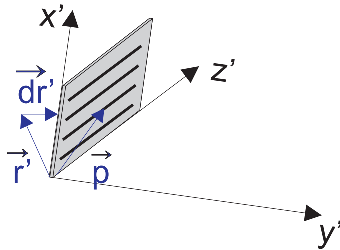

Figure 5.20: Position vector $\vec{r'}$, direction vector $\vec{dr'}$ of the track and the track point of impact $\vec{p}$, given in the local coordinate system S', which is fixed to the sensor.

The rotation angles θ, ϕ, ψ and the components of the translation vector $\vec{t}$ are calculated by minimising the residuals between the predicted and the measured track positions. The predicted position is given by the beam telescope and the measured value is given by the device under test. A χ^2 is defined as

$$\chi^2 = \sum \left(\frac{(p_x - x_{\text{dut}})^2}{\sigma_x^2} + \frac{(p_z - z_{\text{dut}})^2}{\sigma_z^2} \right) \tag{5.11}$$

and minimised using ROOT [ROO] fitting routines. The sum extends over all events. In the direction perpendicularly to the readout strips, the device under test measures the position x_{dut}. It is the x'-coordinate of the centre of the readout strip which measures the highest signal in the respective event. Events are disregarded if the signal-to-noise ratio is below a threshold, to exclude tracks which did not traverse the sensor. Only strip detectors were investigated, therefore the coordinate parallel to the readout strips, z_{dut}, is set to be the middle of the strips in the z'-direction for all hits. The coordinates p_x and p_z are measured by the beam telescope and calculated according to Eq. 5.10. The errors are composed of the track extrapolation uncertainties of the telescope, σ_{tel}, and the binary resolution of the strip detectors to be aligned:

$$\sigma_x = \sqrt{\sigma_{\text{tel}}^2 + \left(\frac{\text{pitch}}{\sqrt{12}}\right)^2} \approx \frac{\text{pitch}}{\sqrt{12}} \tag{5.12}$$

$$\sigma_z = \sqrt{\sigma_{\text{tel}}^2 + \left(\frac{\text{strip length}}{\sqrt{12}}\right)^2} \approx \frac{\text{strip length}}{\sqrt{12}} \tag{5.13}$$

For readout pitches of 80 or 100 µm and strip lengths of several millimetres, the telescope resolution of approximately 3 µm can be neglected.

During the beam tests, measurement runs with typically about 100000 triggers were executed. Since the areas of the devices under test are much smaller than the active area of the telescope, only a limited fraction of the total number of tracks are of interest. For the analysis, several runs performed with the same bias voltage are combined. Depending on the size and the position of the beam spot and the beam intensity, the period of these measurements could extend over several hours. Sometimes, the measurements were interrupted by necessary maintenance work or adjustments of the beam telescope. These interventions had an influence on the alignment. Furthermore, it could be observed that

the alignment slightly changed with time, especially if the temperature of the beam telescope was not fully stabilised. For these reasons, the alignment was calculated for groups of a few runs. After each intervention, a new alignment was calculated.

The total track extrapolation uncertainty, composed of the telescope resolution and the alignment uncertainty, can be estimated from the residual distribution. Distributions of residuals, defined as the difference between the track position measured by the device under test and the track position predicted by the beam telescope, are shown in Fig. 5.21. Only hits with negligible charge sharing between neighbouring readout strips were considered. First, the strip having the highest signal was determined. To limit the number of noise hits, the search window included only the predicted strip and its two nearest neighbours. Events were included if the predicted track point of impact was well within the active region of the device under test. Then, the signal-to-noise ratios of the nearest neighbours of the strip having the highest signal were calculated. If one of the signal-to-noise ratios was larger than three, which is a sign for considerable charge sharing, the hit was disregarded. The track position measured by the device under test, in the direction perpendicularly to the strips, is given by the centre of the strip having the highest signal.

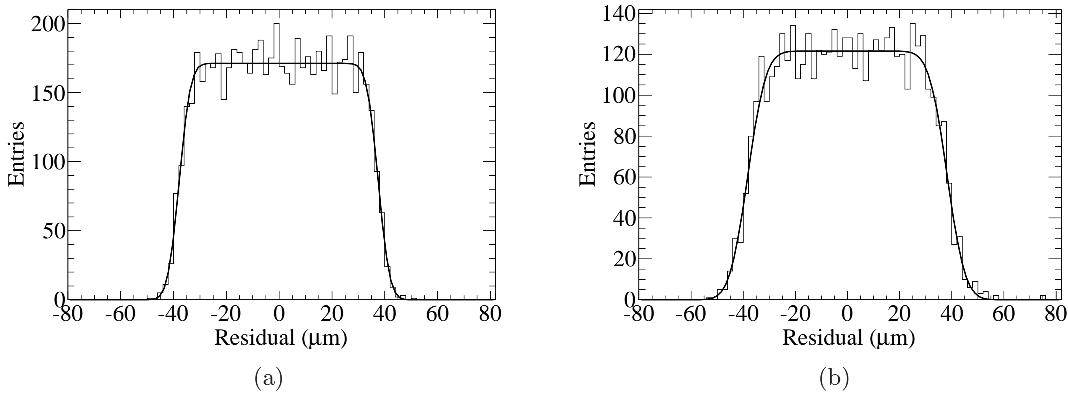

Figure 5.21: Residuals of single hits in the direction perpendicular to the readout strips. (a) For an unirradiated 3D detector (70 V bias) and (b) for a 3D detector irradiated with $2 \times 10^{15}\,\mathrm{n_{eq}/cm^2}$ (230 V bias). The fit superimposed is composed of an increasing and a decreasing error function.

Ideally, a distribution with steep edges would be expected. The smearing of the edges is a measure of the track extrapolation uncertainty. The distributions shown in Fig. 5.21 are fitted with a function composed of an increasing and a decreasing error function. The Gaussian width of the error function is considered as the track extrapolation error. In Fig. 5.21(a), the residual distribution of an unirradiated 3D sensor, measured with a bias voltage of 70 V, is shown. An extrapolation error of $\sigma = (3.4 \pm 0.2)\,\mu\mathrm{m}$ was determined by the fit. Figure 5.21(b) shows the residual distribution of a 3D detector irradiated with an equivalent fluence of $2 \times 10^{15}\,\mathrm{n_{eq}/cm^2}$, measured at a bias voltage of 230 V. A track extrapolation error of $\sigma = (5.5 \pm 0.3)\,\mu\mathrm{m}$ is obtained, which is significantly larger than the one obtained for the unirradiated detector. This highlights the variations of the alignment uncertainties of the different groups of measurement runs. The alignment of the

group of runs considered for Fig. 5.21(b) represents the worst case. Typically, the track extrapolation uncertainties are well below $\sigma = 5.5\,\mu\text{m}$. High noise and low statistics can lead to a reduced precision of the alignment. In the case of Fig. 5.21(b), the data taking extended over a long period with relatively low beam intensity. The measurements were interrupted by several interventions, therefore the number of tracks which could be used for each alignment was relatively low.

5.5.2 Analysis Procedure

Contrary to the beta and laser measurements described in Sections 5.3 and 5.4, separate pedestal measurements were not performed. In a first step, noise and pedestals are directly calculated from the measurements with traversing tracks. These data are used for the alignment procedure. After calculating the alignment, pedestal and noise data are recalculated for the subsequent data analysis. The data of strips which were predicted to be hit by a track and two neighbouring strips on either side are excluded from the calculation. This procedure assures that signals induced by traversing particles do not influence the final noise and pedestal calculation.

For the data analysis of the beam test performed in 2008, the common mode was calculated as the average over a group of channels as described in Section 5.3.1 for the beta source measurements. The tracking information is used to exclude the hit strips and two neighbours per side. The data acquired during the beam test in 2009 were subject to more pronounced common mode fluctuations and an advanced procedure is applied. Figure 5.22(a) shows the raw data of ten events as a function of the channel number, measured with an unirradiated 3D detector in the 2009 beam test. Strong common mode fluctuations are apparent. Signals induced by traversing particles can be seen as peaks directed downward. After subtracting the pedestal values for each channel, second order polynomials are fitted to the data for each event. The application of a second order common mode correction led to improved results compared to a calculation of the common mode as a simple average. The channels are subdivided into two groups, a separate fit is performed for each of the groups. The result of the final data, which are corrected for the common mode and the pedestal values, are shown in Fig. 5.22(b). The data have been inverted in order to show physical signals as positive values.

Presumably, the pronounced common mode fluctuations originated to a large extent from pickup of noise in the cables used for biasing the detectors. The cables had a length of approximately 20 m and were possibly not shielded sufficiently. The application of low-pass filters close to the sensors potentially could have reduced the fluctuations, however, filter circuits were not installed. A further problem encountered during the analysis of the 2009 beam test data is a high number of dead or very noisy channels. These have been masked and are excluded from the data analysis. In one sensor, even somewhat more than 50% of the total strips have been masked. Faults leading to dead channels can occur in the sensor itself, the fanins which connect sensors and readout chips, the wirebond connections or the readout chips. Since the beam time was very limited, the aforementioned problems could not be solved during the measurements. It can be assumed that the final noise distributions are still broadened by common mode effects.

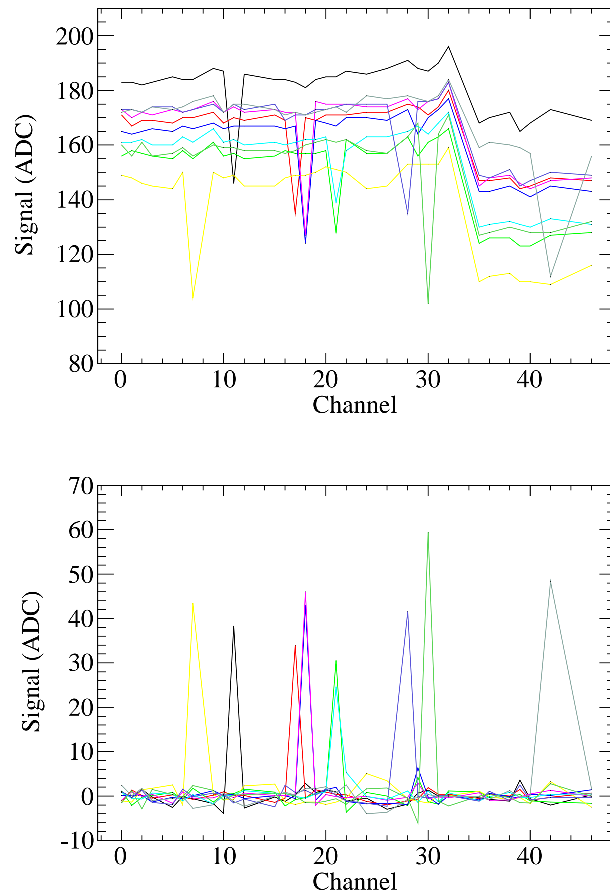

Figure 5.22: Signal as a function of the channel number, measured in the 2009 beam test with an unirradiated 3D detector. Each line represents an individual event. Dead or extremely noisy channels are excluded. Top: raw signals, bottom: signals after subtracting the pedestal values and correcting for the common mode. The signals shown in the lower plot are inverted to show hits as positive signals.

The data analysis includes calculation of the signal and the detection efficiency, partially as a function of the track point of incidence. The detection efficiency is defined as the ratio of the number of the tracks predicted by the telescope and the hits measured by the devices under test. In most cases, the signal is determined as the most probable value of a Landau function. It is extracted from a fit of a convolution of a Landau function and a Gaussian to the signal spectrum, as discussed for the analysis of the beta source measurements (see Section 5.3.1). Another approach is the investigation of the mean signal. It is applied for the investigation of the space-resolved signal when the amount of tracks is not sufficient to reliably extract the most probable value of a Landau distribution.

5.5.3 Calibration

The calibration, needed for the conversion of the detector signals from ADC counts into charge, is performed using the signal yield of the telescope's planar reference detectors. The planar detectors are expected to yield the full signal which is expected for the given thickness. Figure 5.23 shows the signal for seven telescope detectors as a function of the number of strips included for the generation of the signal spectra. The detectors were operated with a bias voltage of 150 V, while full depletion is reached around 110 V [Mä08]. Due to the intermediate strips between the readout strips and the relatively small readout strip pitch of 60 µm, the signals are distributed over broad clusters. The signal spectra are generated by summing up the signals of the strips around the track point of incidence. A convolution of a Landau function and a Gaussian is fitted to the spectra, the signals shown in Fig. 5.23 reflect the most probable value of the deconvoluted Landau function.

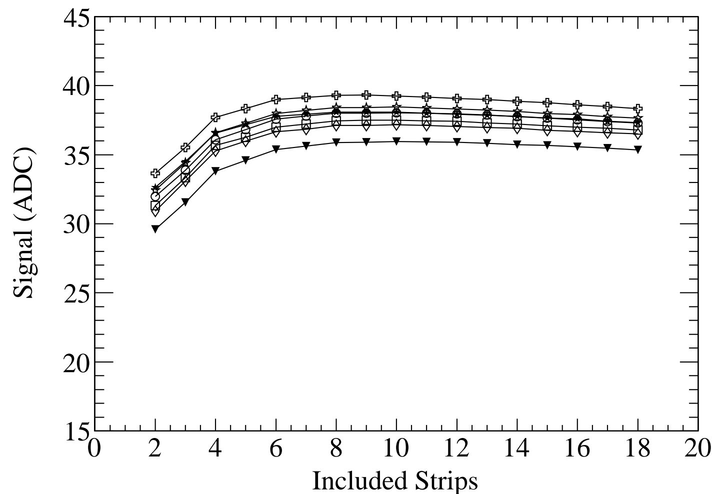

Figure 5.23: Signals of the telescope detectors as a function of the number of strips for which the signal has been summed to generate the signal spectra. The lines connect the data points of the different telescope detectors. Seven detectors are considered, as one detector was not functioning.

The maximum signal is obtained when including nine strips. Including more strips leads to a decrease of the resulting signal. Probably, this decrease results from negative signals induced on strips far away from the hit strip. This behaviour is not fully understood, however, the investigation of the telescope reference detectors is beyond the scope of this thesis. When summing the signals of nine strips, the mean signal of all reference detectors is

$$S(\text{ADC}) = (37.8 \pm 1.1)\ \text{ADC}. \tag{5.14}$$

The error is the standard deviation and indicates the variation of the signals measured by the different reference detectors. The signal variations can originate from variations of the sensor thicknesses, the timing adjustments or the gains of the APV25 chips. The reference detectors have a specified thickness of $(320 \pm 20)\ \mu\text{m}$ [Mä08, Dem03], therefore

a signal of

$$Q = (24.7 \pm 1.6)\,\mathrm{ke}^- \tag{5.15}$$

is expected according to Eq. (3.17). As discussed above, the analogue pulses of the APV25 front-end chips are not always sampled at the maximum. Therefore, an average signal degradation of approximately 10% is expected for the signals of both the reference detectors and the detectors under test. However, as long as one detector is calibrated against the other one with the same signal shape, this charge loss is not relevant. The gain, converting the signal measured in ADC counts into ke$^-$, becomes

$$G = \frac{Q}{S(\mathrm{ADC})} = (0.65 \pm 0.05)\frac{\mathrm{ke}^-}{\mathrm{ADC}}, \tag{5.16}$$

where the error has been calculated according to

$$\sigma_G = G\sqrt{\left(\frac{\sigma_Q}{Q}\right)^2 + \left(\frac{\sigma_{S(\mathrm{ADC})}}{S(\mathrm{ADC})}\right)^2}. \tag{5.17}$$

Contrary to the gain calibration of the beta source measurements (see Section 5.3.2), a dependence of the gain on the sensor capacitance and on the measurement temperature is not taken into account here. The beam test measurements were not performed as a function of the operation temperature. The dependence of the gain on the load capacitance is much lower for the APV25 front-end chip than for the Beetle front-end chip. The load capacitance of the reference detectors was approximately 10 pF per readout strip [Dem03], while it was $3-7$ pF for the 3D detectors under test. In this range, the gain of the APV25 varies only slightly [Fre01].

As for the beta source measurements, signal or noise values measured in ADC counts are converted into units of ke$^-$ according to

$$S(\mathrm{ke}^-) = S(\mathrm{ADC}) \cdot G \tag{5.18}$$

with the total error

$$\sigma_{S(\mathrm{ke}^-)} = \sqrt{\left(G \cdot \sigma_{S(\mathrm{ADC})}\right)^2 + \left(S(\mathrm{ADC}) \cdot \sigma_G\right)^2 + \left(0.03 \cdot S(\mathrm{ke}^-)\right)^2}. \tag{5.19}$$

The last term in Eq. 5.19 is a systematic error due to variations of the different methods applied to generate the signal spectra. A relative error of 3% has been conservatively estimated. For the conversion of noise values into ke$^-$, this term is ignored. As mentioned above, the signal spectra can be generated using a standard clustering algorithm or by summing up the signals of the channels around the channel where the track is pointing to. The results obtained with the different methods are compared in Chapter 6. In total, a relative error of about $\pm 8\%$ results from Eq. 5.19. The error is somewhat larger than that for the calibration of the beta source measurements, which is approximately $\pm 6\%$. The difference is mainly due to the larger uncertainty of the thickness of the reference detectors used for the beam test calibration.

Chapter 6

Measurements of 3D Detectors

In this chapter, measurements of double-sided 3D silicon strip detectors are presented. Although the key advantage of the detectors is the advanced radiation hardness, the performance of unirradiated detectors was investigated before proceeding to measure irradiated detectors. As double-sided 3D detectors are a new detector technology, it was considered necessary to gain a detailed understanding of the detector behaviour prior to any radiation-induced modification of the detector.

6.1 Measurements before Irradiation

In this section, investigations of charge collection and detection efficiency of unirradiated detectors are presented. These quantities are studied as a function of the point of incidence of a particle track or a laser beam. Due to the specific structure of the devices under test, with columns only partially etched into the substrate, the electric field distribution is inhomogeneous (see Section 5.1.1). In regions with lower electric field strength, the charge collection could be slower, resulting in a ballistic deficit when fast shaping electronics is employed. This observation was made for 3D Single Type Column (STC) detectors, where columnar electrodes of only one doping type are etched into the sensor from one side. Measurements of 3D-STC detectors with electronics using 25 ns shaping proved reduced charge collection [Ehr07, Kü08, Eck08, Pah09], especially in regions with low electric fields. In double-sided 3D detectors this deficit is expected to be overcome due to the presence of columnar electrodes of both doping types.

6.1.1 Beam Test Measurements

Beam test measurements with high-energy pions were performed in 2008 and 2009. In 2008, two unirradiated double-sided 3D strip detectors were investigated: FBK08 and CNM08, see Tab. 6.1. In 2009, the unirradiated detectors FBK09 and CNM09 were tested in addition to several irradiated detectors, the results of which will be described in Section 6.2.2. The amount of data collected with the unirradiated detectors was larger in the 2008 beam test, therefore the investigations of space-resolved properties primarily use these measurements. The results of the 2008 beam test measurements are published in Refs. [Kö09, Kö10b, Kö10a], those of the 2009 beam test are published in Ref. [Kö11a].

Table 6.1: Properties of the unirradiated detectors investigated in the beam tests. The expected signal was calculated according to Eq. (3.17).

Property	FBK08	CNM08	FBK09	CNM09
Structure	p-in-n	p-in-n	n-in-p	n-in-p
Thickness	(300 ± 15) µm	(285 ± 15) µm	(200 ± 10) µm	(285 ± 15) µm
Expected signal	$(23.1 \pm 1.2)\,\mathrm{ke}^-$	$(21.9 \pm 1.2)\,\mathrm{ke}^-$	$(15.0 \pm 0.8)\,\mathrm{ke}^-$	$(21.9 \pm 1.2)\,\mathrm{ke}^-$
Junction column depth	190 µm	~ 100 µm[a]	160 µm	250 µm
Ohmic column depth	160 µm	250 µm	180 µm	250 µm
Column spacing	100 µm	80 µm	80 µm	80 µm

[a]The junction columns were designed to have a depth of 250 µm, however, it was later found that they were in fact much shallower (see description in the text).

Signal

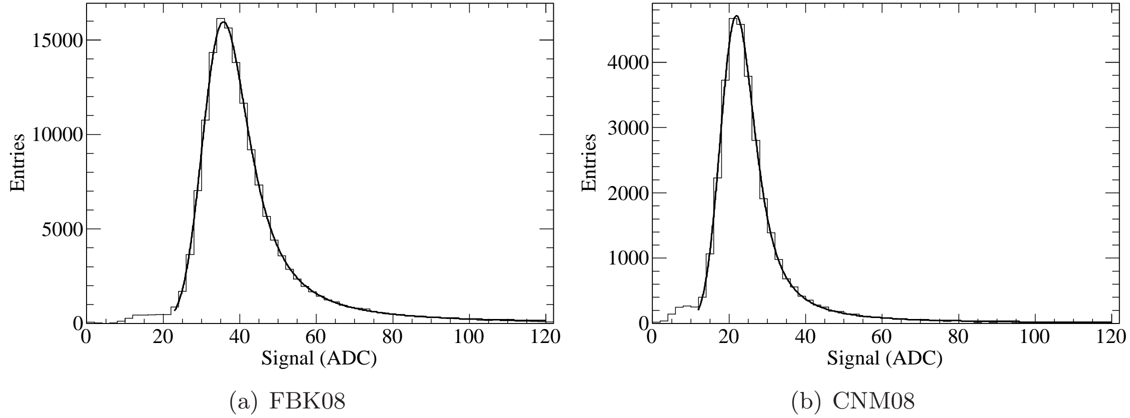

(a) FBK08 (b) CNM08

Figure 6.1: Spectra of measured signals for (a) the sensor FBK08 (40 V bias) and (b) the sensor CNM08 (9 V bias). Tracks impinging all over the sensor are included. The fit superimposed is a convolution of a Landau function and a Gaussian.

The measured signal distributions of both sensors for selected voltages are displayed in Fig. 6.1. The signals are shown in ADC counts and are not converted into units of charge. Runs with bias voltages of 40 V (FBK08) and 9 V (CNM08) have been chosen since for these runs the highest statistics is available. A convolution of a Landau function and a Gaussian is fitted to the data.

To correct for charge sharing, the signals of the two channels closest to the track impact position have been summed. This approach facilitates a detailed investigation of the signal spectra. It does not require any signal cuts as in clustering algorithms, which are usually applied if the track impact position is not precisely known. Track impact positions across the entire sensor surface are included in the plot. The bump at low charges is caused by particles which penetrate the sensor at the positions of the columns. Since the columns are either empty (FBK) or partially filled with polysilicon (CNM), they constitute inactive volume. To illustrate this effect, the signal spectra measured for tracks penetrating at the positions of the columns and far away from the columns are shown in Fig. 6.2.

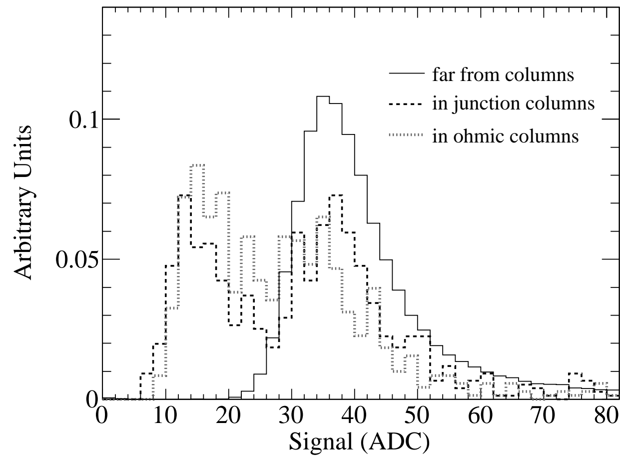

(a) FBK08

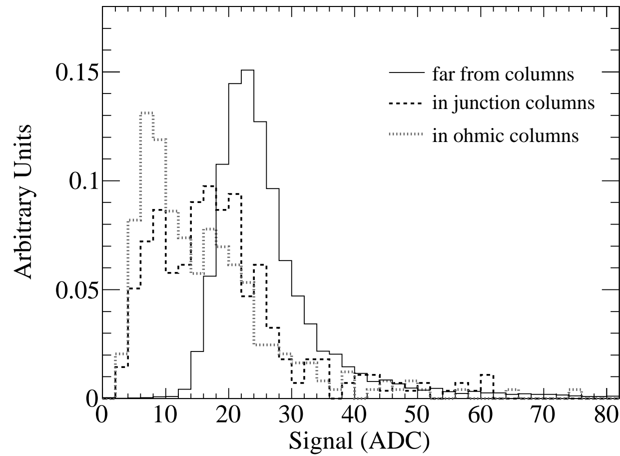

(b) CNM08

Figure 6.2: Normalised signal spectra measured in different regions relative to the column centres for (a) the detector FBK08 (40 V bias) and (b) the detector CNM08 (9 V bias): in junction columns (distance to junction column centre $< 4\,\mu$m), in ohmic columns (distance to ohmic column centre $< 4\,\mu$m) and far away from the columns (distance to any column centre larger than $25\,\mu$m).

Again, the signals of two strips adjacent to the track impact position are summed. It can be seen that the spectra of tracks impinging in the column regions exhibit two peaks. The peak at lower signal values is attributed to particles which travel directly through a column. Only the charge deposited below or above the inactive column volume can be measured. Due to the finite track extrapolation uncertainty of about $4\,\mu$m, some tracks are mis-assigned to the “in column” spectra and cause the peak at higher signals. The spectrum generated from tracks impinging far away from the columns does not contain the peak at lower signals.

Figure 6.3 summarises the signal height of the unirradiated detectors as a function of the

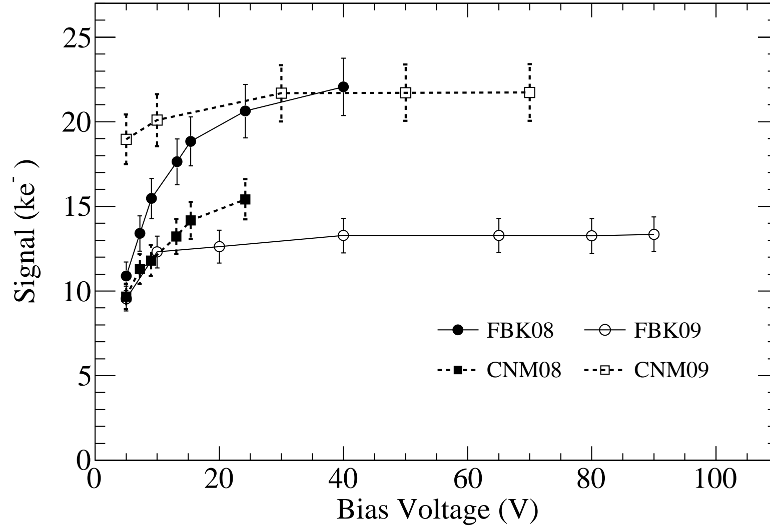

Figure 6.3: Signal of the unirradiated 3D detectors as a function of the applied bias voltage. The data points are connected to guide the eye. The errors are dominated by a systematic contribution due to the calibration uncertainty.

applied bias voltage. The range of applied bias voltages was chosen in order to comply with a safe current limit. The signal reflects the most probable value of a Landau function, extracted from a fit of a convolution of a Landau function and a Gaussian to the signal spectra, as shown in Fig. 6.1. As above, signals of the two strips closest to the extrapolated track point of incidence are summed to correct for charge sharing. The maximum signal of the detector FBK08, $(22.1 \pm 1.7)\,\mathrm{ke}^-$, and that of the detector CNM09, $(21.7 \pm 1.7)\,\mathrm{ke}^-$, are in agreement with the expected values (see Table 6.1). The curves indicate that full depletion of the devices is achieved well below 40 V.

The highest signal of the detector CNM08, measured at a bias voltage of 24 V, is only $(15.4 \pm 1.2)\,\mathrm{ke}^-$. This is approximately 30% less than expected for the given detector thickness. Considering the shape of the curve, it can be assumed that a saturation is not yet reached at 24 V. However, a flattening of the signal curve can be observed and therefore it is not expected that the signal would reach the expected value of approximately $22\,\mathrm{ke}^-$ at higher voltages. The signal loss is attributed to processing imperfections in this production run. It has to be noted that both detectors FBK08 and CNM08 originate from the first batch of double-sided 3D detectors ever produced by the respective manufacturers. The reason for the charge loss in the detector CNM08 is not fully understood, however, it has been discovered that the depth of the junction columns was much shorter than the design depth of 250 µm. Scanning electron microscopy investigations of this sensor were performed after the beam test and showed that the depth of the junction columns was only approximately 100 µm [Pel10]. The depth of the ohmic columns was close to the target depth of 250 µm. The reduced depth of the junction columns might have led to low electric field strengths in certain regions, comparable to the low-field regions present in 3D STC detectors with only one type of columns. Microscopic investigations of sensors produced on other wafers showed that the processing fault was limited to one wafer from the first

production run. The observed charge loss is not a principle problem of the detector design, since the full signal was measured with the detector CNM09. Furthermore, the full signal was measured with beta source measurements of unirradiated 3D detectors produced by CNM (see Section 6.1.2). These detectors originate from later production runs than the sensor CNM08.

The sensor FBK09 yields a maximum signal of $(13.4 \pm 1.0)\,\mathrm{ke}^-$, measured at a bias voltage of 90 V. Taking into account the uncertainty of the detector thickness, this value is still in agreement with the expected signal of $(15.0 \pm 0.8)\,\mathrm{ke}^-$. However, the difference between the measured value and the expected value is larger than for the detectors FBK08 and CNM09. A possible signal deficit could be explained by a lower value of the capacitance of the AC-coupling structure of the sensor. The production technique of the sensor FBK09 was optimised for pixel detectors, which usually do not require AC coupling. A relatively thick oxide layer provides the insulating layer for the AC-coupling structure and hence the coupling capacitance is comparatively low. However, lossless signal transmission requires that the coupling capacitance is sufficiently large compared to the detector capacitance. The reduced coupling capacitance can account for a signal loss of approximately 10% [DB10].

In the above discussion, the signals of the two strips adjacent to the extrapolated track point of incidence were combined for each event. Alternatively, other clustering strategies could be applied. This can influence the shape of the signal spectra and hence the most probable value of the fitted Landau function. Figure 6.4 shows the Landau most probable signals of the detectors FBK09 and CNM09 calculated using eight different clustering strategies:

1. Only the signal of the strip where the track is pointing to is considered.
2. The highest signal of the three strips around the track impact point is used.
3. The signals of the two strips around the extrapolated track point of incidence are summed.
4. The sum of the highest and the second highest signal of the three strips around the track impact positions.
5. The signals of three strips around the track point of incidence are summed.
6. The signals of five strips around the track point of incidence are summed.
7. The signals of seven strips around the track point of incidence are summed.
8. A traditional clustering algorithm is used: The channel having the highest signal-to-noise ratio is determined, where the search window is limited to five strips around the track impact point. The signal is accepted if the signal-to-noise ratio is larger than five (seed cut) and discarded otherwise. The signals of neighbouring channels are added as long as the signal-to-noise ratio is larger than three (neighbour cut).

Events with tracks impinging on or close to dead or noisy channels are discarded. For the strategies 1 and 2, charge sharing between neighbouring readout strips is not corrected

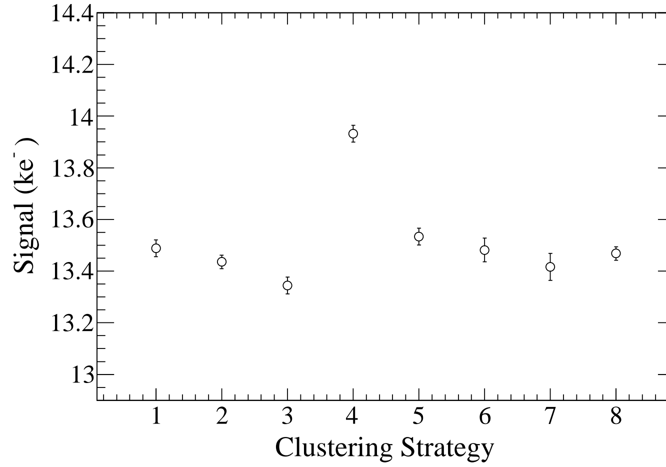

(a) FBK09

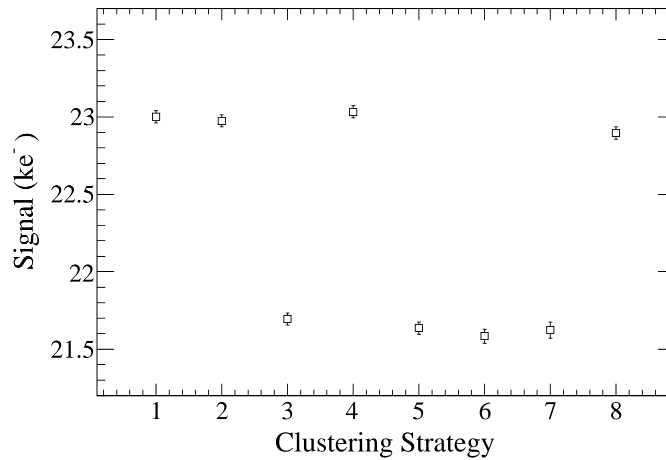

(b) CNM09

Figure 6.4: Landau most probable signal (a) of the detector FBK09 (90 V bias) and (b) of the detector CNM09 (70 V bias), calculated using different clustering strategies (see text). Only statistical errors are shown.

for since only the signals of one strip are used. Strategy 3 is used for the investigations presented in this chapter. Strategy 8 can be applied if the track point of incidence is not precisely known. It is typically applied for analyses of beta source measurements, however, in that case the search window for the highest channel extends over the entire sensor. This strategy was not chosen for the studies presented in this section. It requires application of a threshold, therefore an investigation of events where a low amount of energy is deposited, for example by tracks traversing the columns (see Fig. 6.2), is not possible. The full difference of the results obtained with the various clustering strategies is $0.6\,\mathrm{ke}^-$ for the detector FBK09 and $1.4\,\mathrm{ke}^-$ for the detector CNM09. Due to these differences, a systematic error of 3% has been added for signals calculated as the Landau most probable value as explained in Section 5.5.3. The different results of the clustering strategies will become clearer when the signals induced on the neighbours of a hit channel are discussed. An investigation of the induced signals is presented below together with the investigation

of the space-resolved signal.

Signal-to-Noise Ratio

The data acquired during the 2009 beam test were affected by strong common mode noise (see Section 5.5.2). Although a common mode correction was applied for all measurements, it can be assumed that the common mode contributions could not be fully eliminated from the data of the 2009 beam test. Hence the remaining noise is larger than the random noise originating from fluctuations in the sensor and in the readout electronics. Therefore, the discussion of noise and signal-to-noise ratio is limited to the data of the 2008 beam test, which are less affected by common mode noise.

The noise of the sensor FBK08 measured at a bias voltage of 40 V is $(710 \pm 60)\,e^-$, leading to a signal-to-noise ratio of 31. The sensor CNM08 exhibits a noise of $(520 \pm 40)\,e^-$ at a bias voltage of 24 V, which results in a signal-to-noise ratio of 30. Therefore the signal-to-noise ratio of both sensors is approximately equal, despite the different signal levels. Using the relationship between load capacitance and the noise of the APV25 front-end chip (see Section 5.5), the detector capacitance can be calculated. To this end, the average noise of the APV25 channels connected to detector strips and that of the channels not connected to detector strips are compared. In the sensor FBK08, the noise of the two groups of channels differs by $(250 \pm 20)\,e^-$, which corresponds to a detector strip capacitance of (8.7 ± 0.7) pF/cm. In the case of the sensor CNM08, the noise difference is $(91 \pm 7)\,e^-$, thus the strip capacitance is (6.3 ± 0.5) pF/cm. Due to a lower depth of the junction columns, the detector CNM08 is expected to show a lower capacitance per strip length than the detector FBK08.

Space-Resolved Signal

Figure 6.5 shows the mean signal as a function of the distance between the track point of impact and the centre of the readout strip. The mean value has been favoured over the Landau most probable value since the signal spectra of the channels adjacent to a hit channel exhibit a Gaussian distribution rather than a Landau distribution.

Due to the presence of the hollow junction columns, the mean signal is lower for tracks impinging on the centre of the readout strip. At low voltages (here 5 V, see Fig. 6.5(a)), a readout strip of the sensor FBK09 measures weak negative signals if the track impinges on the near half of the neighbouring strip. Distinct positive signals are measured if the track impinges on the far half of the neighbour. At a bias voltage of 90 V (see Fig. 6.5(b)), the average signals of tracks impinging on the near half of the neighbours are not negative any more. However, positive signals are still measured for tracks at the far half of the neighbours. The occurrence of negative signals measured on neighbours of hit strips is further investigated with laser measurements, which are presented in Section 6.1.4. Due to pronounced positive signals on one of the neighbours of the hit channel, clustering strategy 4, see Section 6.1.1, leads to the highest most probable signal. This effect can be seen in Fig. 6.4(a). For clustering strategy 4, the strips having the highest and the second highest signal are combined. The strip having the second highest signal is usually

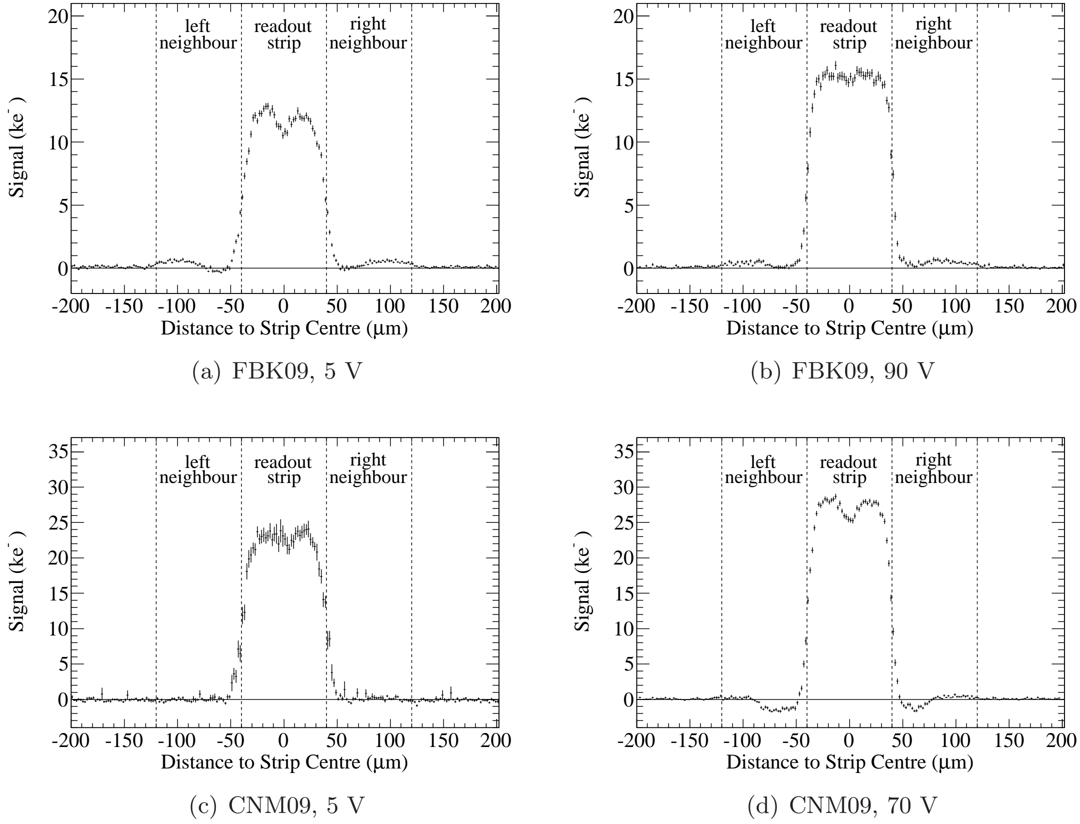

(a) FBK09, 5 V

(b) FBK09, 90 V

(c) CNM09, 5 V

(d) CNM09, 70 V

Figure 6.5: Mean signal as a function of the distance to the readout strip centre for the detectors FBK09 (5 V, 90 V) and CNM09 (5 V, 70 V). Only statistical errors are shown.

the second neighbour. First and second neighbours are defined in Fig. 6.6.

The detector CNM09 behaves differently. At low voltages (here 5 V, see Fig. 6.5(c)), the neighbours do not exhibit significant signals, apart from charge sharing for tracks impinging close to the border between two strips. However, at high voltages (here 70 V, see Fig. 6.5(d)), pronounced negative signals are measured for tracks impinging on the near half of neighbouring readout strips. Due to these distinct negative signals on the neighbours of hit strips, the signals calculated with clustering strategies 3, 5, 6 and 7 are lower than those calculated with the other strategies (see Fig. 6.4(b)). In the strategies 3, 5, 6 and 7 the signals of several neighbouring strips are summed.

An asymmetry between the left and right neighbours can be seen in Fig. 6.5. This is attributed to a displacement of the ohmic columns from the nominal position in the middle between the readout strips. The column displacements can also clearly be seen in laser measurements, see Section 6.1.4.

Given the periodic structure of the sensor, the sensor area can be divided into quadratic unit cells with the junction column in the centre and one quarter of the ohmic column in

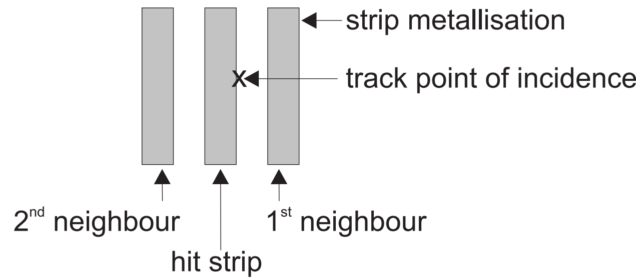

Figure 6.6: Hit strip, first and second neighbour.

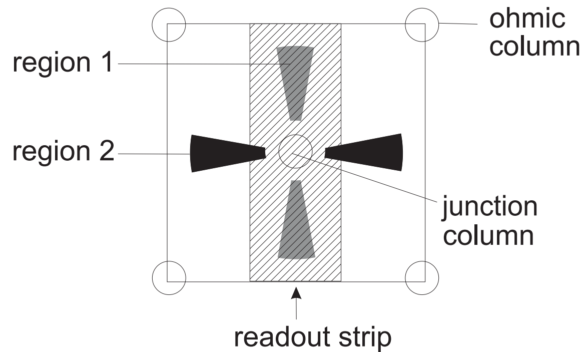

Figure 6.7: Sketch of the unit cell of a 3D detector with the readout strip, represented as the hatched region, running vertically. The signals measured for tracks impinging on region 1 (grey) and region 2 (black) are investigated separately and compared to each other (see text).

each of its corners, see Fig. 6.7. A two-dimensional visualisation of the charge collection in a unit cell of the sensor FBK08 is given in Fig. 6.8. For this sensor, the highest statistics are available. The sensor surface is divided within a unit cell into bins of $4\,\mu\text{m} \times 4\,\mu\text{m}$. For each bin the means of the measured signals are presented as a surface plot. As the signal distribution is not Landau-like in all bins (especially close to the column centres, see Fig. 6.2) the mean value has been favoured over the most probable value for the illustration.

At 5 V bias voltage (Fig. 6.8, top) a ring-shaped region around the junction column with relative high signal is visible, but the signal is not yet uniform across the unit cell. In Fig. 6.8(a) only the signal of the channel that the track is pointing to is considered, corresponding to clustering strategy 1. At the left and right margins, where the border between neighbouring readout strips is located, the signal drops strongly due to charge sharing. Summing the signals of the two strips around the track point of incidence (corresponding to clustering strategy 3) recovers this signal drop to some extent. As can be seen in Fig. 6.8(c), the charge collection is more uniform at 40 V bias voltage. The signal drop at the left and right margins vanishes when summing the signals of the two strips adjacent to the track impact position (see Fig. 6.8(d)). This demonstrates that the signal drop is caused by charge sharing and not by a low-field region with insufficient charge collection. Significantly lower signals are only measured at the column positions.

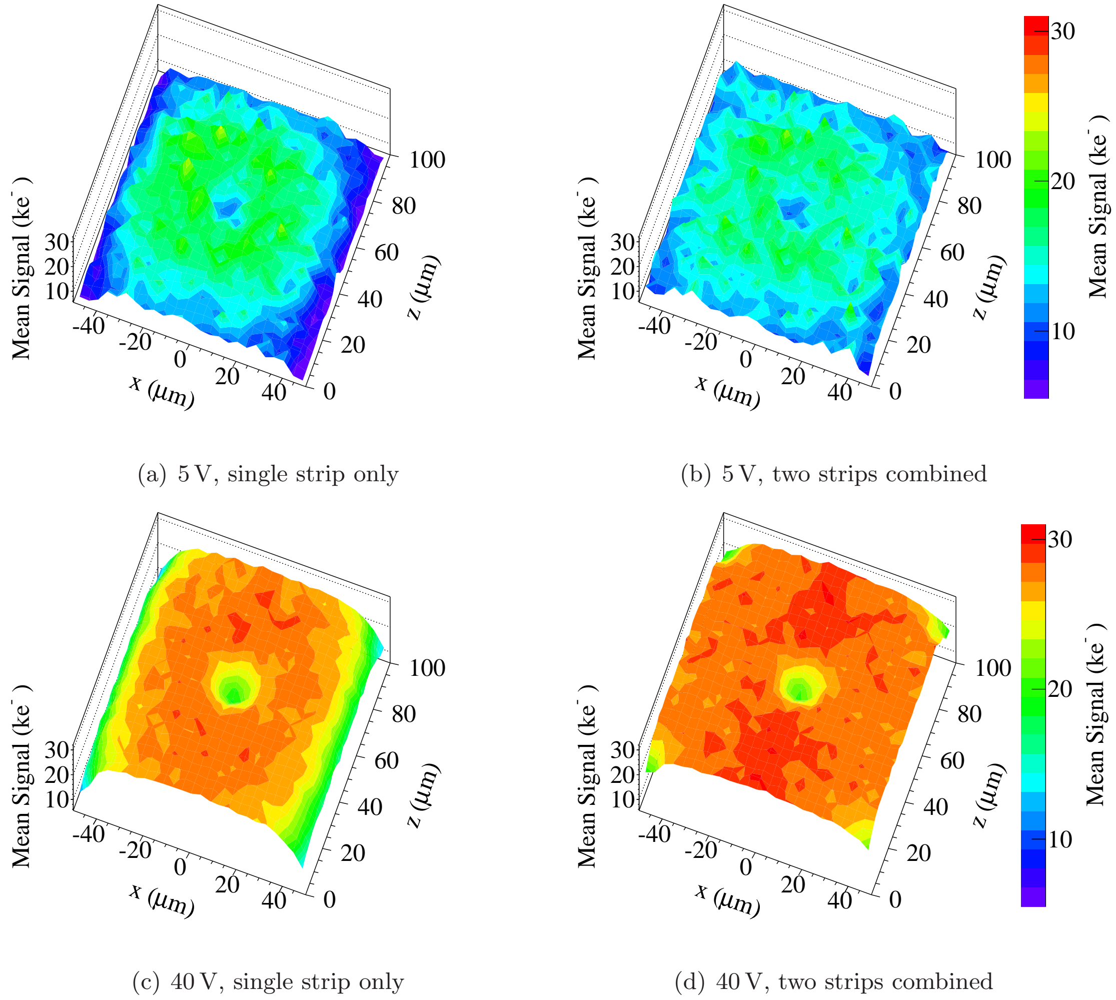

(a) 5 V, single strip only

(b) 5 V, two strips combined

(c) 40 V, single strip only

(d) 40 V, two strips combined

Figure 6.8: Representation of the signal measured with the sensor FBK08, superimposed onto one unit cell. The junction column is centred at (x,y)=(0,50). In each corner, one quarter of the ohmic column is visible. The readout strip is running parallel to the z-coordinate at $x = 0\,\mu\text{m}$.

However, it can be seen in Fig. 6.8(d) that slightly higher signals are measured at the centre of the readout strip (at $x = 0\,\mu\text{m}$) compared to the rest of the detector. To investigate this effect in more detail, the Landau most probable signals induced by tracks impinging on different regions of the sensor are compared. The comparison is made for tracks impinging on two different regions: on the readout strips (region 1, see Fig. 6.7) and perpendicularly to the strips (region 2, see Fig. 6.7). The most probable signals extracted from a Landau distribution are somewhat higher in region 1 than in region 2. The signal difference depends on the applied clustering strategy. Negative signals on the first neighbour of a hit strip cause the difference to be largest for strategy 3. Using this approach, the signals measured with the detectors FBK08 and FBK09 are approximately 1.3 ke^- larger for tracks impinging on region 1 than for tracks impinging on region 2. In the case of the detectors CNM08 and CNM09, this difference is only approximately 0.6 ke^-. The

signals measured for tracks impinging on the two distinct regions are more similar when the negative signals of neighbouring strips are not taken into account. Using clustering strategies 1 or 8, the difference is about 0.5 ke^- for the FBK detectors and about 0.4 ke^- for the detector CNM09. In the case of the sensor CNM08, the difference vanishes.

The observed signal asymmetry is somewhat more pronounced in the FBK detectors than in the CNM detectors. The length of the column overlap does not seem to play a major role, since the overlap is very different in the detectors FBK08 and FBK09, however, the observed signal asymmetry is similar. Therefore, the asymmetry possibly originates from the differences in the connection of the junction columns on the front surface and the connection of the ohmic columns on the sensor backplane (see Section 5.1.1). The different layouts influence the distributions of the weighting field and the electric field close to the surface. Altogether the signal is to a large extent uniform across the sensor area. Apart from the column positions, regions exhibiting distinct lower signals are not present.

Efficiency

The detection efficiency is of particular importance. In 3D-detectors with a passive volume in the columns and a non-uniform electric field configuration, the efficiency as a function of the track impact positions is a matter of special concern. The efficiency ε is defined as the fraction of events where the signal is higher than a chosen threshold:

$$\varepsilon = \frac{k}{n}, \tag{6.1}$$

where k is the number of hits above the threshold and n is the total number of tracks. The error of the efficiency was calculated according to a Bayesian approach [Ull07]:

$$\sigma_\varepsilon = \frac{(k+1)\,(k+2)}{(n+2)\,(n+3)} - \frac{(k+1)^2}{(n+2)^2}. \tag{6.2}$$

This approach has been favoured over a Poissonian or Binomial error calculation, as those methods lead to unphysical results in the limits of 0% or 100% efficiency [Ull07]. The investigations of space-resolved efficiency are limited to the data of the 2008 beam test. If not mentioned otherwise, the signals of the two strips closest to the track position were summed to eliminate charge sharing effects (corresponding to clustering strategy 3, see Section 6.1.1). Only tracks within a fiducial area well away from the sensor edges are included.

A two-dimensional illustration of the efficiency for a threshold of 2 fC (12.5 ke^-) is shown in Fig. 6.9, measured with the highest bias voltages applied to the detectors. The unit cell is shown six times next to each other. The relatively high threshold of 2 fC has been chosen to make the column positions visible. A threshold of 1 fC (6.2 ke^-) is typically applied for the binary readout of the ATLAS semiconductor tracker (SCT), while the ATLAS pixel detector is designed for thresholds of $3-4\,\mathrm{ke}^-$ [Aad08c].

Since the amount of data collected with the CNM detector is considerably lower, the plot in Fig. 6.9(b) shows more fluctuations and the positions of the columns do not appear as

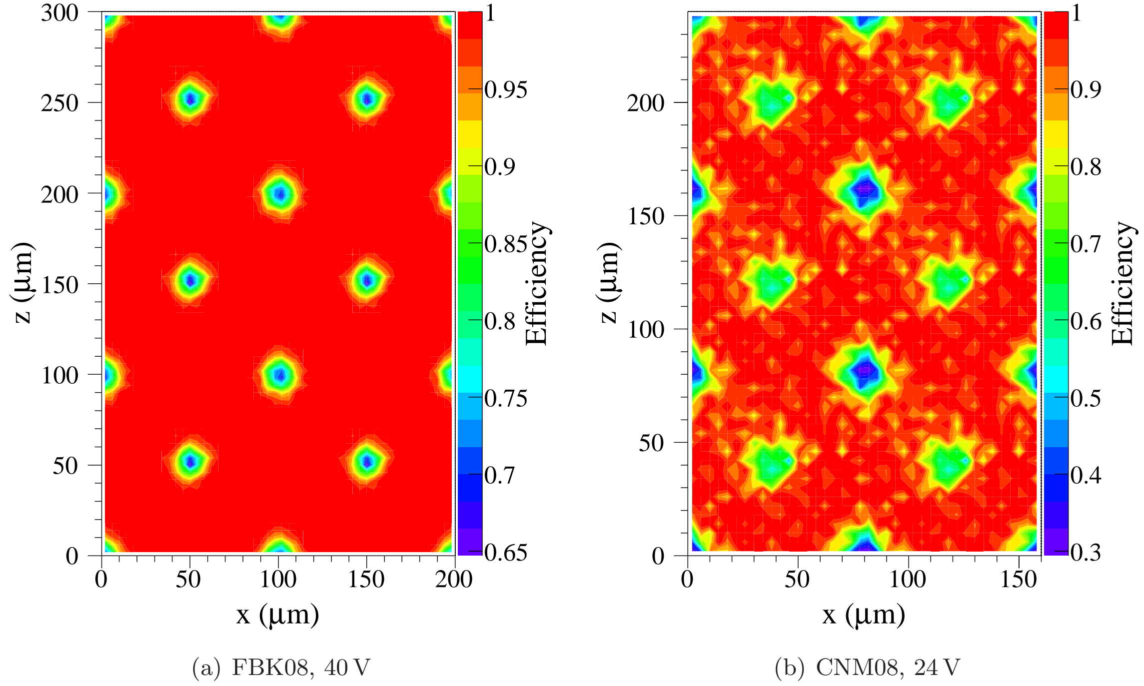

(a) FBK08, 40 V

(b) CNM08, 24 V

Figure 6.9: Two-dimensional representation of the efficiency measured with a threshold of 2 fC, (a) for the detector FBK08 (40 V bias) and (b) for the detector CNM08 (24 V bias). A superposition of all events onto one unit cell is displayed 6 times side by side. The readout strips are running parallel to the z-axis at $x = 50\,\mu\text{m}$ and $x = 150\,\mu\text{m}$ for the FBK device and at $x = 40\,\mu\text{m}$ and $x = 120\,\mu\text{m}$ for the CNM device. Due to the different pitches, the scales of the horizontal and vertical axes on the two figures are different.

well defined as in Fig. 6.9(a). However, the efficiency outside the columns appears uniform in both sensors. At a bias voltage of 40 V, the total efficiency of the FBK detector is $(99.80 \pm 0.01)\%$ at a threshold of 1 fC and $(98.53 \pm 0.03)\%$ at a threshold of 2 fC. The efficiency of the CNM detector at 24 V bias is $(97.9 \pm 0.2)\%$ at a threshold of 1 fC and $(92.1 \pm 0.3)\%$ at a threshold of 2 fC. It should be noted that the lower charge yield (as explained in Section 6.1.1) causes a lower efficiency of the CNM detector at a given threshold.

To get a more quantitative view, a one-dimensional illustration of the efficiency for different thresholds is presented in Fig. 6.10. A projection of the efficiency is shown along the coordinate perpendicular to the strips. The column positions are visible as drops of the efficiency. In addition to the position of the front columns at $x = 0\,\mu\text{m}$, a decrease of the efficiency is observed at the left and right margins, where the border between two neighbouring readout strips is located. With Fig. 6.11 it can be seen that this decrease in efficiency is caused by lower charge collection in the back columns and not by a general low-field region between the strips. In Fig. 6.11 the efficiency versus distance to the strip centre is shown for tracks impinging in the fiducial region marked in Fig. 6.12, thus contributions from lower deposited charge in the ohmic columns are excluded.

Due to charge sharing effects the efficiencies at the left and right margins decrease when

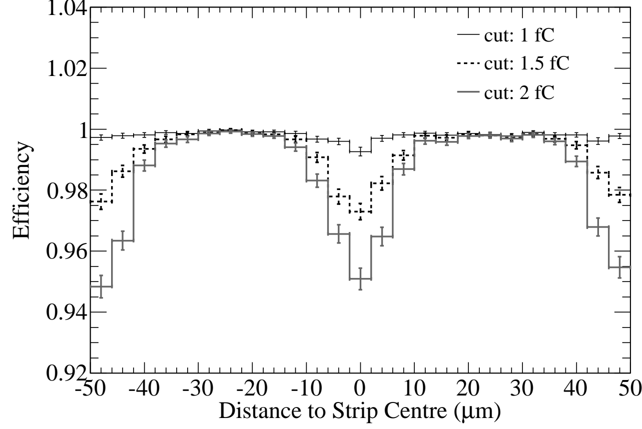

(a) FBK08, 40 V

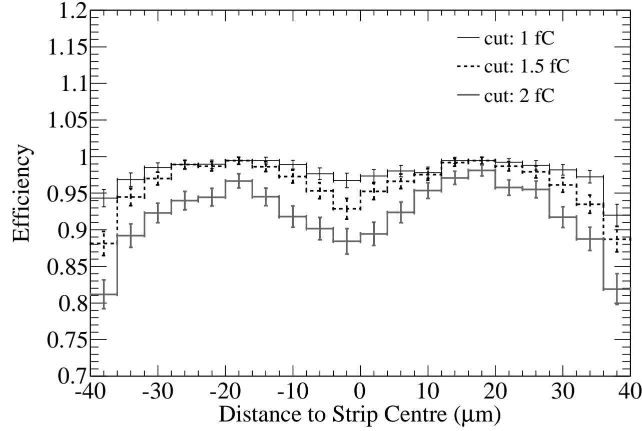

(b) CNM08, 24 V

Figure 6.10: Efficiency as a function of the distance to the centre of the readout strip. The efficiency is shown for three different threshold cuts in (a) for the detector FBK08 at 40 V bias and in (b) for the detector CNM08 at 24 V bias. The position of the junction columns appears around $x = 0\,\mu\text{m}$ and the position of the ohmic columns appears at the left and right edges.

signals of single strips are used, but no decrease is visible when the signals of two strips adjacent to the track position are summed. When restricting to signals of single strips, the highest signal of the strips in the vicinity of the track impact position was used (corresponding to clustering strategy 2). The left and right margins correspond to the region with minimum electric field, which is located in the middle of the square spanned by two junction columns and two ohmic columns (see Section 5.1.1). Thus, apart from at the column positions, the efficiency is uniform across the entire surface of both sensors, even in the low electric field region.

The uniform charge collection (see Section 6.1.1) and efficiency are improvements compared to 3D single type column (3D-STC) detectors with columns of only one doping type. In 3D-STC detectors, a lower signal yield in the region with low electric field was measured (see Section 4.4.5). The efficiency drops in the column regions do not lead to

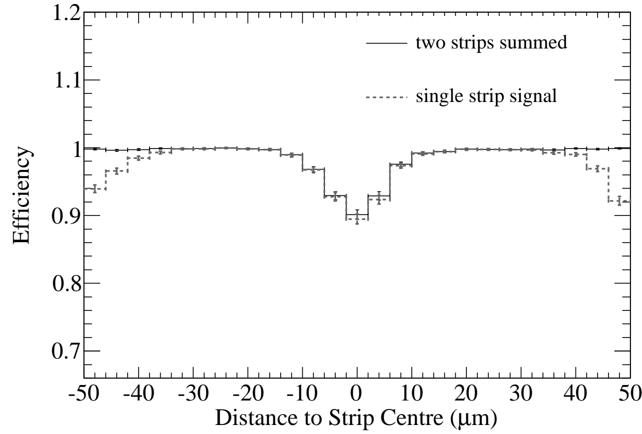

(a) FBK08, 40 V

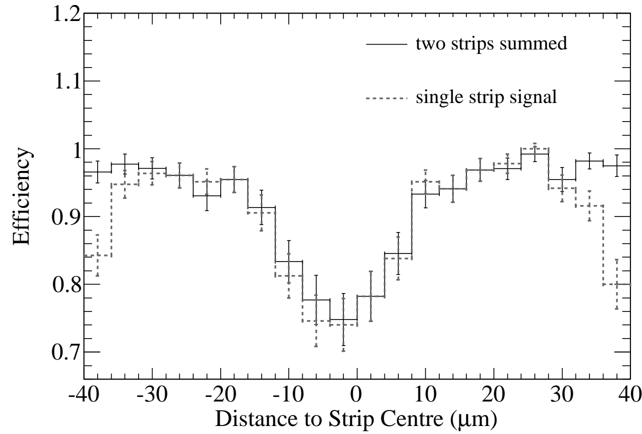

(b) CNM08, 40 V

Figure 6.11: Efficiency for a threshold of 2 fC versus distance to the strip centre, including only tracks in the fiducial region marked in Fig. 6.12. The efficiency is shown using signals of single strips and the sum of the two strips closest to the track position, (a) for the FBK detector at 40 V bias and (b) for the CNM detector at 24 V bias.

significant performance degradation as long as the sensors are tilted, so that the normal of the sensor surface does not coincide with the direction of the impinging particle tracks. This configuration, which is often applied in high energy physics tracking detectors as in the ATLAS experiment [Aad08c], avoids that particles travel through the entire passive volume of the columns.

Charge Sharing

An intrinsic property of 3D sensors is the reduced charge sharing compared to planar sensors. Since the electric field inside the sensor is dominated by a component perpendicular to the boundary between two readout strips, broadening of the charge cloud due to diffusion over neighbouring strips is reduced. A comparison of charge sharing in 3D and planar detectors using synchrotron measurements is reported in Ref. [Pen10]. While charge sharing can be exploited to improve the spatial resolution (see Section 6.2.2), it can

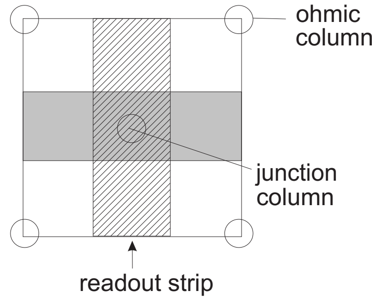

Figure 6.12: Unit cell of a 3D detector. Tracks impinging on the grey region, which has a width of 30 µm in the direction of the readout strips, are used for the measurement of the efficiency presented in Fig. 6.11.

also be disadvantageous when the signal-to-noise ratio is low and the broadening of the charge cloud leads to further decrease of the signal measured per readout channel. This is especially true for binary readout systems as envisaged for the upgrade of the ATLAS semiconductor tracker (SCT). Charge sharing reduces the detection efficiency if the liberated charge is not much higher than the threshold value. The spatial resolution of the detector CNM09 is discussed in Section 6.2.2 together with the results of an irradiated detector.

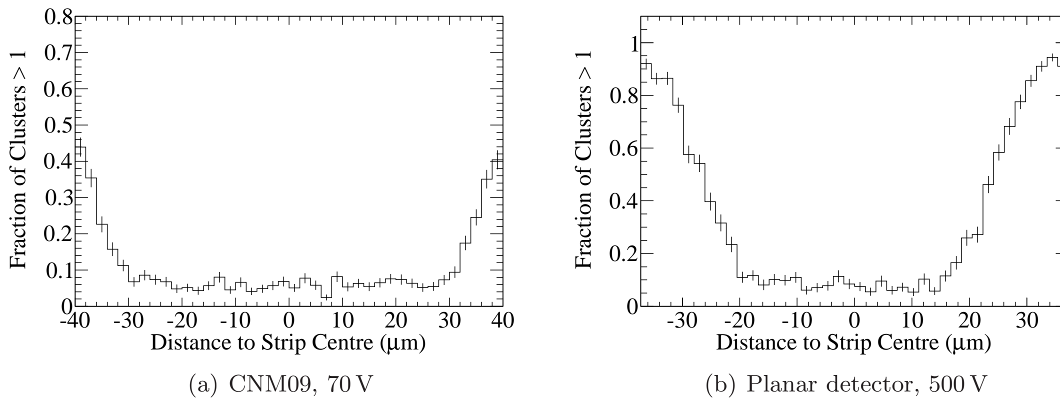

(a) CNM09, 70 V

(b) Planar detector, 500 V

Figure 6.13: Fraction of clusters consisting of more than one readout strip as a function of the distance to the readout strip centre: (a) for the detector CNM09 and (b) for a planar n-in-p strip detector irradiated with a fluence of $5 \times 10^{13}\,\mathrm{n_{eq}/cm^2}$ [Kö11a]. For the calculation of the cluster width, a seed cut of 5 and a neighbour cut of 3 for the signal-to-noie ratio was used.

The fraction of clusters consisting of more than one strip as a function of the distance to the readout strip centre is shown in Fig. 6.13(a) for the detector CNM09. As a comparison, Fig. 6.13(b) shows the same measurement performed with a planar detector produced by Hamamatsu (see Section 5.1.2). The planar sensor was irradiated with an irradiation fluence of $5 \times 10^{13}\,\mathrm{n_{eq}/cm^2}$. A significant radiation damage leading to a lower signal is not expected for this comparatively low fluence. Planar sensors irradiated with different fluences were measured in the 2009 beam test together with the 3D detectors, results are

presented in Ref. [Kö11a, Wii].

The cluster width was calculated applying clustering strategy 8 (see Section 6.1.1), using a seed cut of 5 and a neighbour cut of 3 for the signal-to-noie ratio. The data originate from measurements with bias voltages well above the full depletion voltages, 70 V for the 3D detector and 500 V for the planar detector. Due to comparable noise and signal values in the two detectors investigated, the signal-to-noise cuts applied for the clustering algorithm have essentially the same effects for both detectors. In both detectors, only tracks impinging close to mid-pitch, shown at the left and right margins in Fig. 6.13, exhibit a significant charge sharing probability. The width of the region with high charge sharing is visibly lower in the 3D detector, where it is limited to a narrow band smaller than 10 µm at the left and right margins. In the planar detector this region extends up to 20 µm. In total, only 11% of the hits in the 3D detector and 35% of the hits in the planar detector are shared between neighbouring readout strips.

6.1.2 Beta Source Measurements

Beta source measurements were performed with two 3D detectors in an unirradiated state: an n-in-p detector and a p-in-n detector produced by CNM. The detectors originate from the second production run, the specifications are the same as those of the detector CNM09 summarised in Table 6.1. Since a readout system based on the Beetle chip (see Section 5.3) is used for the beta source measurements, the integration time of the shaping amplifier is below 30 ns. In contrast to that, the APV25 readout chip (see Section 5.5) used for the beam test measurements applies a 50 ns shaping. Therefore, it can be investigated whether the shorter shaping time has any effect on the collected charge due to ballistic deficit.

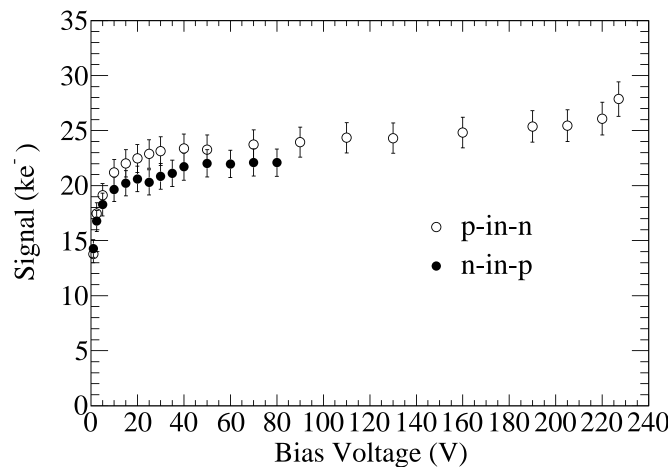

Figure 6.14: Beta source measurements: signal of the unirradiated 3D detectors as a function of the applied bias voltage.

Figure 6.14 shows the Landau most probable signal as a function of the applied bias voltage for the n-in-p and the p-in-n sensor. The measurements were performed at a temperature of −16 °C. The signal of the n-in-p detector reaches a plateau at about 40 V, which

indicates full depletion of the sensor. The expected signal of approximately 22 ke$^-$, corresponding to the sensor thickness of 285 µm (see Table 6.1), can be measured. An electrical breakdown occurs at a voltage of approximately 80 V, therefore higher voltages cannot be applied. The results are in agreement with the beam test measurements described in Section 6.1.1. Thus, it can be concluded that the shorter shaping time used in the beta measurements does not lead to a lower signal.

The electrical breakdown of the p-in-n detector occurs at a bias voltage of about 230 V, hence it can be operated at considerably higher voltages than the n-in-p detector. Possibly, higher electric field strengths around the p-stop implants cause an early breakdown of the n-in-p detector.

The signal that is expected for the given detector thickness can also be measured with the p-in-n detector. The signal in the plateau is somewhat higher than that of the n-in-p detector. This difference can be attributed to calibration uncertainties or to slightly different thicknesses of the two sensors. After reaching a plateau at approximately 40 V, the signal of the p-in-n detector increases significantly at bias voltages above 200 V. Between 205 V and 227 V, the signal increases by 2.6 ke$^-$. It has to be mentioned that the errors indicated in Fig. 6.14 are dominated by a correlated systematic uncertainty. The statistical uncertainty, originating from the fit of a convolution of a Landau function and a Gaussian, is below 0.2 ke$^-$ for these measurements. An overlay of the signal spectra measured at bias voltages of 205 V and 227 V is shown in Fig. 6.15. It is apparent that higher signals are measured at 227 V. The average noise of all channels does not increase between 205 V and 227 V, see Section 6.1.3.

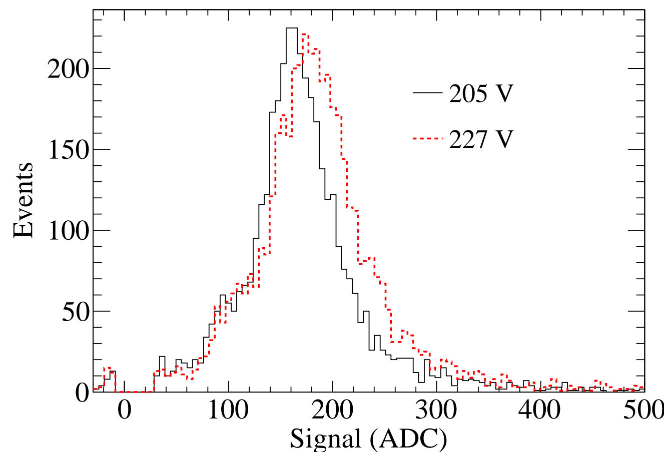

Figure 6.15: Signal spectra of the unirradiated p-in-n detector measured at bias voltages of 205 V and 227 V.

The significant increase of the signal can be attributed to charge multiplication due to impact ionisation (see Section 3.3.7). So far, charge multiplication in silicon tracking detectors designed for high-energy physics purposes has only been reported after exposing the detectors to high irradiation fluences (see Section 4.3.5). Charge multiplication in irradiated double-sided 3D detectors is discussed in Section 6.2. The assumption that

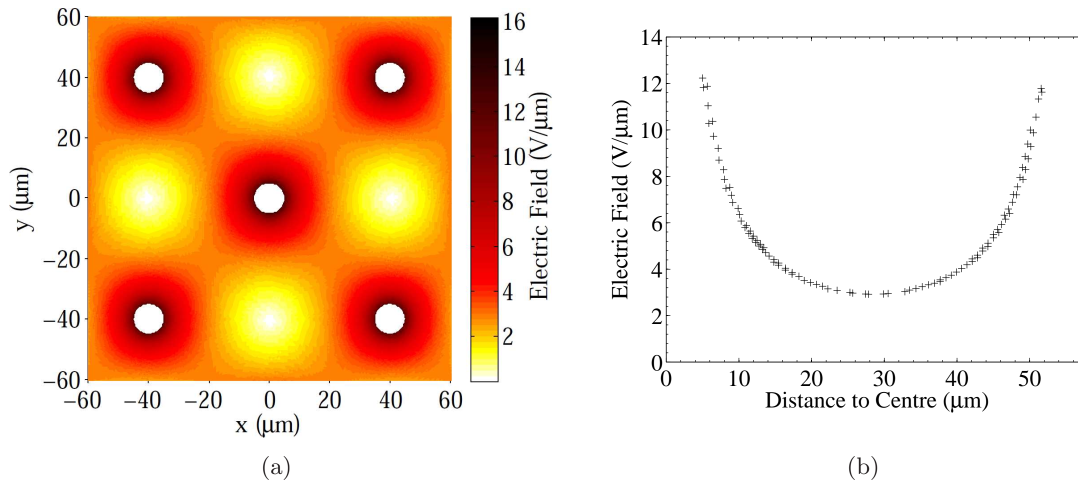

Figure 6.16: Simulated electric field strength in a 3D detector for a bias voltage of 227 V and an effective doping concentration of 3×10^{11} cm^{-3}. (a) Two-dimensional representation of the field strength, the junction column is located in the centre and an ohmic column is located in each of the four corners. (b) Electric field on the direct line between a junction column and an ohmic column, as a function of the distance to the junction column centre. The field inside the columns was not simulated.

charge multiplication leads to the signal increase can be substantiated by calculations of the electric field. Figure 6.16 shows the results of electric field simulations, which were performed as described in Section 5.1.1. The electric field strength was calculated for a detector with an effective doping concentration of 3×10^{11} cm^{-3} at a bias voltage of 227 V. The doping concentration corresponds to that of the p-in-n detector investigated here. The electric field strength exceeds 12 V/µm close to the junction columns and close to the ohmic columns. These high values of the electric field strength are already reached at relatively low bias voltages due to the short distance between the columnar electrodes and due to the circular shape of the electrodes. As a consequence of the low doping concentration of the substrate, the field strengths around the junction columns and around the ohmic columns are approximately equal. The field strength close to the ohmic column decreases with increasing doping concentration.

To highlight the effect of the electrodes' shape on the electric field, the maximum field strength can be compared to the one in a planar detector. In a pad detector with a thickness of 50 µm, which corresponds to the spacing of the junction columns and the ohmic columns, Eq. 3.11 (see Section 3.3.1) yields a maximum electric field of only 5 V/µm for a bias voltage of 227 V. This is considerably lower than the maximum electric field for the same bias voltage in a 3D detector.

As discussed in Section 3.3.7, impact ionisation of electrons is expected to come into effect at electric fields higher than approximately 10 V/µm. Therefore, the increase of the signal at voltages above 220 V is attributed to multiplication of electrons in the vicinity of the ohmic columns. It should be kept in mind that these simulations can only serve as an approximation. While the simulations are assumed to well approximate the real field

distribution close to the middle of the detector depth, deviations are expected in other regions. Especially close to the detector surfaces and around the column tips, the field distribution will be different. The highest fields are expected in the vicinity of the column tips due to more pronounced focusing of the electric field lines.

6.1.3 Noise

This chapter reports noise measurements of the CNM n-in-p and p-in-n detectors. These detectors were also measured with the beta source setup (see Section 6.1.2) and the laser setup (see Section 6.1.4). The design of the detectors corresponds to that of the sensor CNM08, see Table 6.1. As the noise depends on the detector capacitance, the noise is expected to decrease as the depletion zone increases.

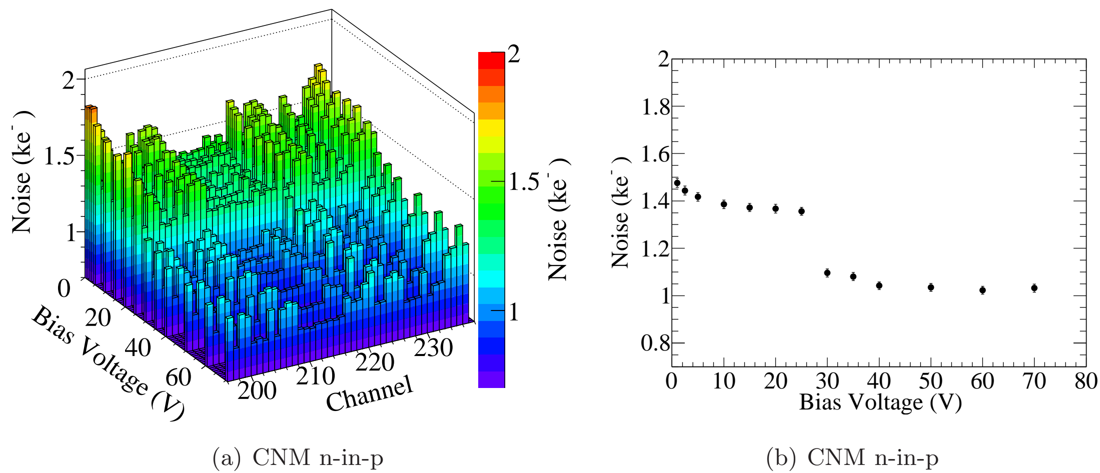

(a) CNM n-in-p (b) CNM n-in-p

Figure 6.17: Noise as a function of the applied voltage, measured with the CNM n-in-p detector at a temperature of $-16\,^{\circ}$C. In (a), the noise is shown for all readout channels, (b) shows the average noise of these channels. Only the errors of the mean are considered.

Figure 6.17 shows the noise of the CNM n-in-p detector as a function of the applied bias voltage. The noise reaches a first plateau around a bias voltages of 10 V. It is assumed that this voltage corresponds to the lateral depletion voltage. A strong decrease of the noise can be observed between 25 V and 30 V. Potentially, the regions around the p-stop isolation structures deplete at these voltages, which could lead to a strong decrease of the detector capacitance. Hence, the noise also decreases strongly. It is assumed that full depletion of the sensor is reached at a bias voltage of 30 V. Considerable variations of the noise of the different channels can be seen in Fig. 6.17(a).

The noise of the CNM p-in-n detector is illustrated in Fig. 6.18. The noise of the different channels is more uniform compared to the CNM n-in-p sensor. Furthermore, it decreases more rapidly at low bias voltages and reaches a plateau already at a bias voltage of 10 V. At voltages higher than 220 V, where onset of charge multiplication can be observed (see Section 6.1.2), the noise does not increase considerably. At the highest voltages, the

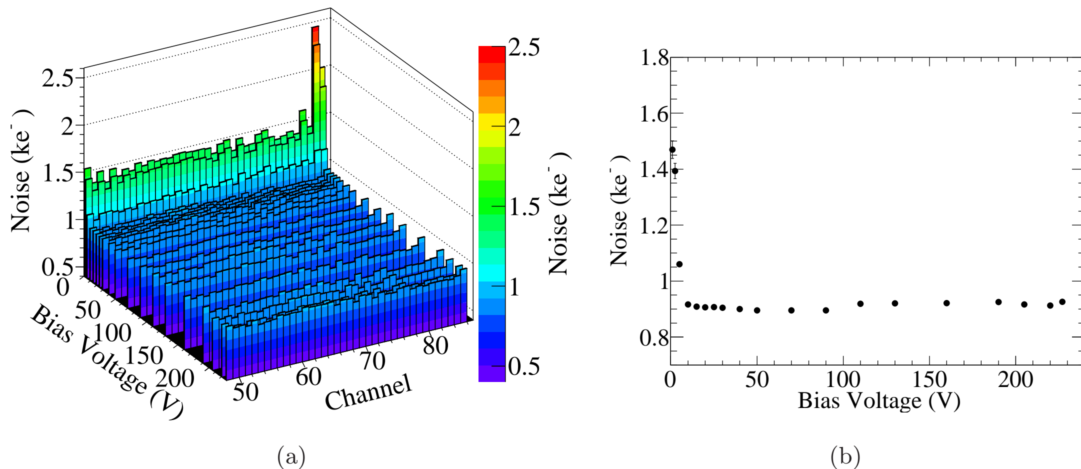

Figure 6.18: Noise of the CNM p-in-n detector, measured at a temperature of $-16\,°\mathrm{C}$. In (b), the mean noise of the channels is shown. Only the errors of the mean are considered.

mean noise is approximately $0.9\,\mathrm{ke}^-$, whereas the noise of the CNM n-in-p detector is about $0.1\,\mathrm{ke}^-$ higher. Possibly, the difference is due to the p-stop implants in the n-in-p detector.

6.1.4 Laser Measurements

The laser measurements were performed to investigate the detector's response as a function of the position of the energy deposition. Three double-sided 3D detectors were measured in an unirradiated state: an n-in-p and a p-in-n detector produced by CNM, and an n-in-p detector produced by FBK. The CNM sensors have the same design as the detector CNM08, the FBK sensor is the sensor FBK09, see Table 6.1. The CNM sensors were also measured with the beta source setup (see Section 6.1.2), the FBK sensor was measured in the beam test 2009 (see Section 6.1.1).

Since the laser is reflected by the metal of the readout strips, only the region between the strip metallisations can be investigated. Typically, the measurements are performed by scanning the laser over a rectangular area around the position of an ohmic column, as illustrated in Fig. 6.19. All laser scans reported within this thesis were made using a step size of $2\,\mu\mathrm{m}$ in x- and y-direction. As explained in Section 5.4, the signals measured with the laser setup are reported in units of ADC counts, a conversion into charge is not performed.

An example of the signals measured on the two strips adjacent to the area scanned by the laser is shown in Fig. 6.20. These measurements were performed with the unirradiated CNM n-in-p sensor at a bias voltage of 77 V. When the laser illuminates the left part of the region in between the strips, only the left channel measures high signals. As the laser moves to the right part of this region, the signal of the left channel decreases and that of the right channel increases. In the middle, charge sharing and the finite laser spot size allow both channels to measure appreciable signals. The non-collecting strip can measure negative signals for certain laser positions. This effect, which was already mentioned in

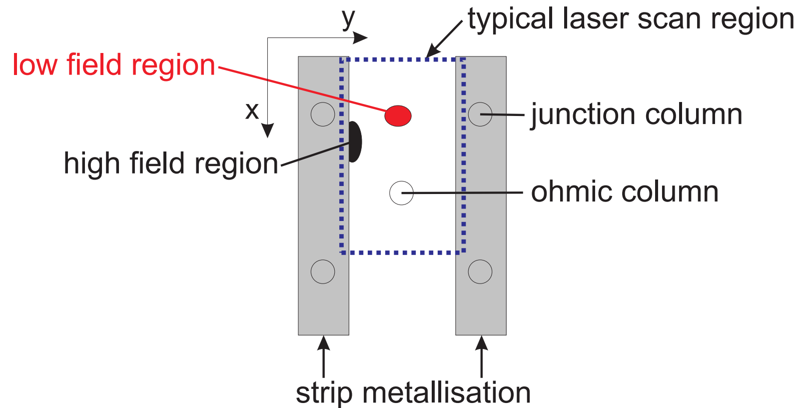

Figure 6.19: Unit cell of a 3D strip detector. The region typically scanned with the infrared laser is delimited by the dashed line. Signals induced by the laser shining on the high and low-field regions are investigated in Fig. 6.23.

the discussion of the beam test results (see Section 6.1.1), is investigated in more detail below. Negative signals on neighbours of the hit channel were also observed with 3D STC detectors [Ehr07, Eck08, Pah09].

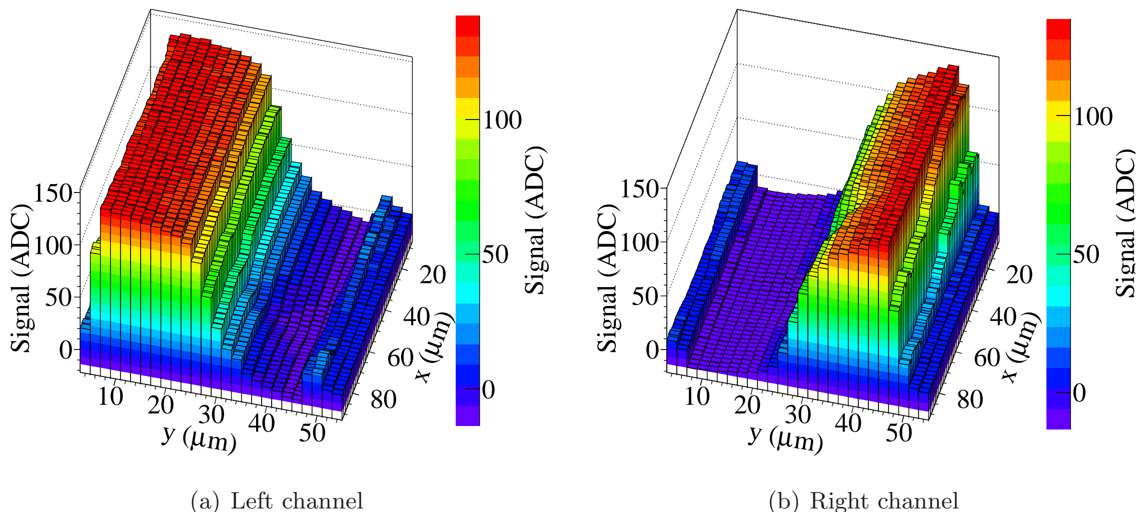

(a) Left channel (b) Right channel

Figure 6.20: Laser measurement of the CNM n-in-p detector at a bias voltage of 77 V. The signal of the left and the right channel, which border the scan area, are shown separately.

The transition between high and low signals of the two readout strips does not coincide with the middle between these strips. This asymmetry is ascribed to a displacement of the ohmic columns from the nominal position in the middle between four junction columns. The junction columns are located in the middle of the strip metallisations, as can be seen optically on the sensor surface (see Fig. 5.2). The displacement of the ohmic columns is further discussed below.

To investigate the uniformity of the signal across the sensor area, the signals of neighbouring readout strips are summed. Figure 6.21 shows the resulting plot of laser measurements performed with the CNM n-in-p detector at two different voltages. At a bias voltage of 4 V, the volume between the columnar electrodes is already depleted. Hence the detector is active all over the scanned region. At higher voltages, the electric field in the depleted volume increases and the depletion zone expands further towards the detector front surface and to the backplane. Therefore, higher signals are measured at a bias voltage of 77 V. The signal is uniform, apart from the position of the ohmic column.

It is apparent from Fig. 6.21 that the ohmic column is shifted by $5-10$ μm from its nominal position in the middle between the strips. As the positions of the ohmic columns cannot be seen optically, this displacement was initially unexpected. In principle, an observation of such a shift could also be a measurement artefact, caused by a non-perpendicular incidence of the laser on the sensor surface. However, in that case the column would appear oval-shaped rather than circular. Furthermore, a systematic effect of the setup could be excluded by performing a laser measurement with the sensor rotated about 180°. The result of that measurement was consistent with the measurements performed before the rotation. Therefore, it is concluded that the ohmic columns are indeed displaced. The displacement is assumed to result from a misalignment of the masks applied in the numerous production steps. Displacements of the ohmic columns can be observed in all detectors investigated within this thesis, however, the magnitudes are different.

Figure 6.22 shows the results of laser measurements performed with the CNM p-in-n sensor and the FBK n-in-p sensor, in both cases with a bias voltage of 80 V. A displacement of the ohmic columns from the nominal positions is visible again. The signals are less uniform than those measured with the CNM n-in-p detector discussed above. The CNM p-in-n detector (Fig. 6.22(a)) yields slightly lower signals if the laser illuminates the region around the ohmic column and the middle between the readout strips. Somewhat higher signals are measured if the laser impinges close to the junction columns. In the case of the FBK detector (Fig 6.22(b)), the signal non-uniformity is even more pronounced. Here, higher signals are measured for laser impact positions around the ohmic column. Lower signals are measured if the laser impinges very close to the strip metallisations. Potentially, these lower signals could result from a higher reflectivity close to the metal traces due to additional passivation layers. The absolute signals measured with the different detectors cannot be compared directly since it is not guaranteed that the oxide layer on all sensors has the same thickness and the same reflectivity. Furthermore, the temperature during the measurement of the FBK detector was much higher than the temperature of the other detectors[1]: the FBK detector was measured at a temperature of $+30\,^{\circ}$C, whereas the other ones were operated at $-20\,^{\circ}$C. The temperature has a strong effect on the gain of the Beetle chip and the absorption length of the laser photons decreases with increasing temperature (see Section 3.3.4).

The different extent of the signal non-uniformity in the CNM detectors and the FBK

[1] The FBK sensor was physically the same as measured during the 2009 beam test and was still mounted on the beam test module. Due to its large dimensions this module could not be installed in the cold box of the laser setup, hence cooling was not possible.

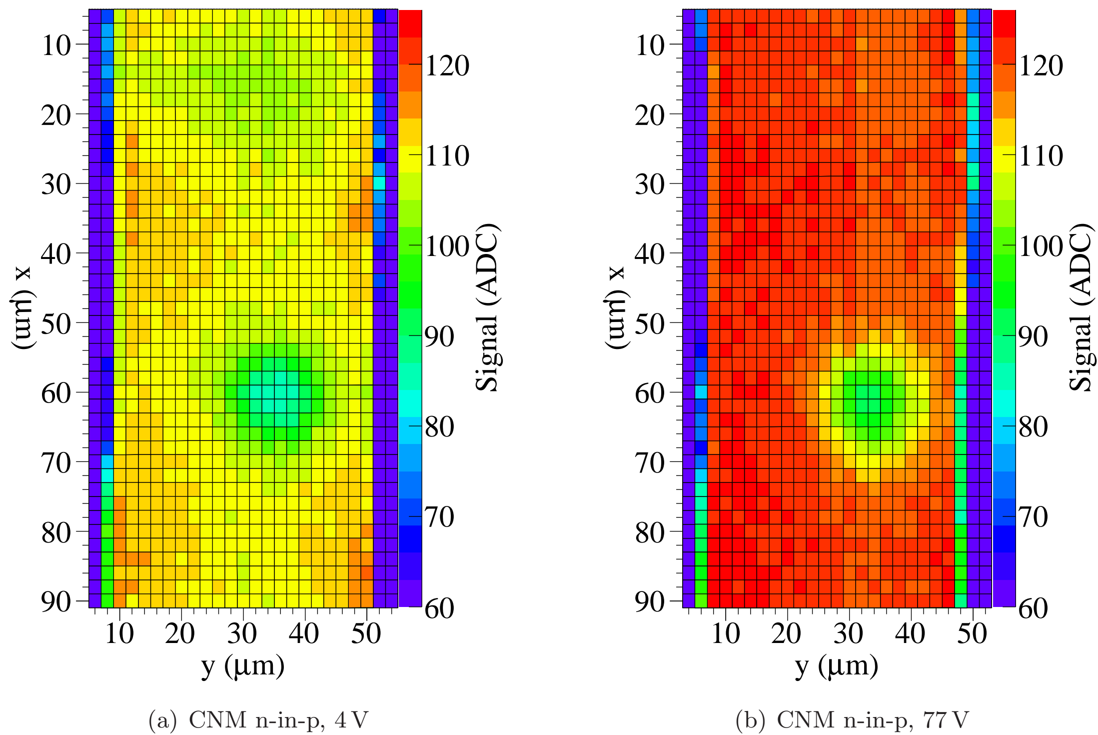

(a) CNM n-in-p, 4 V

(b) CNM n-in-p, 77 V

Figure 6.21: Signal as a function of the laser point of incidence measured with the CNM n-in-p detector, (a) at a low bias voltage (4 V) and (b) at a high bias voltage (77 V). The signals of two adjacent channels are summed. The sensor temperature during the measurement was −20 °C.

detector is not fully understood. As discussed in Section 6.1.1, a slight non-uniformity was also observed with the beam test measurements. However, this is of minor concern since the full signal can be measured with all detectors. In the case of the beam test measurements, the non-uniformity of the FBK detector was also more expressed than that of the CNM detector. Possibly, the differences can be related to the different schemes the two manufacturers apply for the connection of the columnar electrodes. Especially, the additional doping layer below the strip metallisation in the FBK design can lead to different weighting field distributions in the surface region. As the absorption probability of the laser photons is higher in the surface region, these differences have a large effect on the laser measurements. In the case of the FBK detector, p-spray implantations have an additional effect on the electric field close to the surface. It is possible that not all charge carriers, which are generated close to the surface, are collected within the amplifier integration time of approximately 25 ns.

This interpretation is further substantiated by the observation of negative signals on electrodes which do not collect any charge carriers (see below). Non-collecting electrodes which do not collect any charge carriers can only measure nonzero signals in the case of trapping or if the integration time is shorter than the length of the induced current pulse (ballistic deficit). As these detectors are unirradiated, trapping can be neglected. The induced current on non-collecting electrodes can change the sign if the scalar product of

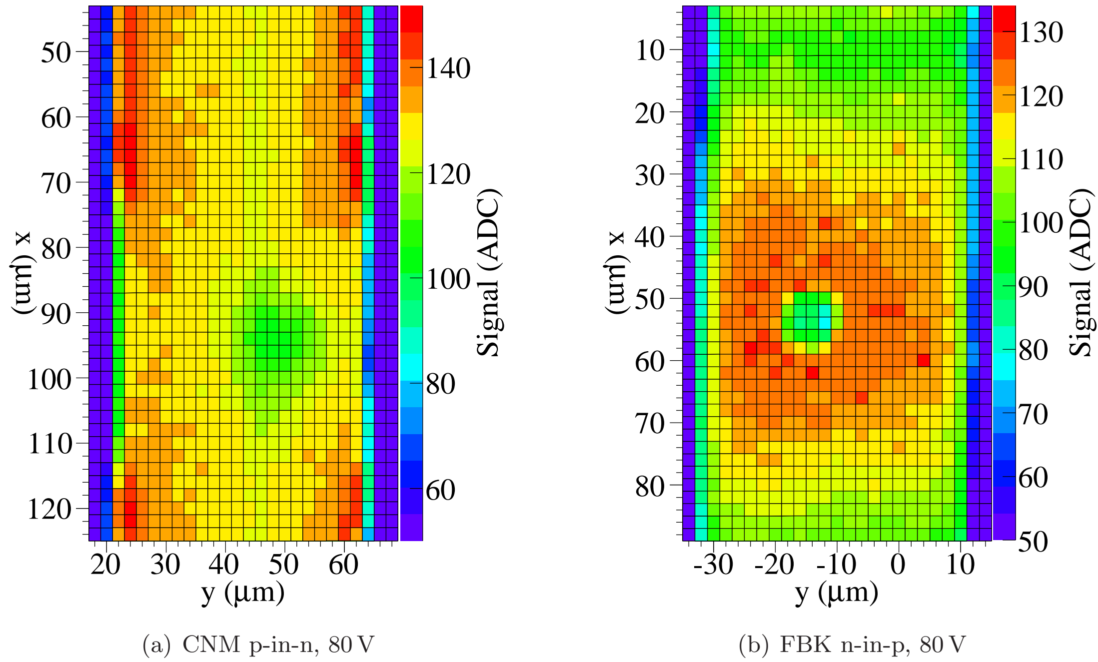

(a) CNM p-in-n, 80 V

(b) FBK n-in-p, 80 V

Figure 6.22: Signal as a function of the laser point of incidence measured with (a) the CNM p-in-n detector and (b) the FBK n-in-p detector. Both measurements were performed at a bias voltage of 80 V. The signals of two adjacent channels are summed. The sensor temperature during the measurement was −20 °C for the CNM detector and +30 °C for the FBK detector.

the drift velocity and the weighting field changes its sign (see Section 3.3.6). If the induced current pulse on non-collecting electrodes is composed of a fast negative component and a slow positive one, ballistic deficit can lead to negative signals. It would be possible to further investigate these effects with measurements using the transient current technique TCT [Mur70]. In TCT measurements the induced current, generated by a laser pulse, can be analysed directly for selected electrodes. Also, transient simulations of the signal generation applying a three-dimensional model of the detectors could help to gain further insight into the observed behaviour. However, those studies are beyond the scope of this thesis.

Signal in Selected Regions

To get a more quantitative view, the signals are extracted for selected laser points of incidence. Figure 6.23 summarises the signals extracted in four different regions as a function of the applied bias voltage. The high and low-field regions correspond to the regions marked in Fig. 6.19. The high-field region is located on the direct line between an ohmic column and a junction column. The low-field region is located in the middle of the rectangle bordered by two junction columns and two ohmic columns. These regions are characterised by a very high and a very low electric field, respectively, as can be seen in the field maps presented in Fig. 5.4, Section 5.1.1, and Fig. 6.16, Section 6.1.2. The signals have been extracted from laser scan measurements, which are described in the preceding

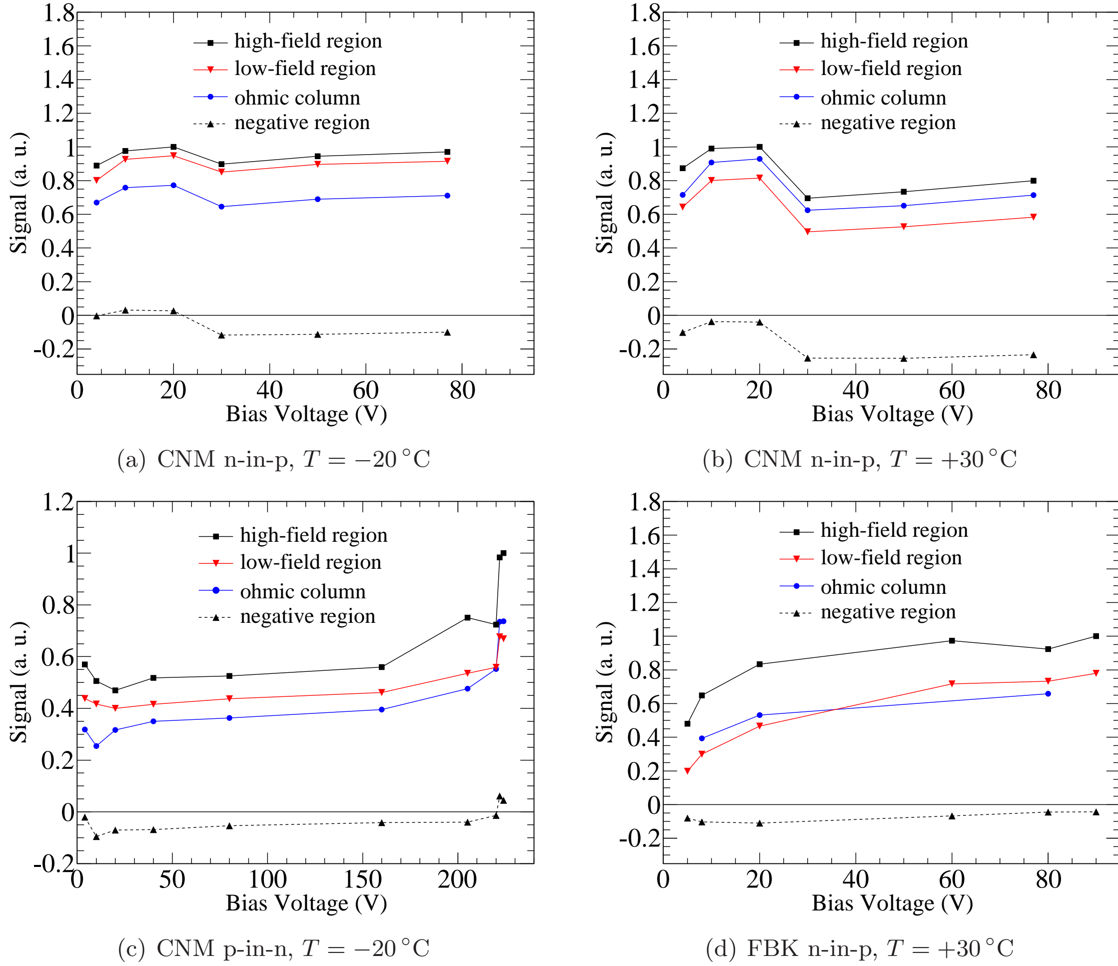

(a) CNM n-in-p, $T = -20\,^\circ\mathrm{C}$

(b) CNM n-in-p, $T = +30\,^\circ\mathrm{C}$

(c) CNM p-in-n, $T = -20\,^\circ\mathrm{C}$

(d) FBK n-in-p, $T = +30\,^\circ\mathrm{C}$

Figure 6.23: Signal for selected laser positions as a function of the applied bias voltage for different detectors and different temperatures. The signal values are normalised to the highest signal measured in a measurement series of one detector.

section. The data points reflect the mean signal, averaged over four neighbouring laser positions (the scans were performed with a step size of $2\,\mu\mathrm{m}$). The "negative region" corresponds to the position where the most pronounced negative signals are measured. In this case the data of a single readout strip are considered. In the other regions the signals of two adjacent strips were summed. The signals are normalised to the highest signal obtained in the measurement series for one detector at a constant temperature.

The measurements of the CNM n-in-p detector are shown in Figs. 6.23(a) and 6.23(b). The measurements were performed at $-20\,^\circ\mathrm{C}$ and $+30\,^\circ\mathrm{C}$, respectively. In all regions, the signal decreases for bias voltages between 20 V and 30 V. As can be deduced from noise measurements (see Section 6.1.3), 30 V is the full depletion voltage of the sensor. More pronounced negative signals on one of the strips around the laser point of incidence lead to a lower sum of the signal. It is remarkable that considerably more pronounced negative signals are measured if the sensor is fully depleted. This observation gives rise to the assumption that the negative signals are induced by charge carriers generated close

to the detector surface. At voltages lower than the full depletion voltage, these charge carriers quickly recombine and do not contribute to the measured signal. In the case of full depletion, the electric field is particularly low close to the surface. Charge carriers generated in these regions with low electric field are likely to suffer from ballistic deficit that can cause negative signals on electrodes which do not collect any charge carriers.

At low temperature ($-20\,^{\circ}$C, Fig. 6.23(a)), negative signals are only measured for bias voltages higher than 20 V. In contrast to that, negative signals can be observed at all bias voltages in the measurements performed at higher temperature ($+30\,^{\circ}$C, Fig. 6.23(b)). This observation confirms the interpretation that the negative signals are induced by charge carriers generated in the volume close to the detector surface. An increase of the temperature leads to a shorter absorption length of the laser photons and more charge carriers are liberated in the upper detector volume. The decreased absorption length also causes the signals measured in the region of the ohmic column to be higher at higher temperatures. Since the columns represent essentially passive volume, the signal is mainly generated in the silicon above the column tips. The signals measured at $+30\,^{\circ}$C are less uniform than those measured at $-20\,^{\circ}$C, where only a slight difference between the high-field region and the low-field region exists.

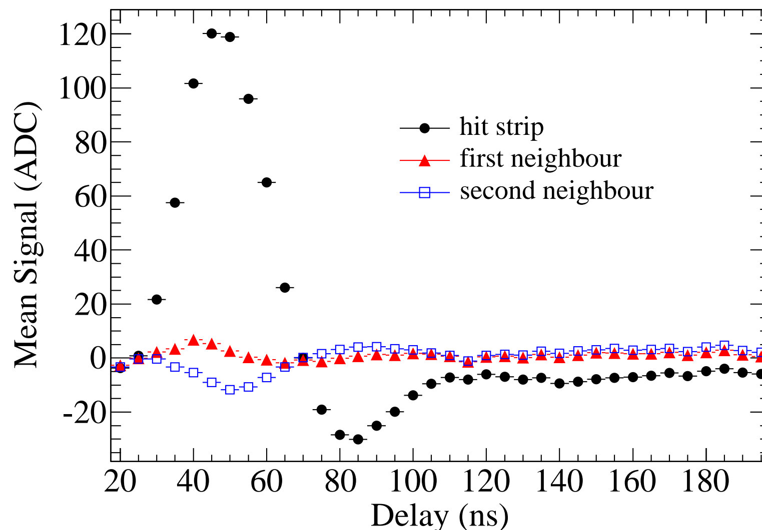

Figure 6.24: Time profile of the analogue output pulse of the Beetle front-end chip for the hit strip, the first neighbour and the second neighbour. The measurement was performed with the CNM n-in-p detector at a bias voltage of 50 V, which is higher than the full depletion voltage. The pulse shape was reconstructed by varying the delay between the laser pulse and the data acquisition.

Figure 6.24 shows the time profile of the analogue output pulse of the Beetle front-end chip for the hit strip, the first and the second neighbour. The measurement was performed by varying the delay between the generation of the laser pulse and the trigger for the data acquisition in steps of 5 ns (see Section 5.4.1). It was conducted with the CNM n-in-p detector at a bias voltage of 50 V, the laser was impinging on the high-field region.

The first neighbour and the second neighbour are the strips which are second-closest and third-closest to the laser point of incidence (see Fig. 6.6). It can be seen that in this case the Beetle output pulses of the three channels have their maxima at different delays. The pulse of the second neighbour reaches the maximum earlier, whereas the pulse of the first neighbour reaches the maximum later than that of the hit strip. For delays higher than 70 ns, the tail of the Beetle pulse is visible, which has the opposite polarity than the first part of the pulse.

For the final measurements, the timing has to be adjusted by fixing the delay between the laser pulse and the trigger for the data acquisition. The delay is chosen to assure that the analogue Beetle pulse of the hit strip is sampled at its maximum. The corresponding delay for the measurement shown in Fig. 6.24 is 47 ns (see also the discussion in Section 5.4.1). Therefore, it is possible that the analogue pulses of the neighbouring channels are not sampled at their maxima, as this would require different delays. Hence, the signals of the neighbouring channels investigated in this and the following subsection do not correspond to the maxima of the pulses. It has to be emphasised that the pulses illustrated in Fig. 6.24 reflect the output pulses of the Beetle shaping amplifier and not the pulses of the currents induced on the electrodes. The underlying induced current cannot be reproduced with the experimental equipment used for the work described within this thesis.

The results of the CNM p-in-n detector are shown in (Fig. 6.23(c)). Negative signals are measured as well, however, the magnitude is lower than in the case of the CNM n-in-p detector. At voltages above 220 V, the signals increase strongly. At these voltages, an increase of the signal is also observed with the beta source measurements (see Section 6.1.2) and is attributed to charge multiplication. However, the relative signal increase observed with the laser measurements is larger than that of the beta source measurement. This observation points to the fact that predominantly the charge carriers generated close to the detector surface are multiplied. This would also explain why no negative signals are measured once charge multiplication occurs: The extra generation of charge carriers counterbalances the ballistic deficit. It can be assumed that most of the charge multiplication takes place around the tip of the ohmic column, where particularly strong electric fields are expected. Therefore, the signal induced by the laser shining onto the position of the ohmic column also increases rapidly.

The FBK detector (Fig. 6.23(d)) was measured up to a bias voltage of 95 V, an electrical breakdown occurs at approximately 100 V. Negative signals are measured at all bias voltages applied. As in the beam test measurements, the signal saturates at approximately 20 V and is relatively constant up to the highest bias voltage applied.

Signal Projections

Figure 6.25 shows the signals measured by single strips as a function of the distance to the strip centre. The data are computed from laser scans with a step size of 2 μm, spanning a region which was approximately 80 μm long in the direction of the readout strips. The signals measured for the different laser impact positions along the strip direction are averaged. The representations highlight the different responses of the detectors if the laser shines on the left side or on the right side of the readout strip. In the CNM n-in-p and

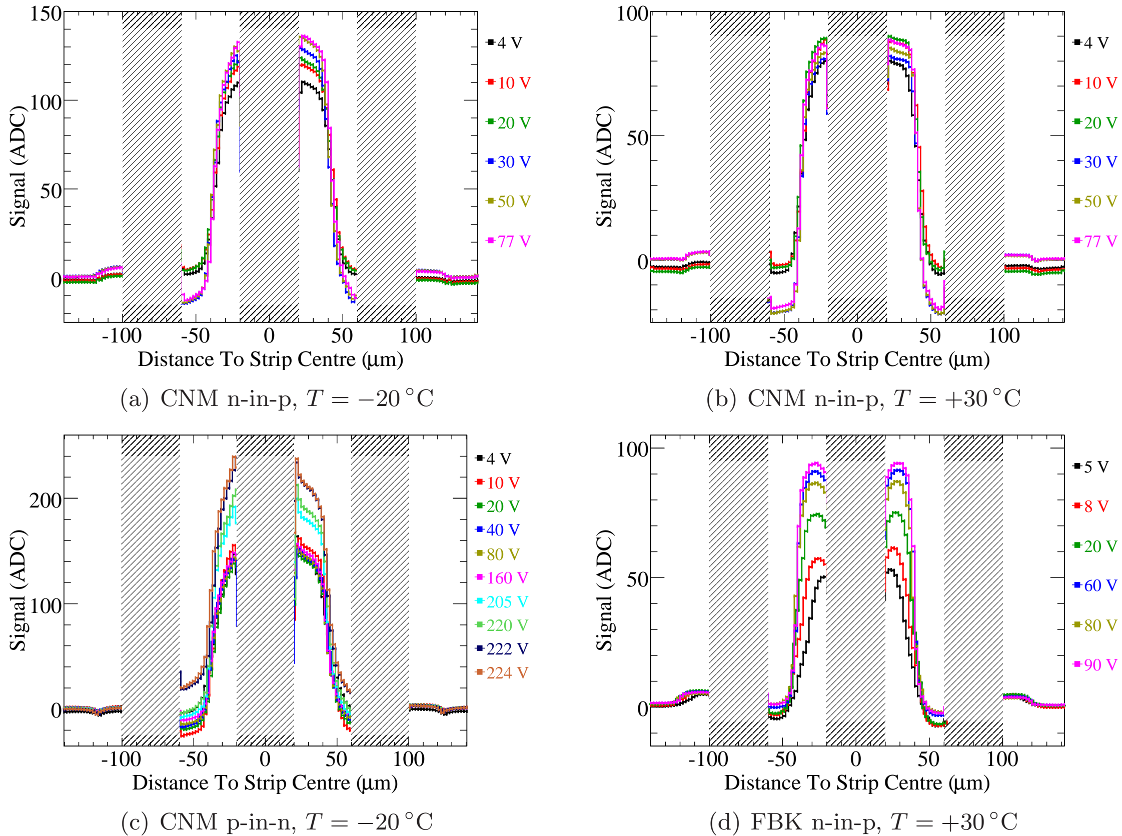

(a) CNM n-in-p, $T = -20\,^\circ$C

(b) CNM n-in-p, $T = +30\,^\circ$C

(c) CNM p-in-n, $T = -20\,^\circ$C

(d) FBK n-in-p, $T = +30\,^\circ$C

Figure 6.25: Single strip signals as a function of the distance between the laser point of incidence and the readout strip centre. The signals are averaged over laser impact positions along the direction of the readout strips. The hatched regions correspond to the strip metallisations, these cannot be investigated with the laser measurements.

p-in-n detectors, it can be clearly seen that the transition between high and low signals occurs further away from the strip if the laser impinges on the right hand side of the strip. An asymmetry is also apparent for the negative signals, which are measured if the laser impinges between approximately $40\,\mu$m and $60\,\mu$m away from the strip centre. These asymmetries are ascribed to the displacements of the ohmic columns from the nominal positions in the middle between the strips (see above).

The CNM n-in-p detector was measured at a temperature of $-20\,^\circ$C (Fig. 6.25(a)) and at a temperature of $+30\,^\circ$C (Fig. 6.25(b)). Due to the temperature dependence of the Beetle chip gain on the temperature, the absolute signals measured at a higher temperature are lower. However, it is visible that the negative signals, compared to the positive signals in the same measurement, are more pronounced at low temperatures (see also the discussion of Fig. 6.23).

If the laser approaches the strip metallisations, the signal of the CNM detectors increases, whereas the signal of the FBK detector decreases. As mentioned above, this can result from a different reflectivity close to the metallisation edges, possibly due to different pas-

sivation structures. The CNM n-in-p detector and the FBK n-in-p detector exhibit strong positive signals if the laser impinges far away (more than 100 µm) from the readout strip centre. These signals are more pronounced than those induced by high-energy particles impinging on the same sensor regions, as visualised in Fig. 6.5. It is assumed that these signals originate from charge carriers generated in the upper regions of the detector. The charge carriers are not collected by the readout strip under consideration, however, a current is induced due to a nonzero weighting field. High-energy particles cause ionisation uniformly in the sensor, whereas the absorption of the laser photons takes place mainly in the upper sensor regions. As it is the case for negative signals discussed in detail above, these positive signals on far neighbours are believed to originate from ballistic deficit. The fast positive component of the induced current is integrated by the shaping amplifier, whereas the negative component of the pulse occurs too late and cannot be integrated.

6.2 Measurements After Irradiation

6.2.1 Punch-Through Biasing Problems in FBK Detectors

In the 2009 beam test, FBK 3D n-in-p detectors irradiated to fluences of 1×10^{15} n_{eq}/cm^2 and 3×10^{15} n_{eq}/cm^2 were measured. While an unirradiated detector of the same detector design showed good performance (see Section 6.1.1), the data of the irradiated FBK devices could not be analysed. The signal was not large enough to achieve a clear separation from the detector noise, hence no alignment and no analysis could be performed. These observations could be traced back to problems of the detectors' biasing structures.

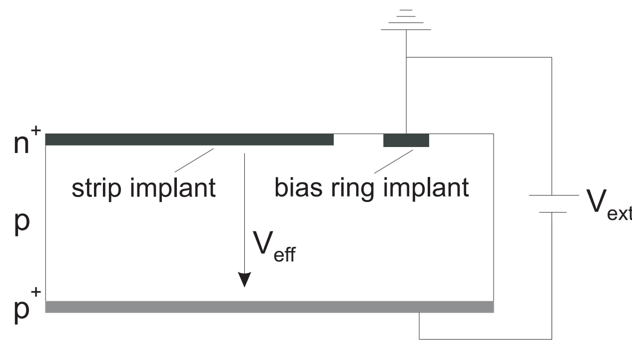

Figure 6.26: Cross-sectional view of a strip detector parallel to the strip direction. A punch-through channel evolves between the strip implant and the bias ring. Columnar electrodes and AC-coupling structures are not shown. The external voltage V_{ext} is applied between the bias ring and the sensor backplane. V_{eff} is the effective voltage between the strip implant and the backplane.

The strip implants of the FBK detectors are biased by means of a punch-through structure [Lut99, Ros06], which is realised as a gap between the strip implant and the bias ring, see Fig. 6.26. Punch-through biasing has the advantage of requiring less space on the sensor and fewer processing steps than the implementation of bias resistors. In contrast to the FBK detectors, the 3D detectors produced by CNM do not have any biasing structures. The strips are connected to an AC-coupled fanin, which connects the readout strips to a common bias line by means of bias resistors (see Sec.5.1.1).

Commonly, the bias ring is kept on ground potential while a non-zero potential is applied to the sensor backplane. With increasing external bias voltages, the depletion zone around the bias ring grows and reaches the intrinsic depletion zone around the strip implants at the punch-through voltage. From this voltage onwards, the strip potential follows the bias ring potential with a certain offset. It is desired to keep the punch-through voltage small so that the potential of the strip implant is close to ground potential. This assures that the effective bias voltage V_{eff} between the strip and the sensor backplane is close to the external bias voltage V_{ext}, which is applied between the bias ring and the sensor backplane (see Fig. 6.26). It was found that this requirement was not fulfilled for the FBK 3D n-in-p detectors tested in the 2009 beam test.

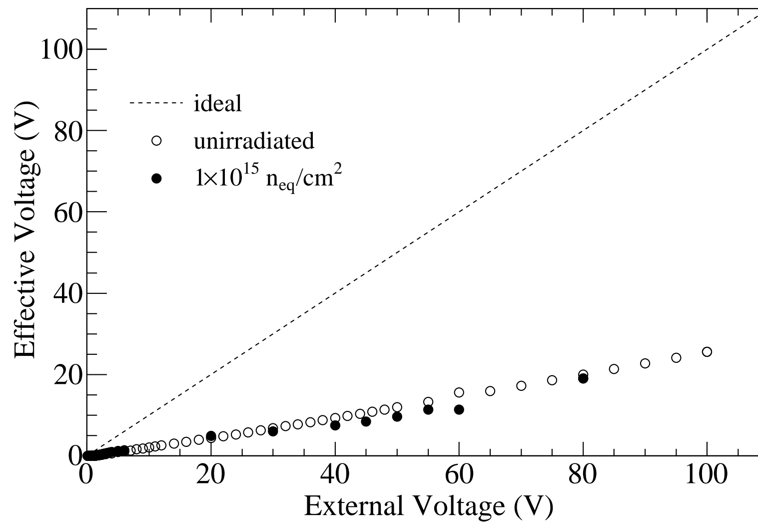

Figure 6.27: Measurement of the effective voltage between the strip and the sensor backplane as a function of the external voltage. The dashed line shows the ideal behaviour, for which the effective voltage is equal to the external voltage.

Figure 6.27 shows measurements of the effective bias voltage as a function of the external bias voltage. The effective voltage could be measured by contacting the DC pads of the strips and the detector back contact. Ideally, the effective voltage should coincide with the external bias voltage. The ideal behaviour is illustrated by the dashed line. However, the effective voltage stays well below this level for both the unirradiated detector and the detector irradiated with a fluence of $1 \times 10^{15}\,\mathrm{n_{eq}/cm^2}$. In both cases, the effective voltage reaches only approximately 25% of the external voltage. The remainder, 75% of the applied voltage, drops over the punch-through structure.

The maximum bias voltages applied to the detectors irradiated to $1 \times 10^{15}\,\mathrm{n_{eq}/cm^2}$ and $3 \times 10^{15}\,\mathrm{n_{eq}/cm^2}$ were 110 V and 130 V, respectively. Higher voltages could not be applied as they would lead to electrical breakdown of the devices. Due to the voltage drop over the punch-through structure, the maximum effective bias voltages between the strips and the sensor backplane were only 28 V and 33 V, respectively. These voltages were too low to measure any appreciable signal. Therefore, the large voltage drop is assumed to be the reason why the beam test measurements of the irradiated FBK detectors could not be analysed. In an unirradiated state, sufficiently high effective voltages could be achieved, despite the sizeable voltage drop over the punch-through structure.

The problem of the punch-through biasing structure could be understood and reproduced using device simulations [Pov11]. A strong coupling between the p^+-doped ohmic columns, which extend into the substrate from the sensor backplane, and the p-spray implantation cause the strip potential to follow the potential on the backplane more than the bias ring potential. The presence of p-spray between the ends of the strips and the bias ring, where the punch-through mechanism is expected to occur, further increases the potential drop between the strips and the bias ring. The interpretation that the problem is related to the

presence of p-spray is substantiated by the fact that FBK 3D p-in-n detectors, which were produced in a similar design, could be successfully measured after irradiation [Zob08b]. Those detectors do not have p-spray implantations, as additional strip isolation structures are not required in detectors with p-side readout (see Section 4.1.1). The problems of the punch-through biasing structures are expected to be overcome in a new design, which features a reduced gap between the strip and the bias ring [Pov11].

6.2.2 Beam Test Measurements

Beam test measurements with high-energy pions passing through irradiated 3D detectors were performed in 2009. Detectors produced by CNM and FBK were studied, however, the FBK detectors were affected by a failure of the punch-through biasing structure (see Section 6.2.1). Therefore, the discussion in this section is limited to the results obtained with the CNM detectors. The devices under test are three identical CNM n-in-p detectors. In addition to an unirradiated detector, two devices irradiated with different fluences ($1 \times 10^{15}\,\mathrm{n_{eq}/cm^2}$ and $2\times10^{15}\,\mathrm{n_{eq}/cm^2}$) were measured. The results of the unirradiated detector (CNM09) are described in Section 6.1.1. The amount of data collected for each sensor was considerably lower in the 2009 beam test than in the 2008 beam test. Therefore, high-resolution investigations of the space-resolved charge collection and efficiency as performed for the unirradiated detectors (see Section 6.1.1) are not possible. The results of the 2009 beam test measurements are published in [Kö11a].

Signal

The signal of the detectors is calculated by applying a traditional clustering algorithm as explained in Section 6.1.1 (clustering strategy 8). In the following investigation, tracks having impact positions across the entire sensor surfaces are considered.

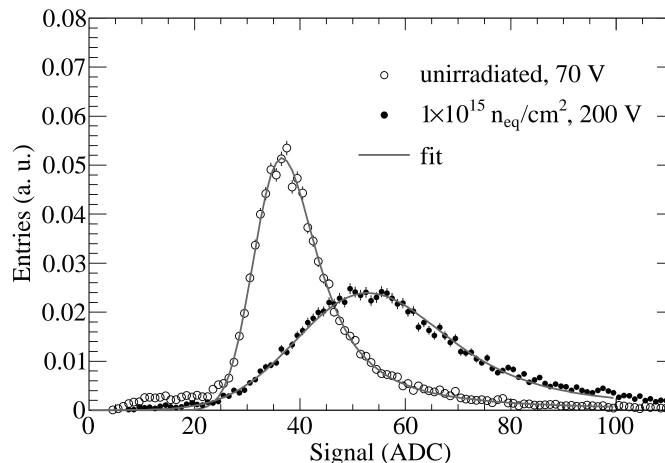

Figure 6.28: Normalised signal distributions for the unirradiated detector (measured at a bias voltage of 70 V) and the detector irradiated with a fluence of $1 \times 10^{15}\,\mathrm{n_{eq}/cm^2}$ (measured at a bias voltage of 200 V). The fit superimposed is a convolution of a Landau function and a Gaussian. The signals are given in ADC counts.

Figure 6.28 shows a comparison of the signal distributions measured with the unirradiated detector and the detector irradiated with a fluence of $1 \times 10^{15}\ \mathrm{n_{eq}/cm^2}$. A fit of a convolution of a Landau function and a Gaussian is superimposed and describes the spectra well. The data of the unirradiated detector were measured at a bias voltage of 70 V, which is the highest voltage applied to this sensor. The most probable value of the Landau function is $(22.9 \pm 1.8)\,\mathrm{ke^-}$, which corresponds to the signal expected for the given thickness of 285 µm (see also the discussion in Section 6.1.1). The spectrum of the detector irradiated to $1 \times 10^{15}\ \mathrm{n_{eq}/cm^2}$ has a higher most probable value and a larger width than the spectrum of the unirradiated detector. The most probable signal, extracted from the fitted Landau function, is $(30.2 \pm 2.3)\,\mathrm{ke^-}$

In addition to higher noise, the broadening of the spectrum of the irradiated detector is caused by a strong common mode contribution which could not be completely subtracted and effectively increases the measured noise (see Section 5.5.2). A further broadening is caused by the dependence of the signal on the track impact position, as will be discussed below. The lower tail of the distribution, below approximately 25 ADC, is caused by tracks going directly through the passive columns and therefore leading to lower signal (see Section 6.1.1).

The fact that more charge is measured than liberated by the penetrating particle can be attributed to charge multiplication due to impact ionisation. Indications for charge multiplication in irradiated 3D p-in-n silicon strip detectors produced by FBK were also observed in measurements using a radioactive source and an infrared laser setup [Zob08b]. In Section 6.2.3 and Section 6.2.6, charge multiplication of irradiated double sided 3D detectors produced by CNM is investigated with beta source and laser measurements. An observation of charge multiplication in an unirradiated CNM p-in-n double-sided 3D detector is discussed in Section 6.1.2.

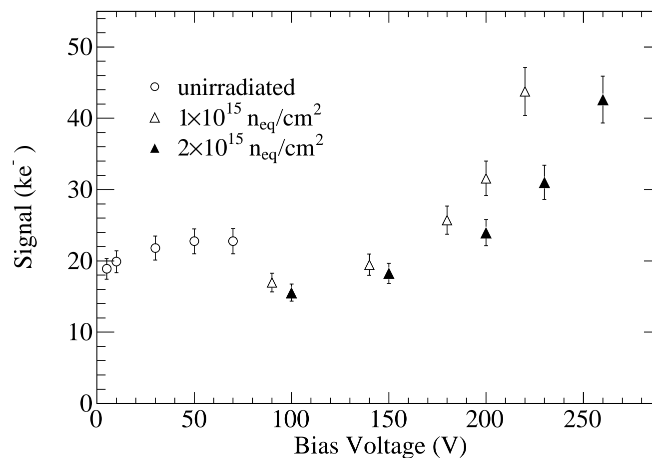

Figure 6.29: Signal as a function of the applied bias voltage for different detectors irradiated with different fluences.

Figure 6.29 summarises the signal as a function of the applied bias voltage for the investigated detectors. All signals reflect the most probable value of a Landau function

calculated by a fit as shown in Fig. 6.28. The signals measured with the irradiated 3D detectors exceed the signal of the unirradiated detector and increase strongly for voltages above approximately 150 V. At the highest bias voltages applied, 220 V for the sensor irradiated to $1 \times 10^{15}\, n_{eq}/cm^2$ and 260 V for the sensor irradiated to $2 \times 10^{15}\, n_{eq}/cm^2$, the signal is approximately twice as high as the signal of the unirradiated sensor. Due to an increased effective doping concentration and an increased trapping probability, the detector irradiated to $2 \times 10^{15}\, n_{eq}/cm^2$ requires higher voltages to yield the same signal magnitude as the detector irradiated to $1 \times 10^{15}\, n_{eq}/cm^2$.

These measurements provide evidence that the radiation-induced increase of the effective doping concentration leads to electric field strengths sufficiently high for strong charge multiplication. This effect has also been observed with highly irradiated planar silicon strip detectors [Man10], [Cas11b], [Kra10b] and epitaxial silicon pad detectors [Lan10] (see also Section 4.3.5). In planar detectors, charge multiplication requires higher voltages due to a larger spacing between the electrodes. The specific geometry and the short distance of about 50 µm between junction columns and ohmic columns in the 3D detectors investigated here leads to a high electric field and therefore to strong charge multiplication already at comparatively low voltages.

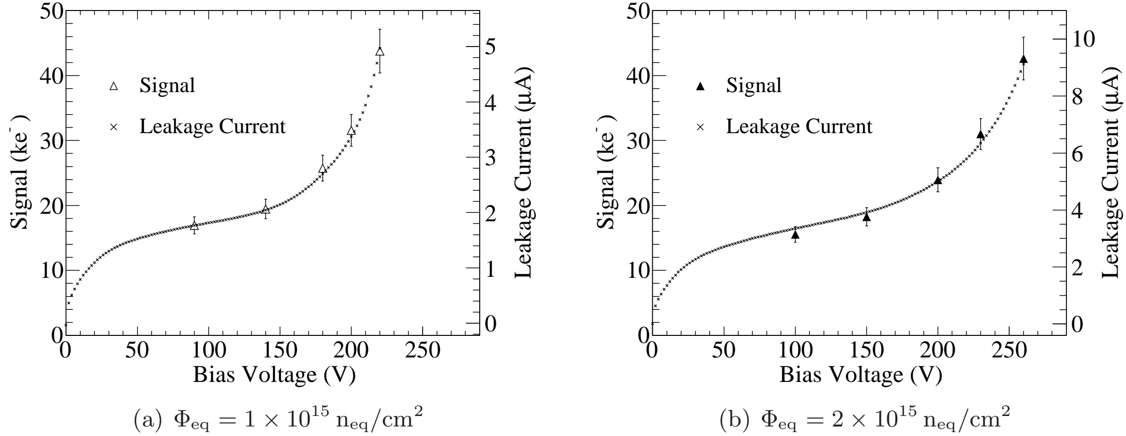

(a) $\Phi_{eq} = 1 \times 10^{15}\, n_{eq}/cm^2$ (b) $\Phi_{eq} = 2 \times 10^{15}\, n_{eq}/cm^2$

Figure 6.30: Overlay of the measured signal and the leakage current, (a) for the 3D detector irradiated to $1 \times 10^{15}\, n_{eq}/cm^2$ and (b) for the 3D detector irradiated to $2 \times 10^{15}\, n_{eq}/cm^2$. The leakage current was measured at $-20\,°C$.

The measured signal and the leakage current of the irradiated 3D detectors are strongly correlated, as shown in Fig. 6.30. The measurements of the leakage current were performed at approximately $-20\,°C$ and reflect the current drawn by all strips, as the current flowing through the guard ring has been subtracted. The guard ring current accounted for 10%-15% of the total current. After tending to saturate at about 50 V, the leakage current increases strongly above 150 V, in agreement with the signal curves. Around 150 V, where the curve of the leakage current has the weakest slope, the current of the detector irradiated with a fluence of $2 \times 10^{15}\, n_{eq}/cm^2$ is approximately twice as high as the current of the detector irradiated to $1 \times 10^{15}\, n_{eq}/cm^2$. This agrees with the expectation that the leakage current in fully depleted irradiated detectors is proportional to the irradiation fluence (cf.

Section 4.3.2).

The correlation between the leakage current and the signal shows that charge carriers generated both by traversing particles and by thermal excitation are multiplied by the same factor if the electric field is sufficiently high. This confirms that charge multiplication due to impact ionisation leads to the higher signal of irradiated detectors compared to unirradiated ones. These studies are currently the only beam test measurements in which charge multiplication in highly irradiated silicon tracking detectors could be conclusively observed. Other studies were made with radioactive sources and laser measurements [Man10, Cas11b, Lan10, Kra10b]

Space-Resolved Signal

The path of liberated charge carriers drifting towards the electrodes depends strongly on the impact position of the particle track. Both the drift length and the electric field along the drift path are affected by the position where the charge carriers are created. The electric field and the drift length can influence the probability of trapping and charge multiplication. Therefore, it is interesting to investigate the dependence of the signal on the track point of incidence.

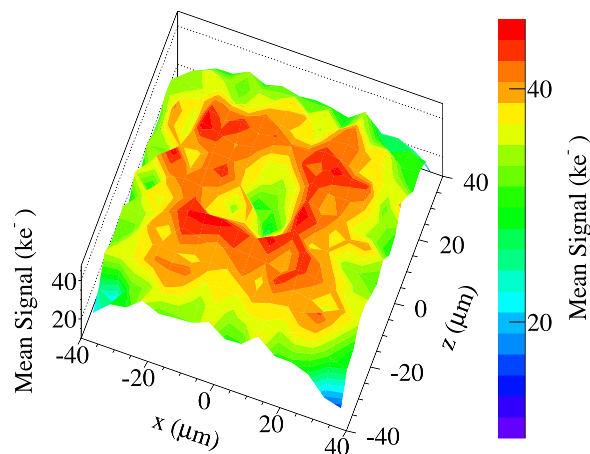

Figure 6.31: Two-dimensional representation of the signal height as a function of the track point of incidence, superimposed onto one unit cell. The measurement was performed with the detector irradiated to $2 \times 10^{15}\,\mathrm{n_{eq}/cm^2}$ at a bias voltage of 230 V. The junction column is centred at (0,0). In each corner, one quarter of the ohmic column is visible. The readout strip is running parallel to the z-coordinate at $x = 0\,\mu\mathrm{m}$.

As in Fig. 6.8, Section 6.1.1, the illustration in Fig. 6.31 shows the mean charge as a function of the track point of incidence in a unit cell of the detector. A measurement performed with the sensor irradiated to $2 \times 10^{15}\,\mathrm{n_{eq}/cm^2}$ at a bias voltage of 230 V was selected, since for this measurement the highest statistics are available. In contrast to the other considerations in this section, which apply the clustering strategy 8 (see Section 6.1.1), the signal shown in Fig. 6.31 was calculated using the clustering strategy 3.

Since the clustering algorithm of strategy 8 employs a seed cut, it is possible that tracks, which pass directly through the columns and deposit less energy, would be disregarded for the analysis. In order to include also these signals, strategy 3 was chosen, which does not apply any signal cut.

It is apparent from Fig. 6.31 that tracks impinging close to the junction columns induce higher signals than tracks impinging elsewhere. The measurement was performed at a bias voltage of 230 V, hence strong charge multiplication takes place, as discussed in Section 6.2.2. The signal distribution is considerably less uniform than that of the unirradiated detectors (see Section 6.1.1). However, the statistics acquired during the 2009 beam test is not sufficient to perform a detailed two-dimensional investigation of the dependence of the signal on the track impact point.

To get a more quantitative view, the Landau most probable signals induced by tracks impinging on different regions of the sensor are investigated separately. As discussed in Section 5.1.1, distinctly high electric fields are present close to the columns and on the direct line between an ohmic column and a junction column. Minima of the electric fields are present in the middle of the rectangle spanned by two junction columns and two ohmic columns (see Fig. 5.4, Section 5.1.1, and Fig. 6.16, Section 6.1.2). Charge carriers liberated in the regions shown in Fig. 6.32(a) experience relatively low electric fields during their drift, whereas the field is considerably higher for charge carriers generated in the regions illustrated in Fig. 6.32(b). Tracks impinging on the low-field regions located at the left and right margins of the unit cell (see Fig. 6.32(a)) lead to higher charge sharing between neighbouring readout strips. As the effects of charge sharing should be separated from the following discussion, these tracks are not considered for the following investigation.

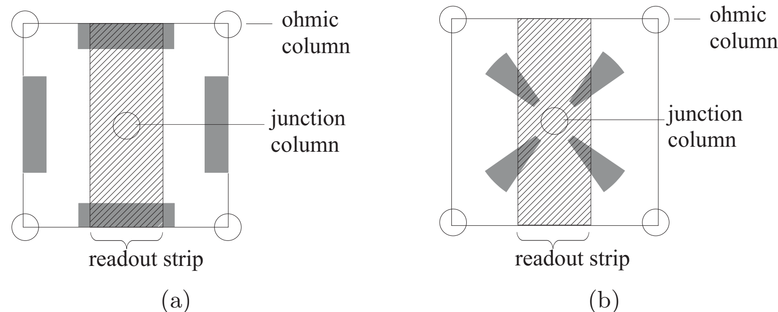

Figure 6.32: Sketch of the unit cell of a 3D detector with the readout strip, represented as the hatched region, running vertically. In (a) regions with low electric field and in (b) regions with high electric field are shown as grey shaded areas (see text).

While the signals for tracks impinging in the two distinct regions do not differ in the unirradiated 3D detector, substantial differences are measured for the irradiated sensors. The Landau most probable signals of tracks impinging on the high-field region and the low-field region are shown as a function of the applied bias voltage in Fig. 6.33 for the 3D detectors irradiated to $1 \times 10^{15}\,\mathrm{n_{eq}/cm^2}$ and $2 \times 10^{15}\,\mathrm{n_{eq}/cm^2}$. Results from the measurements at lower voltages are not included as the limited number of tracks does not allow a statistically significant investigation. A difference of the signals measured for tracks impinging

in the distinct regions can be clearly identified. Charge carriers generated in both regions evidently undergo charge multiplication. The results indicate that the multiplication takes place only in a thin region around the junction column. Otherwise a higher multiplication for charge carriers generated in the low-field region, which have a longer drift path, would be expected.

Several effects lead to the observed signal non-uniformity. In the low-field region the charge carriers have longer drift distances and lower drift velocities, which leads to a higher trapping probability. Furthermore, as the charge multiplication coefficients exhibit a strong dependence on the electric field (see Section 3.3.7), the charge carriers drifting along a path with a higher electric field have a larger probability of being multiplied. The difference between the signals in the distinct regions increases with increasing voltage.

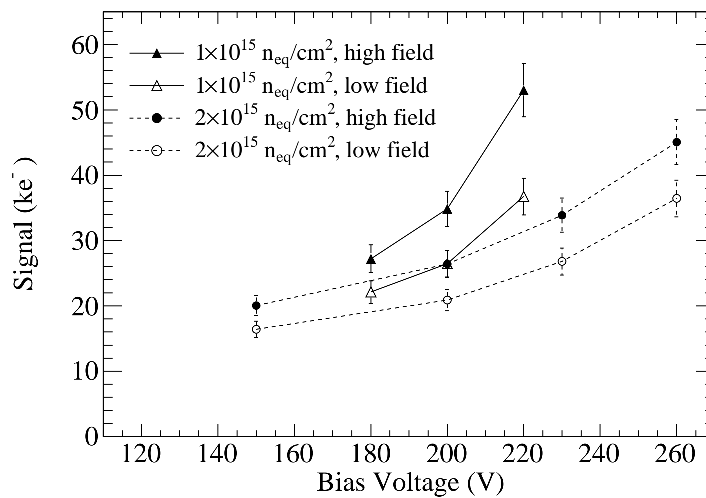

Figure 6.33: Signals for tracks impinging in the regions with low and high electric field as a function of the applied bias voltage for the 3D detectors irradiated to $1 \times 10^{15}\,\mathrm{n_{eq}/cm^2}$ and $2 \times 10^{15}\,\mathrm{n_{eq}/cm^2}$. The lines connecting the data points are shown to guide the eye.

Spatial Resolution

To assess the tracking capabilities after irradiation, the spatial resolution is investigated. The standard deviation of the residuals between the track location determined by the devices under test and the beam telescope quantifies the spatial resolution. If the charge deposited by impinging particles is not shared between adjacent strips, the spatial resolution of a detector having a pitch p is expected to coincide with the binary resolution $\sigma_{\mathrm{bin}} = p/\sqrt{12}$. For the CNM 3D detectors investigated here, which have a pitch of 80 µm, the binary resolution is 23.1 µm. When the liberated charge carriers are collected by more than one readout strip, the resolution can be further improved. Charge sharing can be used to interpolate the track impact position between two neighbouring strips.

For each event the seed strip is determined as the strip having the highest signal-to-noise ratio among the strips which the track is pointing to and its direct neighbours on either side of the track position. Accordingly, the highest neighbour of the seed strip is determined.

If the signal-to-noise ratio of this strip exceeds 3, the event is regarded as a multiple-strip event and charge sharing is exploited for the calculation of the track position. The track position measured by the device under test is given by the charge weighted mean between the seed strip and its highest neighbour. If both neighbours of a seed strip have signal-to-noise ratios below 3, the event is regarded as a single-strip event. In this case, the track position is given by the centre of the seed strip. Events are excluded if the strip which the track is pointing to or one of its direct neighbours is dead or has extraordinarily high noise.

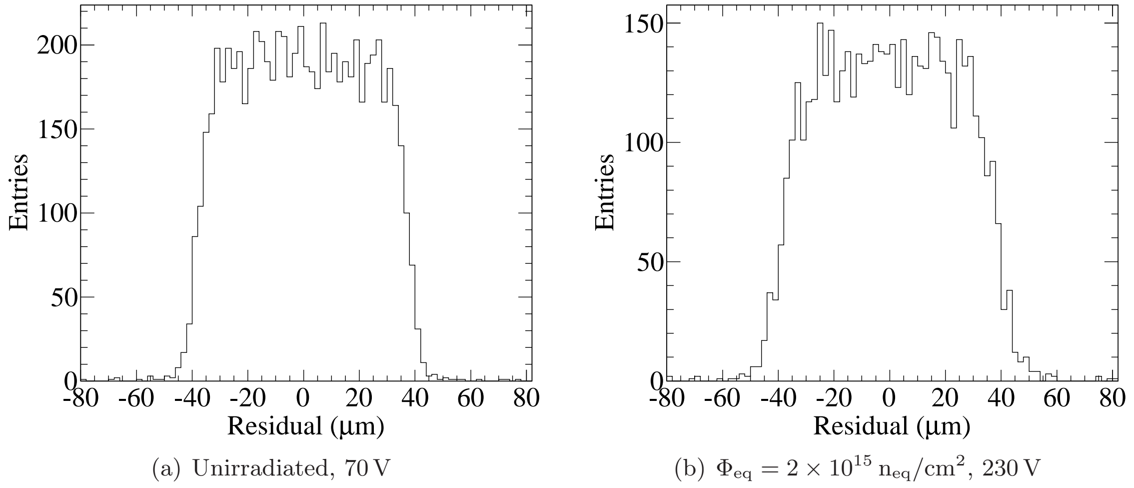

(a) Unirradiated, 70 V

(b) $\Phi_{eq} = 2 \times 10^{15}\ \mathrm{n_{eq}/cm^2}$, 230 V

Figure 6.34: Residuals between the track position measured by the device under test and the track position determined by the beam telescope: (a) unirradiated detector (bias voltage 70 V), (b) detector irradiated to $2 \times 10^{15}\ \mathrm{n_{eq}/cm^2}$ (bias voltage 230 V).

Figure 6.34 shows the residual distributions of the unirradiated sensor and the sensor irradiated to $2 \times 10^{15}\ \mathrm{n_{eq}/cm^2}$. The measurements were performed with a bias voltages of 70 V and 230 V, respectively. For these voltages the highest statistics are available. The spatial resolution is given by the standard deviations of these distributions. Due to the limited statistics remaining for the 3D sensor irradiated to $1 \times 10^{15}\ \mathrm{n_{eq}/cm^2}$, after excluding noisy or dead channels and their neighbours, the interpolation of the track position could not be exploited. Hence this detector was excluded from the analysis of the spatial resolution.

The resolution as a function of applied bias voltage is shown in Fig. 6.35 for the unirradiated detector and the detector irradiated to $2 \times 10^{15}\ \mathrm{n_{eq}/cm^2}$. The track extrapolation uncertainty, which is approximately 4 μm and dominated by the telescope resolution (see Section 5.5.1), was not subtracted. Statistical errors are indicated. The resolution measured with the unirradiated 3D detector at a bias voltage of 70 V is (22.2 ± 0.2) μm. Therefore, the binary resolution of 23.1 μm can be slightly improved using the information of charge sharing. The detector irradiated to $2 \times 10^{15}\ \mathrm{n_{eq}/cm^2}$ yields a resolution of (23.4 ± 0.4) μm at a bias voltage of 260 V, which is somewhat worse than for the unirradiated sensor but still in agreement with the binary resolution. The resolution degrades slightly after irradiation. However, the increasing influence of charge multiplication for voltages higher than approximately 150 V does not negatively affect the resolution. Within the error margins, the resolution determined for the 3D detector irradiated to $2 \times 10^{15}\ \mathrm{n_{eq}/cm^2}$ does not

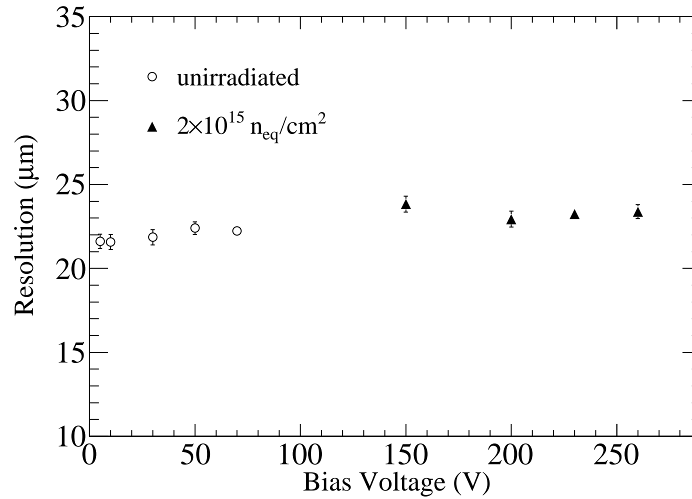

Figure 6.35: Spatial resolution versus applied bias voltage of the unirradiated detector and the detector irradiated with a fluence of $2 \times 10^{15}\,\mathrm{n_{eq}/cm^2}$.

depend on the bias voltage in the voltage range shown.

Due to more pronounced charge sharing, a better spatial resolution can be obtained with planar detectors. This is expected from the charge sharing studies presented in Section 6.1.1. With the method described above, a resolution of approximately $(16.7 \pm 0.2)\,\mu\mathrm{m}$ has been calculated for planar detectors having a readout pitch of $74.5\,\mu\mathrm{m}$ [Kö11a]. For the given readout pitch, the binary resolution is $21.5\,\mu\mathrm{m}$. Hence, the improvement of the resolution using the information of charge sharing is larger than for 3D detectors.

Efficiency

The detection efficiency for a threshold of 1 fC is shown in Fig. 6.36. The efficiency is calculated for all tracks and for the tracks impinging at least $10\,\mu\mathrm{m}$ away from a column centre separately. The amount of data is not sufficient to perform a detailed space-resolved investigation of the efficiency as it was done for the data of the 2008 beam test (see Section 6.1.1). The calculation was made applying the clustering strategy 2 (see Section 6.1.1): a hit is considered as detected if the signal of at least one of the three strips around the track point of incidence is higher than the chosen threshold of 1 fC. A correction of charge sharing by summing up the signals of neighbouring strips is not performed on purpose. Hence, this approach is comparable to binary readout. The chosen threshold of 1 fC corresponds to the threshold which is typically applied for the binary readout of the ATLAS semiconductor tracker (SCT) [Aad08c]. Tracks impinging close to dead or noisy channels are excluded.

The total efficiency measured with the unirradiated detector at a bias voltage of 70 V is $(98.87 \pm 0.08)\%$. It can be seen in Fig. 6.36 that even higher efficiencies can be reached if only the tracks impinging far away from the columns are considered. The efficiency of the detector irradiated to a fluence of $2 \times 10^{15}\,\mathrm{n_{eq}/cm^2}$ does not show a strong degradation.

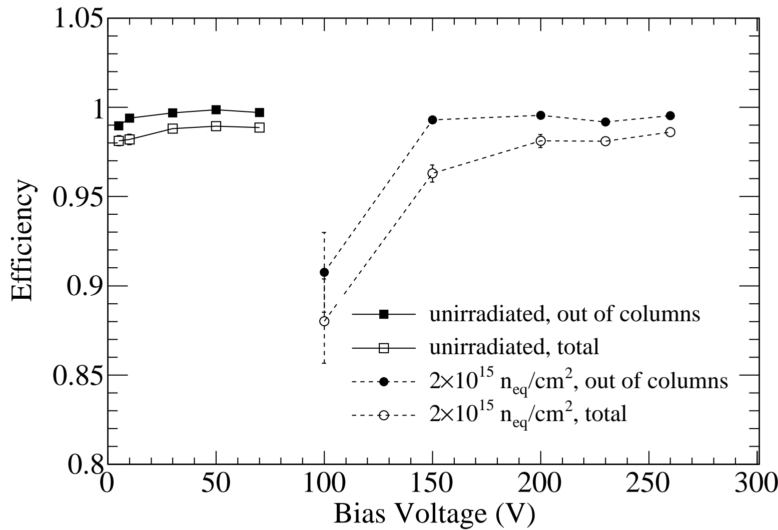

Figure 6.36: Efficiency for a threshold of 1 fC for the unirradiated detector and the detector irradiated with a fluence of $2 \times 10^{15}\,\mathrm{n_{eq}/cm^2}$. Open symbols represent the efficiency for all tracks, filled symbols illustrate the efficiency for tracks impinging at least 10 μm away from a column centre.

At a bias voltage of 260 V, a total efficiency of $(98.7 \pm 0.2)\%$ can be measured. Tracks impinging outside of the columns are detected with an efficiency of larger than 99%. The presence of the inactive column volume is expected to not reduce the detection efficiency significantly if the particle tracks do not impinge perpendicularly to the sensor surface. Such a configuration is already realised for the current silicon tracking detectors of the ATLAS experiment.

The onset of charge multiplication does not lead to a decrease of the efficiency. Charge multiplication leads to a broadening of the signal spectra (see the discussion above), however, the efficiency does not degrade when applying a fixed threshold.

6.2.3 Beta Source Measurements

Beta source measurements were performed with 3D detectors produced by CNM, both in n-in-p and p-in-n layouts. The detectors were irradiated with protons at the proton cyclotron in Karlsruhe (see Section 5.1.3). The equivalent irradiation fluences of the detectors are summarised in Table 6.2. The highest irradiation fluence, $2 \times 10^{16}\,\mathrm{n_{eq}/cm^2}$, corresponds to the fluence expected for the innermost pixel layer of the ATLAS detector at the LHC upgrade. Part of the results of the measurements reported in this section are published in Ref. [Kö11b].

Beta source measurements could be performed at lower temperatures than the beam test measurements and the temperature could be controlled in a wide range (see Section 5.3). Strong cooling of highly irradiated detectors is necessary due to the radiation-induced increase of the leakage current. Therefore, it was possible to investigate detectors irradiated with higher fluences than those studied in the beam test. Signal and noise measurements

Table 6.2: Irradiation fluences of the CNM n-in-p and p-in-n 3D detectors for which beta source measurements were performed.

	n-in-p	p-in-n
Fluence	1×10^{15}	
($\mathrm{n_{eq}/cm^2}$)	2×10^{15}	2×10^{15}
	5×10^{15}	
	2×10^{16}	2×10^{16}

were performed at different temperatures. One aim of the beta source measurements is to provide a direct comparison of the radiation hardness of 3D n-in-p and p-in-n detectors. In the case of planar detectors, p-in-n sensors are much less radiation-hard than sensors with n-side readout (n-in-p or n-in-n sensors), see Sections 4.3.5 and 4.4.2.

n-in-p Detectors

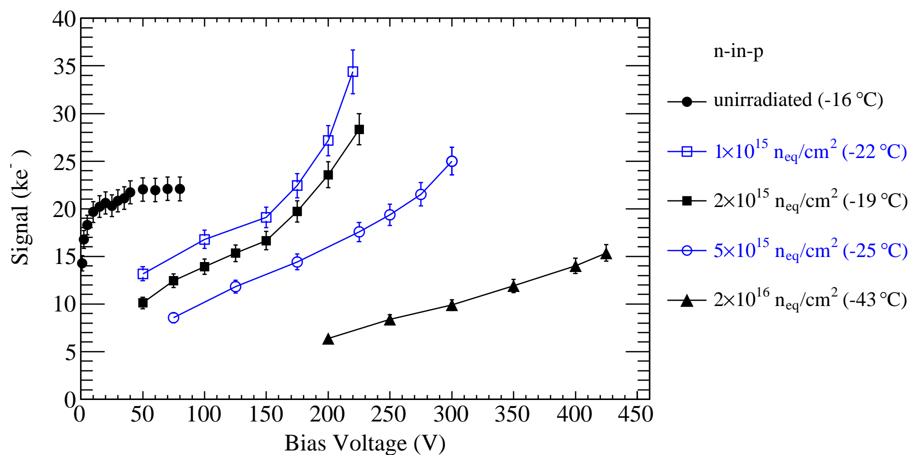

Figure 6.37: Beta source measurements: signal of the n-in-p detectors irradiated to different fluences as a function of the applied bias voltage. The data points are connected to guide the eye.

Figure 6.37 summarises the Landau most probable signals of the n-in-p detectors. The figure shows measurements performed at selected temperatures. The dependence of the measured signal on the operating temperature is discussed below. The measurement of the unirradiated detector shown in the illustration is discussed in Section 6.1.2. In agreement with the beam test measurements described in Section 6.2.2, the signal measured with the sensors irradiated to fluences of $1 \times 10^{15}\ \mathrm{n_{eq}/cm^2}$ and $2 \times 10^{15}\ \mathrm{n_{eq}/cm^2}$ increases strongly for bias voltages higher than 150 V. Due to charge multiplication, the signal of the unirradiated detector is exceeded at bias voltages between 175 V and 200 V. The signals measured with the detector irradiated with a fluence of $2 \times 10^{15}\ \mathrm{n_{eq}/cm^2}$ correspond to those measured in the beam test with a detector of the same fluence. However, the signal of the detector irradiated to $1 \times 10^{15}\ \mathrm{n_{eq}/cm^2}$ is somewhat lower than that measured in

the beam test. Given the uncertainty of the irradiation fluence of 20%, it is possible that the exact fluence was higher for the detector measured in the beta source setup. This assumption is supported by a comparison of the leakage currents of the detectors irradiated to fluences of $1 \times 10^{15}\,\mathrm{n_{eq}/cm^2}$ and $2 \times 10^{15}\,\mathrm{n_{eq}/cm^2}$ (see below). The leakage current of the detector irradiated with a fluence of $2 \times 10^{15}\,\mathrm{n_{eq}/cm^2}$ is less than a factor of two larger than that of the detector irradiated to $1 \times 10^{15}\,\mathrm{n_{eq}/cm^2}$. A factor of two would be expected for these fluences.

The signal of the detector irradiated with a fluence of $5 \times 10^{15}\,\mathrm{n_{eq}/cm^2}$ also increases beyond that of the unirradiated detector, however, the curve is flatter than those of the detectors discussed above. The signal measured with the detector irradiated with the highest fluence, $2 \times 10^{16}\,\mathrm{n_{eq}/cm^2}$, increases linearly with the applied bias voltage. At a voltage of 425 V, which was the maximum bias voltage applied, a signal of $(15.3 \pm 0.9)\,\mathrm{ke^-}$ is measured, corresponding to almost 70% of the signal measured with the unirradiated detector.

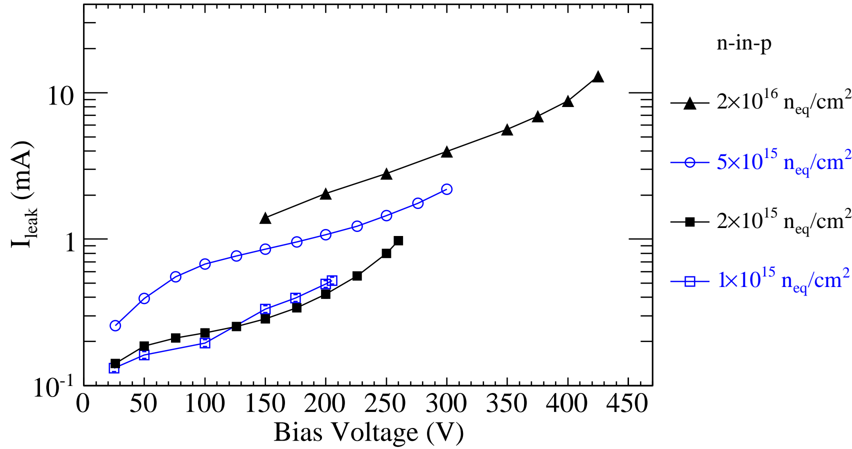

Figure 6.38: Leakage current of the irradiated n-in-p detectors, scaled to a temperature of +20 °C. The values include the guard ring current. The data points are connected to guide the eye.

The maximum bias voltages, for which the signal could be measured, were constrained by a strong increase of the leakage current or by an excessive increase of the noise at high bias voltages. The leakage current of all irradiated detectors increases strongly at high bias voltage, see below. The n-in-p detectors irradiated to $1 \times 10^{15}\,\mathrm{n_{eq}/cm^2}$, $5 \times 10^{15}\,\mathrm{n_{eq}/cm^2}$ and $2 \times 10^{16}\,\mathrm{n_{eq}/cm^2}$ exhibited an electrical breakdown slightly above the highest voltages included in Fig. 6.37. For the detector irradiated to $2 \times 10^{15}\,\mathrm{n_{eq}/cm^2}$, a strong noise increase rendered a separation of signal and noise impossible at higher bias voltages.

Figure 6.38 shows leakage current measurements of the irradiated n-in-p detectors. The values are scaled to a temperature of +20 °C using Eq. (3.14). The measurements reflect the total current drawn by all strips and the guard ring. As the guard ring current was not measured separately, it could not be subtracted. Therefore, it is possible that a significant amount of surface current contributes to the measured current. As mentioned

above, the current of the detectors irradiated with a target fluence of $1 \times 10^{15}\,\mathrm{n_{eq}/cm^2}$ and $2 \times 10^{15}\,\mathrm{n_{eq}/cm^2}$ differs less than expected. At high bias voltages, the current of the detector irradiated with a target fluence of $1 \times 10^{15}\,\mathrm{n_{eq}/cm^2}$ is even higher. However, the unknown contribution of the surface current does not allow to conclusively determine the irradiation fluences from the leakage current measurement.

p-in-n Detectors

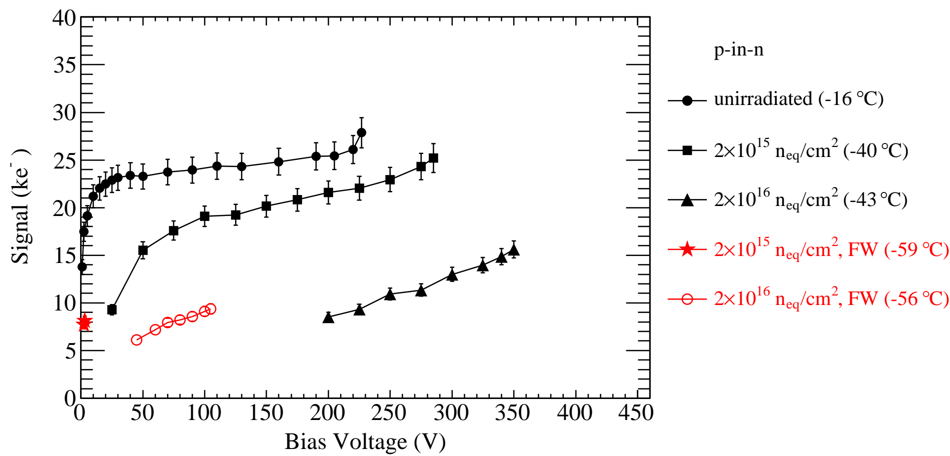

Figure 6.39: Beta source measurements: signal of the p-in-n detectors as a function of the applied bias voltage. The signals measured with forward bias ("FW") are shown in red. The error is dominated by a systematic error due to the calibration uncertainty. The data points are connected to guide the eye.

The signal measurements of the irradiated p-in-n detectors are summarised in Fig. 6.39. The signal of the detector irradiated to a fluence of $2 \times 10^{15}\,\mathrm{n_{eq}/cm^2}$ increases strongly with increasing bias voltage up to approximately 75 V. At higher bias voltages, it increases moderately and finally reaches the signal measured with the unirradiated detector before the onset of charge multiplication. It can be assumed that charge multiplication contributes to the signal increase at high bias voltages. An electrical breakdown of a voltage of approximately 290 V does not allow to apply higher bias voltages. Compared to the n-in-p detector irradiated to the same fluence, the signal curve of the p-in-n detector is visibly flatter and the effect of charge multiplication is less pronounced.

The signal measured with the p-in-n detector irradiated with a fluence of $2 \times 10^{16}\,\mathrm{n_{eq}/cm^2}$ increases linearly as a function of the applied bias voltage. The shape of the signal curve is similar to the n-in-p detector irradiated to the same fluence. At the maximum bias voltage, a signal of $(15.6 \pm 0.9)\,\mathrm{ke^-}$ is measured, which is in agreement with that of the n-in-p detector. The p-in-n sensor irradiated to $2 \times 10^{16}\,\mathrm{n_{eq}/cm^2}$ could be measured up to a bias voltage of 350 V. At higher bias voltages, a strong increase of the noise renders a separation of signal and noise impossible. The n-in-p detector irradiated to $2 \times 10^{16}\,\mathrm{n_{eq}/cm^2}$ requires higher bias voltages to yield the same signal as the p-in-n detector irradiated to

the same fluence.

The irradiated p-in-n detectors were also measured in forward bias mode. The concept of silicon detector operation under forward bias is discussed in Section 4.4.4. The measured signals are included in Fig. 6.39. The maximum signals measured in forward bias operation are considerably lower than those measured in reverse bias. The maximum signal in forward bias mode of the detector irradiated to $2 \times 10^{16}\,\mathrm{n_{eq}/cm^2}$ is $(9.3 \pm 0.6)\,\mathrm{ke^-}$. However, this signal is already measured at a bias voltage of 105 V, whereas a bias voltage of 225 V is required to measure the same signal in reverse bias mode. Due to a strong increase of the leakage current (see Fig. 6.40), the measurements in forward bias were not performed at higher voltages. A strong cooling of the detectors was required to achieve acceptable leakage current levels. The measurements were performed at $-59\,^\circ\mathrm{C}$ and $-56\,^\circ\mathrm{C}$ for the detectors irradiated to $2 \times 10^{15}\,\mathrm{n_{eq}/cm^2}$ and $2 \times 10^{16}\,\mathrm{n_{eq}/cm^2}$, respectively.

Figure 6.40 shows the leakage current of the p-in-n sensors as a function of the applied bias voltage. The values are scaled to a temperature of $+20\,^\circ\mathrm{C}$ and contain the current drawn by the sensor strips and the guard ring. As for the n-in-p sensors, a saturation of the currents is not observed. However, the leakage current of the p-in-n detector irradiated to a fluence of $2 \times 10^{15}\,\mathrm{n_{eq}/cm^2}$ is much flatter in a wide range than that of the n-in-p detector irradiated to the same fluence. The leakage current increases only moderately up to bias voltages of approximately 250 V and exhibits a strong increase only at higher voltages. This is in agreement with the signal curve, which is also much flatter than that of the n-in-p detector irradiated to the same fluence. The strong increase of the leakage current at voltages above 250 V is assumed to be related to charge multiplication, which also leads to an increase of the signal at these voltages.

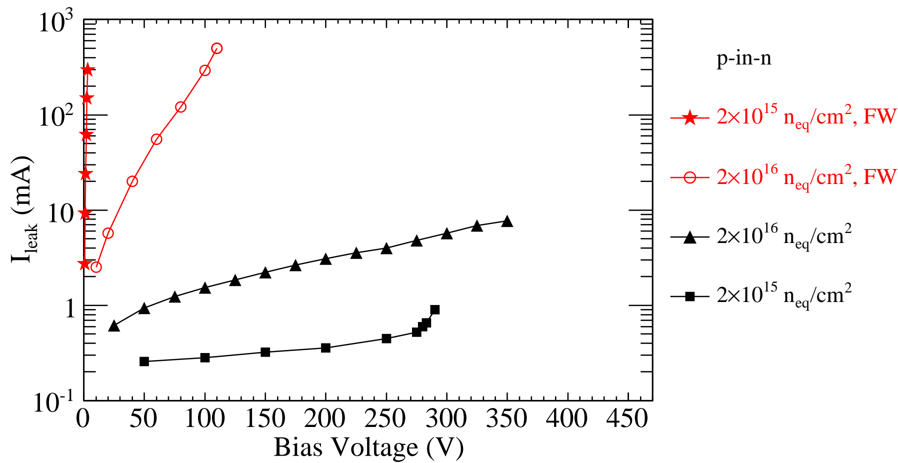

Figure 6.40: Leakage current of the irradiated p-in-n detectors, scaled to a temperature of $+20\,^\circ\mathrm{C}$. The values include the guard ring current. The leakage current measured in forward bias mode ("FW") is shown in red. The data points are connected to guide the eye.

Conclusion

The results presented above prove a superior radiation hardness of 3D detectors compared to planar detectors in terms of the most probable signal. After the highest irradiation fluence studied ($2 \times 10^{16}\,n_{eq}/cm^2$), a signal of approximately $15\,ke^-$ could be measured with the 3D detectors. This is more than twice as high as the signal of approximately $7\,ke^-$ measured with planar n-in-p detectors [Cas11b] irradiated with the same fluence. The voltages required to achieve these signals were much higher for the planar sensors, which leads to higher power consumption. Due to the short distance between the columnar electrodes, the drift distances are shorter and the electric fields are higher in 3D detectors. These effects limit the trapping probability of drifting charge carriers and enhance the charge multiplication probability.

Based on measurements of trapping of drifting charge carriers, the expected signal in highly irradiated detectors can be estimated (see Eq. 4.18, Section 4.3.3). For an irradiation fluence of $2 \times 10^{16}\,n_{eq}/cm^2$, an expected signal of $1.5\,ke^-$ can be calculated. As this model relies on a uniform weighting field distribution as in planar pad detectors, it can only serve as an estimation. However, the observation that remarkably larger signals are measured points to the fact that the signal is considerably enhanced by charge multiplication or by trap-to-band tunnelling [Ben10, Hur92] (see also Section 4.3.3) in regions with high electric field strengths.

A further very important result is the observation that the maximum signals of the n-in-p and p-in-n 3D detectors irradiated to $2 \times 10^{16}\,n_{eq}/cm^2$ are equal. For planar sensors the situation is different: segmented planar sensors (strip or pixel detectors) with n-side readout are much more radiation hard than planar detectors with p-side readout (see Section 4.4.2). The production of p-in-n detectors requires less processing steps, as no p-spray or p-stop isolation structures are required. Therefore, p-in-n detectors are cheaper than n-in-p or n-in-n detectors.

In planar strip or pixel sensors, the signal is dominated by the type of charge carriers which are accelerated towards the readout electrodes, as the weighting field exhibits a strong peak close to these electrodes (see Section 3.3.6). In 3D detectors, however, the weighting field has maxima close to both the junction columns and the ohmic columns, see Fig. 5.6, Section 5.1.1. Therefore, both electrons and holes contribute to the signal significantly in n-in-p and p-in-n 3D detectors. This property is assumed to be partly responsible for the similar behaviour of n-in-p and p-in-n 3D detectors after very intense irradiation.

Due to the high weighting field around the ohmic column, multiplication of charge carriers close to the ohmic columns can strongly increase the signal in 3D detectors, even if none of the created charge carriers reach the junction electrode. In planar detectors, charge multiplication close to the detector backplane, which is the ohmic electrode, can only induce a strong signal if the created charge carriers reach the region close to the junction electrode. In highly irradiated detectors, however, charge carriers liberated close to the ohmic electrode are unlikely to reach the junction electrode due to a high trapping probability. For these reasons, multiplication of electrons close to the ohmic electrode can

increase the signal in highly irradiated p-in-n 3D detectors. The same effect in highly irradiated planar p-in-n detectors has only a low influence on the signal.

Beta Source Measurements: Temperature Dependence

Beta source measurements were performed at different temperatures to investigate the influence of the sensor temperature on the measured signal. A temperature-dependent calibration of the setup was performed (see Section 5.3.2), hence the temperature dependence of the gain of the Beetle chip is taken into account. The energy deposited in a silicon sensor by penetrating particles does not depend on the temperature. As the width of the silicon band gap does not vary considerably in the temperature range under consideration, the amount of liberated charge carriers does not depend on the operating temperature either. Hence, the signal of unirradiated detectors, where all liberated charge carriers are collected, can be expected to be temperature-independent. This assumption is taken as a basis for the calibration.

In highly irradiated detectors, several effects can lead to a temperature dependence of the measured signal. As discussed in Section 4.3.3, the trapping probability increases with decreasing temperature. In the temperature range between $-20\,^{\circ}\mathrm{C}$ and $-50\,^{\circ}\mathrm{C}$, which is considered for the studies presented in this section, the effective life times of electrons and holes decrease by approximately 10% and 20%, respectively (see Eq. 4.13). This effect can lead to lower signals at lower temperatures. On the other hand, the increased trapping probability can be counterbalanced by an increase of the mobility and the saturation drift velocity with decreasing temperature. At lower temperatures, reduced lattice vibrations lead to increased mean free paths of the charge carriers and therefore to higher drift velocities. An increase of the drift velocity decreases the time required to reach an electrode, therefore it limits the susceptibility for trapping. While the saturation velocity in high purity silicon only increases very weakly with decreasing temperature in the temperature range considered here [Sze81], the mobility increases more strongly. The mobilities of electrons and holes are proportional to $T^{-2.42}$ and $T^{-2.20}$ in n- and p-type silicon, respectively [Sze81], where T is the temperature in Kelvin. Therefore, the mobilities increase by more than 30% between $-20\,^{\circ}\mathrm{C}$ and $-50\,^{\circ}\mathrm{C}$.

As described in Section 3.3.7, the ionisation rates of impact ionisation increase with decreasing temperature. Figure 6.41 shows the electron ionisation rates for temperatures of $-20\,^{\circ}\mathrm{C}$ and $-50\,^{\circ}\mathrm{C}$, calculated using Eq. (3.22), Section 3.3.7. In the electric field range shown in Fig 6.41, the electron ionisation rates at a temperature of $-50\,^{\circ}\mathrm{C}$ are between 20% and 40% larger than those at a temperature of $-20\,^{\circ}\mathrm{C}$. The relative difference decreases from low electric fields to high electric fields. If charge multiplication contributes to the measured signal strongly, it can be expected that the signal is considerably larger at lower temperatures.

A further effect, which could lead to a temperature dependence of the measured signal, is the temperature dependence of the leakage current. Increased leakage current at higher temperatures can lead to an increased density of trapped charge. This can modify the distribution of the electric field. However, the signal variation as a function of the temperature cannot be easily estimated. Detailed simulations would be necessary to take into

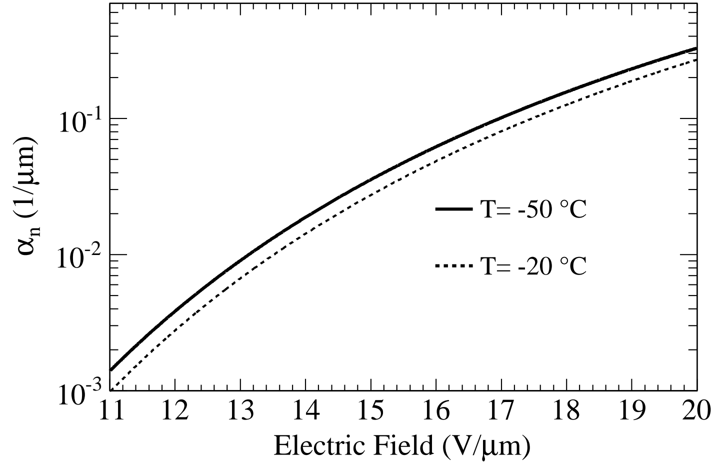

Figure 6.41: Ionisation rate α_n of electrons as a function of the electric field for two different temperatures ($-50\,^{\circ}$C and $-20\,^{\circ}$C).

account the different effects which could influence the measured signal.

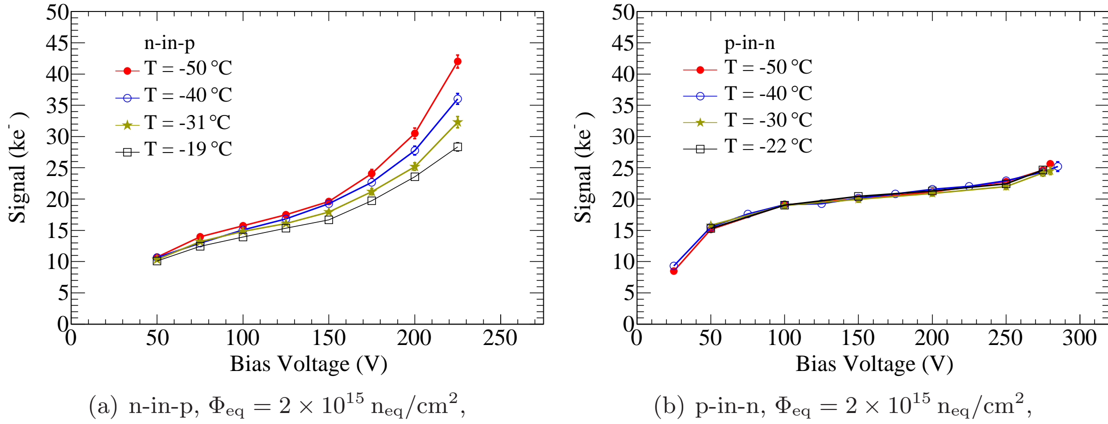

(a) n-in-p, $\Phi_{\text{eq}} = 2 \times 10^{15}\ \text{n}_{\text{eq}}/\text{cm}^2$,

(b) p-in-n, $\Phi_{\text{eq}} = 2 \times 10^{15}\ \text{n}_{\text{eq}}/\text{cm}^2$,

Figure 6.42: Signal as a function of the applied bias voltage for different sensor temperatures, measured with the n-in-p and the p-in-n detectors irradiated to $2 \times 10^{15}\ \text{n}_{\text{eq}}/\text{cm}^2$. The data points are connected to guide the eye.

Figure 6.42 shows signal measurements performed at different temperatures with the n-in-p and the p-in-n detectors irradiated to a fluence of $2 \times 10^{15}\ \text{n}_{\text{eq}}/\text{cm}^2$. The measurements were performed at temperatures between approximately $-20\,^{\circ}$C and $-50\,^{\circ}$C. For the investigation of the temperature dependence of the signal, only the statistical errors and a systematic error of the gain originating from the uncertainty of the temperature are considered. As different measurements performed with the same sensor are compared, the systematic errors of the gain which originate from the thickness uncertainty of the reference detectors and the error on the capacitance correction are neglected (see Sec-

tion 5.3.2). A decrease of the signal with increasing temperature can be seen for the n-in-p detector, whereas the signal of the p-in-n detector does not depend on the temperature. The temperature dependence of the signals measured with the n-in-p detector is particularly pronounced at high bias voltages, where strong charge multiplication occurs. At a bias voltage of 225 V, which is the highest voltage applied, the signal at a temperature of $-50\,°C$ is approximately 50% higher than the signal measured at $-19\,°C$. This behaviour highlights the temperature dependence of impact ionisation.

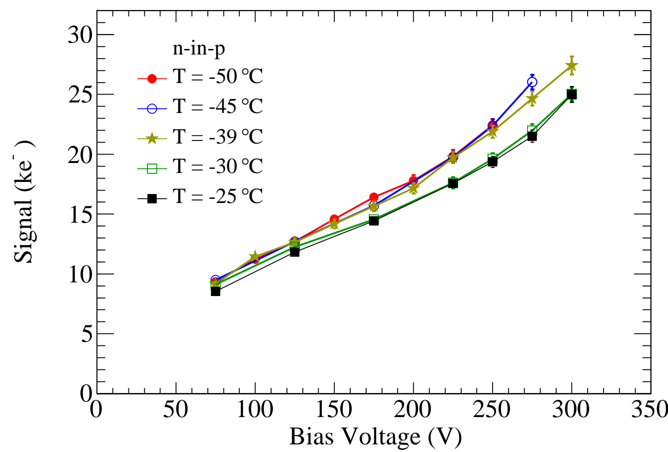

Figure 6.43: Signal as a function of the applied bias voltage for different sensor temperatures, measured with the n-in-p detector irradiated to $5 \times 10^{15}\,n_{eq}/cm^2$. The data points are connected to guide the eye.

The signals measured at different temperatures with the n-in-p detector irradiated to $5 \times 10^{15}\,n_{eq}/cm^2$ are summarised in Fig. 6.43. It can be seen that decreasing temperatures tend to result in higher signals, however, the effect is much less pronounced than for the n-in-p detector irradiated to $2 \times 10^{15}\,n_{eq}/cm^2$. It can be seen that the signals measured at some temperatures coincide. For example, the measurements performed at temperatures of $-30\,°C$ and $-25\,°C$ almost fully agree with each other.

Figure 6.44 summarises the signals measured at different temperatures with the detectors irradiated to $2 \times 10^{16}\,n_{eq}/cm^2$. The signals of the n-in-p detector show a weak dependence on the temperature. Somewhat higher signals are measured at lower temperatures. The signals measured at a temperature of $-50\,°C$ are approximately $2\,ke^-$ higher than the signals measured at $-30\,°C$. The temperature dependence of the signals measured with the p-in-n detector is much less pronounced. However, lowering the temperature leads to decreased noise (see the following section) and therefore facilitates to measure the p-in-n sensor at higher bias voltages. For this sensor, a strong noise increase limits the maximum bias voltage as it makes a separation between the signal and the noise distribution impossible. In contrast to that, the n-in-p sensor could be measured at least up to 425 V at all temperatures.

In summary, it was observed that the signals of the n-in-p detectors irradiated to differ-

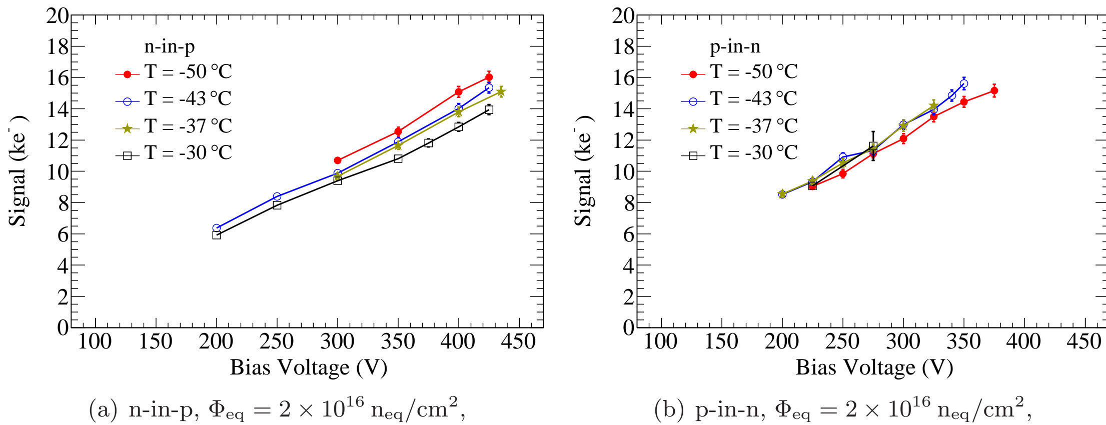

(a) n-in-p, $\Phi_{eq} = 2 \times 10^{16}\,\mathrm{n_{eq}/cm^2}$, (b) p-in-n, $\Phi_{eq} = 2 \times 10^{16}\,\mathrm{n_{eq}/cm^2}$,

Figure 6.44: Signal as a function of the applied bias voltage for different sensor temperatures, measured with the n-in-p and the p-in-n detectors irradiated to $2 \times 10^{16}\,\mathrm{n_{eq}/cm^2}$. The data points are connected to guide the eye.

ent fluences increase with decreasing temperature. The temperature dependence is the strongest for the n-in-p detector irradiated with a fluence of $2 \times 10^{15}\,\mathrm{n_{eq}/cm^2}$. For this sensor, a strong temperature dependence at high bias voltages can be attributed to the temperature dependence of impact ionisation. The signals of the n-in-p detectors irradiated to higher fluences vary less strongly with the temperature, and the p-in-n detectors did not show a clear temperature dependence. The details are theoretically not yet understood.

6.2.4 Noise Studies

Figure 6.45 displays a schematic sketch of the signal and noise distributions, which are ideally clearly separated. The noise is characterised by the width of the spectrum measured in absence of penetrating particles. As charged particles produce a signal spectrum which follows a Landau distribution, the most probable value of this distribution is commonly used to quantify the signal.

Often, the signal-to-noise ratio is used as a figure of merit for tracking detectors. High signal-to-noise ratios are desired, as these imply a clear separation of the signal and noise distributions. In binary readout systems, which are employed in the ATLAS tracking detectors, a threshold is set to separate signal from noise. The threshold has to be high enough to exclude noise hits and low enough to include as much signals of penetrating particles as possible. In this case, the ratio of the signal and the chosen threshold could be a more adequate figure of merit of a detector.

In this section, investigations of the noise, the signal-to-noise ratio and the signal-to-threshold ratio are presented. The effect of the operating temperature on the noise is discussed. Special emphasis is put on the investigation of the noise at high bias voltages, where the occurrence of charge multiplication could be observed in the signal measurements presented above. Charge multiplication can only be beneficial for the detector

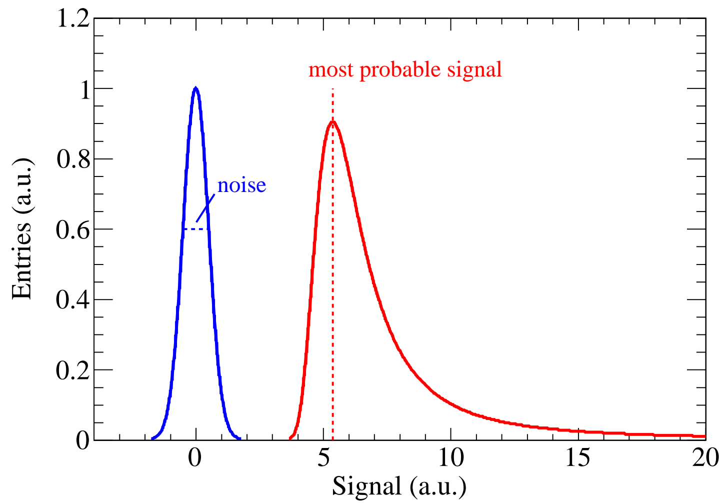

Figure 6.45: Illustration of the signal and noise distributions.

operation if it does not lead to particularly excessive noise. In contrast to the signal, the noise depends strongly on the readout electronics employed and the detector configuration, particularly on the readout strip length. For example, it is not possible to compare absolute noise values measured with strip detectors and pixel detectors. Therefore, absolute noise values are of limited importance.

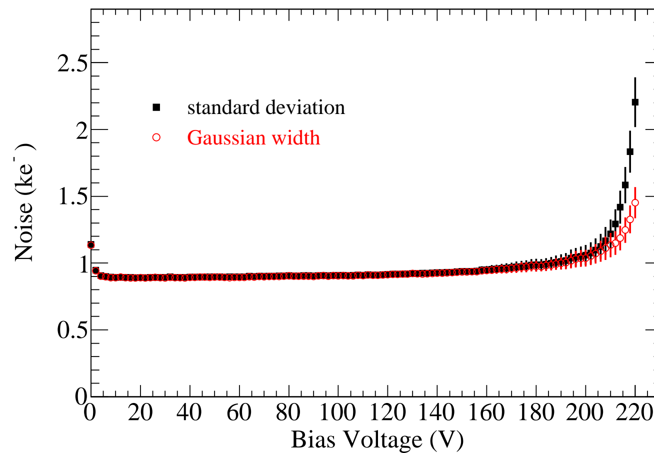

Figure 6.46: Noise, averaged over all channels, as a function of the bias voltage for the n-in-p detector irradiated to 1×10^{15} n_{eq}/cm^2, measured at a temperature of $-20\,°C$. The noise was calculated as the standard deviation (RMS) of the noise spectrum and as the width of a Gaussian fitted to the spectrum. Only statistical errors are shown.

Figure 6.46 shows the noise, averaged over all readout strips, as a function of the applied bias voltage for the n-in-p detector irradiated with a fluence of 1×10^{15} n_{eq}/cm^2. The illustration shows the noise calculated according to two approaches: the standard deviation of the noise spectrum, corresponding to the root mean squared deviation (RMS), and

the width of a Gaussian which was fitted to the noise spectrum. In order to exclude the effect of non-Gaussian tails on the results of the Gaussian fit, the fit range is limited to a region around the maximum of the spectrum. Initially, the fit range is limited to the mean of the spectrum ± 2 times the RMS value. Then, the fit result is improved in three further iterations, where the fit range is limited to the maximum of the previous fit ± 2 times the width of the previous fit. This approach assures that the fit only extends over the Gaussian core of the spectrum.

After a decrease of the noise for bias voltages below 10 V, the noise reaches a plateau value corresponding to approximately 900 e^-. This corresponds to the noise of the fully depleted unirradiated detector (see Section 6.1.3). In contrast to the unirradiated detector, the full depletion voltage of the irradiated sensor cannot be extracted from the shape of the noise curve. In the case of the unirradiated sensor, a strong decrease of the noise at voltages between 25 V and 30 V was interpreted as the onset of full depletion. In irradiated sensors, the undepleted bulk becomes conductive (see Section 4.3.1), hence the increase of the depletion zone does not lead to a decrease of the capacitance and the noise.

At bias voltages above 180 V, the noise of the n-in-p detector irradiated to $1 \times 10^{15}\ n_{eq}/cm^2$ increases strongly. The RMS noise measured at high bias voltages is significantly higher than the Gaussian noise. Commonly, the noise is expected to follow a Gaussian distribution, since the noise originates from random fluctuations of the number of charge carriers or of the charge carrier velocity (see Section 3.3.8). The fact that the RMS noise is partially much larger than the Gaussian noise points to non-Gaussian tails of the noise distribution at high bias voltages. The occurrence of non-Gaussian tails of the noise spectra is investigated below.

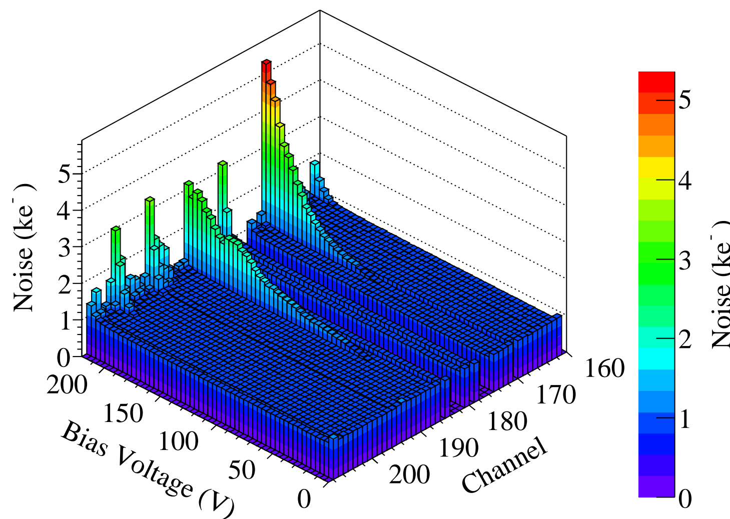

Figure 6.47: Noise for all channels as a function of the bias voltage for the n-in-p detector irradiated to $1 \times 10^{15}\ n_{eq}/cm^2$, measured at a temperature of $-20\,^{\circ}$C. The noise was calculated as the standard deviation of the noise spectrum.

In the bias voltage range where the noise increases steeply, charge multiplication leads to a strong increase of the signal measured with this detector (see Section 6.2.3). It is therefore tempting to assume that charge multiplication generally leads to a strong noise increase. However, the readout channels behave very differently, as can be seen in Fig. 6.47. The figure shows the noise for all channels of the sensor as a function of the applied bias voltage. Strips which are dead or which exhibit a very high noise already at low bias voltages were excluded from the analysis. It can be seen that the noise increase of the channels starts at different bias voltages. The strong increase of the average noise at bias voltages above 180 V is mainly caused by two channels. The increase of the noise in the majority of the channels starts at voltages above 200 V.

Spectra of noise runs measured at selected bias voltages with the n-in-p detector irradiated to $1 \times 10^{15}\,\mathrm{n_{eq}/cm^2}$ are shown in Fig. 6.48. Corresponding illustrations of the n-in-p and the p-in-n detector irradiated to $2 \times 10^{16}\,\mathrm{n_{eq}/cm^2}$ are shown in Figs. 6.49 and 6.50, respectively. The spectra are raw data distributions of pedestal runs. Common mode fluctuations and the pedestal values are subtracted. Furthermore, the different polarity of the signals of the n-in-p and p-in-n detectors is corrected for by inverting the spectra of the n-in-p detectors. Thus, penetrating particles would lead to positive signals in all spectra. Without this correction, penetrating particles induce negative signals in n-in-p detectors and positive signals in p-in-n detectors. The different sign of the signals is due to the different types of charge carriers which are drifting towards the readout electrodes. During these measurements, the radioactive source was not directed onto the sensors in order to avoid any signal creation of penetrating particles.

At a bias voltage of 50 V, the spectra of all channels of the n-in-p detector irradiated to $1 \times 10^{15}\,\mathrm{n_{eq}/cm^2}$ obviously follow a Gaussian distribution with a similar width (see (Fig. 6.48(a)). Therefore, the RMS noise and the Gaussian noise coincide, as apparent from Fig. 6.46. At a bias voltage of 204 V (Fig. 6.48(b)), single channels exhibit non-Gaussian tails. Furthermore, it is apparent that these tails are longer in the positive direction. At the maximum bias voltage applied, 220 V (Fig. 6.48(c)), the spectra of almost all channels exhibit long non-Gaussian tails with a preference in the positive direction. In these cases, the commonly applied consideration of the noise as random fluctuations leading to a Gaussian distribution (see Section 3.3.8) appears questionable. It can make a difference whether noise figures are calculated as the RMS deviation or as the Gaussian width.

The steep increase of the noise at high bias voltages, the asymmetries and the tails of the noise distributions point to the occurrence of micro-discharges [Ohs94, Ohs96b, Ohs96a]. These can occur in regions with high electric fields. Micro-discharges are localised electrical breakdowns, which occur before the onset of a complete junction breakdown. It is conceivable that the probability of micro-discharges increases if pronounced charge multiplication occurs, as both effects are related to high electric fields. In micro-discharges, additional free charge carriers are liberated, which contribute to the noise. However, this process is fundamentally different from the statistical nature of generation and recombination of electron-hole pairs, therefore the noise related to micro-discharges does not follow a Gaussian distribution. The additional number of charge carriers created leads to a distortion of the noise spectrum towards positive values. As electrical breakdowns can be

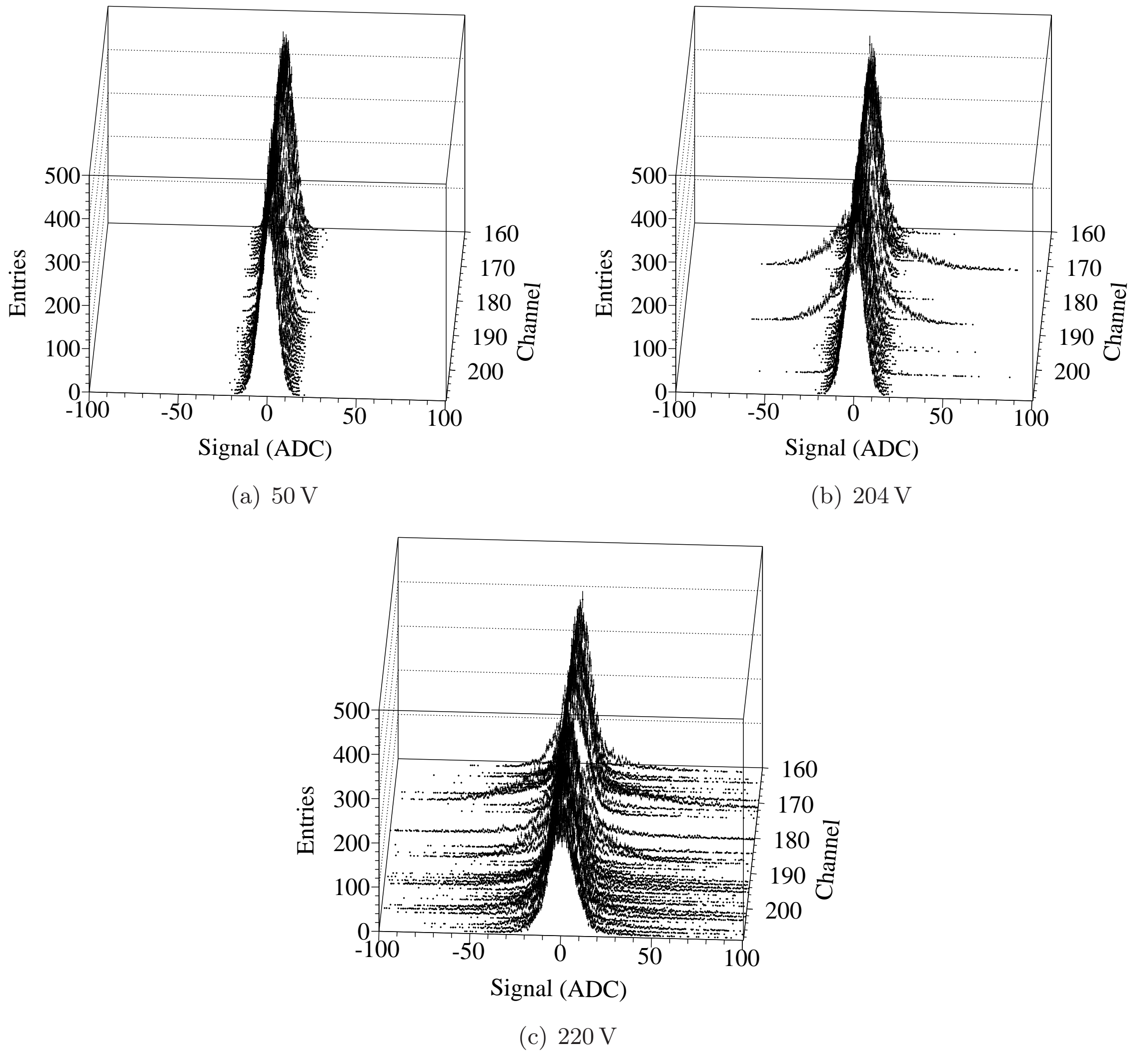

(a) 50 V

(b) 204 V

(c) 220 V

Figure 6.48: Spectra of noise runs, measured with the n-in-p detector irradiated to $1 \times 10^{15}\,\mathrm{n_{eq}/cm^2}$. The measurements were performed at (a) 50 V, (b) 204 V and (c) 220 V. The temperature during the measurements was $-22\,^{\circ}\mathrm{C}$ ($1\,\mathrm{ADC} \approx 190\,\mathrm{e^-}$).

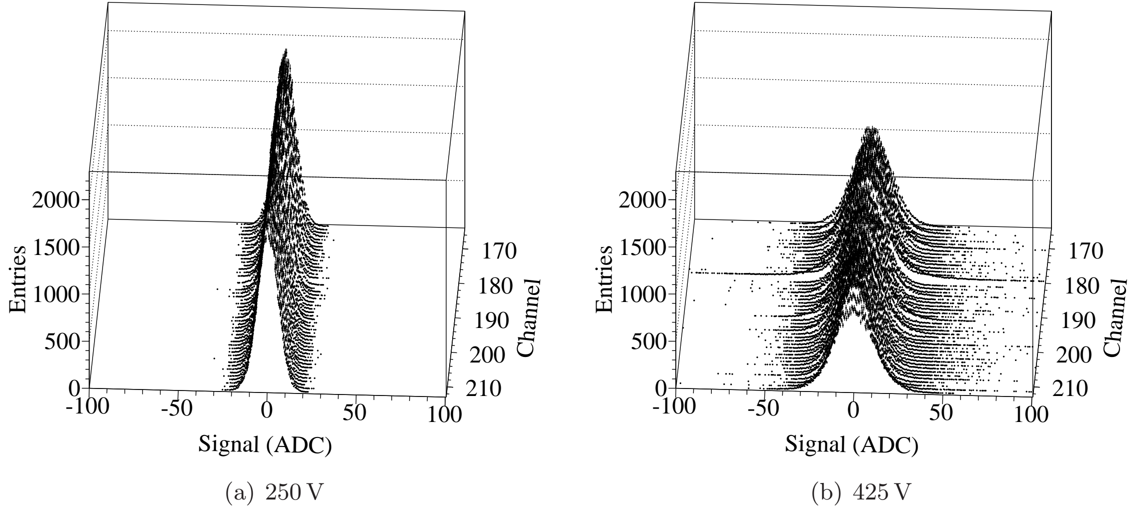

(a) 250 V

(b) 425 V

Figure 6.49: Spectra of noise runs, measured with the n-in-p detector irradiated to $2 \times 10^{16}\,\mathrm{n_{eq}/cm^2}$. The measurements were performed at (a) 250 V and (b) 425 V. The temperature during the measurements was $-43\,^{\circ}\mathrm{C}$ ($1\,\mathrm{ADC} \approx 170\,\mathrm{e}^-$).

caused either by tunnelling effects or avalanche multiplication [Sze81], these mechanisms are also assumed to be the cause of micro-discharges.

The n-in-p detector and the p-in-n detector irradiated with a fluence of $2 \times 10^{16}\,\mathrm{n_{eq}/cm^2}$ show a similar behaviour as the n-in-p detector irradiated to $1 \times 10^{15}\,\mathrm{n_{eq}/cm^2}$, which was discussed above. At low bias voltages, see Fig. 6.49(a) for the n-in-p detector and Fig. 6.50(a) for the p-in-n detector, the noise spectra follow a Gaussian distribution. Outliers and tails are not present. At high bias voltages, see Figs. 6.49(b) and 6.50(b), all channels exhibit visibly broader spectra with tails. Again, the tails are more pronounced in the positive direction.

Broad noise distributions and especially outliers and long tails can be extremely adverse for the signal identification. The occurrence of tails in the noise spectra requires an increase of the threshold in order to limit the rate of false counts. However, the efficiency of particle detection will decrease with increasing thresholds. These effects are investigated further below.

The RMS noise, averaged over all channels, of the n-in-p and the p-in-n detectors irradiated to $2 \times 10^{15}\,\mathrm{n_{eq}/cm^2}$ and $2 \times 10^{16}\,\mathrm{n_{eq}/cm^2}$ is shown in Fig. 6.51 as a function of the applied bias voltage. The measurements were performed at different temperatures between $-19\,^{\circ}\mathrm{C}$ and $-50\,^{\circ}\mathrm{C}$. For all detectors, the noise curves are flat at low voltages and exhibit a strong increase at high bias voltages. In the range of low voltages, the influence of shot noise is negligible and the total noise is given by the noise of the readout chip due to the load capacitance. At high bias voltages, the noise increases due to shot noise and due to emerging micro-discharges. The noise increase at high bias voltages is steeper for the detectors irradiated to $2 \times 10^{15}\,\mathrm{n_{eq}/cm^2}$. Possibly, the short trapping length in the detectors irradiated with a fluence of $2 \times 10^{16}\,\mathrm{n_{eq}/cm^2}$ provides an attenuation of emerging

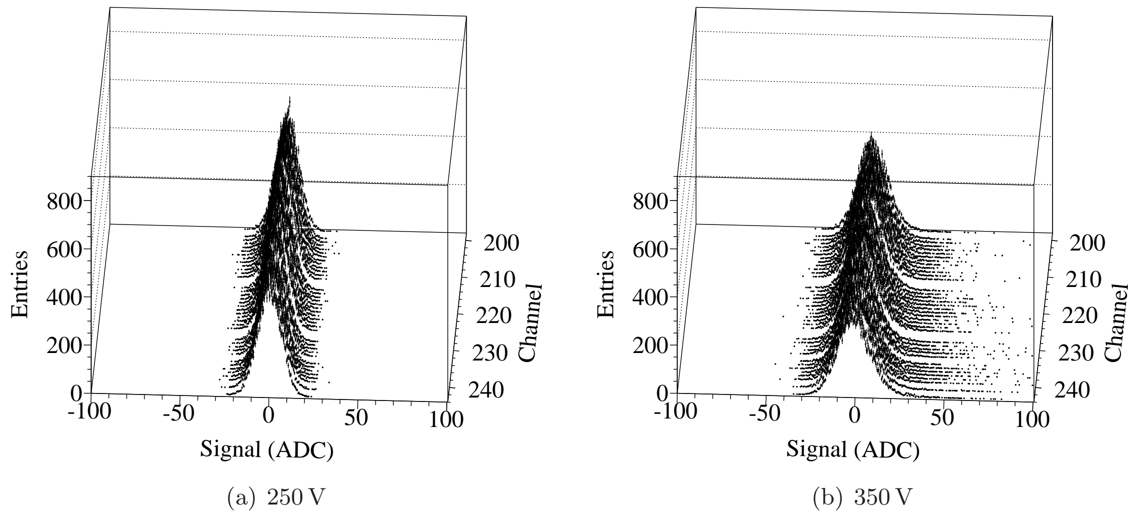

(a) 250 V

(b) 350 V

Figure 6.50: Signal spectra of noise runs, measured with the p-in-n detector irradiated to $2 \times 10^{16}\,\mathrm{n_{eq}/cm^2}$. The measurements were performed at (a) 250 V and (b) 350 V. The temperature during the measurements was $-43\,^{\circ}\mathrm{C}$ ($1\,\mathrm{ADC} \approx 170\,\mathrm{e^-}$).

breakdowns.

The noise measured at low bias voltages hardly depends on the temperature. This demonstrates that the noise of the Beetle chip due to the capacitive load depends only weakly on the temperature in the range investigated here. However, the noise measured at high bias voltages increases strongly with the temperature. There could be several reasons for the positive temperature coefficient of the noise at high bias voltages. Higher temperatures lead to higher leakage current and hence to larger shot noise. Higher leakage current also increases the probability that charge carriers are injected into regions with extremely high fields. These charge carriers can undergo extraordinarily strong multiplication, which could lead to tails of the noise distribution.

Also, the increase of the noise at high bias voltages could suggest an increase of micro-discharges with increasing temperature. If the micro-discharges are caused by localised avalanche-type breakdowns, the opposite effect would be expected as the impact ionisation rates increase with decreasing temperature (see Section 3.3.7 and Section 6.2.3). Correspondingly, a decrease of micro-discharges in unirradiated silicon sensors with increasing temperature has been observed [Ohs94]. A positive temperature coefficient could originate from the fact that the micro-discharges in this case are not related to avalanche effects, but to tunnelling effects. These increase with increasing temperature [Sze81]. Another possibility is that the higher leakage current density at higher temperatures leads to higher trapped charge and hence to higher electric fields. This effect could also result in a higher rate of avalanche-type micro-discharges.

In the following, the agreement between the standard noise modelling (see Section 3.3.8) and the measured noise in a highly irradiated detector is investigated. Figure 6.52 compares the calculated noise and the measured noise for the p-in-n detector irradiated with

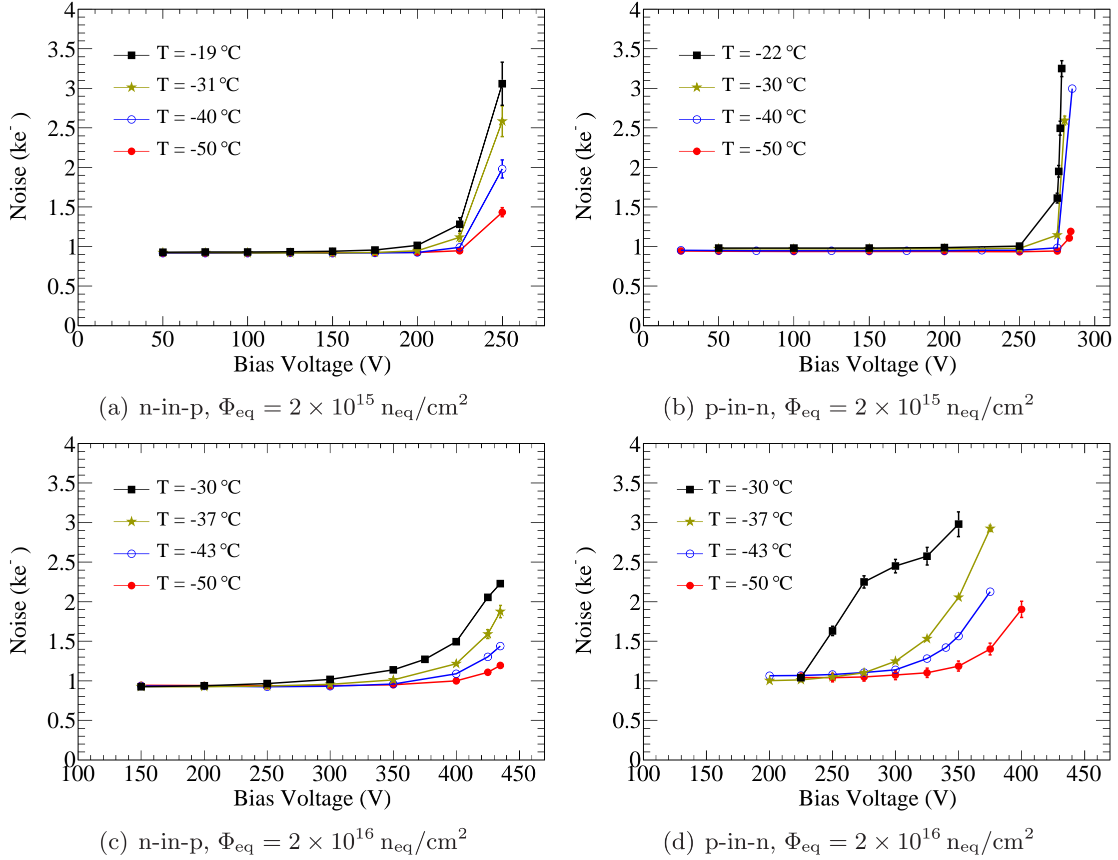

(a) n-in-p, $\Phi_{\mathrm{eq}} = 2 \times 10^{15}\ \mathrm{n_{eq}/cm^2}$ (b) p-in-n, $\Phi_{\mathrm{eq}} = 2 \times 10^{15}\ \mathrm{n_{eq}/cm^2}$

(c) n-in-p, $\Phi_{\mathrm{eq}} = 2 \times 10^{16}\ \mathrm{n_{eq}/cm^2}$ (d) p-in-n, $\Phi_{\mathrm{eq}} = 2 \times 10^{16}\ \mathrm{n_{eq}/cm^2}$

Figure 6.51: RMS noise as a function of the applied bias voltage for different sensor temperatures, measured with the n-in-p and the p-in-n detectors irradiated to $2\times10^{15}\ \mathrm{n_{eq}/cm^2}$ and $2 \times 10^{16}\ \mathrm{n_{eq}/cm^2}$. The data points are connected to guide the eye.

a fluence of $2 \times 10^{16}\ \mathrm{n_{eq}/cm^2}$. A measurement performed in reverse bias mode at a temperature of $-50\,°\mathrm{C}$ (Fig. 6.52(a)) and a measurement performed with forward bias at a temperature of $-56\,°\mathrm{C}$ are shown (Fig. 6.52(b)). The equivalent noise charge (ENC) was calculated according to the equation (see Section 3.3.8)

$$\mathrm{ENC} = \sqrt{\mathrm{ENC}_{\mathrm{shot}}^2 + \mathrm{ENC}_{\mathrm{load}}^2}, \tag{6.3}$$

where $\mathrm{ENC}_{\mathrm{load}}$ is the noise due to the load capacitance and $\mathrm{ENC}_{\mathrm{shot}}$ is the shot noise. The noise due to the load capacitance was adjusted to achieve a matching of the measured noise and the calculated noise at the lowest bias voltage. At low bias voltage, the shot noise contribution is expected to be negligible. The shot noise is calculated according to (see Section 3.3.8)

$$\mathrm{ENC}_{\mathrm{shot}} = \sqrt{B\, I_l}\, e, \tag{6.4}$$

where I_l is the leakage current per readout strip, e is the elementary charge and B is a constant specific to the readout chip. Here, the Beetle chip with an adjusted frontend shaper voltage of 1000 mV was used, hence $B = (210 \pm 20)\,\mathrm{nA}^{-1}$ [Loi04]. The excess noise related to charge multiplication was not included in the calculation. According to

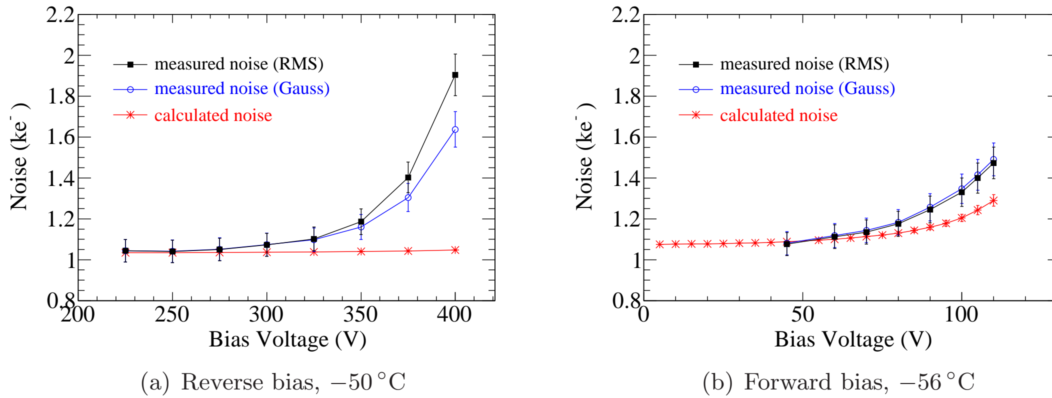

(a) Reverse bias, $-50\,°$C

(b) Forward bias, $-56\,°$C

Figure 6.52: Calculated and measured noise as a function of the applied bias voltage for the p-in-n detector irradiated to $2 \times 10^{16}\ \mathrm{n_{eq}/cm^2}$: (a) reverse bias operation, (b) forward bias operation. The error bars include a statistical error and a systematic error due to the calibration uncertainty.

the standard theory it can be modelled by the substitution $B \to BMF$, where M is the multiplication factor and F is the excess noise factor (see Section 3.3.8).

As can be seen in Fig. 6.52(a), a large disagreement exists between the calculated noise and the measured noise for the measurement in reverse bias. The calculated noise does hardly depend on the voltage, since the influence of the calculated shot noise is low. The calculated noise is dominated by the noise due to the load capacitance. The disagreement can be attributed to originate from excess noise due to charge multiplication and from emerging micro-discharges at high voltages. A consideration of the multiplication factor M and the excess noise factor F for the noise calculation ($B \to BMF$) is not easy, as M and F are not known. Considering the linear increase of the signal as a function of the bias voltage, it could be assumed that the multiplication factor M increases linearly, too. Assuming that only electrons are multiplied, F increases between 1 and 2 as a function of M (see Section 3.3.8). It can be directly seen that these contributions cannot fully account for the strong increase of the noise at high bias voltages.

The increasing difference between the RMS noise and the Gaussian noise[2] shows the increasing influence of micro-discharges. Therefore, any noise modelling which assumes a Gaussian distribution of the noise cannot reproduce the experimental observation. However, it is not possible to conclude whether the occurrence of micro-discharges is necessarily connected to charge multiplication in highly irradiated detectors. It could also be a property specific to the detectors investigated here.

The agreement of calculated noise and measured noise is visibly better for reverse bias operation, see Fig. 6.52(b). The RMS noise and the Gaussian noise almost coincide, which indicates the absence of micro-discharges. Although the leakage current is considerably higher in forward bias operation, the noise is lower than in reverse bias mode. At a forward

[2]The Gaussian noise was determined as described on page 142.

bias voltage of 110 V, the leakage current is approximately a factor of 14 higher than that in reverse bias operation at a voltage of 400 V. However, the noise at these voltages is approximately 20% higher in reverse bias operation. The lower noise and the absence of micro-discharges in forward bias mode could be related to a more uniform electric field distribution than in reverse bias mode. The electric field in forward bias operation is expected to exhibit less pronounced peaks compared to reverse bias operation [Ere07].

Signal-to-Noise Ratio

The signal-to-noise ratio is often regarded as the figure of merit of detectors. Figure 6.53 illustrates the signal-to-noise ratio of the n-in-p and p-in-n detectors as a function of the applied bias voltage. The signals were measured with the beta source (see Section 6.2.3). The noise was calculated as the RMS deviation of the noise spectra. In all irradiated detectors, the signal-to-noise ratio increases with the bias voltages until it reaches a maximum. Even the detectors irradiated to the highest fluence of $2 \times 10^{16}\,\mathrm{n_{eq}/cm^2}$ exhibit a maximum signal-to-noise ratio of more than 10. At high bias voltages, the noise increases more steeply than the signal, which leads to a decrease of the signal-to-noise ratio. The highest bias voltage applied to the p-in-n detector irradiated to $2 \times 10^{15}\,\mathrm{n_{eq}/cm^2}$ is close to the breakdown voltage, which could explain the extreme decrease of the signal-to-noise ratio. The absolute values of the measured signal-to-noise ratio have to be interpreted with care due to the strong dependence of the noise on the size of the detector segmentation and on the readout electronics.

The signals of the n-in-p detectors irradiated to fluences of $1 \times 10^{15}\,\mathrm{n_{eq}/cm^2}$ and $2 \times 10^{15}\,\mathrm{n_{eq}/cm^2}$ increase strongly at voltages above 150 V (see Fig. 6.37, Section 6.2.3). This distinct increase can be attributed to charge multiplication. It can be seen in Fig. 6.53 that also the signal-to-noise ratio of these detectors increases at voltages higher than 150 V and only decreases at the highest voltages applied. The signal-to-noise ratios exceed even those of the unirradiated detector. Therefore, it can be concluded that charge multiplication can be beneficial for the signal-to-noise ratio. Only at very high voltages, a strong noise increase and micro-discharges lead to a decrease of the signal-to-noise ratio.

The temperature can have a strong effect on the signal-to-noise ratio. As discussed above, the noise decreases with decreasing temperature, particularly at high bias voltages. Furthermore, in some cases the signal increases with decreasing temperature (see Section 6.2.3). As a result, decreasing the temperature can be very beneficial for the ratio of signal and noise. In Fig. 6.54, the signal-to-noise ratio of the detectors irradiated with a fluence of $2 \times 10^{16}\,\mathrm{n_{eq}/cm^2}$ is shown as a function of the temperature. For the illustration, measurements at bias voltages of 400 V and 300 V were chosen for the n-in-p an the p-in-n detector, respectively. At a temperature of $-43\,^\circ\mathrm{C}$, these are the voltages for which the highest signal-to-noise ratio is measured for the two detectors (see Fig. 6.53).

Between $-30\,^\circ\mathrm{C}$ and $-50\,^\circ\mathrm{C}$, the signal-to-noise ratio of the n-in-p detector increases by approximately 80%. This considerable increase is caused by an increase of the signal (see Fig. 6.44(a)) and a decrease of the noise (see Fig. 6.51(c)) with decreasing temperature. In contrast to that, the p-in-n detector exhibits a much less pronounced dependence on

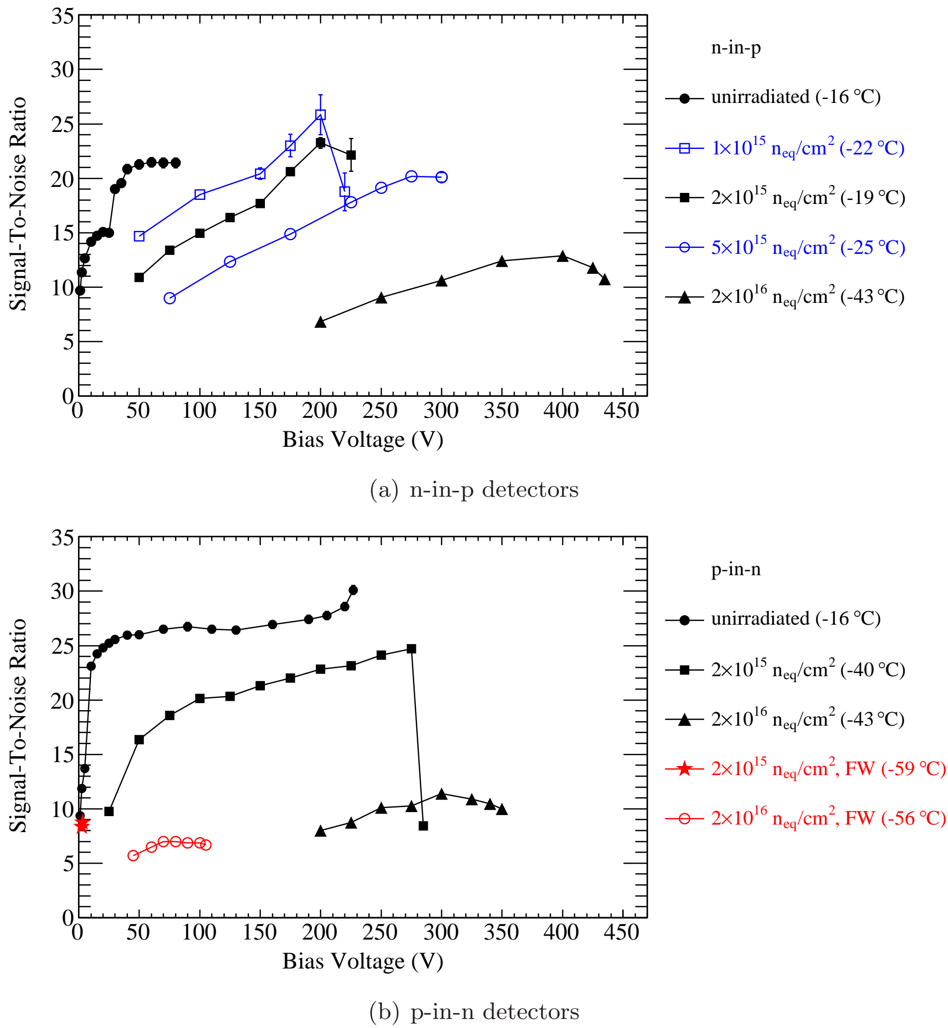

(a) n-in-p detectors

(b) p-in-n detectors

Figure 6.53: Signal-to-noise ratio as a function of the applied bias voltage, (a) for the n-in-p detectors and (b) for the p-in-n detectors. The RMS noise is considered. The measurements performed with forward bias ("FW") are shown in red. For most data points, the errors are smaller than the markers.

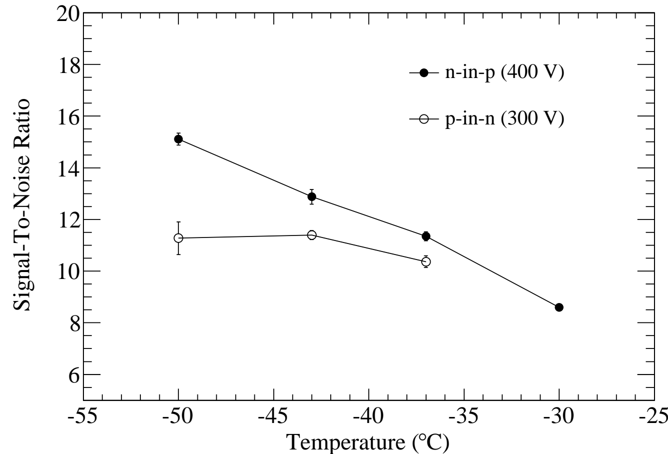

Figure 6.54: Signal-to-noise ratio at fixed bias voltages as a function of the temperature for the n-in-p an the p-in-n detector irradiated to $2 \times 10^{16}\,\mathrm{n_{eq}/cm^2}$. The RMS noise was used.

the temperature. Both the signal and the noise depend only weakly on the temperature (see Figs. 6.44(b) and 6.51(d)) for a bias voltage of 300 V in the range between $-37\,°\mathrm{C}$ and $-50\,°\mathrm{C}$. Only at a temperature of $-30\,°\mathrm{C}$, a very high noise rendered a separation of signal and noise impossible. Therefore, this measurement could not be analysed.

Signal-to-Threshold Ratio

In binary readout systems, a fixed threshold is applied to identify hits with a signal above the threshold. As examples, the ATLAS SCT and the ATLAS pixel detector apply a hit identification based on a signal threshold [Aad08c]. An efficient identification of hits requires a low threshold. The detection efficiency decreases if the threshold approaches the signal spectra. On the other hand, the threshold must be sufficiently high in order to limit the noise occupancy. In a measurement without penetrating particles, the noise occupancy is defined as the fraction of signals above the threshold and the total number of events. In the ATLAS SCT, a threshold of 1 fC was chosen. A noise occupancy target below 5×10^{-4} is envisaged even after the highest radiation dose [Aad08c].

An increase of the noise requires an increase of the threshold to keep the noise occupancy below a fixed limit. This is especially the case if the noise distribution exhibits tails and outliers, as observed in measurements with irradiated detectors (see above). In this section, the relationship between a target occupancy and the threshold required for this occupancy is investigated. These investigations use noise measurements, in which no radioactive source was directed onto the detectors. Finally, the ratio of the most probable signal and the threshold is studied. Alternatively to the signal-to-noise ratio, the signal-to-threshold ratio can serve as a figure of merit of a detector. The studies described in this section use the n-in-p detectors irradiated to $1 \times 10^{15}\,\mathrm{n_{eq}/cm^2}$, $2 \times 10^{15}\,\mathrm{n_{eq}/cm^2}$ and $2 \times 10^{16}\,\mathrm{n_{eq}/cm^2}$ and the p-in-n detector irradiated to $2 \times 10^{16}\,\mathrm{n_{eq}/cm^2}$.

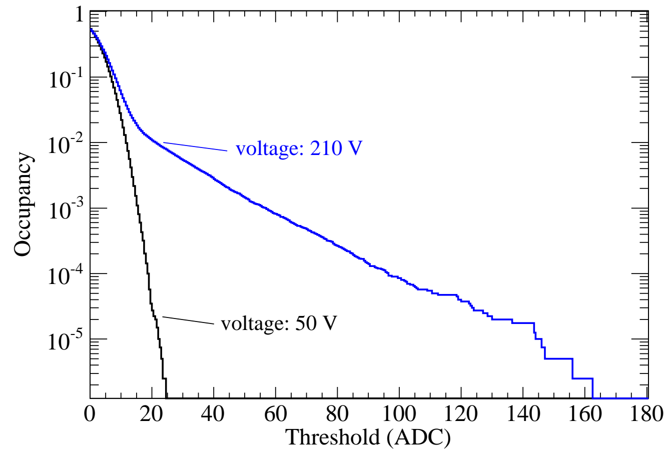

Figure 6.55: Noise occupancy as a function of the threshold for measurements of the n-in-p detector irradiated to $1 \times 10^{15}\,\mathrm{n_{eq}/cm^2}$ at bias voltages of 50 V and 210 V. The temperature during the measurements was $-22\,^{\circ}$C ($1\,\mathrm{ADC} \approx 190\,\mathrm{e}^-$).

Figure 6.55 shows the noise occupancy as a function of the applied threshold. The measurements were performed at bias voltages of 50 V and 210 V with the n-in-p detector irradiated to $1 \times 10^{15}\,\mathrm{n_{eq}/cm^2}$. The spectra contain the data of all strips, where extraordinarily noisy or dead strips are excluded. At a bias voltage of 50 V, the noise is low and follows a Gaussian distribution, see Fig. 6.48. Therefore, a threshold of approximately 22 ADC ($\approx 4.2\,\mathrm{ke}^-$) is sufficient to keep the occupancy below 5×10^{-4}. At a bias voltage of 210 V, the increased noise and especially the outliers require increasing the threshold by a factor of 6.5 in order to maintain the same noise occupancy.

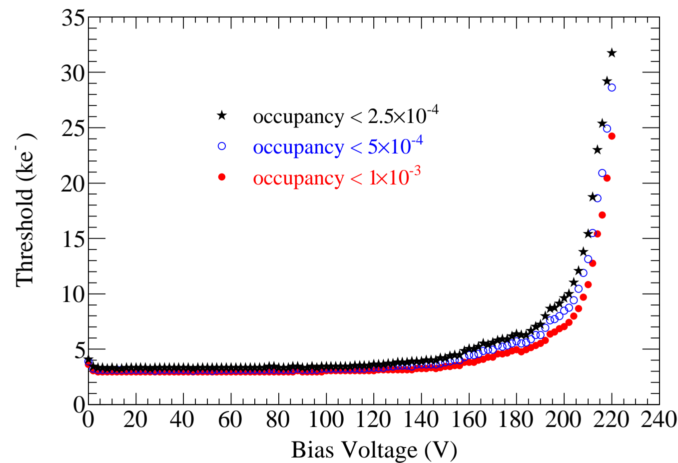

Figure 6.56: Threshold as a function of the applied bias voltage for measurements of the n-in-p detector irradiated to $1 \times 10^{15}\,\mathrm{n_{eq}/cm^2}$. The threshold required for three different noise occupancies is shown.

Figure 6.56 shows the threshold required for three different noise occupancies as a function

of the applied bias voltage. At high bias voltages, when the noise spectra exhibit long tails (see Fig. 6.48), the threshold has to be increased strongly. It can also be seen that the threshold depends considerably on the target occupancy at high voltages. This is again a consequence of long tails in the noise distribution. As an estimation of the error of the threshold, the half of the bin width of the histogram shown in Fig. 6.55 is used. However, the errors are smaller than the markers in the illustration.

The signal-to-threshold ratio as a function of the applied bias voltage is shown in Fig. 6.57 for different detectors and a target occupancy of 5×10^{-4}. The signals were measured with the beta source (see Section 6.2.3). For all detectors, signal-to-threshold ratios exceeding 2 can be achieved. As it is the case for the signal-to-noise ratio (see Fig. 6.53), the signal-to-threshold ratio increases up to a certain voltage and then decreases strongly. The maximum of the signal-to-threshold ratio of the n-in-p detectors irradiated to $1 \times 10^{15}\,\mathrm{n_{eq}/cm^2}$ and $2 \times 10^{15}\,\mathrm{n_{eq}/cm^2}$ is reached at lower voltages than that of the signal-to-noise ratio. The signal-to-threshold ratio decreases already at the voltage where charge multiplication increases the signal above that of the unirradiated detector.

This observation could indicate that charge multiplication is not beneficial for detector operation. However, it has to be noted that the signal-to-threshold ratio is strongly influenced by outliers or noise tails of single channels. Excluding certain channels would influence the results considerably. The calculation of the signal-to-noise ratio, where the mean noise of all strips is considered, is much less influenced by outliers in single channels.

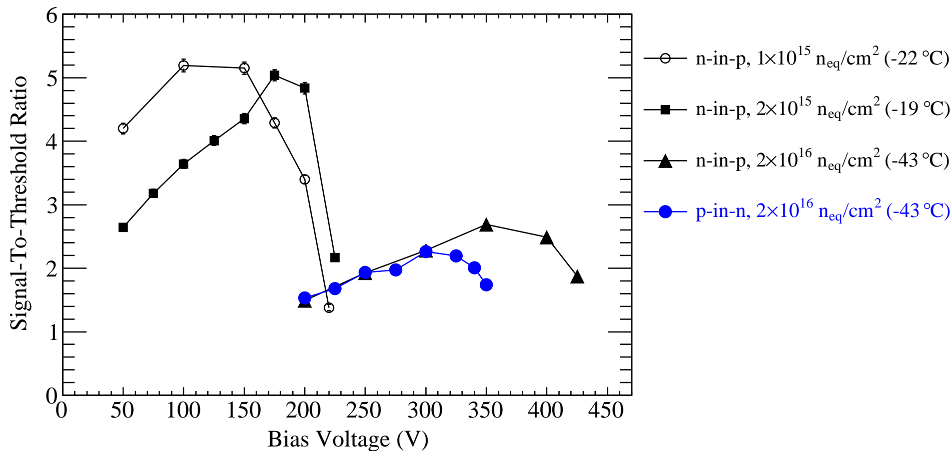

Figure 6.57: Signal-to-threshold ratio for a target occupancy of 5×10^{-4} as a function of the applied bias voltage for different detectors.

In Fig. 6.58, the temperature dependence of the threshold and the signal-to-threshold ratio is illustrated for the n-in-p detector irradiated to $2 \times 10^{15}\,\mathrm{n_{eq}/cm^2}$. As above, the threshold was calculated for an occupancy of 5×10^{-4}. The temperature has a strong effect at bias voltages exceeding 175 V. Lower temperatures allow a considerable reduction of the threshold. Also, the voltage, for which the the maximum of the signal-to-threshold ratio is reached, is affected by the temperature. At a temperature of $-19\,^{\circ}\mathrm{C}$, the maximum

is reached at a bias voltage of 175 V, whereas the maximum is reached at 200 V in the measurements at lower temperatures. Possible reasons for the strong dependence of the noise and the micro-discharges on the temperature were discussed above.

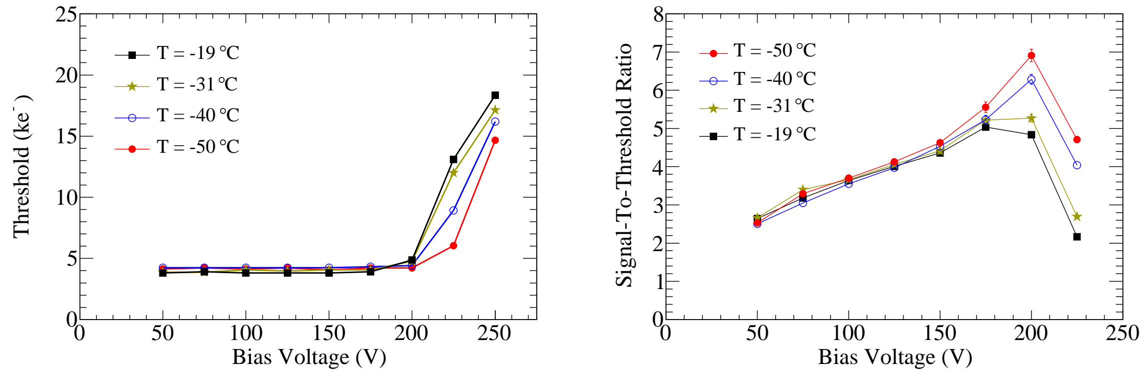

Figure 6.58: Threshold and signal-to-threshold ratio for a target occupancy of 5×10^{-4} as a function of the bias voltage. The measurements were performed at different temperatures with the n-in-p detector irradiated to $2 \times 10^{15}\,\mathrm{n_{eq}/cm^2}$.

6.2.5 Annealing Studies

Accelerated annealing studies were conducted to study the performance of the detectors after storing them at elevated temperatures. This is of particular importance since detectors in high-energy physics experiments have to be kept at room temperature during maintenance periods. Annealing studies were performed with three detectors: a p-in-n and a n-in-p detector both irradiated to $2 \times 10^{16}\,\mathrm{n_{eq}/cm^2}$ and a p-in-n detector irradiated to $2\times10^{15}\,\mathrm{n_{eq}/cm^2}$. The results of the measurements reported in this section are published in Ref. [Kö11b].

The detectors were exposed to a temperature of 60 °C for increasing periods of time. In a number of annealing steps, beta source measurements, noise measurements and leakage current measurements were performed. The results of these measurements are presented in this section. Additionally, laser measurements were performed after the last annealing step. Those results are presented in Section 6.2.6 together with the results of laser measurements performed before annealing.

Using the activation energy of the long-term annealing of the effective doping concentration, $E_a = 1.33\,\mathrm{eV}$ [Mol99], the annealing times at a temperature of 60 °C can be scaled to room temperature ($T = 20\,°\mathrm{C}$) by multiplying them with a factor 560 (see also Section 4.1.2). However, it should be noted that this activation energy was determined for the long-term annealing behaviour of the effective doping concentration [Mol99] and not for the annealing of the signal or the noise. It can serve as an estimate, however, the agreement with the annealing of the signal or the noise, particularly in highly irradiated detectors, is not fully established. Recent annealing studies of the signal measured with highly irradiated planar n-in-p detectors indicate some disagreement [Cas11a]. In the studies presented in this section, the detectors were annealed up to 2560 min at a temperature

of 60 °C. This corresponds to approximately 33 months (1000 days) at room temperature according to the aforementioned scaling.

Beta Source Measurements

Figure 6.59 shows the signal of the p-in-n detector irradiated to $2 \times 10^{15}\,n_{eq}/cm^2$ for selected bias voltages as a function of the accumulated annealing time. In this and the following illustrations, errors are not shown. The statistical errors are smaller than 3%, a systematic error of approximately 5% due to the calibration uncertainty can be assumed. The axis on the top of the figure indicates the accumulated annealing time scaled to a temperature of 20 °C, where the aforementioned scaling was used.

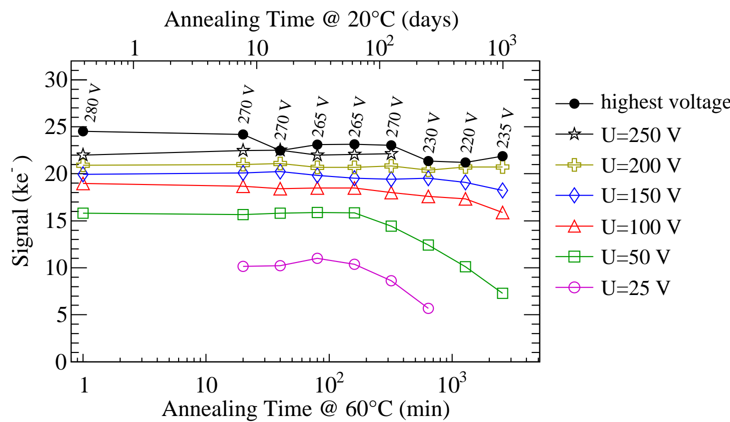

Figure 6.59: Signal of the p-in-n detector irradiated to $2 \times 10^{15}\,n_{eq}/cm^2$ as a function of the accumulated annealing time for different bias voltages. The measurement performed before annealing is represented by the data point shown at 1 min at 60 °C. "Highest voltage" is the maximum voltage for which a measurement could be performed, these voltages are indicated for each annealing step.

Up to an accumulated annealing time of approximately 160 min at 60 °C, the signal remains relatively constant. Longer annealing times lead to a signal decrease for bias voltages up to 150 V. The signal measured at bias voltages of 200 V or higher does not decrease with the annealing time. However, a decrease of the breakdown voltage required that the maximum bias voltage was lowered. Therefore, the signal measured at the highest bias voltage applied decreases during the annealing studies. A decrease of the breakdown voltage from approximately 290 V before annealing to approximately 235 V after the last annealing step could be observed.

The signal for different bias voltages as a function of the accumulated annealing time is shown in Fig. 6.60 for the n-in-p detector irradiated to $2 \times 10^{16}\,n_{eq}/cm^2$. Figure 6.61 shows the signal measurements of the p-in-n detector irradiated to the same fluence. For both detectors, the long-term annealing leads to an increase of the signal measured at high bias voltages (above 250 V).

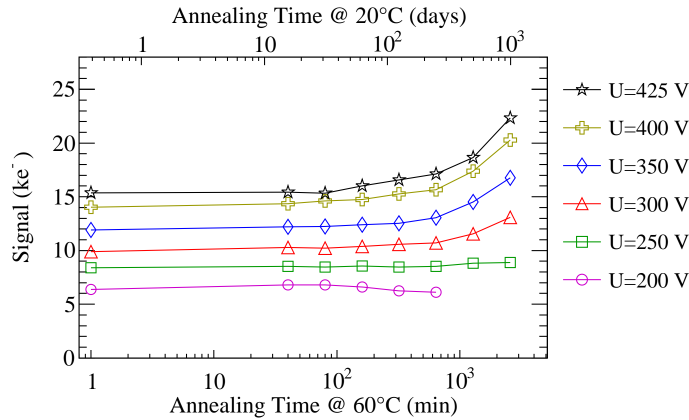

Figure 6.60: Signal of the n-in-p detector irradiated to $2 \times 10^{16}\,\mathrm{n_{eq}/cm^2}$ as a function of the accumulated annealing time for different bias voltages. The measurement performed before annealing is represented by the data point shown at 1 min at 60 °C.

The signal of the n-in-p detector irradiated to $2 \times 10^{16}\,\mathrm{n_{eq}/cm^2}$ (Fig. 6.60) measured at a voltage of 425 V starts to increase after an accumulated annealing time of 160 min at 60 °C. The signal measured at lower bias voltages, down to 250 V, also increases during the long-term annealing. However, longer annealing times are necessary to see this effect. The signal measured at a bias voltage of 200 V increases very slightly up to an annealing of 80 min. Thereafter the signal decreases and finally, after an accumulated annealing time of 1280 min, it is too low to achieve a separation from the noise distribution. After an accumulated annealing time of 2560 min, the signal measured at 425 V, the highest bias voltage applied, is $(22.4 \pm 1.2)\,\mathrm{ke^-}$. Therefore, the maximum signal of the unirradiated detector could be reached and a signal-to-noise ratio of 19 could be measured. The bias voltages were not increased beyond 425 V due to a strong increase of the leakage current (see below).

The signal measured with the p-in-n detector irradiated to $2 \times 10^{16}\,\mathrm{n_{eq}/cm^2}$ (Fig. 6.61) remains relatively constant for low bias voltages (below 250 V) up to an annealing time of 320 min at 60 °C. Subsequently, the signal measured at these voltages decreases. In contrast to that, the signal measured at high voltages decreases somewhat up to an annealing time of 640 min and increases after subsequent annealing steps. After intermediate annealing times, strong noise at high bias voltages (see below) made the separation of signal and noise difficult. Hence, after an accumulated annealing time of 80 min and 160 min, the highest voltage, for which a signal measurement could be performed, was lower than 325 V. The highest bias voltage could be increased after long annealing times, as a strong decrease of the noise facilitated to separate signal and noise for measurements performed at higher bias voltages. The maximum bias voltage for this detector is limited by an increase of the noise, which renders a separation of signal and noise impossible. After an accumulated annealing time of 2560 min at 60 °C, the signal of the unirradiated detector could be recovered and a signal-to-noise ratio of 20 could be obtained at a bias voltage of 400 V.

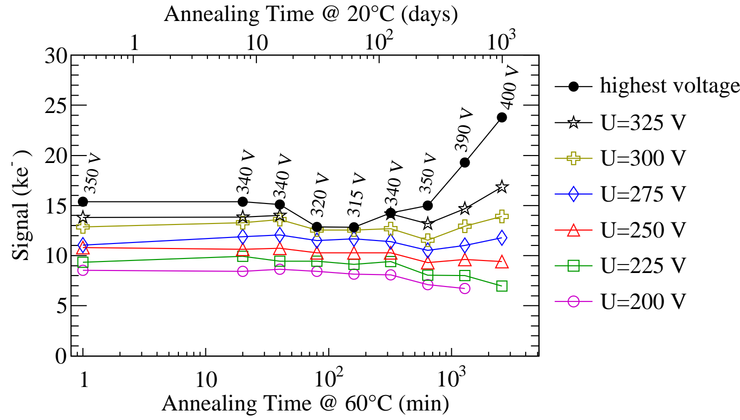

Figure 6.61: Signal of the p-in-n detector irradiated to $2 \times 10^{16}\,\mathrm{n_{eq}/cm^2}$ as a function of the accumulated annealing time for different bias voltages. The measurement performed before annealing is represented by the data point shown at 1 min at 60 °C. "Highest voltage" is the maximum voltage for which a measurement could be performed, these voltages are indicated for each annealing step.

The observations presented above can be correlated to the well-established model of annealing (see Section 4.3.1): the effective doping concentration decreases during short-term annealing (up to approximately 80 min at 60 °C) and increases during long-term annealing. The increase of the effective doping concentration during long-term annealing increases the gradient of the electric field in the detector volume. Therefore, the volume which exhibits high electric fields is reduced at low bias voltages and lower signals are measured. At high voltages, the charge multiplication probability increases since the increased doping concentration leads to more pronounced peaks of the electric field. This effect can enhance the signal of the detectors irradiated to $2 \times 10^{16}\,\mathrm{n_{eq}/cm^2}$. A similar behaviour was observed in measurements of planar n-in-p detectors irradiated up to a fluence of $5 \times 10^{15}\,\mathrm{n_{eq}/cm^2}$ [Man11].

A decrease of the breakdown voltage of the p-in-n detector irradiated to a fluence of $2 \times 10^{15}\,\mathrm{n_{eq}/cm^2}$ during the annealing could be observed. Potentially, this observation is related to the increase of the maxima of the electric field. Due to the early breakdown, a possible increase of the signal during the long-term annealing could not be observed with this detector.

The annealing of the trapping probability (see Section 4.3.3) could in principle further influence the dependence of the measured signal on the annealing time. Annealing leads to an increase of the trapping probability of holes and to a decrease of the trapping probability of electrons. Since both types of charge carriers significantly contribute to the signal in 3D detectors (see Section 5.1.1), the total trapping probability will hardly change with annealing.

Noise Measurements

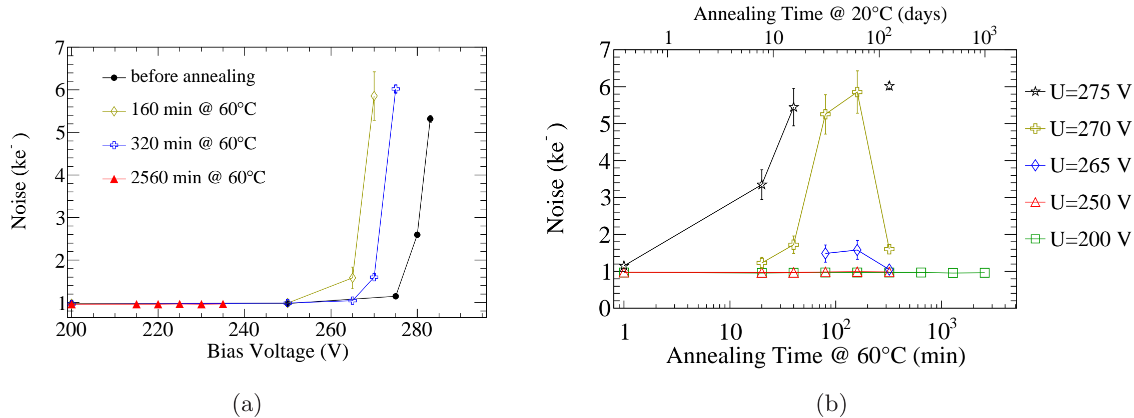

Figure 6.62: Average noise of the p-in-n detector irradiated to $2 \times 10^{15}\,\mathrm{n_{eq}/cm^2}$. (a) Noise as a function of the applied bias voltage for selected annealing times, (b) noise for different bias voltages as a function of the annealing time. Only statistical errors are shown, in most cases the error bars are smaller than the markers. The measurement performed before annealing is represented by the data point shown at 1 min at 60 °C.

The results of noise measurements are shown in Figs. 6.62-6.64 for the three detectors investigated. In the left part of the figures, the noise is shown as a function of the applied bias voltage for selected annealing times. The right part shows the noise for selected bias voltages as a function of the accumulated annealing time.

The dependence of the noise on the annealing time is similar for all detectors: short-term annealing (up to approximately 80 min at 60 °C) increases the noise, long-term annealing decreases the noise. However, the annealing behaviour of the noise of the p-in-n detector irradiated to $2 \times 10^{16}\,\mathrm{n_{eq}/cm^2}$ (see Fig. 6.64) shows a somewhat accelerated annealing behaviour compared to that of the other detectors. The maximum of the noise of this sensor is measured after an accumulated annealing time of 80 min, whereas the maximum noise of the other sensors is measured after an annealing time of 160 min.

After long annealing times, the noise of the detectors irradiated to $2 \times 10^{16}\,\mathrm{n_{eq}/cm^2}$ at high bias voltages is considerably lower than it was before annealing. At low bias voltages, the noise is given by the capacitive noise of the amplifier, which does not change during the annealing. The noise of the n-in-p detector irradiated to $2 \times 10^{16}\,\mathrm{n_{eq}/cm^2}$ (see Fig. 6.63) measured at high voltages falls below the noise measured before annealing after an annealing time of 1280 min. For the p-in-n detector irradiated to the same fluence (see Fig. 6.64), this is the case already after an annealing time of $320 - 640$ min, depending on the bias voltage under consideration.

The annealing of the noise behaviour is not fully understood. Especially, the increase of the noise during the short-term annealing appears surprising. According to the shot noise parameterisation $\mathrm{ENC_{shot}} = \sqrt{B\,I_l\,M\,F}\,e$ (see Section 3.3.8 and Section 6.2.4), a decrease

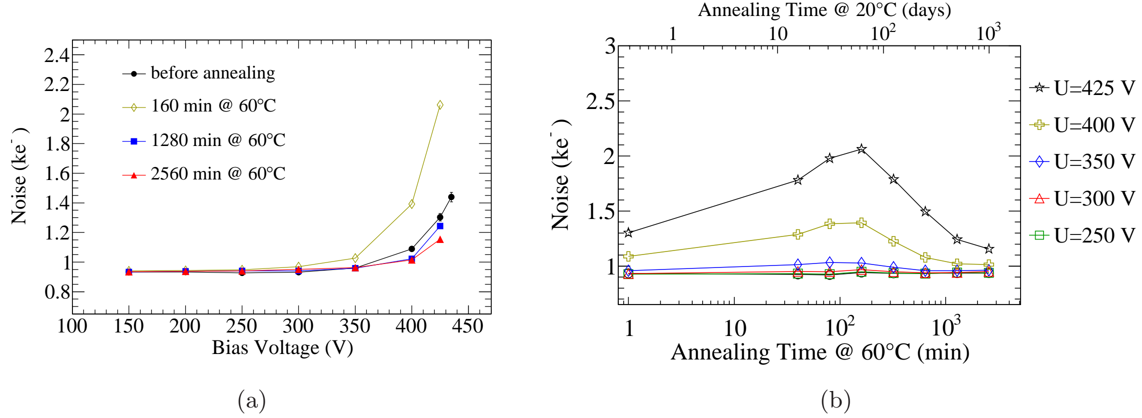

(a)

(b)

Figure 6.63: Average noise of the n-in-p detector irradiated to 2×10^{16} n_{eq}/cm^2. (a) Noise as a function of the applied bias voltage for selected annealing times, (b) noise for different bias voltages as a function of the annealing time. Only statistical errors are shown, in most cases the error bars are smaller than the markers. The measurement performed before annealing is represented by the data point shown at 1 min at 60 °C.

of the current I_l, as observed in the p-in-n detectors (see below), would lead to lower noise. The other factors are assumed to be constant. The multiplication M does not change during the short-term annealing, as can be seen from the signal measurements. Hence, the excess noise factor F is assumed to be constant, too. A further contribution to the noise could originate from an increased rate of micro-discharge. However, the opposite would be expected, since the decrease of the effective doping concentration during the beginning of the annealing would lead to a reduction of the peaks of the electric field.

The long-term annealing can be regarded as very beneficial for the operation of highly irradiated 3D detectors. It leads to increased signal and to decreased noise. This is in contrast to expectations obtained from the standard annealing model [Lin01, Mol99] (see also Section 4.3.1), which is based on measurements at lower irradiation fluences. Based on considerations of the effective doping concentration, short term annealing was for a long time regarded as beneficial and long-term annealing was regarded to have negative consequences. However, these traditional considerations did not take into account any charge multiplication effects.

Leakage Current

As discussed in Section 4.3.2, a gradual decrease of the leakage current is expected during the annealing. Figure 6.65 shows the leakage current as a function of the applied bias voltage for the three detectors investigated. The measurements were performed after each annealing step. The current of the guard ring was not measured separately, therefore the quoted values can include surface or edge currents in addition to the bulk current. According to Eq. (4.10), Section 4.3.2, a decrease of the bulk generated leakage current by a factor of 2.4 is expected during the annealing of 2560 min at 60 °C. For this calcu-

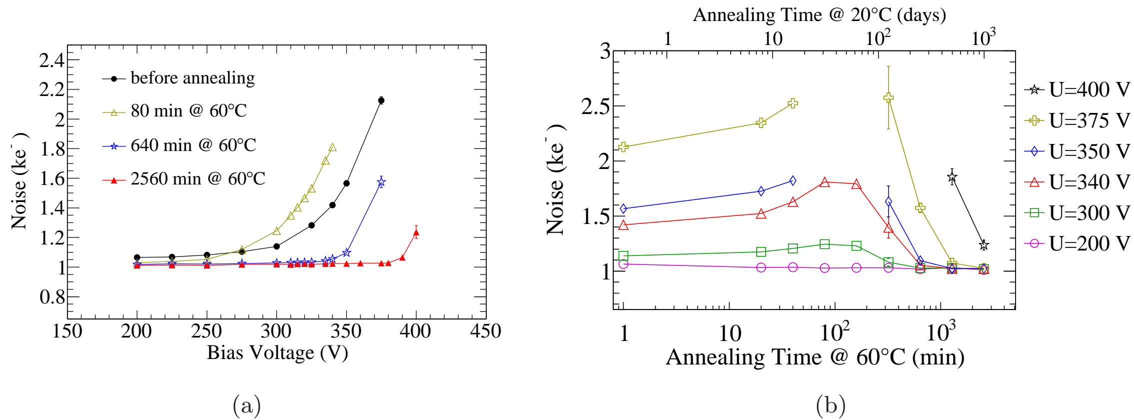

(a)

(b)

Figure 6.64: Average noise of the p-in-n detector irradiated to $2 \times 10^{16}\,\mathrm{n_{eq}/cm^2}$. (a) Noise as a function of the applied bias voltage for selected annealing times, (b) noise for different bias voltages as a function of the annealing time. Only statistical errors are shown, in most cases the error bars are smaller than the markers. The measurement performed before annealing is represented by the data point shown at 1 min at 60 °C.

lation, unintentional annealing before the beginning of the measurement series has been neglected. Strictly, this calculation applies only as long as the fraction of the volume which exhibits a non-negligible electric field remains constant during the annealing. Since even the undepleted bulk of highly irradiated detectors is resistive (see Section 4.3.4), this assumption can be taken as a basis.

The leakage current measurements of the p-in-n detector irradiated with a fluence of $2 \times 10^{15}\,\mathrm{n_{eq}/cm^2}$ are shown in Fig. 6.65(a). In the plateau region, between approximately 50 V and 250 V, the current decreases with increasing annealing time. For higher bias voltages, this trend cannot be identified, possibly due to the onset of electrical breakdowns or micro-discharges. At a bias voltage of 200 V, the leakage current measured after an accumulated annealing time of 2560 min at 60 °C is a factor of 2.0 ± 0.2 lower than before annealing. This decrease is somewhat lower than the expected one. A slight increase of the leakage between the last two annealing steps can be observed. Possibly, this effect is related to an increase of the surface current.

Figure 6.65(b) summarises the leakage current measurements of the n-in-p detector irradiated to $2 \times 10^{16}\,\mathrm{n_{eq}/cm^2}$. The observed behaviour differs from the expectation, as a continuous decrease of the current with annealing time cannot be observed. The highest leakage current was measured after an annealing time of 160 min, whereas the leakage current reaches a minimum after an annealing of 640 min. Interestingly, the noise of this detector also reaches a maximum after an accumulated annealing time of 160 min (see above). However, a correlation between the noise and the leakage current effects cannot be generally identified. The noise of the p-in-n detectors irradiated to $2 \times 10^{15}\,\mathrm{n_{eq}/cm^2}$ and $2 \times 10^{16}\,\mathrm{n_{eq}/cm^2}$ also exhibits a maximum after an annealing time of $80 - 160$ min (see above), whereas the current of those detectors decreases continuously during the annealing.

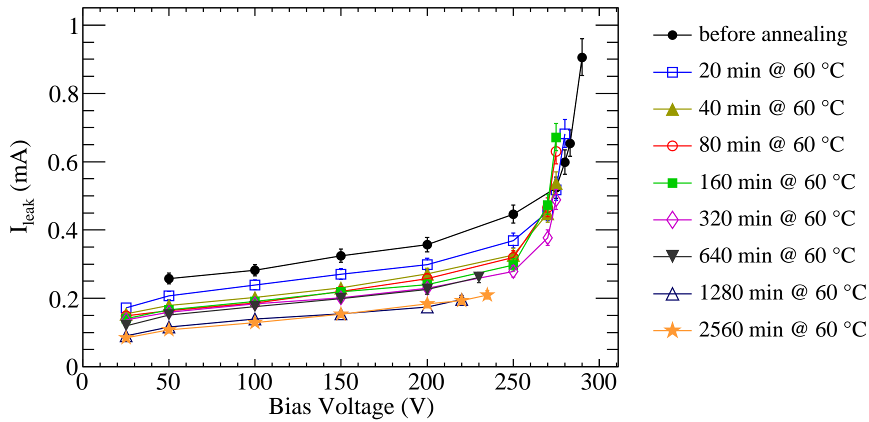

(a) p-in-n detector, $\Phi_{eq} = 2 \times 10^{15}\ n_{eq}/cm^2$

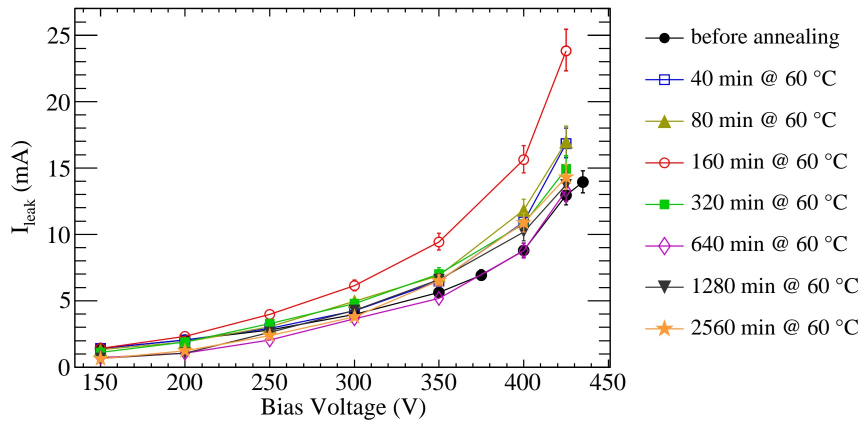

(b) n-in-p detector, $\Phi_{eq} = 2 \times 10^{16}\ n_{eq}/cm^2$

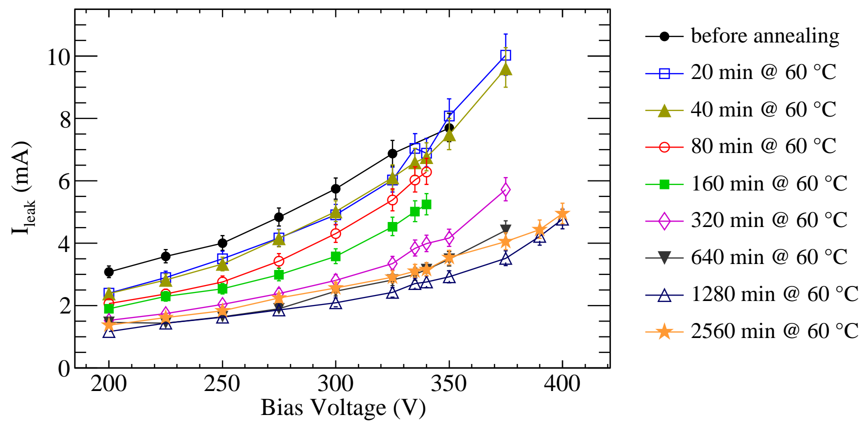

(c) p-in-n detector, $\Phi_{eq} = 2 \times 10^{16}\ n_{eq}/cm^2$

Figure 6.65: Leakage current of the three detectors investigated as a function of the applied bias voltage. The current was measured after each annealing step and is scaled to a reference temperature of $+20\,^{\circ}$C.

Presumably, edge or surface currents lead to the unexpected annealing behaviour of the n-in-p detector irradiated to $2 \times 10^{16}\,n_{eq}/cm^2$. Furthermore, it is possible that a higher charge multiplication probability after annealing increases the leakage current. It could be observed that the leakage current increased with time after changing the bias voltage. Typically, a current increase between 10% and 40% could be observed in a period of approximately 25 min. The current values quoted in Fig. 6.65(b) were measured directly after ramping to a defined bias voltage. Only after performing the annealing studies, it was noticed that the increase of the leakage current with time is related to the presence of the radioactive source. All leakage current measurements reported in this section were performed while the detector was installed in the beta source setup, with the radioactive source being directed towards the sensor. In measurements performed in the absence of the radioactive source, an increase of the leakage current with time was not observed. The reason for this behaviour is not understood. Possibly, an accumulation of charge carriers in the surface region or close to the sensor edges leads to a change of the potential distribution, which then affects the leakage current.

The noise is not affected by the current increase with time, which was verified by a measurement at a bias voltage of 425 V after an accumulated annealing time of 1280 min. The current, measured at a temperature of $-43\,^{\circ}C$, increased from 20 µA to 28 µA within approximately 25 min. The noise, measured before and after the current increase, was constant. Assuming that shot noise has a significant effect on the total noise, this observation indicates that the additional current is mainly drawn by the guard ring. Otherwise, the increase of the leakage current would also increase the noise.

The measurements of the leakage current of the p-in-n detector irradiated to $2\times10^{16}\,n_{eq}/cm^2$ are shown in Fig. 6.65(c). A decrease of the leakage current with annealing time can be observed. At a bias voltage of 250 V, the current measured after an accumulated annealing time of 2560 min is a factor of 2.2 ± 0.2 lower than before annealing. This decrease is in agreement with the expected decrease by a factor of 2.4 (see above). However, the leakage current measured after the last annealing step, corresponding to an accumulated annealing time of 2560 min, exceeds the current measured after the previous annealing step. The last annealing step leads to a current increase of 10%-20%. A similar behaviour was observed with the p-in-n detector irradiated to $2 \times 10^{15}\,n_{eq}/cm^2$ (see above).

6.2.6 Laser Measurements

In this section, laser measurements performed with the p-in-n and n-in-p detectors irradiated with fluences of $2 \times 10^{15}\,n_{eq}/cm^2$ and $2 \times 10^{16}\,n_{eq}/cm^2$ are presented. The measurements were performed at sensor temperatures of approximately $-30\,^{\circ}C$. The discussion of the results follows that of the measurements performed with unirradiated detectors in Section 6.1.4. Details of the measurement and analysis procedures can be found there. The results presented in this section are published in Refs. [Kö11b, Bat11]. The p-in-n detector irradiated to $2 \times 10^{15}\,n_{eq}/cm^2$ and both detectors irradiated to $2 \times 10^{16}\,n_{eq}/cm^2$ were measured before annealing and after an accumulated annealing time of 2560 min at $60\,^{\circ}C$. Below, two-dimensional illustrations of the signal measured in laser scans, where the laser was scanned over a region shown in Fig. 6.66, are presented. The signals of the

two strips around the laser point of incidence are summed. It has to be kept in mind that the absolute signals measured with different detectors cannot be compared directly, due to possible differences of the surface reflectivities.

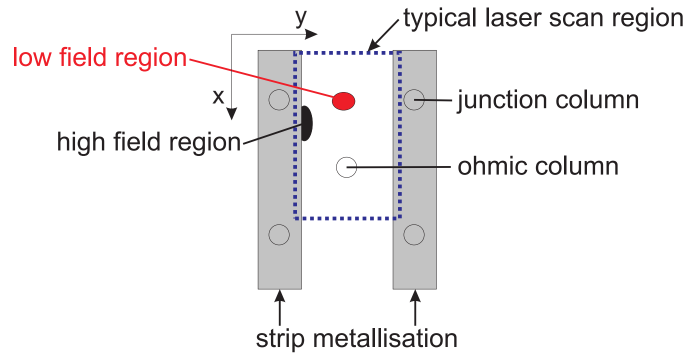

Figure 6.66: Sketch of a unit cell of a 3D strip detector. The region typically scanned with the infrared laser is delimited by the dashed line. A detailed investigation of the signals induced by the laser shining on the high and low-field regions is presented below.

Figure 6.67 shows the results of laser scans of the n-in-p detector irradiated to $2 \times 10^{15}\,\mathrm{n_{eq}/cm^2}$. The measurements were performed at bias voltages between 25 V and 260 V. The metallisation of the readout strips, where the laser light is reflected and only marginal signals are measured, are located at the left and right edges of the scanned regions. The ohmic column appears at the lower right corner. It can be seen that its position deviates significantly from the design position in the middle between the readout strips. The same effect, which is an undesired production feature, was observed in the measurements of the unirradiated detectors, see Section 6.1.4. The positions of the ohmic columns differ from detector to detector, as can be seen in the measurements presented below.

At a bias voltage of 25 V (Fig. 6.67(a)) the signal is very non-uniform. The sensor is not fully depleted, at least the electric field is low in wide regions. Charge carriers liberated in these regions recombine quickly or perform only a very slow drift within the integration time of the amplifier. The regions exhibiting low signals correspond to the regions where the electric field reaches minima, see Fig. 6.16, Section 6.1.2, and Fig. 5.4, Section 5.1.1. The highest signals are measured for laser impact positions close to the strip edge on the direct line between an ohmic column and a junction column. These regions are visible in the upper left corner of Fig. 6.67(a). The junction columns are covered by the strip metallisation, hence an investigation of the area directly around these electrodes is not possible.

The signal is more uniform in the measurement performed at a bias voltage of 150 V, see Fig. 6.67(b). However, lower signals are measured in the low-field region and at the position of the ohmic column. Due to the lower electric field strength, charge carriers generated in the low-field region drift more slowly than charge carriers generated elsewhere. Furthermore, the drift path of these charge carriers is longer. Both effects lead to a higher trapping probability.

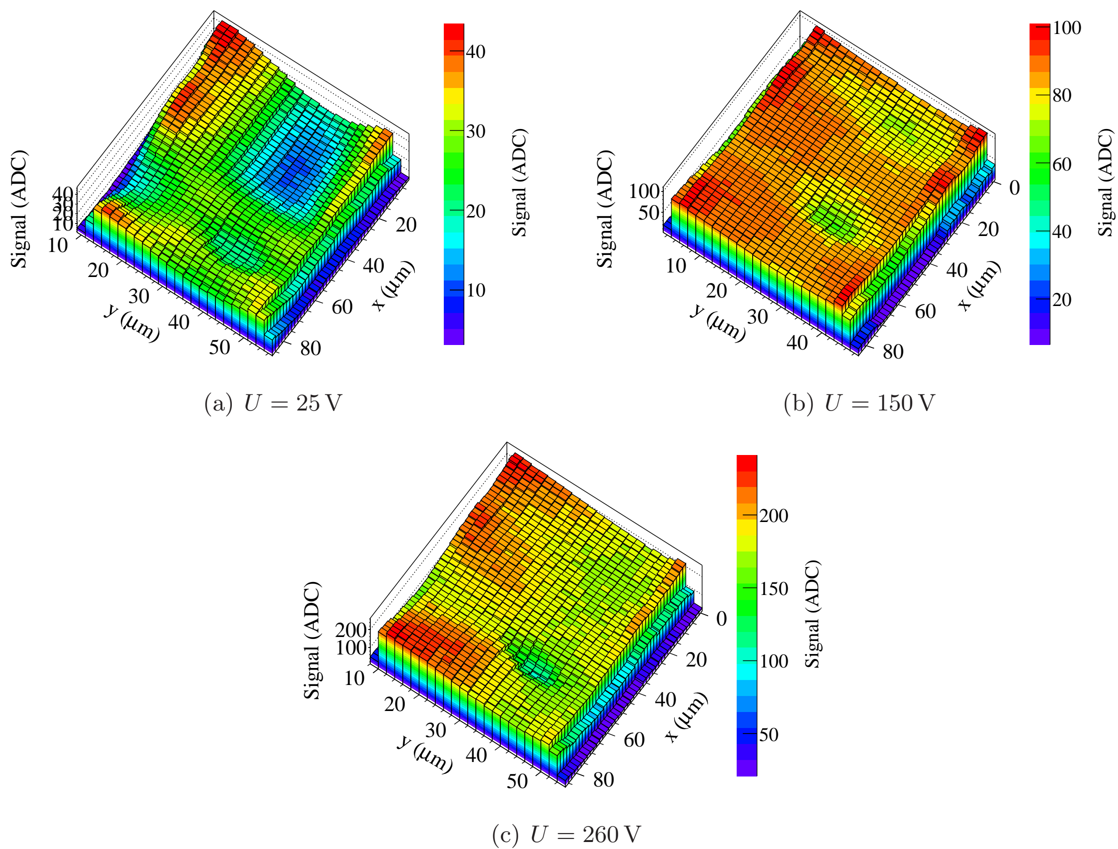

(a) $U = 25\,\mathrm{V}$

(b) $U = 150\,\mathrm{V}$

(c) $U = 260\,\mathrm{V}$

Figure 6.67: Results of laser measurements performed at different bias voltages U (25, 150 and 260 V) with the n-in-p detector irradiated to $2 \times 10^{15}\,\mathrm{n_{eq}/cm^2}$. The different colour scales should be noted.

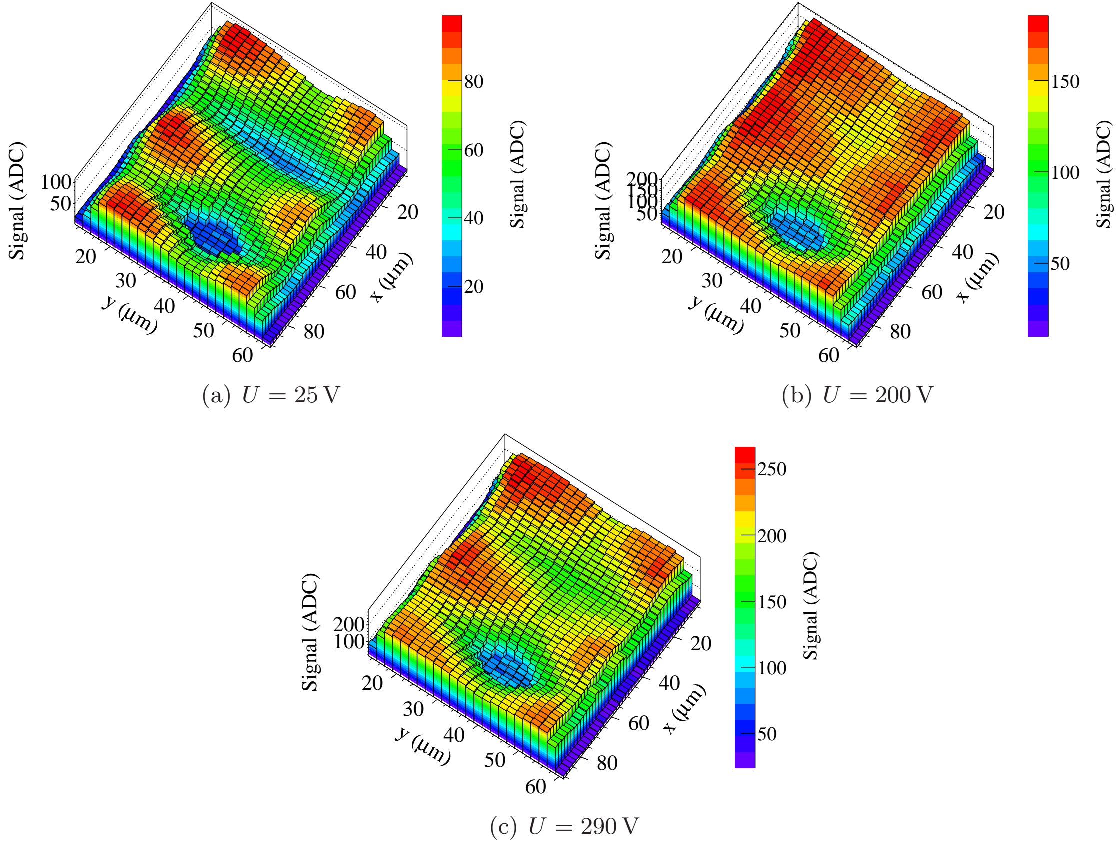

Figure 6.68: Results of laser measurements performed at different bias voltages U (25, 200 and 290 V) with the p-in-n detector irradiated to $2 \times 10^{15}\,\mathrm{n_{eq}/cm^2}$. All measurements were performed before annealing. The different colour scales should be noted.

At 260 V, the maximum bias voltage applied (Fig. 6.67(c)), the signal for all laser impact positions is considerably higher compared to the measurement at a bias voltage of 150 V. Also the beta source measurements (see Section 6.2.3) showed a strong increase of the signal for bias voltages exceeding 150 V, which can be attributed to charge multiplication. Particularly high signals are measured if the laser impinges close to the junction column on the direct line between an ohmic column and a junction column. These regions can be seen at the left hand side of Fig. 6.67(c). Electrons generated in these regions are directly injected into the high-field region around the junction columns, hence they have a high multiplication probability. A similar behaviour was observed in beam test measurements, see Section 6.2.2.

Results of laser scans performed with the p-in-n detector irradiated to $2 \times 10^{15}\,\mathrm{n_{eq}/cm^2}$ are shown in Fig. 6.68. The behaviour is similar to that of the n-in-p detector irradiated to the same fluence (see Fig. 6.67). At a bias voltage of 25 V (see Fig. 6.68(a)), the detector is not yet fully depleted and the signal is very inhomogeneous. At a bias voltage of 200 V (see Fig. 6.68(b)), the entire detector volume is active. Lower signals are measured if the laser impinges on the position of the ohmic column and on the low-field region.

The region exhibiting lower signals at the position of the ohmic column does not appear as sharply bounded as in the measurements performed with the n-in-p detector. If the laser impinges close to the ohmic columns, the signal in 3D p-in-n detectors is largely dominated by holes, which drift towards the junction columns. If the laser impinges further away from the ohmic columns, the drift path of electrons is longer and hence their contribution to the signal increases. Since holes experience a higher trapping probability than electrons, the signal is lower if it is dominated by holes.

In the measurement performed at a bias voltage of 290 V (see Fig. 6.68(c)), considerably higher signals are measured on the line connecting an ohmic column and a junction column. As in the case of the n-in-p detector discussed above, this observation is attributed to charge multiplication. Indications of charge multiplication at bias voltages of approximately 290 V were also found with beta source measurements, see Section 6.2.3. Multiplication of holes requires considerably higher electric fields than multiplication of electrons (see section 3.3.7). Thus, it can be assumed that mainly electrons drifting towards the ohmic electrode are multiplied in 3D p-in-n detectors.

Figure 6.69 shows the results of laser scans of the n-in-p detector irradiated to $2 \times 10^{16}\,\mathrm{n_{eq}/cm^2}$. At a bias voltage of 75 V (Fig. 6.69(a)), only a fraction of the sensor is active. Considerable signals are only measured in ring-shaped regions around the ohmic columns and around the junction columns. This result illustrates the double-junction effect (see Section 4.3.4). Even before full depletion of the sensor, regions with high electric fields are present at both types of electrodes. At a bias voltage of 350 V (Fig. 6.69(b)), the entire sensor volume is active. However, large discrepancies between the high-field region and the low-field regions exist. The discrepancies are larger than in the measurements of the detectors irradiated to lower fluences. Possible reasons are the increased trapping probability and the increased effective doping concentration, which leads to a higher gradient of the electric field. The highest signals are measured on the lines connecting an ohmic column and a junction column, where the electric field is maximal. Hence, charge carriers generated in these regions obtain a higher drift velocity, which reduces the trapping probability. Furthermore, these charge carriers have a higher multiplication probability.

After an annealing of 2560 min at 60 °C (Fig. 6.69(c)), the n-in-p detector irradiated to $2 \times 10^{16}\,\mathrm{n_{eq}/cm^2}$ yields substantially higher signals. The laser power was not changed in between the two measurements. The signals measured at a bias voltage of 350 V are approximately $50\% - 100\%$ higher than before annealing. In beta measurements, a similar relative signal increase was observed with the annealing (see Section 6.2.5). Particularly high signals are measured in the high-field region close to a junction column. Due to the increase of the effective doping concentration during the annealing, stronger charge multiplication is assumed to occur in high-field regions close to the junction columns. Given the high trapping probability, charge carriers generated closer to the junction columns have a higher probability of reaching the region where charge multiplication occurs.

Results of laser scans performed with the p-in-n detector irradiated to $2 \times 10^{16}\,\mathrm{n_{eq}/cm^2}$ are shown in Fig. 6.70. The double-junction effect is visible in the measurement performed at a bias voltage of 75 V (Fig. 6.70(a)). The detector is only active in regions around the

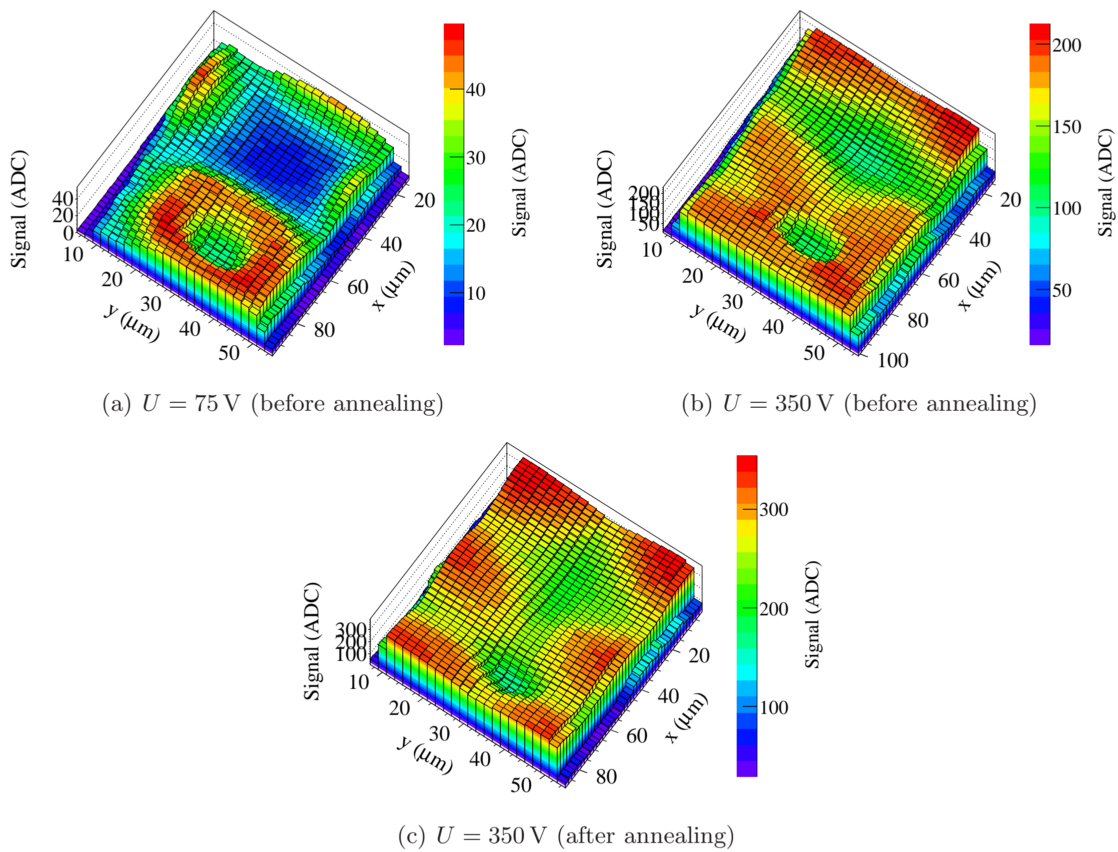

(a) $U = 75\,\mathrm{V}$ (before annealing)

(b) $U = 350\,\mathrm{V}$ (before annealing)

(c) $U = 350\,\mathrm{V}$ (after annealing)

Figure 6.69: Results of laser measurements performed at different bias voltages U with the n-in-p detector irradiated to $2 \times 10^{16}\,\mathrm{n_{eq}/cm^2}$. The measurements shown in (a) and (b) were performed before annealing, the measurement shown in (c) was performed after an accumulated annealing time of 2560 min at 60 °C. The different colour scales should be noted.

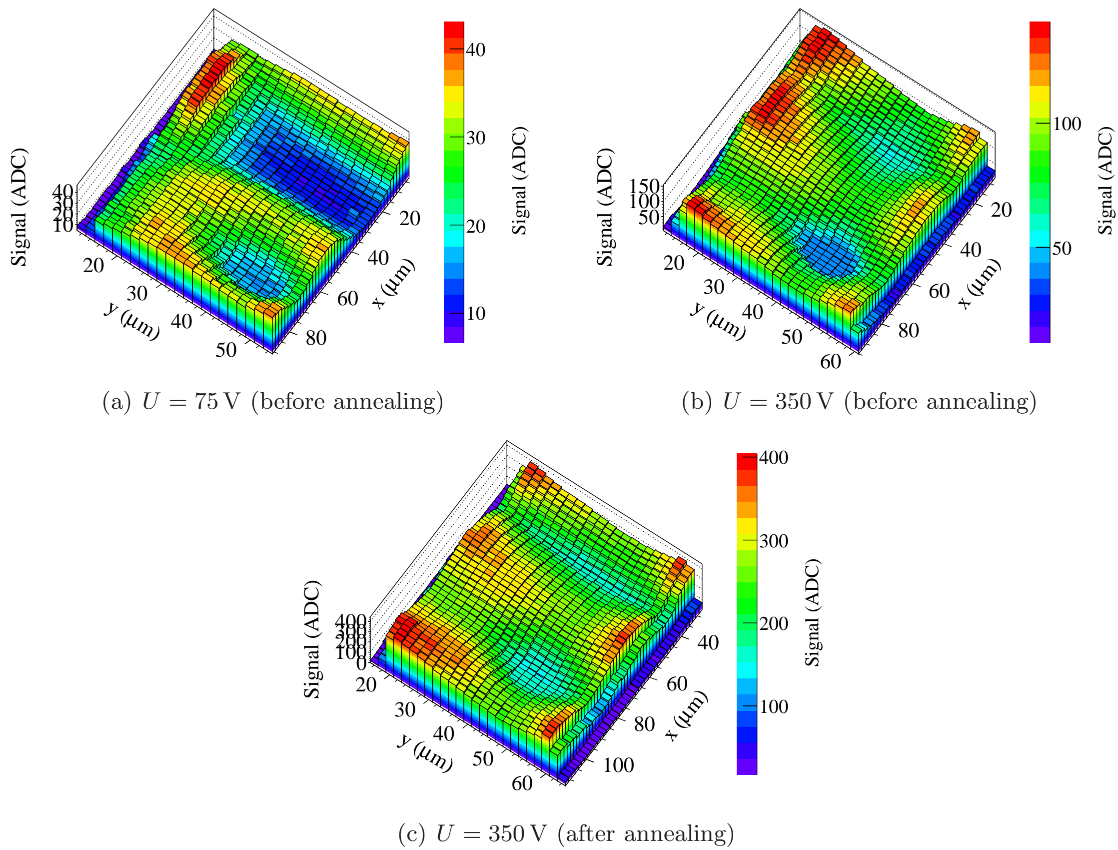

(a) $U = 75\,\text{V}$ (before annealing)

(b) $U = 350\,\text{V}$ (before annealing)

(c) $U = 350\,\text{V}$ (after annealing)

Figure 6.70: Results of laser measurements performed at different bias voltages U with the p-in-n detector irradiated to $2 \times 10^{16}\,\text{n}_{\text{eq}}/\text{cm}^2$. The measurements shown in (a) and (b) were performed before annealing, the measurement shown in (c) was performed after an accumulated annealing time of 2560 min at 60 °C. The different colour scales should be noted.

ohmic columns and around the junction columns. The same behaviour was observed in the measurements of the n-in-p detector irradiated to the same fluence (see above). At a bias voltage of 350 V (Fig. 6.70(b)), the active region extends over the entire sensor. The highest signals are measured close to the junction colum on the connection between an ohmic column and a junction column.

After annealing of 2560 min at 60 °C (Fig. 6.70(c)), the signal is considerably higher than before annealing. An increase of the signal by a factor of approximately three can be observed. This signal increase is substantially higher than that measured with the beta source (see section. 6.2.5). This discrepancy can be explained by the fact that the laser deposits its energy mostly close to the surface, while electrons emitted by a beta source deposit energy uniformly along the track. In p-in-n detectors, electrons are accelerated towards the ohmic column. Since the charge multiplication probability is larger for electrons than for holes, it is assumed that multiplication occurs mainly close to the ohmic columns. Especially strong multiplication is expected to occur around the column tips, where the focusing of the field lines leads to very high field strengths. The column tips are close to the sensor surface, where the laser deposits most of its energy. Therefore, an increase of the charge multiplication probability during the annealing could have a larger effect for the laser measurements than for the beta source measurements. Furthermore, a change of the surface reflectivity during annealing cannot be ruled out. This would strongly affect the laser measurements.

Signal in Selected Regions

Figures 6.71-6.74 show the signals measured for selected laser positions as a function of the applied bias voltage. These representations facilitate a more systematic investigation of the dependence of the signals measured in different regions on the bias voltage. Laser impact positions at the location of an ohmic column, in the high-field region and in the low-field region (see Fig. 6.66) are investigated. In these cases, the signals of the two readout strips around the laser point of impact are summed. Additionally, the signals of single strips are investigated for laser impact positions close to the junction column of the neighbouring strips. In many cases, these signals are negative, therefore this region is named “negative region” in the illustrations presented below. See Section 6.1.4 for further explanations. For each measurement series, the signals are normalised to the signal measured in the high field region at the highest bias voltage.

Figure 6.71 shows the signal of the n-in-p detector irradiated to $2 \times 10^{15}\ n_{eq}/cm^2$ as a function of the applied bias voltage. In agreement with the beta source measurements (see Section 6.2.3) and the beam test measurements (see Section 6.2.2), the signal increases strongly for bias voltages exceeding 150 V. It is apparent that not only the charge carriers generated in the high-field region undergo charge multiplication. The absolute difference between the signals in the high-field region and in the low-field region increases with increasing voltage, which confirms the results of the beam test measurements. The signals measured in the low-field region and in the region of the ohmic column are approximately equal up to a bias voltage of 150 V. However, the signal measured in the low-field region increases more strongly as a function of the applied bias voltage. The absolute values

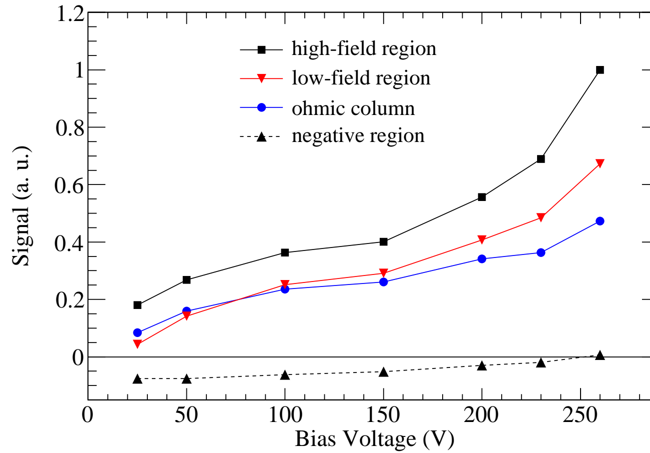

Figure 6.71: Signal for selected laser positions as a function of the applied bias voltage for the n-in-p sensor irradiated to $2 \times 10^{15}\,\mathrm{n_{eq}/cm^2}$.

of the negative signals measured on the neighbours of hit strips decrease with increasing bias voltage. The faster drift due to higher electric fields and the increased number of free charge carriers created by charge multiplication reduce the influence of ballistic deficit (see also the discussion in Section 6.1.4).

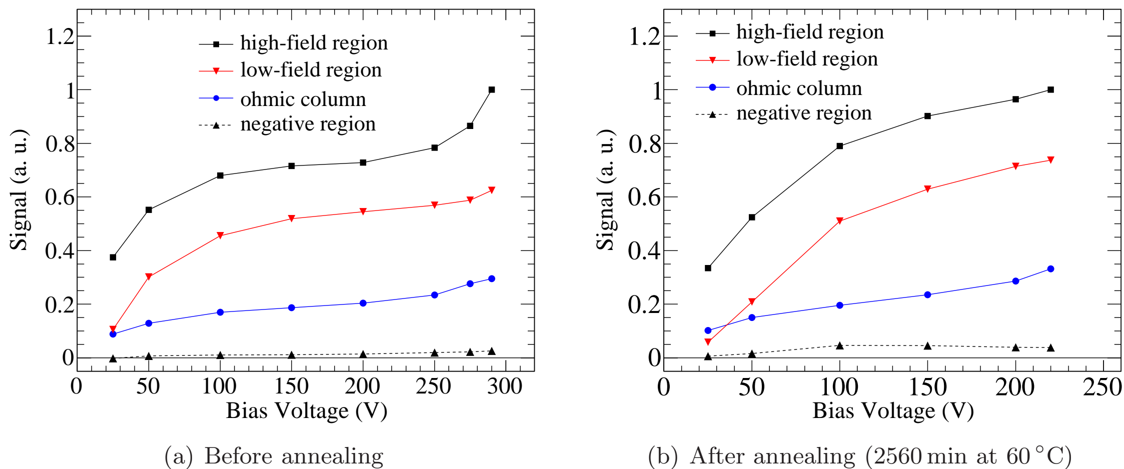

(a) Before annealing

(b) After annealing (2560 min at 60 °C)

Figure 6.72: Signal for selected laser positions as a function of the applied bias voltage for the p-in-n sensor irradiated to $2 \times 10^{15}\,\mathrm{n_{eq}/cm^2}$. The measurements were performed (a) before annealing and (b) after an accumulated annealing time of 2560 min at 60 °C. The different scales of the horizontal axes should be noted.

The signals measured for selected laser positions with the p-in-n detector irradiated to $2 \times 10^{15}\,\mathrm{n_{eq}/cm^2}$ are summarised in Fig. 6.72. Due to charge multiplication, the signals measured before annealing (Fig. 6.72(a)) in the high-field region increase strongly for bias voltages exceeding 200 V. It can be seen that the increase of the signals at high bias voltages for the other laser impact positions is less pronounced. Indications of charge mul-

tiplication were also observed in beta source measurements (see Section 6.2.3). The signals measured at the location of the ohmic column are much lower than those measured with the n-in-p detector irradiated to the same fluence. This could also result from different depths of the ohmic columns.

After annealing (Fig. 6.72(b)), a full saturation of the signal is not observed. Due to the increase of the effective doping concentration, higher voltages are required to extend the electric field through the entire sensor. A decreased breakdown voltage did not allow to apply voltages higher than 220 V. Negative signals are not measured, neither before nor after annealing.

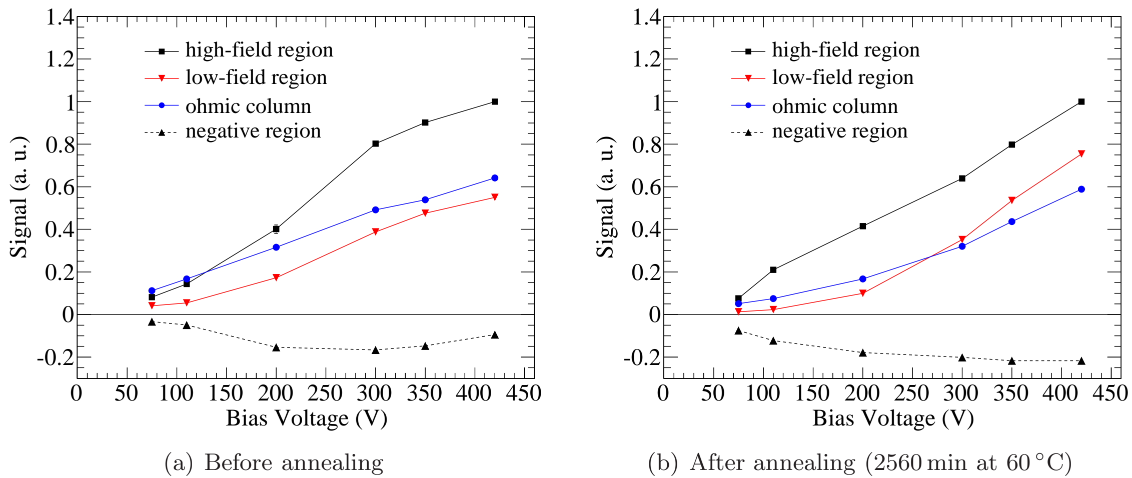

(a) Before annealing

(b) After annealing (2560 min at 60 °C)

Figure 6.73: Signal for selected laser positions as a function of the applied bias voltage for the n-in-p sensor irradiated to $2 \times 10^{16}\,\mathrm{n_{eq}/cm^2}$. The measurements were performed (a) before annealing and (b) after an accumulated annealing time of 2560 min at 60 °C.

Figure 6.73 shows the signals in selected regions for the n-in-p detector irradiated to $2 \times 10^{16}\,\mathrm{n_{eq}/cm^2}$. Before annealing (Fig. 6.73(a)), the signal starts to saturate at a bias voltage of 300 V. This is in contrast to the beta measurements (see Section 6.2.3), where a linear increase of the signal with increasing bias voltage was observed. The signal measured in the low-field region is even lower than that measured at the location of the ohmic column. It was the other way around in the detectors irradiated to lower fluences, which were discussed above. This observation is attributed to the strong increase of the trapping probability with the irradiation fluence. Due to the lower drift velocity and the longer path to the electrodes, charge carriers generated in the low-field region are particularly prone to trapping. Pronounced negative signals are measured at all bias voltages. It can be seen that the absolute values increase up to a bias voltage of 300 V and decrease for higher bias voltages. This decrease could be related to an increasing rate of charge multiplication.

After annealing of 2560 min at 60 °C (Fig. 6.73(b)), a saturation of the signals is not observed. The signal measured in the low-field region exceeds that measured at the location of the back column at voltages higher than 200 V. At a bias voltage of 420 V, which is the highest voltage applied, the signal in the low-field region is only approximately 25% lower

than that measured in the high-field region. Before annealing, the difference was larger. More pronounced negative signals are measured after annealing.

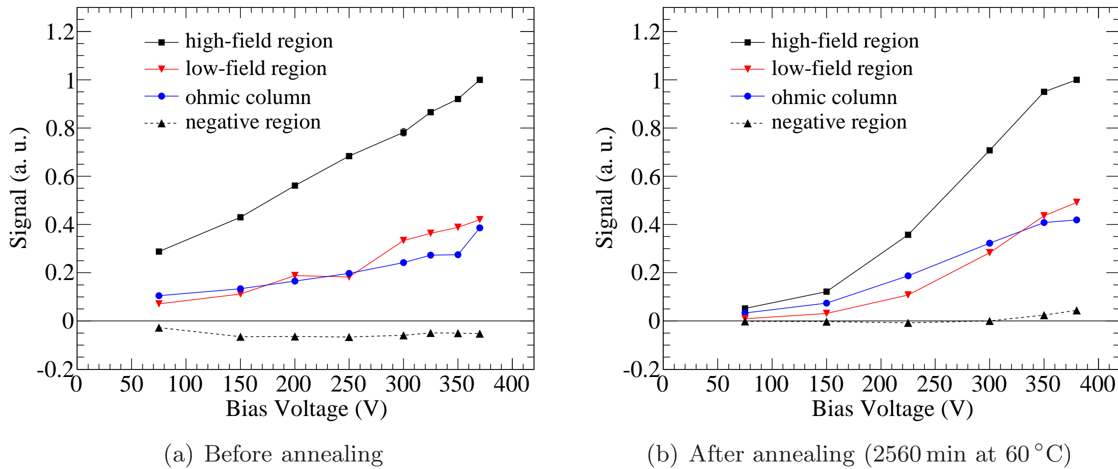

(a) Before annealing

(b) After annealing (2560 min at 60 °C)

Figure 6.74: Signal for selected laser positions as a function of the applied bias voltage for the p-in-n sensor irradiated to $2 \times 10^{16}\,\mathrm{n_{eq}/cm^2}$. The measurements were performed (a) before annealing and (b) after an accumulated annealing time of 2560 min at 60 °C.

The signal of the p-in-n detector irradiated to $2 \times 10^{16}\,\mathrm{n_{eq}/cm^2}$ is displayed in Fig. 6.74. Before annealing (Fig. 6.74(a)), the signal increases linearly with the bias voltage. This is in agreement with the beta measurements. The slope of the signal measured in the high-field region is steeper than that measured in the other regions. In the low-field region and in the position of the ohmic column, the signals are similar. The difference between the signals measured in these regions and the signal in the high-field region is larger compared to the n-in-p detector irradiated to the same fluence. Negative signals at neighbours of hit strips are measured at all bias voltages. Fore these signals, the dependence on the bias voltage is low.

After annealing (Fig. 6.74(b)), the slope of the signal curves is much steeper than before annealing. The curves start to saturate at a bias voltage of 350 V. Negative signals are not observed any more.

Signal Projections

Figures 6.75-6.78 show projections of single strip signals as a function of the distance to the strip centre. The regions of the strip metallisations, where the laser is reflected, are hatched. In contrast to the measurements shown above, the signals of the two strips around the laser point of incidence are not summed. The figures are projections of the signals measured in two-dimensional laser scans as indicated in Fig. 6.66. The regions are typically approximately 80 µm long in the direction of the readout strips (see also the explanations in Section 6.1.4).

These representations facilitate an investigation of the asymmetry, which is induced by the deviation of the position of the ohmic columns from the design position in the middle between two readout strips. As can be seen in the two-dimensional representations of the laser scans (Figs. 6.67-6.70), the ohmic columns of all detectors investigated are shifted into the positive direction in the coordinate system used.

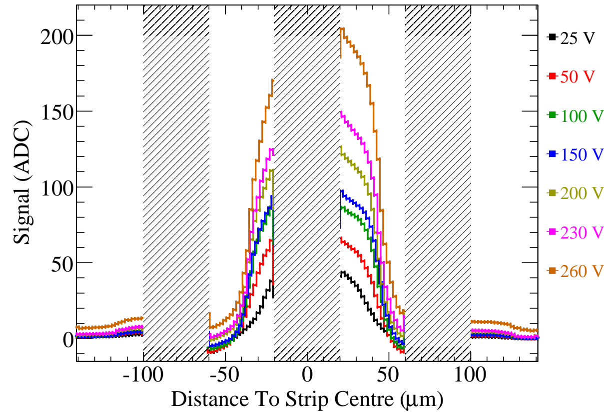

Figure 6.75: Projections of single strip signals of the n-in-p detector irradiated to $2 \times 10^{15}\,\mathrm{n_{eq}/cm^2}$. The regions of the strip metallisations, where the laser is reflected, are hatched.

Figure 6.75 shows signal projections of the n-in-p detector irradiated to $2 \times 10^{15}\,\mathrm{n_{eq}/cm^2}$. A left-right asymmetry of the signal is apparent due to the shift of the ohmic columns into the positive direction of the horizontal axis. Up to bias voltages of 150 V, the maximal signals measured for laser impact positions on the left and right side of the strip are approximately equal. At higher voltages, where strong charge multiplication occurs, the signal on the right side of the strip metallisation increases more strongly than that measured on the left side. The charge multiplication also increases the signals measured on neighbours of hit strips.

Projections of the signal measured with the p-in-n detector irradiated to $2 \times 10^{15}\,\mathrm{n_{eq}/cm^2}$ are displayed in Fig. 6.76. The displacement of the ohmic column is small, therefore the signals are less asymmetric compared to the n-in-p detector irradiated to $2 \times 10^{15}\,\mathrm{n_{eq}/cm^2}$. After annealing, significantly higher signals are measured. This effect was also observed for the other detectors, for which annealing studies were performed (see above). The laser measurements show a more pronounced increase of the signal than the beta measurements. The laser power was not changed in between the measurements. Potentially, the observed behaviour is caused by an increase of the charge multiplication probability close to the sensor surface or by a decrease of the surface reflectivity during the annealing.

Figure 6.77 shows signal projections of the n-in-p detector irradiated to $2 \times 10^{16}\,\mathrm{n_{eq}/cm^2}$. Although the ohmic columns are displaced into the positive x-direction, somewhat higher signals are measured at the left side of the readout strip. After annealing (Fig. 6.77(b)), higher signals are measured, as discussed above. As the effective doping concentration has increased during annealing, higher voltages are necessary in order to extend the active

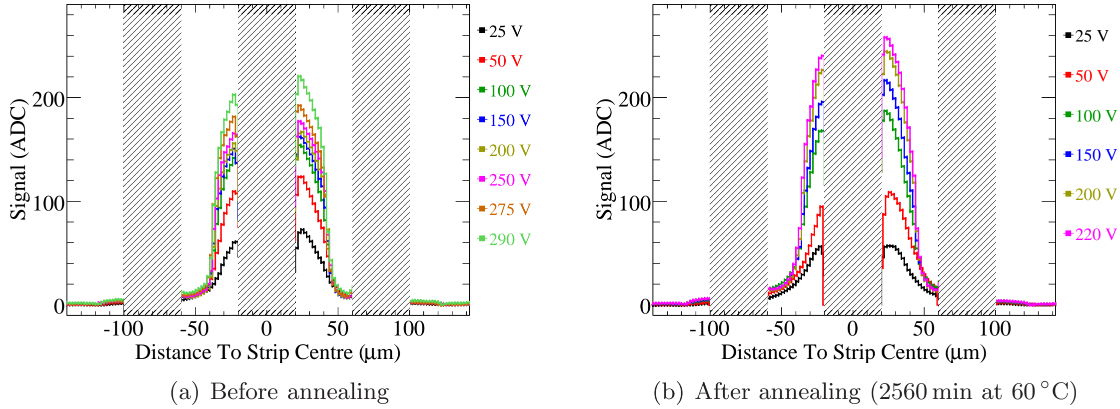

(a) Before annealing (b) After annealing (2560 min at 60 °C)

Figure 6.76: Projections of single strip signals of the p-in-n detector irradiated to $2 \times 10^{15}\,\mathrm{n_{eq}/cm^2}$. The measurements were performed (a) before annealing and (b) after an accumulated annealing time of 2560 min at 60 °C.

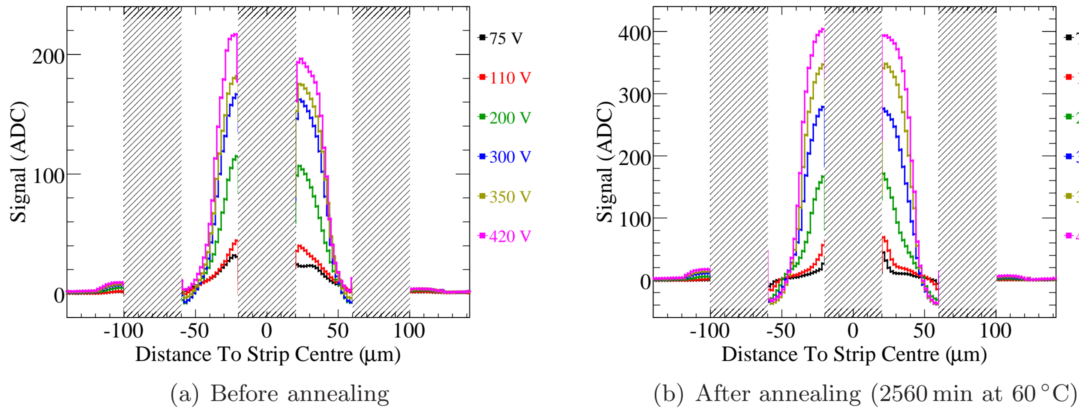

(a) Before annealing (b) After annealing (2560 min at 60 °C)

Figure 6.77: Projections of single strip signals of the n-in-p detector irradiated to $2 \times 10^{16}\,\mathrm{n_{eq}/cm^2}$. The measurements were performed (a) before annealing and (b) after an accumulated annealing time of 2560 min at 60 °C.

region over the entire sensor. Therefore, the region which yields high signals is visibly narrower than before annealing, as long as measurements performed with bias voltages below 300 V are considered.

Figure 6.78 shows signal projections of the p-in-n detector irradiated to $2 \times 10^{16}\,\mathrm{n_{eq}/cm^2}$. The displacement of the ohmic columns is larger compared to the n-in-p detector irradiated to the same fluence. Higher signals are measured at the right side of the strip metallisation. In the measurements performed before annealing, the signal decreases linearly with increasing distance to the centre of the readout strip. After annealing, the shape is more similar to an s-curve, especially at low voltages on the right side of the strip. As mentioned above, considerably higher signals are measured after annealing.

In the p-in-n detector irradiated to $2 \times 10^{16}\,\mathrm{n_{eq}/cm^2}$, considerable signals are measured if the laser impinges close to the metallisation of the neighbouring readout strip. This effect

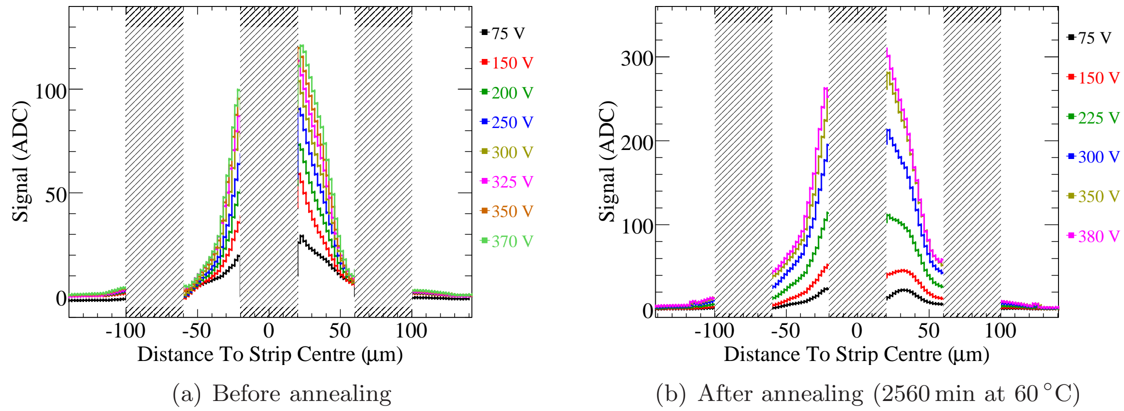

(a) Before annealing

(b) After annealing (2560 min at 60 °C)

Figure 6.78: Projections of single strip signals of the p-in-n detector irradiated to $2 \times 10^{16}\,\mathrm{n_{eq}/cm^2}$. The measurements were performed (a) before annealing and (b) after an accumulated annealing time of 2560 min at 60 °C. The different scales of the vertical axes should be noted.

is even more pronounced after annealing. As most of the charge carriers generated in these regions will be collected by the neighbouring readout strip, these signals are assumed to originate from ballistic deficit or trapping (see also the discussion in Section 6.1.4). The signal induced on an electrode is zero, if all charge carriers reach another electrode within the shaping time of the amplifier. Possibly, the positive signals result from the high trapping probability of holes drifting towards neighbouring electrodes. This would explain the increase of this effect with annealing, since the trapping probability of holes increases with annealing, while that of electrons decreases (see Section 4.3.3).

Conclusion

In summary, it was observed that the entire detector volume is active even after an irradiation fluence of $2 \times 10^{16}\,\mathrm{n_{eq}/cm^2}$. However, the signal magnitude depends on the position of the energy deposition. Lower signals are measured in the middle between the columnar electrodes, especially in the most highly irradiated detectors. Furthermore, the columnar electrodes represent a passive volume, therefore lower signals are also measured for particles impinging on the electrode's locations. This effect also exists, of course, in unirradiated detectors. The performance degradation originating from these inefficient regions can be limited by tilting the detectors. In this approach, particle tracks would impinge on the sensors under a certain angle and they would not only traverse inefficient regions.

Chapter 7

Measurements of Planar Detectors

While the primary focus of this thesis is the detailed investigation of double-sided 3D detectors, the radiation hardness of planar detectors is also investigated. In this chapter, measurements of planar n-in-p strip detectors fabricated by Hamamatsu Photonics K.K. [Ham] (HPK) are presented. The design of the sensors is described in Section 5.1.2. To investigate the performance after irradiation, the sensors have been irradiated with protons at the Karlsruhe Compact Cyclotron (see Section 5.1.3). Table 7.1 summarises the devices under test and the irradiation fluences. The maximum irradiation fluence of $5 \times 10^{15}\,\mathrm{n_{eq}/cm^2}$ corresponds to that expected for the second pixel detector layer of the HL-LHC upgrade of the ATLAS detector (see Section 2.2.2).

Table 7.1: Serial numbers, strip isolation schemes and equivalent irradiation fluences of the planar detectors.

Serial number	Strip isolation	Irradiation fluence ($\mathrm{n_{eq}/cm^2}$)
W53-BZ4B-P10	1 p-stop implant	0
W42-BZ2-P20	2 p-stop implants	5×10^{14}
W02-BZ3-P18	1 p-stop implant	1×10^{15}
W33-BZ3-P15	1 p-stop implant	2×10^{15}
W42-BZ2-P17	2 p-stop implants	5×10^{15}

For all sensors, the strip isolation is achieved with p-stop implants. The sensors irradiated to $5 \times 10^{14}\,\mathrm{n_{eq}/cm^2}$ (serial number W42-BZ2-P20) and the sensor irradiated to $5 \times 10^{15}\,\mathrm{n_{eq}/cm^2}$ (serial number W42-BZ2-P17) have two p-stop implants between adjacent readout strips, whereas in the other sensors only one p-stop implant is present between two strips. The different reflectivity above the p-stop implants affects the laser measurements, as will be discussed in Section 7.4. A sketch of the different p-stop structures is shown in Fig. 7.7, Section 7.4.

7.1 Beta Source Measurements

Beta source measurements were performed with all detectors listed in Table 7.1. Figure 7.1 shows the measured signal as a function of the applied bias voltage. The measurements of

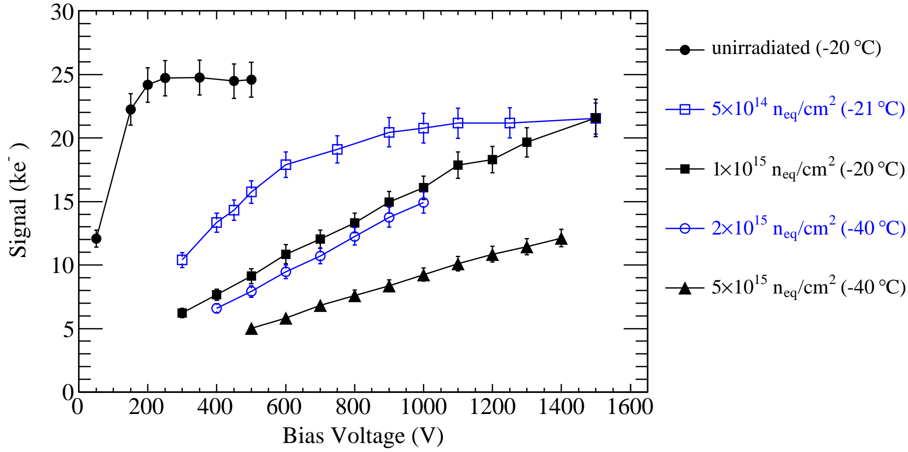

Figure 7.1: Beta source measurements: signal of the planar detectors irradiated to different fluences as a function of the applied bias voltage. The uncertainties are dominated by the calibration uncertainty, the data points are connected to guide the eye.

the sensors irradiated up to a fluence of $2 \times 10^{15}\,\mathrm{n_{eq}/cm^2}$ were performed at temperatures of approximately $-21\,^{\circ}\mathrm{C}$, while the sensors irradiated to higher fluences were measured at $-40\,^{\circ}\mathrm{C}$ to reduce the leakage current. The maximum bias voltages applied to the irradiated detectors were slightly below the breakdown voltages for each detector.

The signal of the unirradiated detector saturates at a bias voltage of approximately 200 V, which corresponds to the full depletion voltage. This sensor was used for the calibration of the setup (see Section 5.3.2), therefore a signal of $(24.7 \pm 1.4)\,\mathrm{ke^-}$, which is expected for the given thickness of 320 µm, is reached by definition.

The detector irradiated to $5 \times 10^{14}\,\mathrm{n_{eq}/cm^2}$ also shows a saturating signal curve. Due to the increased effective doping concentration, the curve saturates at higher voltages than that of the unirradiated detector. At a bias voltage of 1500 V, a signal of $(21.5 \pm 1.2)\,\mathrm{ke^-}$ is measured. Charge carrier trapping causes the plateau signal to be lower than the signal of the unirradiated detector. The signals of the detectors irradiated to fluences of $1 \times 10^{15}\,\mathrm{n_{eq}/cm^2}$ and above increase linearly as a function of the bias voltage. A saturation of the signal curves is not observed. The detector irradiated to $1 \times 10^{15}\,\mathrm{n_{eq}/cm^2}$ yields a maximum signal of $(21.6 \pm 1.5)\,\mathrm{ke^-}$, which corresponds to the maximum signal measured with the detector irradiated to $5 \times 10^{14}\,\mathrm{n_{eq}/cm^2}$. Consequently, it can be assumed that charge multiplication enhances the signal of the detector irradiated to $1 \times 10^{15}\,\mathrm{n_{eq}/cm^2}$. The maximum signals measured with the detectors irradiated to $2 \times 10^{15}\,\mathrm{n_{eq}/cm^2}$ and $5 \times 10^{15}\,\mathrm{n_{eq}/cm^2}$ are $(14.9 \pm 0.9)\,\mathrm{ke^-}$ and $(12.1 \pm 0.7)\,\mathrm{ke^-}$, respectively.

These measurements illustrate that the classical model of sensor depletion and charge carrier trapping does not apply in highly irradiated detectors. According to Eq. (4.18), Section 4.3.3, a signal of approximately $6\,\mathrm{ke^-}$ would be expected in a fully depleted detector irradiated to $5 \times 10^{15}\,\mathrm{n_{eq}/cm^2}$. The full depletion voltage for this fluence would be approximately 5000 V according to Eq. 4.7, Section 4.3.1, and Eq. 3.9, Section 3.3.1.

Although these estimations were derived for pad detectors, a disagreement between the measurements and the classical models is apparent. It is probable that the measured signal is enhanced by charge multiplication.

While the signals measured with the planar detectors are higher than expected, they are still lower than those measured with the irradiated 3D detectors, see Section 6.2. The reduced spacing of the electrodes in the 3D detectors leads to higher electric fields and to lower trapping. With 3D detectors, the effect of charge multiplication was clear as irradiated detectors showed significantly higher signals compared to unirradiated detectors. The effect is less obvious with planar detectors considering the signals of the irradiated detectors do not exceed that of the unirradiated detector. Furthermore, considerably higher bias voltages are required for the planar detectors due to the larger spacing of the electrodes. However, the signal measurements presented above show that planar n-in-p detectors are sufficiently radiation hard for the strip detector layers and the medium pixel layers of the ATLAS upgrade. For all irradiation fluences investigated, signals above 10 ke$^-$ are measured, given that sufficiently high bias voltages can be supplied to the detectors. The maximum signal-to-noise ratio was larger than 10 for all detectors (the noise will be discussed in the following section).

7.2 Noise Measurements

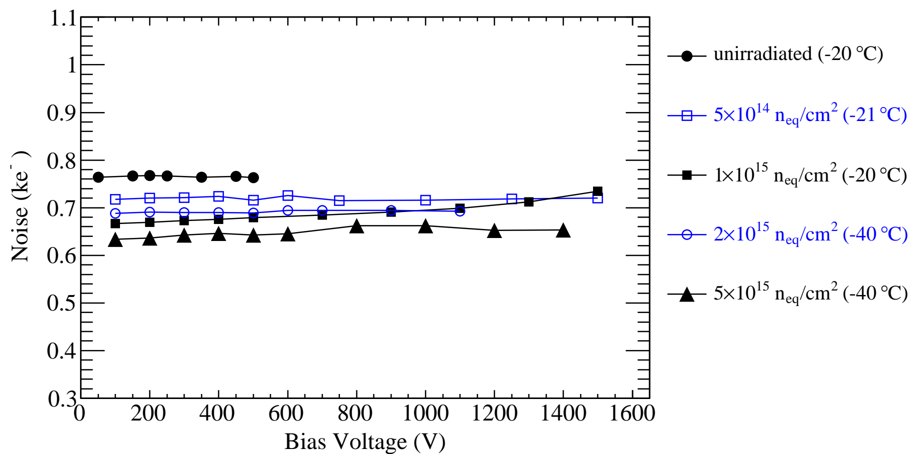

Figure 7.2: RMS noise of the planar detectors irradiated to different fluences as a function of the applied bias voltage. The data points are connected to guide the eye.

Figure 7.2 shows the measured noise values of the detectors irradiated to different fluences. The noise was calculated as the RMS deviation of the signal distributions acquired in pedestal measurements. The average noise of all strips is shown, with extremely noisy strips being excluded from the analysis. Only statistical uncertainties are considered, these are smaller than the markers. Interestingly, the noise tends to decrease with increasing irradiation fluence. The noise of all detectors hardly depends on the bias voltage in the entire voltage range investigated. This indicates that the noise is dominated by the ca-

pacitive noise of the readout chip whereas the shot noise is marginal. Only for the sensor irradiated to $1 \times 10^{15}\,n_{eq}/cm^2$, an increase of the noise with the bias voltage points to an increasing influence of the shot noise. The lower temperature of the detectors irradiated to higher fluences leads to a lower leakage current, hence the influence of shot noise is not visible.

Due to the lower capacitance of the planar detectors, the noise is lower than that of the 3D detectors. The capacitances of both detector types are listed in Table 5.1, Section 5.3.2. A strong increase of the noise at high bias voltages, which was observed in the measurements with 3D detectors (see Section 6.2.4), is not observed in the measurements of the planar detectors.

7.3 Annealing Studies

Accelerated annealing studies were performed with the detectors irradiated to fluences of $2 \times 10^{15}\,n_{eq}/cm^2$ and $5 \times 10^{15}\,n_{eq}/cm^2$. The detectors were exposed to a temperature of $60\,°C$ for increasing periods of time, up to an accumulated time of 6000 min. Using the time scaling of the long-term annealing of the effective doping concentration, this corresponds to approximately 6.4 years at a temperature of $20\,°C$. However, the applicability of this time scaling for signal and noise measurements is not fully established (see also Sections 4.1.2 and 6.2.5). In this section, the results of beta source measurements and noise measurements performed after each annealing step are presented. These measurements were performed at a temperature of $-40\,°C$. Laser measurements were performed only before annealing and after the last annealing step, the results of these measurements are shown in the following section.

Beta Source Measurements

Figures 7.3 and 7.4 show the signal of the detectors irradiated to $2 \times 10^{15}\,n_{eq}/cm^2$ and $5 \times 10^{15}\,n_{eq}/cm^2$, respectively, for different bias voltages as a function of the accumulated annealing time. The time scale on the top of the figure indicates the accumulated annealing time scaled to a reference temperature of $20\,°C$ using the activation energy for long-term annealing of the effective doping concentration. An acceleration factor of 560 was used (see Section 4.1.2). Error bars are not shown in the figures. The statistical uncertainties are smaller than 3%, a systematic uncertainty of 5% originating from the calibration uncertainty are assumed.

The signal of the detector irradiated to $2 \times 10^{15}\,n_{eq}/cm^2$ (see Fig. 7.3) was measured up to a bias voltage of 1000 V. The signal increases up to an annealing time of approximately 80 min at $60\,°C$, particularly at low bias voltages. This signal increase can be related to the short-term annealing of the effective doping concentration. At low bias voltages, the volume which is depleted or which exhibits a high electric field strength increases during short-term annealing due to a decreased effective doping concentration.

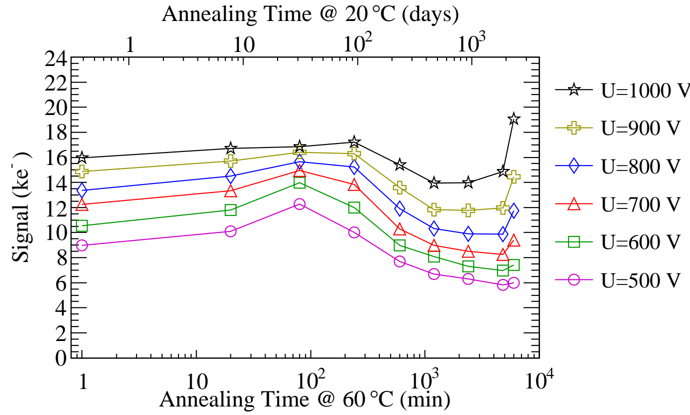

Figure 7.3: Signal of the detector irradiated to $2 \times 10^{15}\,\mathrm{n_{eq}/cm^2}$ as a function of the accumulated annealing time for different bias voltages. The measurement performed before annealing is represented by the data point shown at 1 min at 60 °C.

After longer annealing times, the effective doping concentration increases and the high-field volume decreases, hence the signal decreases. Only after an accumulated annealing time of 4800 min the signal increases again. The increase is more apparent for higher bias voltages than for low bias voltages. The signal enhancement can be attributed to charge multiplication. Due to the increase of the effective doping concentration, the peak of the electric field close to the junction increases and finally leads to expressed charge multiplication. The annealing measurements of the 3D detectors show a similar behaviour (see Section 6.2.5).

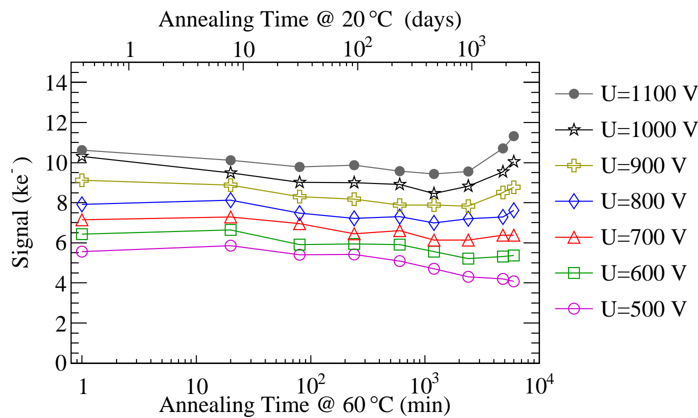

Figure 7.4: Signal of the detector irradiated to $5 \times 10^{15}\,\mathrm{n_{eq}/cm^2}$ as a function of the accumulated annealing time for different bias voltages. The measurement performed before annealing is represented by the data point shown at 1 min at 60 °C.

The annealing measurements of the detector irradiated to $5 \times 10^{15}\,\mathrm{n_{eq}/cm^2}$ (see Fig. 7.4) were performed up to a bias voltage of 1100 V. The effect of the short-term annealing is

weaker than for the detector irradiated to $2 \times 10^{15}\,\mathrm{n_{eq}/cm^2}$. A very slight signal increase can be observed only for low bias voltages during the first 20 min of the annealing series. The signal then decreases due to an increase of the effective doping concentration and a decrease of the volume exhibiting high electric fields. The signal measured at high bias voltages starts to increase after an accumulated annealing time of 2000 min, while the signal measured at low bias voltages starts to increase later. As above, the increase of the signal can be attributed to charge multiplication.

These measurements can be compared with annealing studies reported in Ref. [Man11]. In those studies, identical sensors were used and comparable irradiation fluences were studied. However, those irradiations were performed with reactor neutrons instead of protons, which were used in the studies described here. In the studies reported in Ref. [Man11], a higher signal was measured already before annealing. The signal is up to 40% larger, depending on the irradiation fluence and the bias voltage under consideration. While the signals at low bias voltages agree very well, the disagreement of the measured signals increases with increasing bias voltages. The systematic uncertainty of the calibration and the uncertainty of the irradiation dose, which is approximately 20%, cannot explain the discrepancy.

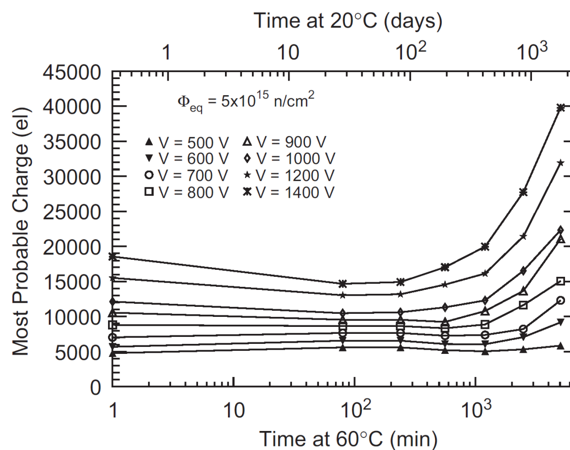

Figure 7.5: Annealing measurements reported in Ref. [Man11]: Signal as a function of the annealing time, measured with an n-in-p detector irradiated to $5 \times 10^{15}\,\mathrm{n_{eq}/cm^2}$ with reactor neutrons.

Annealing measurements of a detector irradiated to a fluence of $5 \times 10^{15}\,\mathrm{n_{eq}/cm^2}$ presented in Ref. [Man11] are shown in Fig. 7.5. The annealing behaviour is similar to that observed in the studies described here. However, the signal of the sensor irradiated to $5 \times 10^{15}\,\mathrm{n_{eq}/cm^2}$ measured here shows a delayed annealing behaviour. In the measurements shown in Fig. 7.5, the signal measured at a bias voltage of 1000 V starts to increase already after an accumulated annealing time of approximately 600 min at 60 °C. After annealing of about 5000 min, a signal of approximately 22 ke$^-$ was measured at a bias voltage of 1000 V. This is almost twice as much as measured in these studies after an annealing time of 6000 min.

These observations could indicate a higher charge multiplication probability in neutron irradiated detectors, which could be a sign for NIEL violation (see also Section 4.2). In irradiations with neutrons, more defect clusters are generated than in irradiations with protons of 25 MeV, where primarily point defects are created (see Section 4.1.2).

Noise Measurements

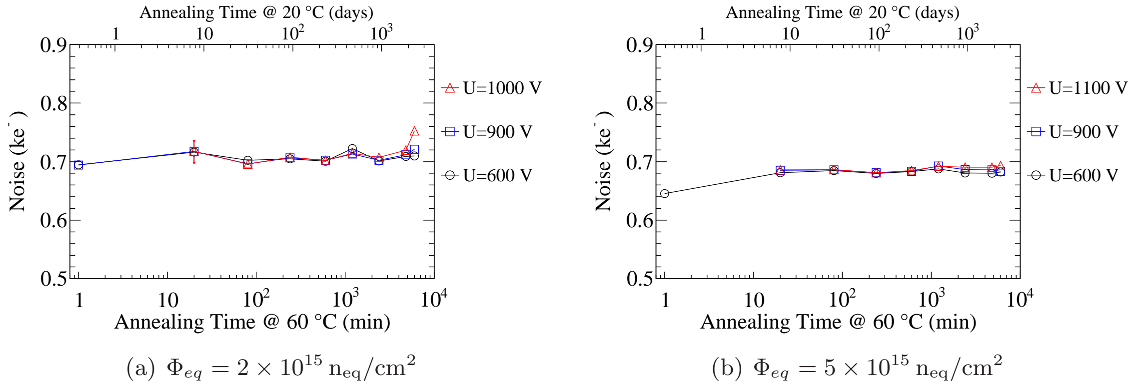

(a) $\Phi_{eq} = 2 \times 10^{15}\ \mathrm{n_{eq}/cm^2}$ (b) $\Phi_{eq} = 5 \times 10^{15}\ \mathrm{n_{eq}/cm^2}$

Figure 7.6: RMS noise for selected bias voltages as a function of the accumulated annealing time: (a) for the detector irradiated to $2 \times 10^{15}\ \mathrm{n_{eq}/cm^2}$, (b) for the detector irradiated to $5 \times 10^{15}\ \mathrm{n_{eq}/cm^2}$. The measurement performed before annealing is represented by the data point shown at 1 min at 60 °C.

Figure 7.6 shows the average strip noise of the detectors irradiated to $2 \times 10^{15}\ \mathrm{n_{eq}/cm^2}$ and $5 \times 10^{15}\ \mathrm{n_{eq}/cm^2}$ as a function of the accumulated annealing time. The noise does not show a strong dependence on the annealing time or on the bias voltage, which indicates that shot noise does not have any appreciable influence and micro-discharges do not occur. Only the noise of the detector irradiated to $2 \times 10^{15}\ \mathrm{n_{eq}/cm^2}$ measured after an accumulated annealing time of 6000 min at 60 °C increases slightly with the bias voltages. Potentially, this points to the increasing influence of excess noise due to charge multiplication or to the onset of micro-discharges.

7.4 Laser Measurements

Laser measurements were performed with the unirradiated detector and the detectors irradiated to fluences of $2 \times 10^{15}\ \mathrm{n_{eq}/cm^2}$ and $5 \times 10^{15}\ \mathrm{n_{eq}/cm^2}$. The irradiated detectors were measured before annealing and after an accumulated annealing time of 6000 min at 60 °C. As explained above, this annealing time corresponds to an annealing of 6.4 years at 20 °C when considering the long-term annealing of the effective doping concentration. It is unlikely that highly irradiated detectors in an HL-LHC experiment will be stored at room temperature for several years. However, measurements of the annealed detectors provide an opportunity to investigate the properties of charge multiplication, as the results of the beta source measurements presented above clearly indicate the occurrence of

charge multiplication after long annealing times. The laser measurements were performed at temperatures of approximately $-27\,^{\circ}$C.

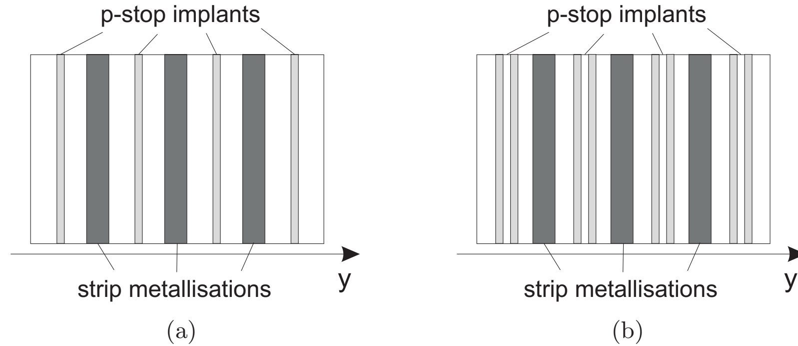

Figure 7.7: Sketch of the planar detectors' surface layout: (a) one p-stop implant, (b) two p-stop implant between two strips. The laser was scanned perpendicularly to the readout strips (along the coordinate y).

Figure 7.7 illustrates the surface layout of the planar detectors. The unirradiated detector and the detector irradiated to $2 \times 10^{15}\,\mathrm{n_{eq}/cm^2}$ have one p-stop implant in the middle between two readout strips, as shown in Fig. 7.7(a). The detector irradiated to $5 \times 10^{15}\,\mathrm{n_{eq}/cm^2}$ has two p-stop implants in the middle between two strips, as displayed in Fig. 7.7(b). The laser measurements were performed by scanning the laser perpendicularly to the readout strips in steps of $2\,\mu$m. In contrast to the laser measurements of 3D detectors described in Sections 6.1.4 and 6.2.6, only a one-dimensional scan was performed for the measurements of the planar detectors. The configuration of the planar detectors does not change along the direction parallel to the readout strips.

Figures 7.8-7.10 show the signal as a function of the coordinate perpendicular to the strip direction. The laser was scanned over the region between two strips and the signals of these two strips were summed to account for charge sharing effects.

The results of laser scans performed with the unirradiated detector at different bias voltages are shown in Fig. 7.8. The laser was scanned between two readout strips. At the left and right margins of the figure, the signal vanishes as the laser is reflected on the strip metallisations. In the middle, around $y = 35\,\mu$m, the signal is higher, corresponding to the locations of the p-stop implant. The oxide above the p-stop implants is thinner, which leads to a lower reflectivity. The p-stop implants can even be seen in a photograph of the sensor (see Fig. 5.7, Section 5.1.2), which illustrates the different optical properties in these regions.

Also apart from the signal non-uniformity induced by the p-stop implants, the signal is not homogeneous. The signal reaches maxima close to the strip metallisations and decreases towards the middle between the readout strips. Apparently, low-field regions exist between the strip implants. It can be assumed that the field is particularly low in the region close to the detectors surface, where the laser deposits most of its energy. Possibly, the integration time of the amplifier is shorter than the charge collection time for charge

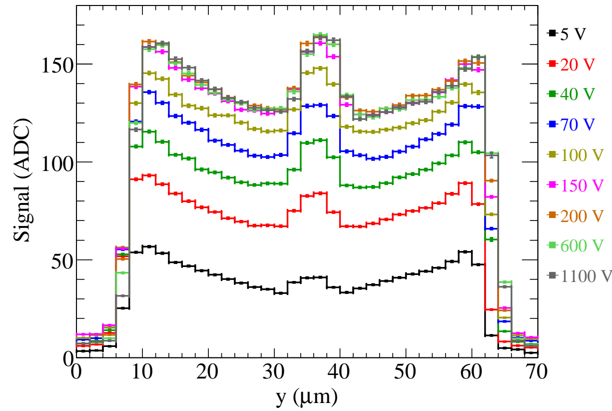

Figure 7.8: Results of laser scans of the region between two strips performed with the unirradiated detector. The signals of two adjacent strips are summed.

carriers generated close to the surface in the middle between the strips. Furthermore, a fraction of the charge is induced on readout strips which are further away, as will be discussed below when investigating the signals of single strips.

At a bias voltage of 5 V, the signal measured in the region of the p-stop implant is visibly lower than close to the strip implants. At higher bias voltages, the signals measured in both regions are comparable. The depletion zone starts to grow from the strip implants and higher bias voltages are required to deplete the regions of the p-stop implants. The signal saturates at a bias voltage of 150 V, which is $50 - 100$ V less than the saturation in the beta source measurements (see Fig. 7.1). Electrons emitted from the beta source deposit energy uniformly along their track, while the laser creates free charge carriers mainly in the upper region of the sensor. Thus, a growth of the depletion zone towards the sensor backplane for bias voltages higher than 150 V does not affect the signal of the laser measurements.

Figure 7.9 shows laser measurements of the detector irradiated to $2 \times 10^{15}\ \mathrm{n_{eq}/cm^2}$. In the measurement performed before annealing (Fig. 7.9(a)), the shape of the curve is comparable to that measured with the unirradiated detector. However, a higher signal is measured with the irradiated detector, although the signal of the beta source measurements was considerably lower than for the unirradiated detector. All laser measurements were performed with the same laser power. This reiterates the statement made in Section 5.4 that the laser measurements only yield relative signals. Due to possible changes of the surface reflectivity, absolute signal measurements of different detectors are not possible.

The measurement performed after an accumulated annealing time of 6000 min at 60 °C (Fig. 7.9(b)) exhibits a substantially different behaviour. The signal measured close to the strip implants is strongly enhanced at high bias voltages. While the signal between a bias voltage of 400 V and 1100 only increases by approximately 60% before annealing, an increase by a factor of almost 4 can be observed after annealing when considering laser impact positions close to the strip metallisations. In the middle between the readout strips, the increase is much less pronounced.

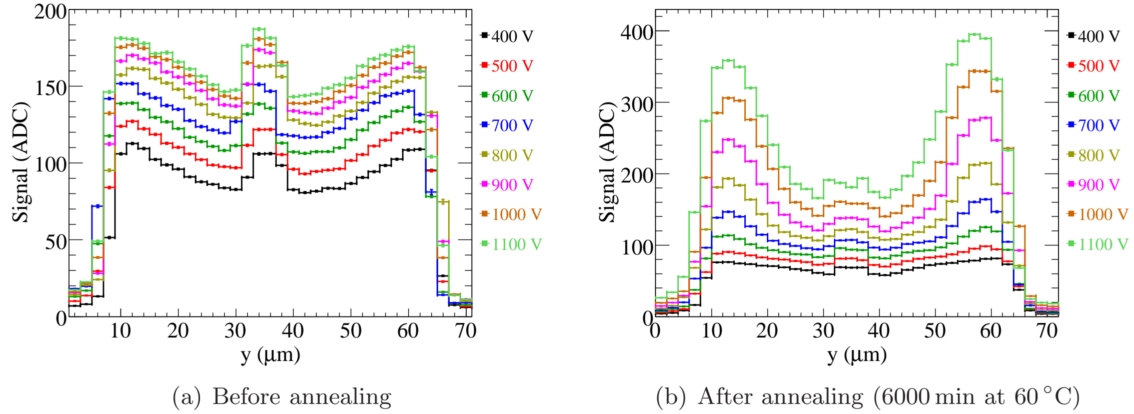

(a) Before annealing

(b) After annealing (6000 min at 60 °C)

Figure 7.9: Results of laser scans of the region between two strips performed with the detector irradiated to $2 \times 10^{15}\,\mathrm{n_{eq}/cm^2}$, (a) before annealing and (b) after annealing. The signals of two adjacent strips were summed up. The different scales of the vertical axes should be noted.

This effect points to the occurrence of charge multiplication in regions close to the strip implants. Charge carriers generated close to the multiplication region have a higher probability of being multiplied, while charge carriers generated further away experience a higher trapping probability before reaching the multiplication region. The occurrence of charge multiplication strongly increases the dependence of the signal on the position of the charge generation.

Due to the strong dependence of the impact ionisation rates on the electric field (see Section 3.3.7), the signal increases strongly with the bias voltage when charge multiplication occurs. Before annealing, the signal almost saturates at high bias voltages. This suggests that there is no significant influence of charge multiplication before annealing, at least in the voltage range studied here.

The laser measurements of the detector irradiated to $5 \times 10^{15}\,\mathrm{n_{eq}/cm^2}$ are shown in Fig. 7.10. This detector has two p-stop implants between the readout strips, therefore the signal exhibits two peaks close to the middle between the strips. Before annealing (Fig. 7.10(a)), the shape of the signal is similar to that of the detectors discussed above: the signal decreases from the edges of the metallisations to the middle between the strips, with the exception of the regions of the p-stop implants.

After annealing (Fig. 7.10(b)), strong charge multiplication leads to an enhanced signal, as it was observed with the detector irradiated to $2 \times 10^{15}\,\mathrm{n_{eq}/cm^2}$. However, the signal increase is less pronounced and the signal measured close to the middle between the readout strips is even somewhat lower after annealing. Both effects can be caused by the higher trapping probability compared to the detector irradiated to $2 \times 10^{15}\,\mathrm{n_{eq}/cm^2}$.

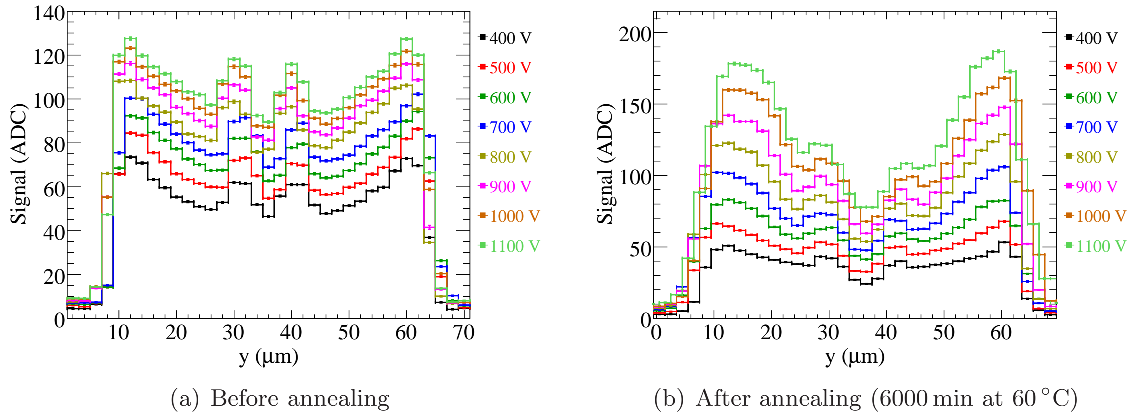

(a) Before annealing

(b) After annealing (6000 min at 60 °C)

Figure 7.10: Results of laser scans of the region between two strips performed with the detector irradiated to $5 \times 10^{15}\,\mathrm{n_{eq}/cm^2}$, (a) before annealing and (b) after annealing. The signals of two adjacent strips were summed up. The different scales of the vertical axes should be noted.

Single Strip Signals

Figures 7.11-7.13 display the signal measured by a single strip for a laser scan of the region shown in Fig. 7.7. The regions of the strip metallisations, where the laser is reflected, are hatched. These representations allow investigation of charge sharing and the extent of signal induced on neighbouring readout strips.

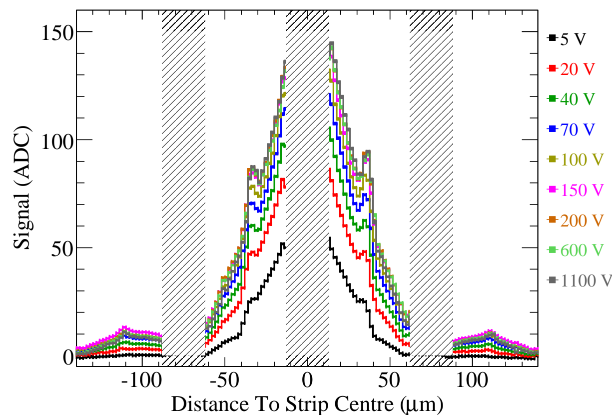

Figure 7.11: Results of laser scans of the unirradiated detector. The signal of the central strip is shown. The regions of the strip metallisations, where the laser is reflected, are hatched.

Figure 7.11 shows the measurements of the unirradiated detector. A pronounced charge sharing between neighbouring strips is visible. If the laser impinges on the domain of a neighbour of the central strip (distance to the strip centre larger than 34 µm), the central strip still measures a considerable signal. In 3D detectors, the charge sharing is less pronounced and the domains of the readout strips are more clearly delimited (see Sections 6.2.6 and 6.1.4). A significant signal is even induced if the laser shines on the far

side of the central strip's neighbour (distance to the strip centre larger than $\sim 90\,\mu$m).

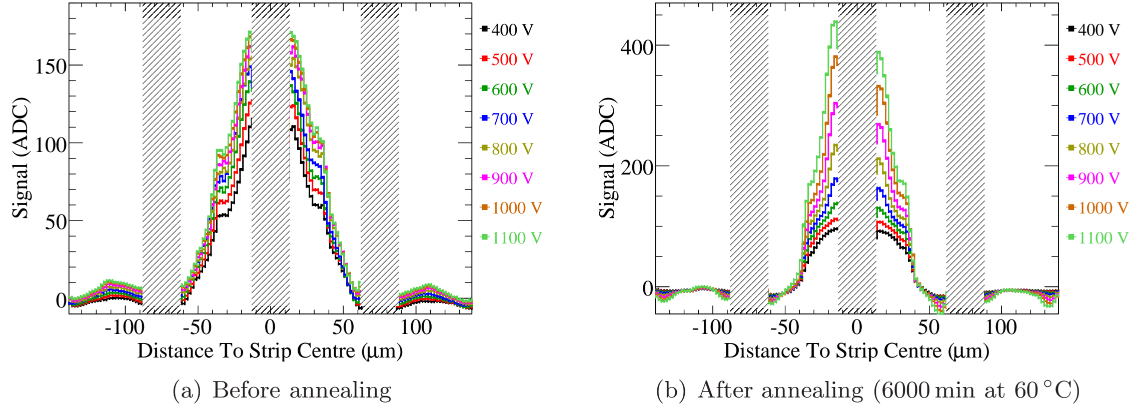

(a) Before annealing

(b) After annealing (6000 min at 60 °C)

Figure 7.12: Results of laser scans of the detector irradiated to $2 \times 10^{15}\,\mathrm{n_{eq}/cm^2}$, (a) before annealing and (b) after annealing. The signal of the central strip is shown. The different scales of the vertical axes should be noted.

The single strip signals of the detector irradiated to $2 \times 10^{15}\,\mathrm{n_{eq}/cm^2}$ are shown in Fig. 7.12. Before annealing (see Fig. 7.12(a)), the shape is comparable to that measured with the unirradiated detector. However, even negative signals are measured if the laser shines close to the strip implants of the neighbouring readout strips. As explained in the discussion of the laser measurements of the 3D detectors, these can result from a ballistic deficit or from trapping. After an accumulated annealing time of 6000 min at 60 °C (see Fig. 7.12(b)), the amount of charge sharing is visibly reduced. High signals are only measured if the laser illuminates the domain of the central strip. The signal decreases rapidly if the laser approaches the middle between the central strip and one of its neighbours. The same observations also apply to the measurements of the detector irradiated to $5 \times 10^{15}\,\mathrm{n_{eq}/cm^2}$, which are shown in Fig. 7.13.

After annealing, a large amount of the signal originates from the charge carriers which are created by impact ionisation. The multiplication processes take place in the regions close to strip implants. Therefore, the liberated charge carriers are unlikely to diffuse across the border to the next readout strip and the charge sharing is reduced.

Conclusion

In summary, the laser measurements show that not only 3D detectors, but also planar detectors exhibit a dependence of the signal on the position of the laser point of incidence. Long-term annealing increases the signal of the irradiated detectors mainly in the region close to the strip implants and decreases the charge sharing between neighbouring readout strips. These effects could be attributed to charge multiplication close to the strip implants. The decreased charge sharing probability is expected to affect the spatial resolution of the detectors and the hit detection efficiency when applying a fixed signal threshold. It would be possible to investigate these effects in detail with beam test measurements.

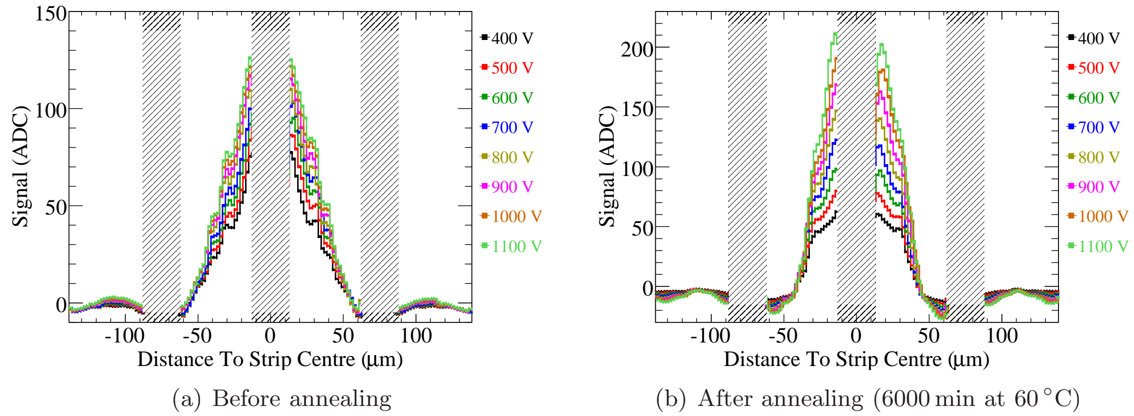

(a) Before annealing

(b) After annealing (6000 min at 60 °C)

Figure 7.13: Results of laser scans of the detector irradiated to 5×10^{15} n_{eq}/cm^2, (a) before annealing and (b) after annealing. The signal of the central strip is shown. The different scales of the vertical axes should be noted.

The dependence of the signal on the particle point of incidence could be decreased by a tilted arrangement of the sensors, so that particle tracks traverse the sensor under a certain angle. With this arrangement, traversing particles would deposit energy in regions which lead to a hich signal and in regions which lead to a low signal.

Chapter 8

Summary and Conclusions

Silicon detectors play a crucial role in modern high-energy physics experiments. In experiments at the HL-LHC, the proposed luminosity upgrade of the LHC, an unprecedentedly high radiation fluence poses a challenge for the tracking detectors. Candidates for radiation tolerant tracking detectors at the HL-LHC experiments are 3D silicon detectors and planar silicon detectors with n-side readout.

In this thesis, measurements of 3D silicon strip detectors in n-in-p and p-in-n layout and measurements of planar strip detectors in n-in-p layout were presented. The results were published in Refs. [Kö09, Kö10a, Kö10b, Kö11a, Kö11b, Kö11c, Bat11]. The investigation of 3D detectors and in particular the study of the radiation hardness was the main focus of this thesis. Specifically, double-sided 3D detectors were investigated, which are a modification of the original design with columns passing through the full substrate. In double-sided 3D detectors, columnar electrodes are etched into the substrate from both detector surfaces, while neither set of columns passes through the entire sensor. The sensors were produced by the institutes IMB-CNM in Barcelona (Spain) and FBK in Trento (Italy).

An important part of this thesis was the study of charge multiplication effects, which were recently observed in highly irradiated silicon tracking detectors. In the presence of high electric fields, impact ionisation can lead to multiplication of liberated charge carriers. Charge multiplication was so far not observed in conventional silicon tracking detectors before any radiation-induced modification of the detectors.

Since double-sided 3D detectors are a new technology, the behaviour of the detectors before any radiation-induced modification of the detector properties was studied in detail before investigating the radiation hardness. The detectors' performances were studied in beam tests with high-energy pions, with beta source measurements and with measurements utilising an infrared laser. Within the scope of this thesis, the first beam test measurements with double-sided 3D detectors in general and the first beam test measurements with irradiated 3D detectors were performed. Quantities under investigation were the signal, the signal as a function of the particle point of incidence, the detection efficiency, the spatial resolution and the charge sharing probability. Furthermore, an emphasis was put on the investigation of the noise. Measurements of 3D detectors were presented in Chapter 6.

The maturity of the design and an excellent performance could be proven with the detectors in an unirradiated state (Section 6.1). The detectors yielded the signal expected for the given substrate thickness. Only one sensor, in which the columns were shorter due to a processing fault, yielded a significantly lower signal. The problem with the reduced column depth could be understood and did not reoccur in later production runs. The signal and the efficiency were found to be very uniform across the sensor, inefficient regions were not observed. However, minor signal inhomogeneities observed point to a lower electric field strength in regions close to the sensors' surfaces.

Both the signal and the signal uniformity in double-sided 3D sensors is increased compared to 3D single type column (3D STC) sensors, where columns of one doping type only extend into the substrate. The additional set of ohmic columns in double-sided 3D detectors has successfully reduced the low-field regions observed in 3D STC detectors. Considerably lower signals and lower efficiencies are only measured for particles traversing the columnar electrodes. This is expected as the columns represent passive volume. A tilted arrangement of the sensors, which is already realised in the current ATLAS tracking detectors, would minimise the path length a particle travels through a column. Hence, the efficiency and the signal uniformity would be improved.

Measurements of an unirradiated 3D p-in-n detector produced by IMB-CNM showed indications for charge multiplication if bias voltages close to the breakdown voltage were applied. This assumption could be substantiated with simulations of the electric field. According to the simulations, the electric field is sufficiently high to cause multiplication of electrons approaching the n^+-doped ohmic columns. These studies are the first measurements indicating charge multiplication in unirradiated silicon detectors designed for tracking purposes in high-energy physics experiments.

The charge sharing between neighbouring readout strips in 3D detectors is considerably lower than in planar detectors. Charge sharing decreases the hit detection efficiency in situations where the signal-to-noise ratio is low, as in highly irradiated detectors. On the other hand, charge sharing can be exploited to improve the spatial resolution, since it facilitates interpolation of the track point of incidence between neighbouring strips.

The measurements of irradiated detectors (Section 6.2) showed an excellent radiation tolerance. The occurrence of charge multiplication in irradiated sensors could be proven. In 3D n-in-p detectors irradiated to fluences of $1 \times 10^{15}\,\mathrm{n_{eq}/cm^2}$ and $2 \times 10^{15}\,\mathrm{n_{eq}/cm^2}$, charge multiplication increased the signal substantially beyond that of unirradiated detectors. With beam tests and laser measurements it could be shown that charge multiplication probably takes place in a thin region around the electrode where electrons are collected. The onset of charge multiplication does not lead to a degradation of the spatial resolution.

The maximum irradiation fluence studied was $2 \times 10^{16}\,\mathrm{n_{eq}/cm^2}$, which corresponds to the fluence expected for the innermost pixel detector layer at the ATLAS HL-LHC upgrade. After this irradiation fluence and at the maximum bias voltage applied, remarkably high signals of $(15.3 \pm 0.9)\,\mathrm{ke^-}$ and $(15.6 \pm 0.9)\,\mathrm{ke^-}$ were measured with the n-in-p and the p-in-n detector, respectively. The maximum bias voltages were only 425 V for the n-in-p

detector and 350 V for the p-in-n detector.

Therefore, highly irradiated 3D detectors in n-in-p and in p-in-n layout yield a comparable signal, which is in strong contrast to the situation of planar detectors. As the signal of planar n-in-p detectors is dominated by electrons, these are considerably more radiation hard than planar p-in-n detectors. With the simulations of the weighting field presented in Section 5.1.1, it could be shown that both types of charge carriers contribute to the signal in 3D detectors significantly. This effect and the lower trapping probability due to the lower spacing of the electrodes cause the signal of highly irradiated 3D n-in-p and p-in-n detectors to be approximately equal.

Therefore, both detector layouts could be candidates for the innermost pixel detector layer of the ATLAS upgrade. Considering the more complex manufacturing of n-in-p detectors due to the required strip isolation structures, the application of 3D p-in-n detectors appears attractive. However, this would demand the development of a readout chip which is designed for the collection of holes. The current ATLAS pixel detector readout chip FE-I3 [Aad08a] is designed for collection of electrons only. Since planar detectors with n-side readout are considered as an option for the pixel detector layers, the future pixel readout chip will probably be designed for electron collection again.

The signal of the 3D detectors irradiated to $2 \times 10^{16}\,\mathrm{n_{eq}/cm^2}$ was more than twice as high as the signal measured with planar detectors irradiated to the same fluence [Cas11b]. Furthermore, 3D detectors require considerably lower bias voltages than planar detectors.

Laser measurements of 3D detectors showed that the entire sensor is active even after being irradiated to $2 \times 10^{16}\,\mathrm{n_{eq}/cm^2}$. However, the increased effective doping concentration and the high trapping probability lead to a pronounced non-uniformity of the measured signal. As expected from electric field simulations, the highest signal was measured for laser impact positions along the line connecting an ohmic column and a junction column, while the signal is minimal in the region being located in the middle between four columns. The non-uniformity of the signal as a function of the point of incidence could probably be reduced in a tilted arrangement of the sensors (see above).

The noise of 3D detectors is larger than that of planar detectors of a given strip length due to the higher capacitance originating from the columnar electrodes. In irradiated 3D detectors, a strong increase of the noise was measured at high bias voltages. Indications for a disagreement between the measured noise and the standard noise parameterisation were found. Furthermore, it was observed that the increase of the noise at high bias voltages is correlated with a deviation of the noise spectrum from a Gaussian distribution. These observations point to the occurrence of micro-discharges. The rate of micro-discharges was found to increase strongly with increasing temperature. This indicates that micro-discharges could be caused by local breakdowns due to tunnelling effects.

The occurrence of charge multiplication does not necessarily lead to a degradation of the signal-to-noise ratio. After an increase of the signal-to-noise ratio with the bias voltage, the onset of micro-discharges leads to a degradation. The voltage for which the maximum signal-to-noise ratio is obtained depends on the temperature.

As an alternative figure of merit of a silicon detector, the signal-to-threshold ratio was investigated. It might be a more useful criterion when a fixed threshold is applied for the hit identification. The occurrence of micro-discharges has more adverse consequences for the signal-to-threshold ratio than for the signal-to-noise ratio.

Annealing of highly irradiated 3D detectors led to a decrease of the signal measured at low bias voltages. The signal measured with the n-in-p and p-in-n detectors irradiated to $2 \times 10^{16}\,\mathrm{n_{eq}/cm^2}$ at high bias voltages increases strongly during the long-term annealing. This is in contrast to the well-established annealing model of the effective doping concentration, according to which a decrease of the signal after long-term annealing would be expected. The increase of the signal can be explained by an enhanced charge multiplication probability due to an increase of the electric field in regions close to the electrodes.

The noise of the irradiated 3D detectors was observed to increase during short-term annealing and to decrease during long-term annealing. This behaviour is not understood and could not be correlated to the standard noise parameterisation. It can be concluded that short-term annealing decreases the signal-to-noise ratio whereas long-term annealing is beneficial as it decreases the noise and increases the signal.

Measurements of planar n-in-p detectors were presented in Chapter 7. The detectors were irradiated up to a fluence of $5 \times 10^{15}\,\mathrm{n_{eq}/cm^2}$, which corresponds to the fluence expected for the medium pixel layers at the ATLAS upgrade. For this fluence, a maximum signal of $(12.1 \pm 0.7)\,\mathrm{ke^-}$ was measured at a bias voltage of 1400 V. This signal is lower than that measured with the 3D detectors irradiated to a four times higher fluence, and considerably higher voltages are necessary for the planar detectors. However, the noise is lower than in 3D detectors and micro-discharges were not observed. During long-term annealing, the signal decreases somewhat and after very long annealing times (corresponding to several years at room temperature), an enhanced charge multiplication probability increases the signal.

Laser measurements performed with unirradiated and irradiated planar sensors revealed a dependence of the signal on the laser point of incidence. The signal decreases with increasing distance to a strip implant, probably due to low-field regions located close to the sensor surface in the middle between two readout strips. The charge sharing probability was observed to decrease with annealing.

In summary, it can be concluded that 3D detectors exhibit a substantially higher radiation tolerance than planar detectors. For the innermost pixel detector layer of the ATLAS HL-LHC upgrade, where the highest radiation fluence is expected, 3D detectors constitute a promising option. While the studies presented in this thesis were performed with prototype detectors in strip layout, the performance of highly irradiated 3D pixel detectors in the final layout has to be investigated. In particular, the production yield is a critical issue, given the complex manufacturing processes of 3D detectors.

For applications in detector layers further outwards from the interaction point, planar detectors with n-side readout exhibit a sufficient radiation hardness. Particularly for the

strip detector layers, 3D detectors do not offer a significant advantage over planar detectors. At fluences of the order of $10^{15}\,\mathrm{n_{eq}/cm^2}$, planar n-in-p or n-in-n detectors yield a sufficient signal, provided that sufficiently high bias voltages can be supplied to the detectors. The manufacturing of planar detectors is less complex and planar detectors exhibit a lower noise due to a smaller capacitance. The latter fact is of particular importance for strip detectors, as the sensor capacitance scales with the size of the readout segments.

Acronyms and Abbreviations

Notation	Description
ADC	Analogue to Digital Converter
Alibava	Analogue Liverpool Barcelona Valencia Readout System
ALICE	A Large Ion Collider Experiment
APD	Avalanche Photodiode
ASIC	Application Specific Integrated Circuit
ATLAS	A Toroidal LHC Apparatus
CMS	Compact Muon Solenoid
Cz	Czochralski
DDTC	Double-Sided, Double Type Column (3D sensor)
DOFZ	Diffusion Oxygenated Float-Zone Silicon
DRIE	Deep Reactive Ion Etching
ENC	Equivalent Noise Charge
fcc	face-centred cubic
FPGA	Field Programmable Gate Array
FZ	Float-Zone
HL-LHC	High-Luminosity Large Hadron Collider
IBL	(ATLAS) Insertable B-Layer
LHC	Large Hadron Collider
LHCb	Large Hadron Collider beauty
LHCf	Large Hadron Collider forward
MCz	Magnetic Czochralski
MIP	Minimum Ionising Particle
MPV	Most Probable Value
NIEL	Non Ionising Energy Loss

Notation	**Description**
PS	Proton Synchrotron
RMS	Root Mean Square
SCSI	Space Charge Sign Inversion
SCT	Semiconductor Tracker
SiBT	Silicon Beam Telescope
sLHC	Super Large Hadron Collider
SPS	Super Proton Synchrotron
STC	Single Type Column (3D sensor)
SUSY	Supersymmetry
TCT	Transient Current Technique
TDC	Time to Digital Converter
TOTEM	Total Cross Section, Elastic Scattering and Diffraction Dissociation at the LHC
TRT	Transition Radiation Tracker

Bibliography

[Aad08a] G. Aad et al., *ATLAS pixel detector electronics and sensors* , JINST **3** (2008), P07007.

[Aad08b] G. Aad et al., *Expected performance of the ATLAS experiment: detector, trigger and physics*, CERN-OPEN-2008-020, CERN, Geneva, 2008.

[Aad08c] G. Aad et al., *The ATLAS experiment at the CERN Large Hadron Collider*, JINST **3** (2008), S08003.

[Aba95] S. Abachi et al., *Search for high mass top quark production in $p\bar{p}$ collisions at $\sqrt{s} = 1.8\ TeV$*, Phys. Rev. Lett. **74** (1995), 2422–2426.

[Aba08] E. Abat et al., *The ATLAS Transition Radiation Tracker (TRT) proportional drift tube: design and performance*, JINST **3** (2008), P02013.

[Abe95] F. Abe et al., *Observation of top quark production in $\bar{p}p$ collisions*, Phys. Rev. Lett. **74** (1995), 2626–2631.

[Ada06] W. Adam et al., *Radiation hard diamond sensors for future tracking applications*, Nucl. Instrum. Meth. A **565** (2006), 278–283.

[Aff10] T. Affolder, P. Allport, and G. Casse, *Collected charge of planar silicon detectors after pion and proton irradiations up to* $2.2 \times 10^{16}\, n_{eq} cm^{-2}$, Nucl. Instrum. Meth. A **623** (2010), 177–179.

[Ahm07] A. Ahmad et al., *The silicon microstrip sensors of the ATLAS Semiconductor Tracker*, Nucl. Instrum. Meth. **578** (2007), 98–118.

[All11a] P. P. Allport, *Long term planning proposal*, Presentation given at the ATLAS Upgrade Week March/April 2011, Oxford (UK), 2011.

[All11b] P. P. Allport et al., *Progress with the single-sided module prototypes for the ATLAS tracker upgrade stave*, Nucl. Instrum. Meth. A **636** (2011), S90–S96.

[Alv08] A. Augusto Alves et al., *The LHCb Detector at the LHC*, JINST **3** (2008), S08005.

[And98] L. Andricek et al., *Single-sided p^+n and double-sided silicon strip detectors exposed to fluences up to* $2 \times 10^{14}\,/cm^2$ *24 GeV protons*, Nucl. Instrum. Meth. A **409** (1998), 184–193.

[ATL98] ATLAS Collaboration, *ATLAS Pixel Petector: technical design report*, CERN-LHCC-98-013, CERN, Geneva, 1998.

[B0́6] M.-M. Bé et al., *Table of radionuclides (vol. 3 – A = 3 to 244)*, Monographie BIPM-5, 2006.

[Bar94] E. Barberis et al., *Capacitances in silicon microstrip detectors*, Nucl. Instrum. Meth. A **342** (1994), 90–95.

[Bat07] G. Battistoni et al., *The FLUKA code: description and benchmarking*, AIP Conference Proceedings **896** (2007), no. 1, 31–49.

[Bat11] R. Bates et al., *Charge collection studies and electrical measurements of heavily irradiated 3D double-sided sensors and comparison to planar strip detectors*, IEEE Trans. Nucl. Sci (2011), accepted for publication.

[Bay06] G. L. Bayatian et al., *CMS physics technical design deport, volume II : physics performance*, CERN-LHCC-2006-021, CERN, Geneva, 2006.

[Ben04] M. Benedikt et al., *LHC design report, vol. 3: the LHC injector chain*, CERN-2004-003-V-3, CERN, Geneva, 2004.

[Ben10] M. Benoit, A. Lounis, and Dinu N., *Simulation of charge multiplication and trap-assisted tunneling in irradiated planar pixel sensors*, IEEE Nuclear Science Symposium and Medical Imaging Conference (NSS - MIC'10), Conference Record, paper N21-6, Knoxville (USA, TN), 2010.

[Ber10] M. J. Berger et al., *Stopping-power and range tables for electrons, protons, and helium ions*, NISTIR 4999, 2010, Computer program ESTAR available at *http://physics.nist.gov/PhysRefData/Star/Text/ESTAR.html*.

[Bic88] H. Bichsel, *Straggling in thin silicon detectors*, Rev. Mod. Phys. **60** (1988), 663–699.

[Bin93] N. Bingefors et al., *A novel technique for fast pulse-shaping using a slow amplifier at LHC*, Nucl. Instrum. Meth. A **326** (1993), 112–119.

[Bre10] M. Breindl, *Erweiterung eines Lasermessstandes und Untersuchung von 3D-Silizium-Detektoren [in German]*, Diploma thesis, University of Freiburg, 2010.

[Bru97] R. Brun and F. Rademakers, *ROOT — An object oriented data analysis framework*, Nucl. Instrum. Meth. A **389** (1997), 81–86.

[Bru04] O. S. Bruening et al., *LHC design report, vol. 1: the LHC main ring*, CERN-2004-003-V-1, CERN, Geneva, 2004.

[Cap11] M. Capeans et al., *ATLAS Insertable B-Layer technical design report*, CERN-LHCC-2010-013, CERN, Geneva, 2011.

[Cas00] G. Casse, P. P. Allport, and M. Hanlon, *Improving the radiation hardness properties of silicon detectors using oxygenated n-type and p-type silicon*, IEEE Trans. Nucl. Sci **47** (2000), 527–532.

[Cas10] M. Casse, *Charge multiplication in highly irradiated planar silicon sensors*, Proceedings of the 19th International Workshop on Vertex Detectors, Loch Lomond (Scotland, UK), PoS(VERTEX 2010)020, 2010.

[Cas11a] G. Casse et al., *Accelerated and room temperature annealing of the CC(V)*, Presented at the 18th RD50 workshop, Liverpool (UK), 2011.

[Cas11b] G. Casse et al., *Evidence of enhanced signal response at high bias voltages in planar silicon detectors irradiated up to* $2.2\times10^{16}\, n_{eq}\, cm^{-2}$, Nucl. Instrum. Meth. A **636** (2011), S56–S61.

[Cha08] S. Chatrchyan et al., *The CMS experiment at the CERN LHC*, JINST **3** (2008), S08004.

[Che76] J. R. Chelikowsky and M. L. Cohen, *Nonlocal pseudopotential calculations for the electronic structure of eleven diamond and zinc-blende semiconductors*, Phys. Rev. B **14** (1976), 556–582.

[Chi97] A. Chilingarov and T. Sloan, *Operation of heavily irradiated silicon detectors under forward bias*, Nucl. Instrum. Meth. A **399** (1997), 35–37.

[Cin09] V. Cindro et al., *Radiation damage in p-type silicon irradiated with neutrons and protons*, Nucl. Instrum. Meth. A **599** (2009), 60–65.

[Daw11] I. Dawson, *Radiation Background Simulations*, URL: https://twiki.cern.ch/twiki/bin/viewauth/Atlas/RadiationBackgroundSimulations, accessed June 2011.

[DB10] G.-F. Dalla Betta et al., *Performance evaluation of 3D-DDTC detectors on p-type substrates*, Nucl. Instrum. Meth. A **624** (2010), 459–464.

[Dem03] M. Demarteau et al., *Characteristics of the outer layer silicon sensors for the run IIb silicon detector*, DØ note 4308, 2003.

[Die10] A. Dierlamm, *Irradiations in Karlsruhe*, Presented at the 16th RD50 workshop, Barcelona (Spain), 2010.

[Eck08] S. Eckert, *Investigation of the applicability of 3D stc silicon strip detectors for the sLHC*, Ph.D. thesis, University of Freiburg, Freiburg, 2008.

[Ehr07] T. Ehrich et al., *Laser characterisation of a 3D single-type column p-type prototype module read out with ATLAS SCT electronics*, Nucl. Instrum. Meth. A **583** (2007), 153–156.

[Eng64] F. Englert and R. Brout, *Broken symmetry and the mass of gauge vector mesons*, Phys. Rev. Lett. **13** (1964), 321–323.

[Ere02] V. Eremin, E. Verbitskaya, and Z. Li, *The origin of double peak electric field distribution in heavily irradiated silicon detectors*, Nucl. Instrum. Meth. A **476** (2002), 556–564.

[Ere07] V. Eremin et al., *Current injected detectors at super-LHC program*, Nucl. Instrum. Meth. A **583** (2007), 91–98.

[FBK] FBK, Fondazione Bruno Kessler, Povo - Via Sommarive 18, 38123 Trento, Italy.

[Fle10] C. Fleta, Personal Communication.

[Fre01] M. J. French et al., *Design and results from the APV25, a deep sub-micron CMOS front-end chip for the CMS tracker*, Nucl. Instrum. Meth. A **466** (2001), 359–365.

[Gar11] R. Garoby, *Plans for the upgrade of the LHC injectors*, Presented at the SLHC, the High-Luminosity Upgrade (public event), CERN, Geneva (Switzerland)), 2011.

[Gia05] F. Gianotti et al., *Physics potential and experimental challenges of the LHC luminosity upgrade*, Eur. Phys. J. **C39** (2005), 293–333.

[Gra73] W. N. Grant, *Electron and hole ionization rates in epitaxial silicon at high electric fields*, Solid-St. Electron. **16** (1973), 1189–1203.

[Gre11] P. Grenier et al., *Test beam results of 3D silicon pixel sensors for the ATLAS upgrade*, Nucl. Instrum. Meth. A **688** (2011), 33–40.

[Gur64] G. Guralnik, C. Hagen, and T. Kibble, *Global conservation laws and massless particles*, Phys. Rev. Lett. **13** (1964), 585–587.

[Ham] Hamamatsu Photonics K.K., 1126-1 Ichino-cho, Hamamatsu-shi 435-8558, Japan.

[Har09] F. Hartmann, *Evolution of silicon sensor technology in particle physics*, Springer, 2009.

[Hig64a] P. W. Higgs, *Broken symmetries and the masses of gauge bosons*, Phys. Rev. Lett. **13** (1964), 508–509.

[Hig64b] P. W. Higgs, *Broken symmetries, massless particles and gauge fields*, Phys. Lett. **12** (1964), 132–133.

[Hig66] P. W. Higgs, *Spontaneous symmetry breakdown without massless bosons*, Phys. Rev. **145** (1966), 1156–1163.

[Huh02] M. Huhtinen, *Simulation of non-ionising energy loss and defect formation in silicon*, Nucl. Instrum. Meth. A **491** (2002), 194–215.

[Hur92] G. A. M. Hurkx, D. B. M. Klaassen, and M. P. G. Knuvers, *A new recombination model for device simulation including tunneling*, IEEE Trans. Electron Devices **39** (1992), 331–338.

[IC] IMB-CNM, Instituto de Microelectrónica de Barcelona, Centro Nacional de Microelectrónica, 08193 Cerdanyola del Vallès (Bellaterra), Barcelona, Spain.

[Jak11] K. Jakobs, *Physics at the LHC and sLHC*, Nucl. Instrum. Meth. **636** (2011), S1–S7.

[Jon99] L. L. Jones et al., *The APV25 deep submicron readout chip for CMS detectors*, Proceedings of the 5th workshop on electronics for LHC experiments, vol. CERN/LHCC/99-09, 1999, pp. 162–166.

[Kem80] J. Kemmer, *Fabrication of low noise silicon radiation detectors by the planar process*, Nucl. Instrum. Meth. **169** (1980), 499–502.

[Ken99] C. Kenney et al., *Silicon detectors with 3-D electrode arrays: fabrication and initial test results*, IEEE Trans. Nucl. Sci **46** (1999), 1224–1236.

[Kib67] T. Kibble, *Symmetry breaking in non-Abelian gauge theories*, Phys. Rev. **155** (1967), 1554–1561.

[Kok10] A. Kok et al., *Fabrication of 3D silicon sensors*, Proceedings of the 19th International Workshop on Vertex Detectors, Loch Lomond (Scotland, UK), PoS(VERTEX 2010)022, 2010.

[Kor09] M. J. Kortelainen et al., *Off-line calibration and data analysis for the silicon beam telescope on the CERN H2 beam*, Nucl. Instrum. Meth. A **602** (2009), 600–606.

[Kra02] G. Kramberger et al., *Effective trapping time of electrons and holes in different silicon materials irradiated with neutrons, protons and pions*, Nucl. Instrum. Meth. A **481** (2002), 297–305.

[Kra07] G. Kramberger et al., *Impact of annealing of trapping times on charge collection in irradiated silicon detectors*, Nucl. Instrum. Meth. A **579** (2007), 762–765.

[Kra09] G. Kramberger et al., *Performance of silicon pad detectors after mixed irradiations with neutrons and fast charged hadrons*, Nucl. Instrum. Meth. A **609** (2009), 142–148.

[Kra10a] G. Kramberger et al., *Comparison of pad detectors produced on different silicon materials after irradiation with neutrons, protons and pions*, Nucl. Instrum. Meth. A **612** (2010), 474–477.

[Kra10b] G. Kramberger et al., *Investigation of irradiated silicon detectors by edge-TCT*, IEEE Trans. Nucl. Sci **57** (2010), 2294 – 2302.

[Kö09] M. Köhler et al., *Measurements of 3D silicon strip sensors by two manufacturers*, Proceedings of the 9th International Conference on Large Scale Applications and Radiation Hardness of Semiconductor Detectors, Florence (Italy), PoS(RD09)031, 2009.

[Kö10a] M. Köhler et al., *Beam test measurements with 3D-DDTC silicon strip detectors on n-type substrate*, IEEE Trans. Nucl. Sci **57** (2010), 2987 – 2994.

[Kö10b] M. Köhler et al., *Test beam measurements with 3D silicon strip detectors*, Astroparticle, Particle and Space Physics, Detectors and Medical Physics Applications. Proceedings of the 11th Conference, Villa Olmo, Como (Italy) (C. Leroy, ed.), World Scientific Publishing, 2010, pp. 864–868.

[Kö11a] M. Köhler et al., *Beam test measurements with planar and 3D silicon strip detectors irradiated to sLHC fluences*, IEEE Trans. Nucl. Sci **58** (2011), 1308 – 1314.

[Kö11b] M. Köhler et al., *Comparative measurements of highly irradiated n-in-p and p-in-n 3D silicon strip detectors*, Nucl. Instrum. Meth. A (2011), in press, doi:10.1016/j.nima.2011.08.041.

[Kö11c] M. Köhler et al., *Measurements with irradiated 3D silicon strip detectors*, Nucl. Phys. B. (Proc. Suppl.) **215** (2011), 247–249, Proceedings of the 12th Topical Seminar on Innovative Particle and Radiation Detectors (IPRD10), Siena (Italy).

[Kü06] S. Kühn, *Untersuchung der Strahlenhärte von Siliziumsensoren mit einer Betaquelle [in German]*, Diploma thesis, University of Freiburg, 2006.

[Kü08] S. Kühn et al., *Short strips for the sLHC: a p-type silicon microstrip detector in 3-D technology*, IEEE Trans. Nucl. Sci **55** (2008), 3638–3642.

[Lan44] L. Landau, *On the energy loss of fast particles by ionization*, J. Phys. (USSR) **8** (1944), 201–205.

[Lan10] J. Lange et al., *Properties of a radiation-induced charge multiplication region in epitaxial silicon diodes*, Nucl. Instrum. Meth. A **622** (2010), 49–58.

[Lea05] J. D. G. Leaver, *Testing and Development of the CMS Silicon Tracker Front End Readout Electronics*, Ph.D. thesis, Imperial College, London, 2005.

[Lef09] C. Lefevre, *LHC: the guide (English version)*, CERN-Brochure-2009-003-Eng, CERN, Geneva, 2009.

[Ler09] C. Leroy and P.-G. Rancoita, *Principles of radiation interaction in matter and detection*, World Scientific Publishing, 2009.

[Li92] Z. Li and H. W. Kraner, *Fast neutron radiation damage effects on high resistivity silicon junction detectors*, J. Electron. Mater. **21** (1992), 701–705.

[Li94] Z. Li, *Modeling and simulation of neutron induced changes and temperature annealing of N_{eff} and changes in resistivity in high resistivity silicon detectors*, Nucl. Instrum. Meth. A **342** (1994), 105–118.

[Lin80] V. A. J. van Lint et al., *Mechanisms of radiation effects in electronic materials*, John Wiley and Sons, 1980.

[Lin01] G. Lindström et al., *Radiation hard silicon detectors–developments by the RD48 (ROSE) collaboration*, Nucl. Instrum. Meth. A **466** (2001), 308–326.

[Loi04] C. Lois et al., *Laboratory measurements on irradiated prototype ladders for the LHCb inner tracker*, CERN-LHCb-2004-112, 2004.

[Lut99] G. Lutz, *Semiconductor radiation detectors: device physics*, Springer, 1999.

[Lö06] S. Löchner and M. Schmelling, *The beetle reference manual - chip version 1.3, 1.4 and 1.5*, CERN-LHCb-2005-105, 2006.

[Mac10] A. Macchiolo et al., *Performance of thin pixel sensors irradiated up to a fluence of $10^{16}\,\mathrm{n_{eq}cm^{-2}}$ and development of a new interconnection technology for the upgrade of the ATLAS pixel system*, Nucl. Instrum. Meth. A (2010), in press, doi:10.1016/j.nima.2010.11.163.

[Mae90] W. Maes, K. de Meyer, and R. van Oeverstraeten, *Impact ionization in silicon: a review and update*, Solid-St. Electron. **33** (1990), no. 6, 705–718.

[Man10] I. Mandić et al., *Observation of full charge collection efficiency in heavily irradiated n+p strip detectors irradiated up to* $3 \times 10^{15}\, n_{eq}/cm^2$, Nucl. Instrum. Meth. A **612** (2010), 474–477.

[Man11] I. Mandić et al., *Annealing effects in* n^+*-p strip detectors irradiated with high neutron fluences*, Nucl. Instrum. Meth. A **629** (2011), 101–105.

[Mar08] S. P. Martin, *A supersymmetry primer*, arXiv:hep-ph/9709356v5, 2008.

[Mat08] M. Mathes et al., *Test beam characterization of 3-D silicon pixel detectors*, IEEE Trans. Nucl. Sci **55** (2008), 3731–3735.

[Mat10] *MATLAB 7.10.0, The MathWorks, Inc.*, URL: http://www.mathworks.com/, 2010.

[McI66] R. J. McIntyre, *Multiplication noise in uniform avalanche diodes*, IEEE Trans. Electron Devices **13** (1966), 164–168.

[MH08] R. Marco-Hernandez, *Design of a readout system for microstrip silicon sensors*, Master's thesis, University of Valencia, 2008.

[MH09] R. Marco-Hernandez et al., *A portable readout system for microstrip silicon sensors (ALIBAVA)*, IEEE Trans. Nucl. Sci **56** (2009), 1642–1649.

[Mol99] M. Moll, *Radiation damage in silicon particle detectors: microscopic defects and macroscopic properties*, Ph.D. thesis, University of Hamburg, Hamburg, 1999.

[Mol10] M. Moll, *Recent advances in the development of radiation tolerant silicon detectors for the Super-LHC*, Astroparticle, Particle and Space Physics, Detectors and Medical Physics Applications. Proceedings of the 11th Conference, Villa Olmo, Como (Italy) (C. Leroy, ed.), World Scientific Publishing, 2010, pp. 101–110.

[Mue10] D. Muenstermann, *Atlas Upgrade*, Proceedings of the 19th International Workshop on Vertex Detectors, Loch Lomond (Scotland, UK), PoS(VERTEX 2010)038, 2010.

[Mur70] A. Murray, A. Lampert, and P. Mark, *Current injection in solids*, Academic Press, 1970.

[Mä08] T. Mäenpää et al., *Silicon beam telescope for LHC upgrade tests*, Nucl. Instrum. Meth. A **593** (2008), 523–529.

[Nak10] K. Nakamura et al., *Review of particle physics*, J. Phys. G **37** (2010), 075021.

[Ohs94] T. Ohsugi et al., *Microdischarges of AC-coupled silicon strip sensors*, Nucl. Instrum. Meth. A **342** (1994), 22–26.

[Ohs96a] T. Ohsugi et al., *Micro-discharge at strip edge of silicon microstrip sensors*, Nucl. Instrum. Meth. A **383** (1996), 116–122.

[Ohs96b] T. Ohsugi et al., *Micro-discharge noise and radiation damage of silicon microstrip sensors*, Nucl. Instrum. Meth. A **383** (1996), 166–173.

[Pah08] G. Pahn, *Teststrahlmessungen mit 3D-stc Silizium-Streifendetektoren [in German]*, Diploma thesis, University of Freiburg, 2008.

[Pah09] G. Pahn et al., *First beam test characterisation of a 3D-STC silicon short strip detector*, IEEE Trans. Nucl. Sci **56** (2009), 3834–3839.

[Par97] S. I. Parker, C. J. Kenney, and J. Segal, *3D – A proposed new architecture for solid-state radiation detectors*, Nucl. Instrum. Meth. A **395** (1997), 328–343.

[Par01] S. I. Parker and C. J. Kenney, *Performance of 3-D architecture silicon sensors after intense proton irradiation*, IEEE Trans. Nucl. Sci **48** (2001), 1629–1638.

[Par11] S. Parker et al., *Increased speed: 3D silicon sensors; fast current amplifiers*, IEEE Trans. Nucl. Sci **58** (2011), 404–417.

[Pel07] G. Pellegrini et al., *Technology of p-type microstrip detectors with radiation hard p-spray, p-stop and moderated p-spray insulations*, Nucl. Instrum. Meth. A **579** (2007), 599–603.

[Pel08] G. Pellegrini et al., *First double-sided 3-D detectors fabricated at CNM-IMB*, Nucl. Instrum. Meth. A **592** (2008), 38–43.

[Pel10] G. Pellegrini, Personal Communication.

[Pen07] D. Pennicard et al., *Simulation results from double-sided 3-D detectors*, IEEE Trans. Nucl. Sci **54** (2007), 1435–1443.

[Pen09] D. Pennicard et al., *Design, simulation and initial characterisation of 3D silicon detectors*, Nucl. Instrum. Meth. A **598** (2009), 67–70.

[Pen10] D. Pennicard et al., *Synchrotron tests of a 3D Medipix2 X-ray detector*, IEEE Trans. Nucl. Sci **57** (2010), 387–394.

[Pie05] C. Piemonte et al., *Development of 3-D detectors featuring columnar electrodes of the same doping type*, Nucl. Instrum. Meth. A **541** (2005), 441–448.

[Pie07] C. Piemonte et al., *Study of the signal formation in single-type column 3D silicon detectors*, Nucl. Instrum. Meth. A **579** (2007), 633–637.

[Pin06] I. Pintilie et al., *Stable radiation-induced donor generation and its influence on the radiation tolerance of silicon diodes*, Nucl. Instrum. Meth. A **556** (2006), 197–208.

[Pin09] I. Pintilie et al., *Radiation-induced point- and cluster defects with strong impact on damage properties of silicon detectors*, Nucl. Instrum. Meth. A **611** (2009), 52–68.

[Pov11] M. Povoli, *Investigation of punch-through bias in 3D sensors*, Presented at the 6th "Trento" Workshop on Advanced Silicon Radiation Detectors (3D and P-Type Technologies), Trento (Italy), 2011.

[pr11] CERN press release, January 2011.

[Pre10] J. Preiss, *Untersuchung von strahlenharten 3D-Siliziumstreifendetektoren mittels eines analogen Auslesesystems [in German]*, Diploma thesis, University of Freiburg, 2010.

[Raj79] K. Rajkanan, R. Singh, and J. Shewchun, *Absorption coefficient of silicon for solar cell calculations*, Solid-St. Electron. **22** (1979), 793–795.

[Ram39] S. Ramo, *Currents induced by electron motion*, Proc. IRE **27** (1939), 584–585.

[RD] *The RD50 Collaboration*, URL: http://cern.ch/rd50/.

[Ren09] D. Renker and E. Lorenz, *Advances in solid state photon detectors*, JINST **4** (2009), P04004.

[Ric96] R. H. Richter et al., *Strip detector design for ATLAS and HERA-B using two-dimensional device simulation*, Nucl. Instrum. Meth. A **377** (1996), 412–421.

[ROO] *ROOT - A Data Analysis Framework*, URL: http://root.cern.ch/.

[Ros06] L. Rossi et al., *Pixel detectors: from fundamentals to applications*, Springer, 2006.

[Sho38] W. Shockley, *Currents to conductors induced by a moving point charge*, J. Appl. Phys. **9** (1938), 635–636.

[Sif04] P. Siffert and E. Krimmel (eds.), *Silicon: evolution and future of a technology*, Springer, 2004.

[SIN] SINTEF, PO Box 124 Blindern, 0314 Oslo, Norway.

[Spi05] H. Spieler, *Semiconductor detector systems*, Oxford University Press,, 2005.

[Sta] Stanford Nanofabrication Facility, 420 Via Palou Mall, Stanford, CA 94305 -407, USA.

[Sze81] S. M. Sze, *Physics of semiconductor devices*, 2nd ed., John Wiley and Sons,, 1981.

[Tuo09] E. Tuominen et al., *Recent progress in CERN RD39: radiation hard cryogenic silicon detectors for applications in LHC experiments and their future upgrades*, IEEE Trans. Nucl. Sci **56** (2009), 2119–2123.

[Ull07] T. Ullrich and Z. Xu, *Treatment of errors in efficiency calculations*, arXiv:physics/0701199v1, 2007.

[Unn11] Y. Unno et al., *Development of n-on-p silicon sensors for very high radiation environments*, Nucl. Instrum. Meth. A **636** (2011), S24–S30.

[Vas11] A. Vasilescu and G. Lindström, *Displacement damage in silicon*, On-line compilation, URL: http://sesam.desy.de/members/gunnar/Si-dfuncs.html, accessed June 2011.

[Ver07] E. Verbitskaya et al., *Concept of double peak electric field distribution in the development of radiation hard silicon detectors*, Nucl. Instrum. Meth. A **583** (2007), 77–86.

[Vä11] S. Väyrynen et al., *The effect of an electrical field on the radiation tolerance of floatzone and magnetic Czochralski silicon particle detectors*, Nucl. Instrum. Meth. A **637** (2011), 95–99.

[Wal10] M. Walz, *Charakterisierung von planaren Siliziumstreifendetektoren zum Einsatz am LHC-Upgrade [in German]*, Diploma thesis, University of Freiburg, 2010.

[Web74] P. P. Webb, R. J. McIntyre, and J. Conradi, *Properties of avalanche photodiodes*, RCA Review **35** (1974), 234–278.

[Wii] L. Wiik, Ph.D. thesis, University of Freiburg, Freiburg, In preparation.

[Wun92] R. Wunstorf, *Systematische Untersuchungen zur Strahlenresistenz von Silizium-Detektoren für die Verwendung in Hochenergiephysik-Experimenten (in German)*, Ph.D. thesis, University of Hamburg, Hamburg, 1992.

[Zim11] F. Zimmermann, *HL-LHC: parameter space, constraints, and possible options*, Proceedings of the Chamonix 2011 Workshop on LHC Performance, CERN-ATS-2011-005, 2011, pp. 295–308.

[Zob08a] A. Zoboli et al., *Double-sided, double-type-column 3-D detectors: design, fabrication, and technology evaluation*, IEEE Trans. Nucl. Sci **55** (2008), 2775–2784.

[Zob08b] A. Zoboli et al., *Functional characterization of p-on-n 3D-DDTC detectors fabricated at FBK-IRST*, IEEE Nuclear Science Symposium and Medical Imaging Conference (NSS - MIC'08), Conference Record, paper N34-4, Dresden (Germany), 2008.

Acknowledgements

This thesis would not have been possible without the assistance, guidance and encouragement of numerous people. Even though it is impossible to thank everybody who contributed to this thesis, I would like to address a few words of thanks.

I am indebted to Prof. Dr. Karl Jakobs for giving me the opportunity to work in his group. It has been a pleasure to work on this interesting hardware project.

Also, I would like to express my special gratitude to my supervisor Dr. Ulrich Parzefall. Thank you for organising the projects of the hardware group, for teaching me about silicon detectors and for motivating me.

I have enjoyed the life in the hardware group and the cooperation with all members of the group: Adrian, Gregor, Jens, Liv, Maira, Michael, Michel, Simon, Sophie, Susanne, Sven and Tom. I thank you for your effort, for your assistance and for many interesting discussions. As all of you know, hardware is related to hard work, and many problems can only be solved with a common effort. To those of you who are still working on their theses: good luck! A great support came also from the "Hiwis" Adrian, Hannah, Robert and Sven. Thanks a lot. I would like to thank Uli, Tom and Sophie for proofreading this thesis. A special thanks goes to "Mr. Bond" Dieter, Ines and Thomas for the technical assistance and for lots of interesting discussions. It was great to know that I could always count on your help. Also, I thank our secretary Chris for support in numerous things.

I have appreciated very much the close collaboration with CNM and FBK, the manufacturers of the 3D detectors we investigated. Many thanks for providing the detectors. I am very grateful for numerous interesting discussions with Celeste and Giulio from CNM and Andrea, Gian-Franco and Marco from FBK.

I would like to thank Henri, Jaakko, Lenny, Panja and Teppo for organising the beam tests at the H2 beam line. Teppo, thank your for reconstructing the tracks and for answering me numerous questions. It has been a pleasure to benefit from your expertise. I also thank Hartmut and other colleagues from the RD50 collaboration for many valuable discussions. Special mention deserve also the colleagues from Karlsruhe, in particular Alexander, for performing the proton irradiations. Thank you for the great service.

Furthermore, I would like to express my appreciation to my family and my friends for giving me emotional support. And, to conclude: Katharina, thanks for you, thanks for everything.